10

ELECTROCATALYSIS AND FUEL CELLS

A. J. Appleby

Institute of Gas Technology
IIT Center
Chicago, Illinois 60616

Introduction

Electrocatalysis may be defined as the relative ability of different substances, when used as electrode surfaces under the same conditions, to accelerate the rate of a given electrochemical process.

Unlike catalytic effects in the conventional sense, the relative electrocatalytic properties of a group of materials at a given temperature and concentration of reactant and product are not necessarily constant. They may vary owing to the different dependence of rates on electrical potential; that is, variation in Tafel slope with substrate, for the same electrochemical reaction. These differences in Tafel slope may come about by variation of the symmetry factor from one substrate to another, or by changes in the adsorption isotherm of reaction intermediates. A problem of fundamental importance in assessing electrocatalytic behavior is, therefore, the rational potential at which relative reaction rates should be compared. It is generally considered that this potential should be the potential of zero charge (p.z.c.) of the particular substrate, as under these conditions there is no charge-dependent electric field to influence electron transfer rates (1).

It is more convenient in practice to measure rates at constant potential with respect to a standard electrode. Under these conditions, electronic factors which are involved in the chemical (p.z.c.) rate equation cancel, so that a simplified dependence of relative rate on free energies of adsorption of reaction intermediates results provided the symmetry factor is constant (2,3). This point will be more completely discussed below.

The concept of electrocatalysis is rather recent, and has arisen since the advent of research into fuel cells as a practical means of energy conversion. The performance of such devices depends, at the present stage of technology, almost entirely on problems concerning electrode reaction rates rather than, for instance, mass-transport processes. Typical H_2/O_2 fuel cells, working at low temperatures in acid electrolyte, are limited by the intrinsic rate of the oxygen electrode. To date, platinum is the most effective material for both hydrogen oxidation and oxygen reduction in acid medium. There is, however, a considerable difference in the relative rates at a given overpotential that can be maintained on a platinum electrode for these two processes. Under ordinary conditions, the hydrogen oxidation rate is approximately 10^7 times more rapid than that of oxygen reduction. This difference results in an effective loss in efficiency, due to cathode polarization, of perhaps 30 percent, and requires the use of platinum metal catalysts in high loadings. This slow rate of the oxygen-reduction reaction is well known, and is manifested in practice by the low open-circuit potential of the cathode which corresponds to rate control by an alternative process, the electrode potential being determined by platinum oxidation (4), or impurity oxidation (5), or by some parasitic redox process.

The hydrogen electrode process on platinum has one of the fastest specific rate constants known (apart from metal-metal ion reactions of reactive metals and some redox processes) in aqueous solutions, whereas oxygen reduction on platinum must by comparison be considered a very slow process, though it is by no means the slowest reaction that has been observed.*

One striking fact about reaction rates on different metal substrates is the wide range of rate constants that are encountered for the same process – for instance, some 10 orders of magnitude for the hydrogen electrode reaction (6), and at least 5 orders of magnitude for oxygen evolution on oxidized platinum (7). Recent work conducted in this laboratory has shown that rate constants for oxygen reduction on oxide-free noble metals in acid electrolyte vary by approximately 7 orders of magnitude. Wide rate variations for other types of reactions, for instance hydrocarbon oxidation, have been noted.

In this paper, past work on electrocatalysis will be briefly reviewed and correlated with some recent work on the electrocatalytic properties of Group VIII and Ib metals and alloys for the oxygen reduction reaction in acid solution. Some of the consequences of this study concerning the fuel cell oxygen electrode are discussed. In particular, the electrocatalytic mechanisms of the hydrogen and oxygen electrodes will be explored in detail, to determine the likelihood of future increase in O_2 electrode exchange currents.

The Mechanism of Electrocatalysis

In general, the study of specific reactions has given some insight into the factors controlling rates on different electrode substrates. The reactions most broadly studied for this purpose have been –

1. Hydrogen evolution in acid solution (6, 9, 10).
2. Oxygen evolution on noble metal oxides in acid solution (11,12).
3. Certain hydrocarbon reactions, for example, ethylene oxidation (13, 14).

In comparing reaction rates for a specific process on different metals, it is important to first ascertain that two necessary conditions are met:

1. The process in question must be the same on the group of metals – that is, the rate-determining step must be the same in each case, and the reaction path, at least as far as the rate-determining step, must also be the same.
2. The process has been compared on the different metals under the same conditions – that is, with the same surface preparation in solutions of the highest possible purity, so that poisoning of the electrode surface by adsorption of capillary-active matter is avoided.

---

* Oxygen reduction on gold (8), and hydrogen evolution on lead or mercury (6) are several orders of magnitude worse.

The Hydrogen Evolution Reaction

It is generally considered (15-22) that the mechanism of the hydrogen evolution reaction in acid solution on the majority of metals studied involves the sequence

$$H_3O^+ + M + e^- \rightarrow M - H + H_2O \text{ (Discharge reaction)} \qquad \text{Step I}$$

which is then followed by either

$$H_3O^+ + M - H + e^- \rightarrow M + H_2O + H_2 \text{ (Electrochemical or ion + atom reaction)} \qquad \text{Step IIa}$$

or

$$2M - H \rightarrow 2M + H_2 \text{ (Combination reaction)} \qquad \text{Step IIb}$$

where M is a surface site on the metal.

Attempts to correlate the overpotential of hydrogen evolution with the properties of the electrode substrate date back several decades. Bonhoeffer (23) in 1924 noted a connection between hydrogen overvoltage and the rate of catalytic hydrogen combination. Correlations between exchange current and interatomic distance (24-27), metal surface energy (28,29), cohesion energy (30), melting point (26), and compressibility (31), have been discussed by a number of authors. In a similar way, Bockris and co-workers (6,32-34) showed that the thermionic work function of the metal and its hydrogen overvoltage were empirically related. Horiuti and Polanyi (35), followed by other authors (36,37) had previously pointed out that the rate of the discharge reaction (I) should be increased (that is, the activation energy decreased assuming a constant entropy of activation) if the heat of adsorption of atomic hydrogen on the metal surface were high. Rüetschi and Delahay (9,38) attempted to establish this relationship by considering an approximate calculation of the S – H bond energy, based on the Pauling equation (39) as used by Eley (40) for chemisorption phenomena, i.e.,

$$D_{M-H} = \frac{1}{2}\left[D_{M-M} + D_{H-H}\right] + 23.06\left(X_M - X_H\right)^2 \qquad (1)$$

where D_{M-H} is the M – H bond strength, D_{M-M} is the metal-metal atom bond strength, D_{H-H} is the adsorbate bond strength, and X_M, X_H are the electronegativities of the metal and adsorbate respectively. As metal-metal atom forces are short range, D_{M-M} is equated to $L_s/6$ for close-packed metals (9), where L_s is the latent heat of sublimation. These authors (9) established that a good dependence of log rate on D_{M-H} existed, but they calculated the latter value neglecting the electronegativity terms; that is, they showed that for certain metals a correlation between L_s and the rate of the hydrogen electrode reaction existed. As L_s is closely related to hardness, cohesion energy, melting point, compressibility and surface energy, this relationship is in good agreement with other correlations based on these parameters (26,28-31). Conway and Bockris (6) developing earlier ideas of Bockris and his coworkers (32,34) showed

that an approximately linear relationship exists between log i and electronic work-functions for many metals with a second (inverse) relationship apparent for a few metals (Tl, Hg, Pb) with very low hydrogen evolution rates ($i_o \sim 10^{-11} - 10^{-13}$). They also point out that, because of the empirical linear relationships between work function and L_s, and work function and X_M, which hold for many metals, D_{M-H} can be written in the form

$$A\,\Phi^2 + B\,\Phi + C \qquad (2)$$

where Φ is the work function, and A, B, and C are constants. In consequence of this relation, and as log i_o and Φ are linearly dependent, a quadratic expression connects log i_o and the calculated (or experimental*) values of D_{M-H} (41,42).

The same authors show that other relationships exist between Φ and the percentage d character (% d contribution to intermetallic dsp single-bond orbitals) (43) which is a function of atomic number and interatomic distance (43,44). This serves to correlate earlier observations of rate dependence on the latter quantity (32). Similarly, a linear % d character-log i_o relation is observed for the transition metals.

The quadratic plot of log i_o (or overpotential) against D_{M-M} has, like the log i_o/Φ plot, two distinct approximately linear regions, with a positive slope for the transition metals and Group Ib, together with Al, Be, and Ga, whereas a negative slope appears for Hg, Tl, and Pb. Conway and Bockris (6) attribute this to the fact that on the latter three metals, which probably have much lower D_{M-H} values than calculated owing to their electronic structures, reaction I is rate determining, whereas on the remaining metals reaction IIa is rate determining.

Volcano Plots

We may, in principle, write the forward rate equations for Reactions I and IIa as follows:

$$(\mathrm{I}) \quad \vec{i} = F \cdot \frac{kT}{h}\,[M]\,[H^+]\exp - \frac{\vec{\Delta g}_o}{RT} - (1-\beta)\frac{\Delta G_H}{RT} - \frac{\beta F\varphi}{RT} \qquad (3)$$

$$(\mathrm{IIa}) \quad \vec{i} = F \cdot \frac{kT}{h}\,[H]\,[H^+]\exp - \frac{\vec{\Delta g}_o'}{RT} + \frac{\beta \Delta G_H}{RT} - \frac{\beta F\varphi}{RT} \qquad (4)$$

where [M], [H] and $[H^+]$ are the activities of metal sites, adsorbed hydrogen, and hydroxonium ions, Δg_o and $\Delta g_o'$ are metal independent (i.e., adsorption independent) free energies of the activated complex at $\varphi = 0$. ΔG_H is the free energy of adsorption of H, and φ is the potential with reference to an arbitrary reference electrode. The other symbols have their usual meanings. Following Frumkin (2), no expression for Φ, the work function, appears in the rate equation, as this quantity is self-cancelling (2,3,46).

---

* Experimental and calculated (metal-hydride) values of D_{M-H} are in relatively good agreement, but differ by about 15 kcal, due to the surface "image potential" (45).

Putting $\theta = [H]$ and $1 - \theta = [M]$, we have

$$\text{(I)} \quad \vec{i} = F \cdot \frac{kT}{h}(1-\theta)[H^+]\exp - \frac{\Delta g_o}{RT} - (1-\beta)\frac{\Delta G_H}{RT} - \beta\frac{F\varphi}{RT} \qquad (5)$$

$$\text{(IIa)} \quad \vec{i} = F \cdot \frac{kT}{h}\theta[H^+]\exp - \frac{\vec{\Delta g}'_o}{RT} + \frac{\beta\Delta G_H}{RT} - \beta\frac{F\varphi}{RT} \qquad (6)$$

Assuming that $\frac{\theta}{1-\theta} = (pH_2)^{1/2} \cdot \exp - \frac{\Delta G_H}{RT}$ (7)

That is, the Langmuir isotherm applies for the equilibrium process IIb,

$$\tfrac{1}{2}H_2 + M \rightarrow M - H$$

We can write $\theta = \dfrac{(pH_2)^{1/2}\exp - \Delta G_H/RT}{1 + (pH_2)^{1/2}\exp - \Delta G_H/RT}$ (8)

Substituting for θ, we obtain

$$\text{I} \quad \vec{i} = F \cdot \frac{kT}{h}\exp\left(-\frac{\vec{\Delta g}_o}{RT} - \beta\frac{F\varphi}{RT}\right)\cdot\frac{[H^+]\exp - (1-\beta)\Delta G_H/RT}{1 + (pH_2)^{1/2}\exp - \Delta G_H/RT} \qquad (9)$$

$$\text{II} \quad \vec{i} = F \cdot \frac{kT}{h}\left(\exp - \frac{\vec{\Delta g}'_o}{RT} - \beta\frac{F\varphi}{RT}\right)\cdot\frac{(pH_2)^{1/2}\cdot\exp(1-\beta)\Delta G_H/RT}{1 + (pH_2)^{1/2}\exp - \Delta G_H/RT} \qquad (10)$$

These equations are similar to those developed by Parsons (4) and Gerischer (48), and indicate that rates for both reactions have, under these conditions, the same dependence on ΔG_H. They indicate that log i would be, at fixed potential and fixed pH_2 and $[H^+]$, an ascending and descending linear function of ΔG_H with a maximum at $\Delta G_H = 0$. If ΔG_H is linearly coverage dependent, that is, if the Temkin isotherm applies, a development of these equations show that a similar relation between i. and ΔG_H, but with a plateau-like rather a sharp maximum around $\Delta G_H = 0$, should occur. Such plots were given the name "volcano plots" by Balandin (49), though he discussed catalytic rather than electrocatalytic cases.

It has been claimed (50) that this approach will explain the fact that metals such as Pb, Hg and Tl have low exchange currents ($\Delta G_H > 0$), whereas metals such as Pt or Pd (ΔG_H presumed to be ~ 0) have high values. In a similar way, metals with $\Delta G_H < 0$ (W, Mo, Ta) also have low exchange currents.

As ΔG_H values are not generally known, the general trend of this parameter is equated to the experimental (or calculated) ΔH_H (i.e., D_{M-H}) values (6,9) assuming that the standard entropy of adsorption is metal independent – that is, it corresponds only to the loss of 3 translational degrees of freedom (9). This assumption is, however, probably not justified, as there is evidence that a compensation effect between ΔS_H and ΔH_H exists. This implies that on surfaces where

D_{M-H} is high, ΔS_H is low owing to the high degree of order in the adsorbate. Similarly, on surfaces with a low D_{M-H}, increased adsorbate mobility and hence increased ΔS_H results. This is well illustrated by Breiter's (51) experimental correlation of ΔH_H and ΔS_H on platinum in different electrolytes where D_{M-H} is modified by differing degrees of anion adsorption.

A second, more important objection involves Parsons' (47) assumption that the adsorbed hydrogen on the surface of the electrode is in equilibrium with gaseous hydrogen via the combination reaction (Equation 7). On platinum, Parsons (47) has estimated the i_o of this reaction to be $\sim 10^{-2}$. As the process is non-electrochemical, it is hard to see how the $H_2 \rightarrow 2H$ equilibrium can be maintained in the Tafel region ($i > 10^{-1}$ A/sq cm). On this basis, it would therefore seem that this thermodynamic equilibrium is not the origin of the volcano-type $i - D_{M-H}$ relationship noted by Bockris and Conway (i increasing with D_{M-H} for Pb, Hg, Tl, decreasing with D_{M-H} for transition metals (6). The relative rates seem best explained by the exponential dependence of i on increasing D_{M-H} for the discharge reaction (Equations 5, 9) as suggested by Conway and Bockris (6,41,42,52), for Pb, Hg, and Tl, where low coverages of molecular hydrogen are encountered, and where ΔG_H is large and positive. For the Group Ib and transition metals (except platinoid metals at low overpotentials (53,55), and perhaps Fe (1)), the ion and atom reaction is considered to be rate determining (56). In this case, we can assume that the previous step, the discharge reaction (I) is in pseudo-equilibrium. The equilibrium condition for this process (assuming Langmuir conditions) is

$$\frac{\theta}{1-\theta} = [H^+]\exp - \Delta G_H/RT \exp - F\varphi/RT \qquad (11)$$

Hence

$$\theta = \frac{[H^+]\exp - \Delta G_H\, RT \exp - F\varphi/RT}{1 + [H^+]\exp - \Delta G_H/RT \exp - F\varphi/RT} \qquad (12)$$

where θ is the surface coverage in [H].

Substituting this in Equation 6 we obtain

$$\vec{i} \propto \frac{FkT}{h}[H^+]^2 \frac{\exp - (1+\beta)\, F\varphi/RT - \beta\Delta G_H/RT}{1 + [H^+]\exp - \Delta G_H/RT - F\varphi/RT} \qquad (13)$$

This expression has exactly the same form as Equation 10, and implies again that a volcano-type relation should occur, with i decreasing with decreasing ΔG_H (increasing D_{M-H}) for $\Delta G_H < 0$ (52,57). The latter condition implies a high coverage of H, and hence favors the ion and atom rate-determining step, as suggested by Conway and Bockris for these metals (6,52,56,57).

Heats of Activation and Frequency Factors

Heats of activation for the hydrogen evolution reaction are only available for a few metals. Glasstone, Laidler, and Eyring (58) quote some early values, which indicate general similarity of preexponential terms. Later values, obtained under conditions of high purity by Parsons (55) for the combination and discharge reactions on platinum, indicate that for both the heat of activation is about 5.2 kcal/mole at the reversible potential. In the same work, Parsons (55) (see also Temkin (59)) derives theoretically the preexponential terms of the combination, ion, and atom and discharge reactions. For the discharge reaction, the quantities are about 2 X 10^6 A/sq cm ($\theta \rightarrow 0$), and 2 X 10^7 A/sq cm ($\theta \rightarrow 1$); for the combination reaction 3 X 10^2 A/sq cm ($\theta \rightarrow 0$) and 2 X 10^7 A/sq cm ($\theta \rightarrow 1$); and for the ion plus atom reaction (assuming a mobile activated complex) 40 A/sq cm ($\theta \rightarrow 0$) and 10^4 A/sq cm ($\theta \rightarrow 1$). These values are in reasonable agreement with experiment (55).

Conway, Beatty, and DeMaine (60) measured activation energies on a series of copper-nickel alloys. They found that in each case the activation energy was temperature dependent, but that the value for copper was less than that for nickel (in agreement with other workers (61, 62)). The values for the alloys were nonlinearly dependent on the atom percentage of the components. However, at constant overpotential, the difference in the heats of activation on copper and nickel was shown to be reasonably consistent with experimental values of D_{M-H} on these metals, assuming Equation 13 applies in its simplified form for ΔG_H negative ($i \propto \exp + (1-\beta)\,\Delta G_H/RT$), hence energy of activation $\propto (1-\beta)\,\Delta H_H$. Hence, the fact that i_o on Ni is greater than that on copper indicates that in all probability the Arrhenius preexponential terms for these two metals are very different, and perhaps implies a higher coverage of H on nickel. Similarly, if coverage is markedly temperature-dependent, the nonlinearity of the Arrhenius plots is accounted for.

On the basis of Parsons' (55) and Temkin's (59) theoretical calculations and the experimental data of Conway et al. (60) the assumption of a constant ΔS_{act} (or preexponential factor, assuming θ to be constant) over a series of metals is improbable. It is clear from Equation 13, assuming ΔG_H is large and negative, that

$$i \propto \exp\,(1-\beta)\,\Delta G_H/RT$$

Hence, assuming that the preexponential factor is independent of the metal, we may write

$$2.303 \log i \propto (1-\beta)\Delta H_H/RT$$

Hence, with $\beta = \frac{1}{2}$, the slope of the linear log $i - \Delta H_H$ plot should be 1/4.6 RT (about 0.36). Data of Conway and Bockris (6,41) show that for metals with a large ΔH_H, the slope is appreciably less than this, again suggesting that the preexponential factor is important in determining the overall rate, and that a "compensation effect" between ΔH_{act} and the preexponential factor, as is often noted in gas-phase catalytic processes, appears to apply in this case.

Recently, Bockris, Damjanovic, and Mannan (10) have reexamined the hydrogen electrode reaction on a number of pure metal and alloy systems. The systems were chosen to maximize the change in one particular parameter – for instance, d-orbital vacancies or internuclear distance. The results obtained again show the dependence of rate constants on % d character and d-orbital vacancies. In addition, i_o appears to be linearly dependent on internuclear distance (which depends on L_s and electronegativity when other electronic characteristics are constant). Essentially, these results confirm that for similar systems, i depends on those characteristics which determine the strength of the M-H bond.

The general picture that emerges is an approximate dependence of log i_o on the heat of adsorption of atomic hydrogen, but experimental evidence of the effect of the preexponential factor in the rate expression is not at present available.

Electrocatalysis in Other Systems

Rüetschi and Delahay (63) have examined Hickling and Hill's (64) oxygen evolution overpotential data in terms of the strength of the M-OH bond, using arguments similar to those for the hydrogen evolution electrode. The rate-determining step for the oxygen evolution reaction in acid solution is generally accepted to be the water discharge reaction (65,66).

$$S + H_2O \rightarrow S\text{-}OH + H^+ + e^-$$

where S is an active surface site on the (oxidized) metal surface. On this basis, the heat of activation of the oxygen evolution reaction should depend on the strength of the S-OH bond. Rüetschi and Delahay (63) assumed that this could be equated to the bond strength of the metal hydroxide, which is reasonable in view of the fact that at oxygen evolution potentials, metallic electrodes are always covered with a superficial oxide layer, which reaches a thickness of several Ångströms on Pt (67).

Dahms and Bockris (13), and Kuhn, Wroblowa and Bockris (14) have examined ethylene oxidation in acid solution on a series of noble metals and alloys. The latter workers established that a volcano-type relationship existed when log i at constant overpotential was plotted against d-orbital vacancies or L_s. Approximately two orders of magnitude positive change in i was noted in going from Au to Pt, with a further negative change of approximately three decades through iridium, rhodium and ruthenium to osmium.

Ethylene oxidation was shown to have a negative reaction order on platinum, and this was interpreted by postulating that increasing ethylene coverage reduces the coverage of adsorbed OH radicals on the electrode (13). The OH is derived from the oxidation of water, and is directly involved in the chemical rate-determining step. This rate, on the ascending side of the volcano, is controlled by increasing metal-adsorbate bonds, whereas in the descending side the major influence is in the preexponential term of the rate expression – that is, the decreasing coverage of ethylene in the face of increasing –O or –OH adsorption.

A process of this type indicates a special case of electrocatalysis where increasing rate as the metal-adsorbate bond-strength increases is compensated by decreasing coverage due to competitive adsorption. This effect would be expected to be even more marked under the Temkin conditions of adsorption, where the strength of the metal-adsorbate bond falls as the total coverage of the adsorbate increases.

Oxygen Reduction on Phase Oxide-Free Precious Metals in Acid Solution

Recent work in this laboratory on the oxygen reduction reaction carried out on a range of precious metals and alloys in 85% orthophosphoric acid solution under high purity conditions indicates that initial electron transfer to an adsorbed oxygen molecule is rate determining on Group Ib and Group VIII metals and alloys, provided the metal surface was initially in the reduced condition – that is, it carried no phase oxide.

In all probability the rate-determining step also involves a proton, thus:

$$S + O_2 + H^+ + e^- \rightarrow SO_2H$$

This is in agreement with pH dependence work carried out on platinum electrodes in dilute perchloric acid at constant ionic strength (68) and is in general agreement with mechanisms suggested for other metals in acid electrolyte (69,70). At potentials above about 800 mV on platinum, 650 mV on rhodium, and 750 mV on palladium, intermediate coverages of absorbed oxygenated species derived from water oxidation are present on these metals (71,72,73). The coverage of these species is linearly potential dependent, and can be approximately described by the Temkin isotherm (72,73). On iridium (73), ruthenium (74), and osmium (75), high coverages of oxygenated compounds are present, and the coverage-potential relationship seems to be more nearly Langmuirian. On gold, very low coverages of the oxygenated compounds are noted (71), and again the appropriate isotherm is Langmuirian.

The rate of the forward reaction in oxygen reduction may be written

$$\vec{i} = \frac{kT}{h}\theta^*[H^+]\exp\frac{-\vec{\Delta}g_o - (1-\beta)\Delta G_p + \beta\Delta G_r}{RT}\exp\frac{-\beta F\varphi}{RT} \qquad (14)$$

where θ^* is the coverage with molecular oxygen, $\vec{\Delta}g_o$ is metal independent, ΔG_p is the standard free energy of adsorption of the reaction product (SO_2H), ΔG_r is the standard free energy of adsorption of oxygen molecules, and β is the symmetry factor. It is assumed that the standard state for θ is $\theta = 1/2$. If ΔG_p and ΔG_r are not potential dependent (that is, the Langmuir isotherm applies), the Tafel slope for this process will be $2RT/F$, if $\beta = 1/2$. This is experimentally observed on gold, silver, osmium, ruthenium, and iridium.

Oxygenated compounds are adsorbed on the electrode according to an equilibrium of the type (5,68)

$$S + H_2O \rightleftharpoons S\text{-}OH + H^+ + e^-*$$

The equilibrium condition for this reaction is

$$\frac{\theta}{1 - \theta^* - \theta} = k[H_2O]\,[H^+]^{-1} \exp\left(-\Delta G_{OH}/RT\right) \exp(F\phi/RT) \qquad (15)$$

where again θ^* is the coverage of molecular oxygen by direct absorption, ΔG_{OH} is the free energy of adsorption of $-OH$, and k is a metal-independent constant.

If we assume θ^* to be small compared with θ in the intermediate coverage range ($0.2 < \theta < 0.8$) where Temkin adsorption might be expected to apply, with $\theta/1-\theta$ approximately constant in this range of θ, we can write

$$\log [H^+] + \Delta G_{OH}\, RT = F\phi/RT + \text{const.} \qquad (16)$$

If we assume that the heat of adsorption of O_2H is similarly affected (68) by the changes in coverage, and heat of adsorption of OH, then with $\beta = 1/2$, and substituting Equation 16 in Equation 14 we obtain

$$i \propto [pO_2]\,[H^+]^{3/2} \exp(-F\phi/RT) \qquad (17)$$

which is in agreement with experimental data on platinum (68), palladium and rhodium. This equation assumes that $\theta^* \propto pO_2$ (that is, θ^* is small, and ΔG_r is small and independent of changes in θ). Under Temkin conditions of adsorption of $-OH$ the effective rate constant of the reaction falls as θ, hence potential, rises and the reaction can be considered to be progressively poisoned by adsorbed oxygen atoms or OH radicals.

It is of interest to consider the type of relation we would expect between the forward reaction rate of the reduction reaction and ΔG_p.

Assuming that molecular oxygen is adsorbed following the Langmuir isotherm, we can write

$$\frac{\theta^*}{1 - \theta^* - \theta} = [pO_2] \exp - \Delta G_r/RT \qquad (18)$$

where $1 - \theta^* - \theta$ is the available activity of vacant metal sites.

Hence, from Equations 18 and 15, at constant pO_2, H_2O and H^+

$$\theta^* = \theta k^{-1} \exp(\Delta G_{OH} - \Delta G_r - F\phi)/RT \qquad (19)$$

---

* The S-OH is probably oxidized further to S-O, but this causes no further change in the total coverage.

From Equation 15 , assuming that θ^* is small compared with θ

$$\theta = \frac{k \exp \left(F\phi - \Delta G_{OH}\right)/RT}{1 + k \exp \left(F\phi - \Delta G_{OH}\right)/RT} \qquad (20)$$

From Equations 14 , 19 , and 20 assuming $\beta = 1/2$

$$i \propto \frac{\exp - \Delta G_r/2RT \exp - \Delta G_p/2RT}{1 + k \exp \left(F\phi - \Delta G_{OH}\right)/RT} \exp - F\phi/RT \qquad (21)$$

As ΔG_p (free energy of adsorption of O_2H) and ΔG_{OH} (free energy of adsorption of OH) should change by similar amounts from metal to metal, Equation 21 can be written at constant θ

$$i \propto \frac{\exp - \Delta G_r/2RT \exp - \Delta G_{OH}/2RT}{1 + k \exp - \Delta G_{OH}/RT} \qquad (22)$$

This expression again has a maximum at $\Delta G_{OH} = 0$; increasing with ΔG_{OH} for $\Delta G_{OH} > 0$, and decreasing for $\Delta G_{OH} < 0$.

Experimental Data on Oxygen Reduction

Figures 1-5 show data for a range of metals and alloys for the oxygen reduction reaction of 85% orthophosphoric acid. Volcano plots are observed when i (at 25°C) at a potential of 800 mV with respect to a hydrogen electrode in the same solution are plotted against metal parameters that are known to influence heat of adsorption (L_s, d-orbital vacancies, % d character). In addition, a plot of i against the heat of adsorption of the oxygenated reaction intermediate is shown.

The latter has been calculated relative to the value for gold, assuming that Paulings' equation for heat of adsorption holds for the adsorbed product in the rate-determining step ($-O_2H$) and assuming that the electronegativity of oxygen in the adsorbate can be put equal to 3.5. Electronegativity values for the metals are derived from Gordy and Thomas (78) and L_s values are from Bond (76). Data are included here for a range of platinum-ruthenium alloy electrodes. In this case, each parameter plotted has been assumed to be directly dependent on the atomic composition of the solid solution.

Published polarization data on platinum-rhodium alloys in dilute sulfuric acid (79) make it appear that they could be accomodated on the rising side of the volcano in the same way as the Pt-Ru alloys and similarly, data on the platinum-gold and palladium-gold alloys (60) suggest that they would fall on the opposite side of the volcano.

In the present work it was possible to compare the heat of activation measured for each metal or alloy system with a calculated value (relative to platinum).† The S-O_2H bond strength (ΔG_p) calculated from Pauling's equation relative to that for platinum was substituted in Equation 14 , assuming $\beta = 1/2$, and ignoring changes in ΔG_r over the series of metals. A plot of this value against experimental activation energy at $\eta = -460$ mV is shown in Figure 6. For the materials exhibiting Temkin adsorption (Pt, Rh, Pd and some Pt-Ru alloys) a small correction had to be made to the experimental energy of activation because of the different value of the Tafel slope under those conditions. Horizontal lines on the plot indicate the uncertainty in the calculated values of heat of activation corresponding to ±0.1 unit uncertainty in metal electronegativity, whereas vertical lines are estimated experimental uncertainties in heats of activation. It can be seen that a satisfactory agreement exists between calculated and experimental values, thus confirming earlier suppositions that this should be the case. It should be noted that no satisfactory correlation was obtained for silver, whose Pauling electronegativity (1.9) predicts a much higher bond strength than would seem to be the case here.‡

It is clear that for this electrode system, the major differences in the rate over the series of metals studied are due to changes in preexponential factors rather than in heat of adsorption. In Figure 7, the experimental value of the preexponential factor for each metal or alloy has been plotted against the experimental heat of activation. For the Group VIII metals and alloys a very good "compensation effect" is exhibited with the preexponential factor increasing over more than five decades from osmium to platinum. Gold and silver have similar preexponential values, but substantially greater heats of adsorption, than those on platinum. From Equations 19 and 20 , assuming ΔG_r not to vary substantially over the series of metals examined (as implied in Figure 6), the coverage of molecular oxygen θ^* can be expected to be proportional to $(1 + k \exp - \Delta G_{OH}/RT)^{-1}$. It will therefore be low for metals of high negative ΔG_{OH} (e.g., osmium), and will rise as ΔG_{OH} increases. The rise will be slow, however, after $\Delta G_{OH} \sim 0$ (platinum). At least part of the variation in preexponential factors may be explained in this manner. It is also apparent that the entropy of the adsorbate may not be metal-independent, but may depend on the heat of adsorption. The experimental values of the preexponential factor on platinum, palladium, gold, and silver are high – of the same magnitude as those calculated by Parsons (55) for mobile adsorbates in the hydrogen reaction. Thus, it is probable that the loosely bound adsorbate on these metals is relatively mobile. Increasing heat of adsorption on going from platinum to osmium should decrease adsorbate mobility so that the adsorbate entropy, hence the standard free energy of the activated complex, is decreased.

‡ The observed difference between the activities of gold and silver in acid and alkaline solution is very striking.

† The absolute value of the O_2H bond strength cannot be determined, as the D_{X-X} value – that is, the strength of the O-O bond in a hypothetical diperoxyl compound – is indeterminate.

Summary and Application to Fuel Cells

It thus appears that the oxygen electrode reaction is thermodynamically limited on the noble metals. Preexponential factors of the rate-determining oxygen reduction reaction are close to those of the hydrogen electrode reaction, but heats of activation are very much higher. Attempts to reduce the heats of activation by increasing the heat of adsorption of reaction intermediates simply result in lowered rates due to compensating changes in the preexponential factor. The rate of the oxygen electrode reaction under Langmuir adsorption conditions is an ascending and descending function of the standard free energy of adsorption of $-O_2H$ (or similar oxygenated species), with a maximum when this quantity is equal to zero. This occurs approximately at platinum as is the case for -H in the hydrogen electrode reaction. Consequently, it seems to be highly improbable that the rate constants of the oxygen reduction mechanism on the noble metals in acid solution can be substantially increased from present levels.

Acknowledgment

The author wishes to thank the sponsors of the TARGET Fuel Cell Program, Pratt & Whitney Aircraft Division of the United Aircraft Corporation, for permission to publish this work, along with the members of IGT who helped in the preparation of the publication.

Literature Cited

1. J. O'M. Bockris and H. Wroblowa, J. Electroanal. Chem. 7 428 (1969).
2. A. N. Frumkin, Elektrokhimiya 1, 394 (1965).
3. R. Parsons, Surface Sci. 2, 418 (1964).
4. J. P. Hoare, J. Electrochem. Soc. 109, 858 (1962).
5. H. Wroblowa et al., J. Electroanal. Chem. 15, 139 (1967).
6. B. E. Conway and J. O'M. Bockris, J. Chem. Phys. 26, 532 (1957).
7. J. J. McDonald and B. E. Conway, Proc. Roy. Soc. London A269, 419 (1962).
8. M. A. Genshaw, A. Damjanovic and J. O'M. Bockris, J. Electroanal. Chem. 15, 163 (1967).
9. P. Rüetschi and P. Delahay, J. Chem. Phys. 23, 195 (1955).
10. J. O'M. Bockris, A. Damjanovic and R. J. Mannan, J. Electroanal. Chem. 18, 349 (1968).
11. P. Rüetschi and P. Delahay, J. Chem. Phys. 23, 556 (1955).
12. A. Damjanovic, A. Dey and J. O'M. Bockris, J. Electrochem. Soc. 113, 739 (1966).
13. H. Dahms and J. O'M. Bockris, J. Electrochem. Soc. 111, 727 (1964).
14. A. T. Kuhn, H. Wroblowa and J. O'M. Bockris, Trans. Faraday Soc. 63, 1458 (1967).
15. J. O'M. Bockris, Modern Aspects of Electrochemistry I, 198. New York: Academic Press, 1954.
16. R. Parsons, Trans. Faraday Soc. 47, 1332 (1951).
17. A. N. Frumkin, Z. Phys. Chem. A164, 121 (1933).
18. J. Heyrovsky, Coll. Czech. Chem. Comm., 9, 273 (1937).
19. J. Tafel, Z. Phys. Chem. A50, 641 (1905).
20. J. Horiuti and G. Okamoto, Sci. Pap. Inst. Phys. Chem. Res. Tokyo 28, 231 (1936).
21. J. Horiuti and M. Ikusima, Proc. Imp. Acad. Tokyo 15, 39 (1939).
22. K. Hirota and J. Horiuti, Bull. Chem. Soc. Jap. 13, 228 (1938).
23. K. F. Bonhoeffer, Z. Phys. Chem. A113, 199 (1924).
24. H. Leidheiser, J.A.C.S. 71, 3634 (1949).

25. E. N. Khomatov, Zhur. Fiz. Khim. 24, 1201 (1950).

26. N. Ontani, Sci. Repts. Research Inst. Tokoku Univ. A8, 399 (1956).

27. S. G. Christov and N. A. Pargarov, Z. Elektrochem. 61, 113 (1957).

28. H. Fischer, Z. Elektrochem. 52, 111 (1948).

29. G. I. Volkov, Zh. Fiz. Khim. 29, 390 (1955).

30. N. I. Kobozev, Zh. Fiz. Khim. 26, 112 (1952).

31. A. K. Lorents, Zh. Fiz. Khim. 27, 317 (1953).

32. J. O'M. Bockris, Trans. Faraday Soc. 43, 417 (1947).

33. J. O'M. Bockris, Chem. Rev. 43, 525 (1948).

34. J. O'M. Bockris and E. C. Potter, J. Electrochem. Soc. 99, 169 (1952).

35. J. Horiuti and M. Polanyi, Acta Physicochem. U.R.S.S. 2, 505 (1935).

36. J. A. V. Butler, Proc. Roy. Soc. London A157, 423 (1936).

37. R. Parsons and J. O'M. Bockris, Trans. Faraday Soc. 47, 914 (1951).

38. P. Rüetschi and P. Delahay, J. Chem. Phys. 23, 1167 (1955).

39. L. Pauling, The Nature of the Chemical Bond, 60. Ithaca N. Y.: Cornell Univ. Press, 1948.

40. D. D. Eley, J. Phys. Colloid Chem. 55, 1017 (1951).

41. B. E. Conway and J. O'M. Bockris, Naturwissenshaft. 43, 446 (1956).

42. B. E. Conway and J. O'M. Bockris, Nature 178, 488 (1956).

43. L. Pauling, Proc. Roy. Soc. London A196, 343 (1949).

44. L. Pauling, J.A.C.S. 69, 542 (1947).

45. R.C.L. Bosworth, Proc. Roy. Soc. N.S. Wales 74, 538 (1941).

46. L. I. Krishtalik, Elektrokhimiya 2, 229 (1966).

47. R. Parsons, Trans. Faraday Soc. 54, 1053 (1958).

48. H. Gerischer, Bull. Soc. Chim. Belg. 67, 506 (1958).

49. A. A. Balandin, Problems of Chemical Kinetics, Catalysis and Reactivity, 462. Moscow: Academy of Sciences, 1955.

50. P. Delahay, Double Layer and Electrode Kinetics, 265. New York: Interscience, 1965.

51. M. Breiter, Ann. New York Acad. Sci. 101, Art 3 709 (1963).

52. B. E. Conway, Trans. Roy. Soc. Can. 54, 19 (1960).

53. J. O'M. Bockris, Z. A. Ammar and A.K.M.S. Huq, J. Phys. Chem. 61, 879 (1957).

54. S. Schuldiner, J. Electrochem. Soc. 106, 891 (1959), 107, 452 (1960).

55. R. Parsons, Trans. Faraday Soc. 59, 1340 (1960).

56. B. E. Conway, Proc. Roy. Soc. London, A247, 400 (1958), A256, 128, (1960).
See also E. Yeager, Ed., Transactions of the Symposium on Electrode Processes, 267. New York: John Wiley, 1961.

57. B. E. Conway and J. O'M. Bockris, Can. J. Chem. 35, 1124 (1957).

58. S. Glasstone, K. J. Laidler and H. Eyring, The Theory of Electrode Processes, 588. New York: McGraw-Hill, 1941.

59. M. Temkin, Proceedings of Conference on Electrochemistry, 181. Moscow, 1953 (Russian text).

60. B. E. Conway, E. M. Beatty and P.A.D. DeMaine, Electrochim. Acta 7, 39 (1962).

61. J. O'M. Bockris and E. C. Potter, J. Chem. Phys. 20, 614 (1952).

62. J. O'M. Bockris and N. Pentland, Trans. Faraday Soc. 48, 833 (1952).

63. P. Rüetschi and P. Delahay, J. Chem. Phys. 23, 556 (1955).

64. A. Hickling and S. Hill, Disc. Faraday Soc. 1, 236 (1947).

65. J. O'M. Bockris and A.K.M.S. Huq, Proc. Roy. Soc. London A237, 277 (1956).

66. A. Damjanovic, A. Dey and J. O'M. Bockris, Electrochim Acta 11, 791 (1966).

67. A.K.N. Reddy, M. Genshaw and J. O'M. Bockris, J. Electroanal. Chem. 8, 406 (1964).

68. A. Damjanovic and V. Brusic, Electrochim. Acta 12, 615 (1967).

69. A. Damjanovic and V. Brusic, Electrochim. Acta 12, 1171 (1967).

70. A. I. Krasil'shchikov, Soviet Electrochemistry II, 151. New York: Plenum Press, 1961.

71. F. G. Will and C. A. Knorr, Z. Elektrochem. 64, 270 (1960).

72. W. Böld and M. Breiter, Electrochim. Acta 5, 145 (1961).

73. W. Böld and M. Breiter, Electrochim. Acta 5, 169 (1961).

74. G. P. Khomchenko, T. N. Stayanovskaya and G. D. Vovchenko, Zh. Fiz. Khim 38, 434 (1964).

75. G. P. Khomchenko, N. G. Ul'ko and G. D. Vovchenko, Elektrokhimiya 1, 659 (1965).

76. G. C. Bond, Catalysis by Metals, 489-90. New York: Academic Press, 1962.

77. M.L.B. Rao, A. Damjanovic and J. O'M. Bockris, J. Phys. Chem. 67, 2508 (1963).

78. W. Gordy and W.J.O. Thomas, J. Chem. Phys. 24, 439 (1956).

79. J. P. Hoare, Extended Abstracts of the 19th Meeting CITCE, 38, Detroit, 1968.

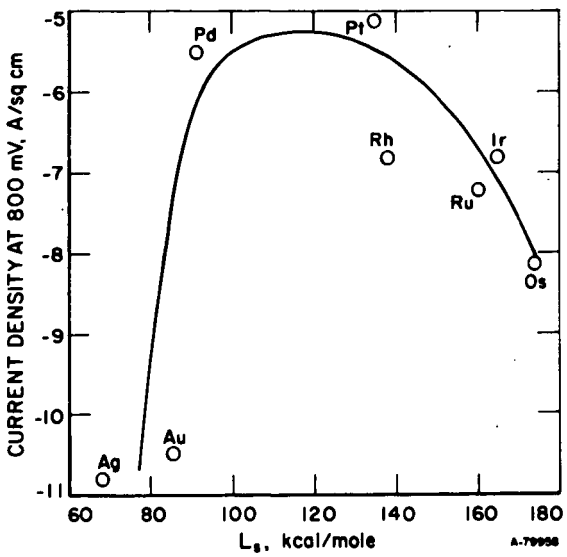

Figure 1. O_2 Reduction in 85% Orthophosphoric Acid: Plot of i at η = −460 mV at 25°C Against Latent Heat of Sublimation of Electrode Metal. (Latent heat of sublimation values are from Bond (77).)

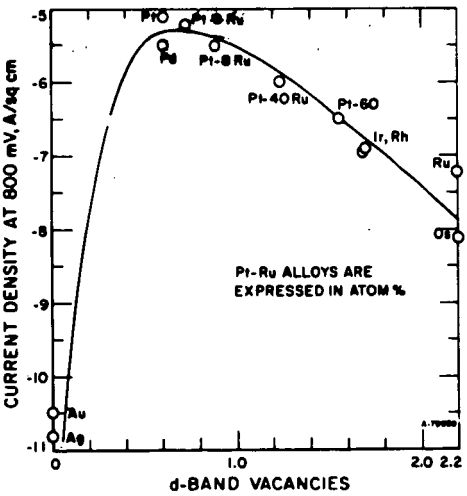

Figure 2. O_2 Reduction in 85% Orthophosphoric Acid: Plot of i at η = −460 mV at 25°C Against d-Orbital Vacancy Value of Electrode Metal. (For d-orbital vacancy values, see Ref. 18. The value for osmium has been considered to be the same as that for ruthenium and iron.)

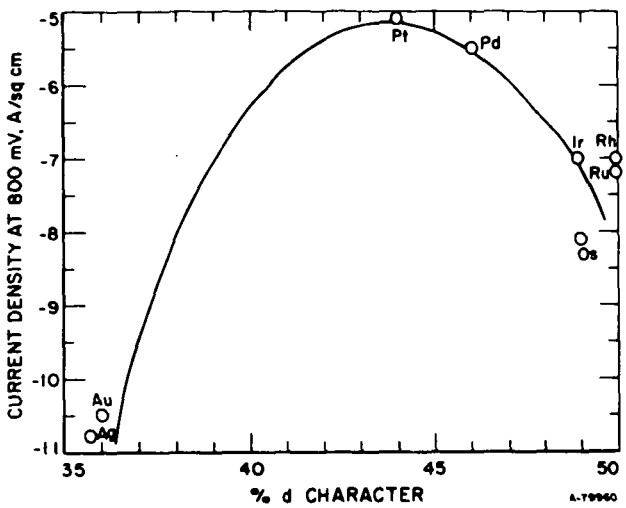

Figure 3. O_2 Reduction in 85% Orthophosphoric Acid: Plot of i at η = −460 mV at 25°C Against % d Character of Electrode Metal. [% d character values (calculated where necessary) from Ref. 43.]

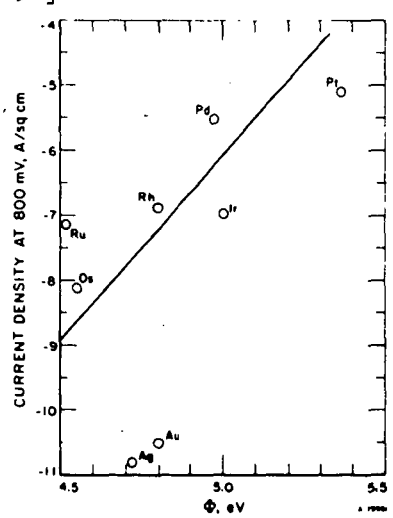

Figure 4. O_2 Reduction in 85% Orthophosphoric Acid: Plot of i at η = −460 mV at 25°C Against Electronic Work Function of Substrate Metal. Φ Values are "Preferred" Values, Except Ru, Os, Ir. Values for Pt (C. W. Oatley, Proc. Phys. Soc. 51, 318 (1939)), Ru and Os (O. Klein and E. Lange, Z. Electrochem. 44, 542 (1938))are by Contact Potential Method. Value for Rh (H.B. Wahlin and L. V. Whitney, J. Chem. Phys. 6, 594 (1938)) is by Thermionic Emission. Values for Pd (L. A. Dubridge and W. W. Roehr, Phys. Rev. 37, 1269 (1931)), and Au (L. W. Morris, Phys. Rev. 37, 1263 (1931)) are by the Photoelectric Method. The Value for Ir is From Ref. 13

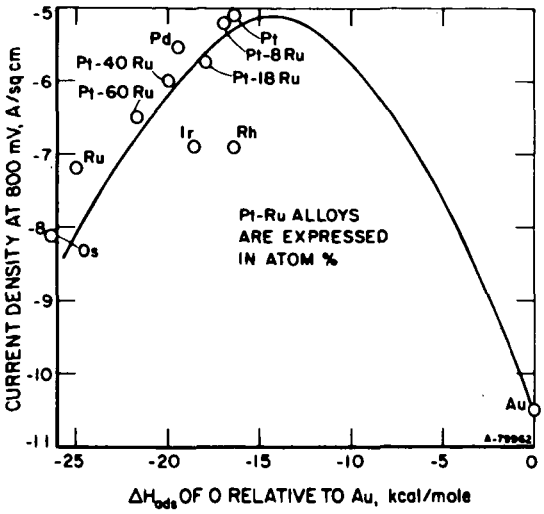

Figure 5. O_2 Reduction in 85% Orthophosphoric Acid: Plot of i at $\eta = -460$ mV at 25°C Against Calculated M–O Adsorbate Bond Strength (Relative to Au).

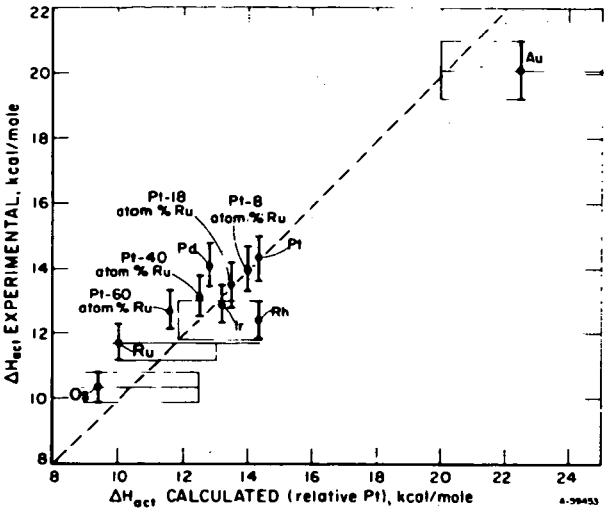

Figure 6. O_2 Reduction in 85% Orthophosphoric Acid: Plot of Experimental Heat of Activation (at η = −460 mV) Against Calculated Value (Relative to Pt).

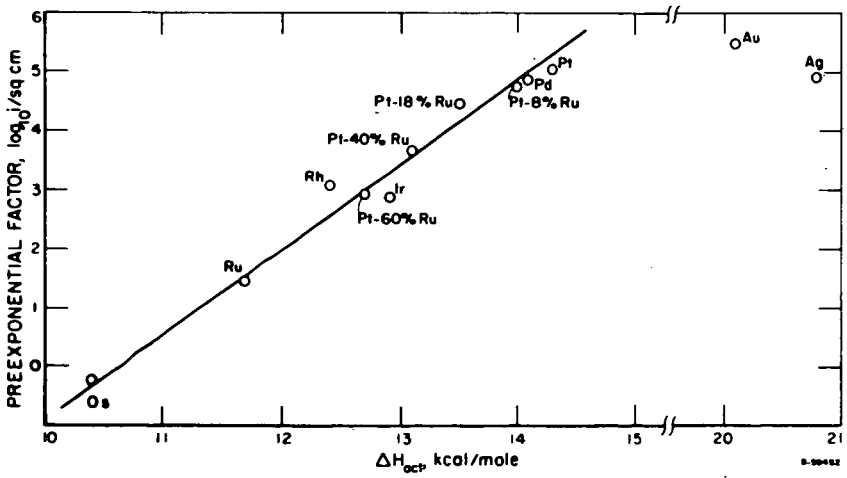

Figure 7. O_2 Reduction in 85% Orthophosphoric Acid: Plot of Experimental Heat of Activation (at η = −460 mV) Against Preexponential Factor.

THE EFFECT OF ADSORPTION OF NEUTRAL AND IONIC SPECIES ON THE KINETICS OF REDUCTION OF OXYGEN AT PLATINUM ELECTRODES

S. Gilman and L. D. Sangermano

NASA/Electronics Research Center
575 Technology Square
Cambridge, Massachusetts 02139

ABSTRACT

The kinetics of electrochemical reduction of oxygen at platinum electrodes is sensitive to the presence of surface-active substances in solution. In acid solutions, the effect of anions and of organic substances is particularly pronounced while in alkaline solutions heavy-metal ions produce the most striking effects. Adsorption from acid solutions has received considerable attention over the past decade but few detailed studies have been performed in alkaline solutions. In the present investigations, the surface of a "clean" polycrystalline platinum electrode was characterized in KOH solutions by means of voltage-sweep techniques. Time effects were studied as a function of solution purity and as a function of controlled additions of carbonate and other common contaminants. Preliminary studies were made of the kinetics and thermodynamics of heavy-metal ion adsorption.

REDUCTION OF OXYGEN ON PLATINUM BLACK AT FUEL CELL ELECTRODES

W. M. Vogel and J. T. Lundquist

Advanced Materials Research and Development Laboratory
Pratt & Whitney Aircraft
Middletown, Connecticut 06457

Introduction

A problem common to the development of fuel cell electrodes and to the evaluation of catalysts has always been the difficulty of separating the effects of the electrode structure from the more fundamental limitations imposed by the intrinsic activity of the particular catalyst. In the past the problem has been attacked theoretically by assuming a model. The current-potential curves for certain porous electrodes can be predicted if the kinetics of the electrode process, the diffusion coefficients and ionic mobilities are known. Thus theories have been developed[1,2] for the Teflon bonded gas diffusion electrode.[3] There can be little doubt about the basic validity of the model used in these treatments.[4]

The usefulness of such theories, however, is severely limited if, as is often the case, the kinetics of the electrode process is not well known. To calculate the kinetic parameters from the overall polarization curve of a porous electrode has been apparently beyond previous capabilities.[5] As a result, in many instances neither the intrinsic electrocatalytic activity of the catalyst nor the structural details of a given electrode could be determined from experiments with such porous electrodes. This was especially true for the reduction of oxygen at Teflon bonded electrodes catalyzed with platinum black. The kinetic parameters for this reaction are poorly known, with the reported data applying mostly to smooth platinum and depending strongly on pretreatment and trace impurities in the electrolyte.

We have studied the reduction of oxygen at platinum catalyzed Teflon bonded porous electrodes in aqueous solutions of KOH, H_2SO_4 and H_3PO_4. A procedure was used which produced current potential curves essentially free of internal iR losses so that kinetic parameters for the electrochemical reaction could be obtained.

Experimental

Methods

The internal iR loss of a porous electrode should become negligible for low catalyst loadings L, i.e., for thin electrodes. A plot of I, the current per 1 cm^2 of electrode area at constant potential, versus the loading should, at low values of L, yield almost straight lines. The initial slope of these curves $i \equiv (dI/dL)_{L=0}$ (ma/mg) represents the current per 1 mg of catalyst loading without internal iR loss. The gas concentration overvoltage within the catalyst agglomerates is not excluded.

These iR-free data were then replotted as log i versus the potential. At small values of i the concentration overvoltage now becomes negligible and the plots yield the exchange current (per 1 mg of catalyst) and the Tafel slope for the electrochemical reaction.

As an independent check the oscillographic potential decay curves were analyzed in a few instances where the internal iR loss could be assumed to be negligible.

Electrodes

It is essential for the procedure just outlined that electrodes be made in such a way that a change in the loading does not produce a qualitatively different structure. Ideally only the electrode thickness should vary. The experimental results indicate clearly whether one is successful in this undertaking. However, we know of no method which will predictably produce the desired results.

It was found that a number of different methods produce satisfactory electrodes. The kind used in this work were the easiest to make and the most reliable.

A layer of Teflon (TFE 30, approximately 1 mg/cm^2) was sprayed on aluminum foil. This layer was air dried, vacuum dried and subsequently sintered to produce a thin porous sheet of Teflon. Upon this layer was sprayed catalyst containing Pt black and 30 W% TFE 30. At this Teflon content the maximum performance was obtained, falling off at higher and lower values. (Different Pt blacks sometimes require different Teflon contents to give maximum performance.) The Pt black was a product of Engelhard Industries and had a specific surface area of 24 m^2/g. The catalyst/Teflon layer was air dried and then lightly compacted with a roller pressed down by hand. Subsequently the electrode was vacuum dried and sintered. A current collector screen was pressed lightly into the catalyst layer. The screen material was pure nickel (for experiments in KOH) or gold plated tantalum (for acids). Finally the aluminum foil was dissolved by treatment with the respective electrolyte to be used. The electrode was washed with distilled water and dried at 120°C.

Apparatus

The measurements were made with the apparatus depicted in Figure 1. The test electrodes were mounted in a screw cap holder and current pick up was made via a platinum ring in contact with the current collector screen of the electrode. The electrode holder was made of Plexiglas[(a)] for use in KOH or of Lexan[(b)] for use in the acids.

The reference was a hydrogen electrode used in conjunction with a Luggin capillary of the design shown in Figure 2. Other designs than that in Figure 2 were tried but, at high current densities, gave poor results.

The cell was a 500 ml jacketed glass reaction kettle. The temperature was controlled by means of an external circulating constant temperature bath. Reagent grade chemicals were used without further purification.

Electrode polarizations were measured galvanostatically employing two 12 volt batteries of high capacity (automobile type) in series and variable resistances in series with cell and batteries. The external iR loss between electrode surface and opening of Luggin capillary was determined from oscilloscopic potential-time traces on turning the current on and off. A relay with mercury wetted contacts[(c)] was used for this purpose. The highest currents used were established with this setup in less than approximately 1 μ second. The time traces were measured with an oscilloscope[(d)] in conjunction with a camera.

Experimental Procedure

In Figure 3 the external iR-losses measured when the current is turned on (η_Ω)

(a) Product of Rohm and Haas.
(b) Product of General Electric Company.
(c) Potter and Brumfield, JMP 8120 12.
(d) Tektronix, Model 561A with plug-in units 3A7 and 3B3.

and on turning it off (η_Ω') are plotted as a function of the current. Approximately 5 minutes elapsed between the two measurements. The plot of η_Ω is linear and the slope equals that calculated from the electrolyte conductance for this particular geometry.

The plot is not linear for η_Ω' values of which fall below the line at high currents. This deviation is due to the changes in temperature and electrolyte concentration in front of the electrode.

By the time the electrode polarization is established the external iR-loss has changed. By using the final value (η_Ω') this effect is eliminated. However, another one is introduced: the concentration change also results in a liquid junction potential ϵ_D and a pH drop between capillary tip and electrode. Both effects decay slowly and are, therefore, not eliminated with the iR measurement. In order to eliminate these external non-ohmic potential drops one would use the initial value η_Ω rather than the value on current interruption (η_Ω'). Based on past experience[6] we believe that the error due to these sources is considerably smaller than the error caused by the temperature change. We therefore used the final value η_Ω' to correct for the external iR loss.

The compromise necessary for correcting the polarization data introduces an unavoidable error which, however, becomes significant only at very high current densities.

The electrodes were prepolarized at low potentials to remove the initial oxygen coverage from the platinum surface. The electrode was then allowed to drift back to 1000 mV after which the measurement was made.

Results and Discussion

The experimental results obtained for 85% H_3PO_4 at 120°C are presented in Figure 4 and Figure 5 for air (1 atm) and Figures 6 and 7 for oxygen (1 atm). Within the experimental reproducibility the curves are linear below certain loadings.

Similar data were measured for 30% KOH at 70°C, for 20% H_2SO_4 at 70°C and for 50% H_3PO_4 at 70°C, all for air (1 atm) and for oxygen (1 atm). The data follow the same general pattern as those in Figures 4 to 7.

Within the initial approximately linear portion of these curves the internal iR loss is very small, certainly smaller than the reproducibility of the results. This means that the potential was the same for every catalyst particle in the electrode and it is physically meaningful to normalize the data by dividing the observed currents by the catalyst loading. The resulting specific current (per mg of catalyst) is proportional to the true current density at the Pt-electrolyte interphase if the concentration overvoltage is negligible, i.e., at low currents and especially on pure oxygen.

Plots of specific currents versus the potential are presented in Figures 8 and 9. This method of plotting the data has the advantage that the difficulties encountered in eliminating the external iR drop at high current densities (I) (per unit electrode area) are largely avoided: quite large specific currents (i) can be obtained at low overall current densities I if the catalyst loading is low. At the other end of the scale problems sometimes occur stemming largely from the increasing influence of impurities in the electrolyte on the performance of very lowly loaded electrodes. This problem is eliminated by measuring the small specific currents at highly loaded electrodes and consequently fairly large external currents. Under these conditions impurities in the electrolyte are ineffective because of the very large ratio of platinum surface to electrolyte in the electrode pores.

The semi-logarithmic plots for pure oxygen in H_2SO_4 and in KOH are linear over such a wide current range that we feel justified in calculating specific exchange currents and Tafel slopes from the curves in Figure 8. The results are given in Table I.

Table I

Values for i_o and b at P_{O_2} = 1 atm obtained from steady state data.

Electrolyte	Temperature	b (mv)	i_o (A/mg)	i_o (mA/cm^2)[a]	E* (mV)[7]
30 W% KOH	70°C	50 ± 5	0.9×10^{-4}	4×10^{-10}	1195
20 W% H_2SO_4	70°C	64 ± 5	1×10^{-4}	4×10^{-10}	1186
50 W% H_3PO_4	70°C	60 ± 5	$\sim 1 \times 10^{-4}$	$\sim 4 \times 10^{-10}$	1175
85 W% H_3PO_4	120°C	60 ± 5	$\sim 1 \times 10^{-4}$	$\sim 4 \times 10^{-10}$	1191

[a] Using 24 m^2/g for specific surface area of the Pt black. This value based on BET and hydrogen stripping experiments.

Included in Table I are values for H_3PO_4 although the data in Figure 8 are not sufficient to accurately extrapolate to equilibrium potential. In H_3PO_4 the concentration overvoltage becomes noticeable at relatively low currents even on pure oxygen. The kinetic data in this case were obtained by determining the Tafel slope b from the oscilloscopic traces and then extrapolating the low current end of the curve in Figure 8 with this value for b.

The Tafel slope was determined by assuming that the electrode capacity C* is potential independent below approximately 800 to 850 mV. We further assumed that at not too large currents the concentration of oxygen at the catalyst surface is approximately constant for a short time after the polarizing current is interrupted. With these assumptions we can integrate the equation for the current after interruption.

$$(1) \qquad 0 = i = i_c + i_F = C^* \frac{dE}{dt} - kce^{-\frac{2.3}{b} E} .$$

In (1) i, i_c and i_F are the total, the charging and the Faradaic currents respectively, E is the electrode potential (iR free since experiment is done within linear range of curves in Figures 4 to 7), k is a constant and b the Tafel slope.

The integration of (1) yields

$$(2) \qquad E = K_1 + b \log (K_2 + t)$$

$$K_1 \equiv b \log \frac{2.3\ kc}{b\ C^*}$$

$$K_2 \equiv \frac{b\ C^*}{2.3\ kc} \exp \frac{2.3\ E\ (t=0)}{b}$$

By varying K_2 until the plot of log $(K_2 + t)$ versus E is a straight line we can determine the Tafel slope b as the slope of this linear plot.

Furthermore we have

$$(3) \qquad \frac{dE}{dt} = \frac{b}{2.303\ (K_2 + t)}$$

$$(4) \qquad \left(\frac{dE}{dt}\right)_{t\,=\,0} = \frac{b}{2.303\ K_2} .$$

The capacity C^* is then given by

$$(5) \qquad C^* = \left(\frac{i_F}{dE/dt}\right)_{t=0}$$

$(i_F)_{t=0}$ is equal to the external current before interruption. We can therefore determine the product k·c from the value of K_1 (or K_2). In Figure 10 plots of log (K_2 + t) versus E are given for the following two cases:

(I) 20% H_2SO_4
P_{O_2} = 1 atm
70°C
L = 4.9 mg Pt/cm^2
i = 300 ma/cm^2

(II) 85% H_3PO_4
P_{O_2} = 1 atm
120°C
L = 4.9 mg Pt/cm^2
i = 300 ma/cm^2

The parameters of these curves (Figure 10) are presented in Table II.

Table II

Determination of Tafel parameters from oscilloscopic E-t traces after current interruption for experiments I and II above.

	K_1 (mv)	K_2 (m sec)	b (mV)	$(dE/dt)_{t=0}$ (Volt/sec)	C^* (μF/cm^2)	kc (ma/cm^2)	i_o (A/cm^2)
I (H_2SO_4)	766	8.0	66	3.56	84.3	9.77×10^{13}	1.1×10^{-4}
II (H_3PO_4)	760	2.5	57	9.90	30.3	1.6×10^{16}	4.3×10^{-5}

The data in Table II are referred to 1 cm^2 external electrode area. The value for the exchange current in H_2SO_4 is for saturation concentration at P_{O_2} = 1 atm since the concentration overvoltage in this case was negligible (see Figure 8). Using the value 24 m^2/g for the specific surface area of the catalyst black we have for the true exchange c.d. $i_o = 1 \times 10^{-10}$ A/cm^2. The agreement with the steady state data (Table I) is satisfactory.

The value for i_o in Table II for H_3PO_4 is of little value because it refers to an unknown value for the oxygen concentration which, however, by evidence of the curve in Figure 8 was less than the solubility at P_{O_2} = 1 atm.

Additional data, also obtained from oscilloscope traces, are listed in Table III. The agreement with the steady state results again is satisfactory.

The data for H_3PO_4 in Table I agree with those determined[8] from experiments on smooth platinum surfaces in highly purified electrolyte.

Table III

Tafel slopes determined from oscilloscope traces for P_{O_2} = 1 atm.

Electrolyte	Temp. (°C)	L (mg Pt/cm^2)	i (ma/cm^2)	b (mV)
30% KOH	70	6.0	840	50
30% KOH	70	3.9	840	51
20% H_2SO_4	70	6.0	1000	67
20% H_2SO_4	70	3.9	1000	70

Curves such as those in Figures 8 and 9 have proven very useful in comparing different catalysts. For this purpose one has to make electrodes which yield curves like II in Figure 8. Other possible applications exist in such development work as reduction in catalyst loading or agglomerate size where progress can be seen clearly by comparing suitably reduced data with those in Figures 8 or 9. The data also indicate how far any structural improvements can possibly be carried.

The shape of the curves for KOH is of particular interest. Curves of this shape, with a sharp bend into a limiting current are not observed for electrodes which do not have porous Teflon backing at the gas side. The present curves have the general form usually expected for a flat sheet electrode with a Nernst diffusion layer. We believe that this behavior is the result, at least in part, of internal flooding of the electrode caused by the same process which, in the absence of a Teflon backing forces electrolytes out the back of the electrode. This force on the electrolyte increases with the current density and produces an increased thickness of the electrolyte film which covers the porous catalyst agglomerates. Thus this electrolyte film depends on the current density and, at high currents, sharply limits the current.

References

(1) R. Brown and L. A. Horve, Abstract No. 203, ECS Meeting, May 1967.

(2) J. Giner and C. Hunter, Abstract No. 327, ECS Meeting, October 1968.

(3) L. W. Niedrach and H. R. Alford, J. Electrochem. Soc., 112 (1965) 117.

(4) J. Giner, J. M. Parry, S. Smith, and M. Turchan, Abstract No. 328, ECS Meeting, October 1968.

(5) E. Yeager, "The Study of the Kinetics of Electrode Processes," Contract No. Nonr. 2391(00), Office of Naval Research, June 30, 1967, AD 673 096.

(6) J. Lundquist and W. Vogel, Abstract No. 335, ECS Meeting, October 1968.

(7) Measured against the hydrogen electrode (P = 1 atm) in the same medium. Standard potentials from: J. Llopis and J. Giner, Quimica, L(B) (1954) 921.

(8) A. J. Appleby and A. Borucka, Abstract No. 338, ECS Meeting, October 1968.

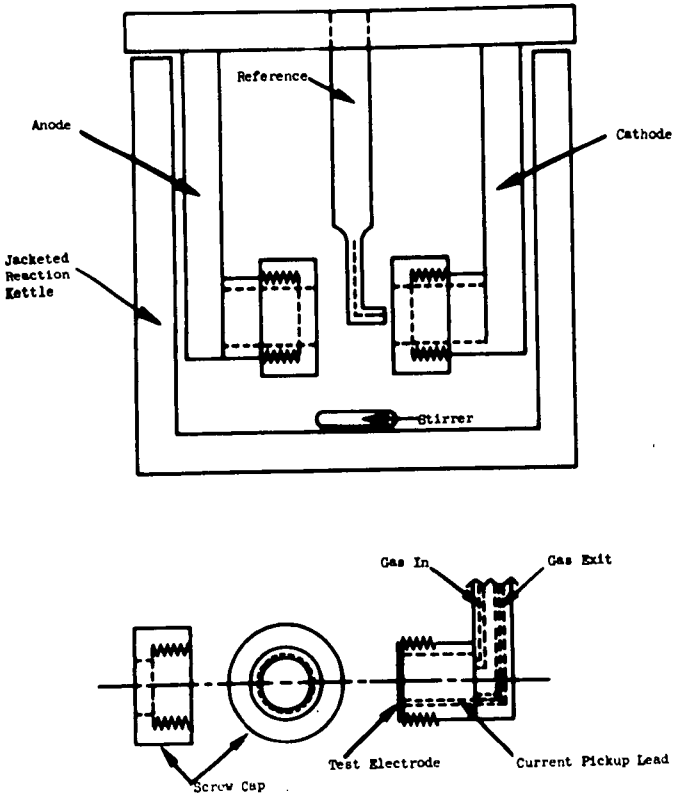

Figure 1. Cell Design

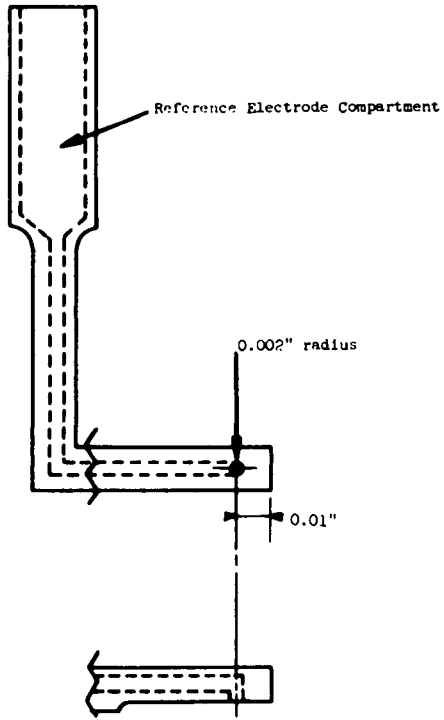

Figure 2. Reference Electrode Assembly

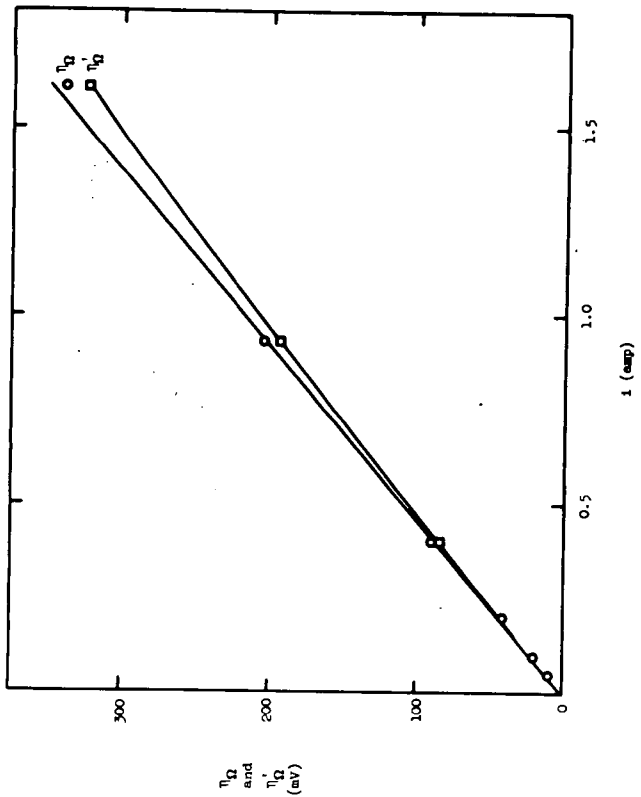

Figure 3. Variation of η_Ω and η_Ω' with Current. Electrode area was 2.81 cm^2.

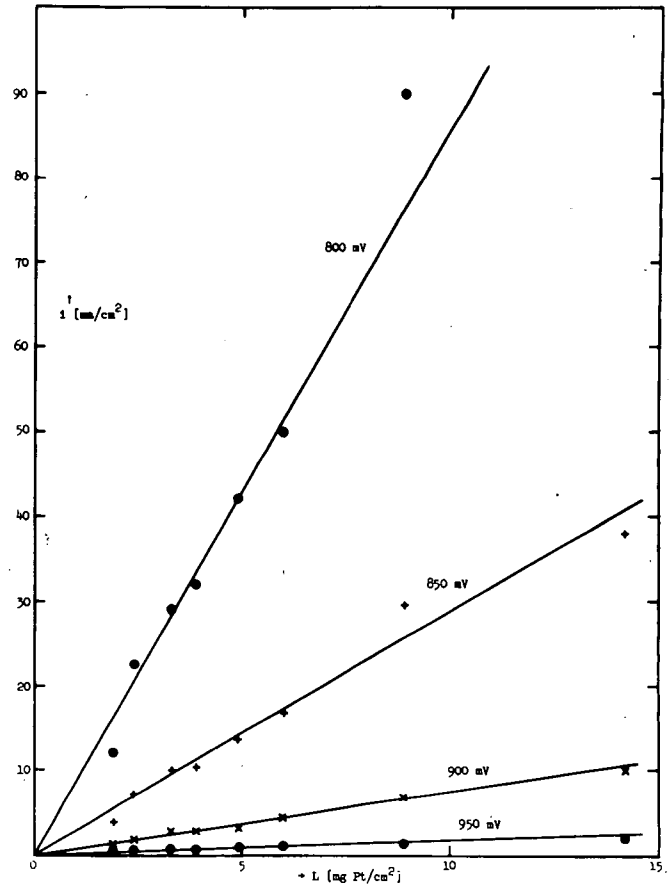

Figure 4. Performance on Air 120°C, 85 W% H_3PO_4

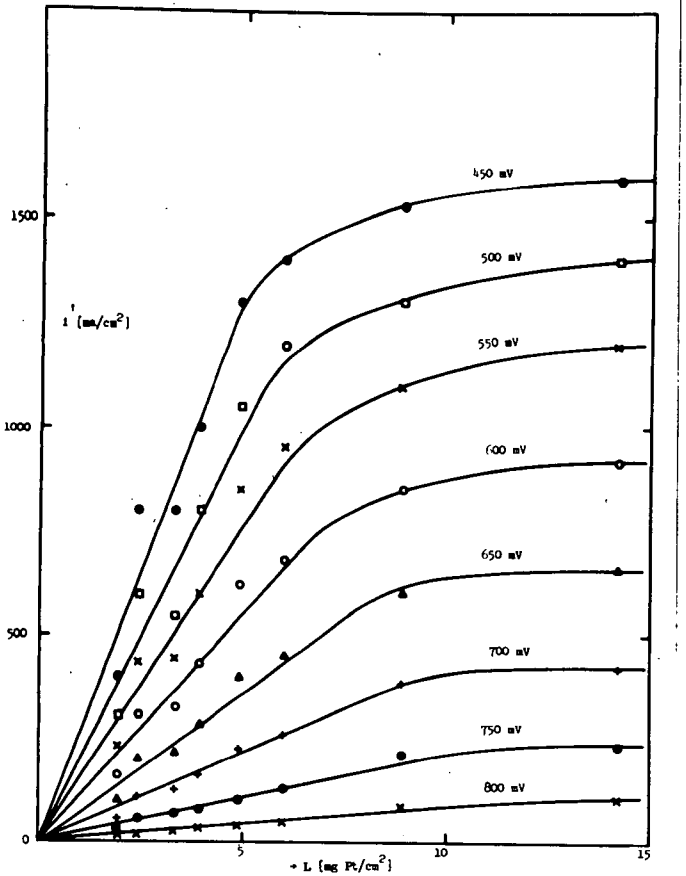

Figure 5. Performance on Air
120°C, 85 W% H_3PO_4

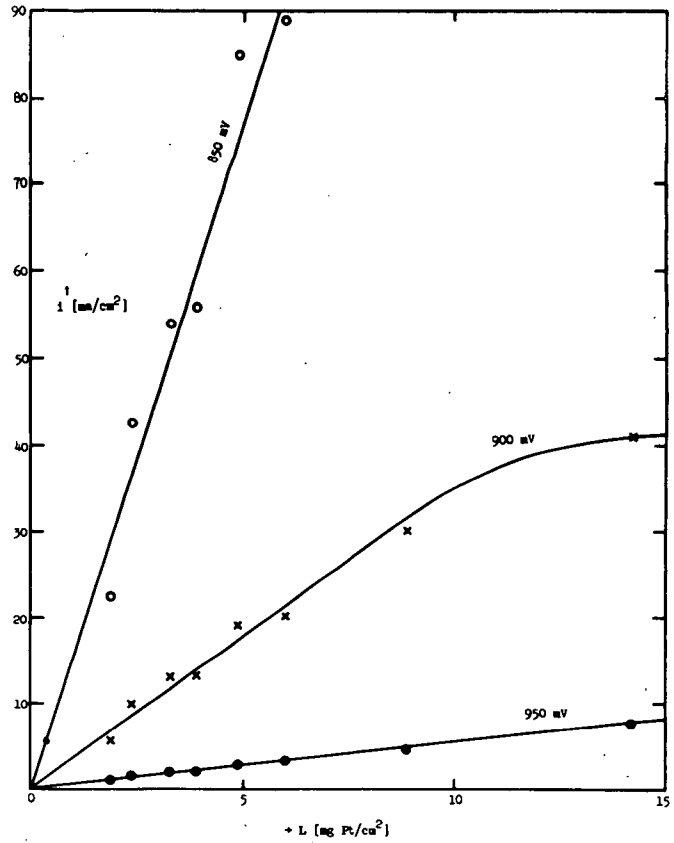

Figure 6. Performance on Oxygen
120°C, 85 W% H_3PO_4

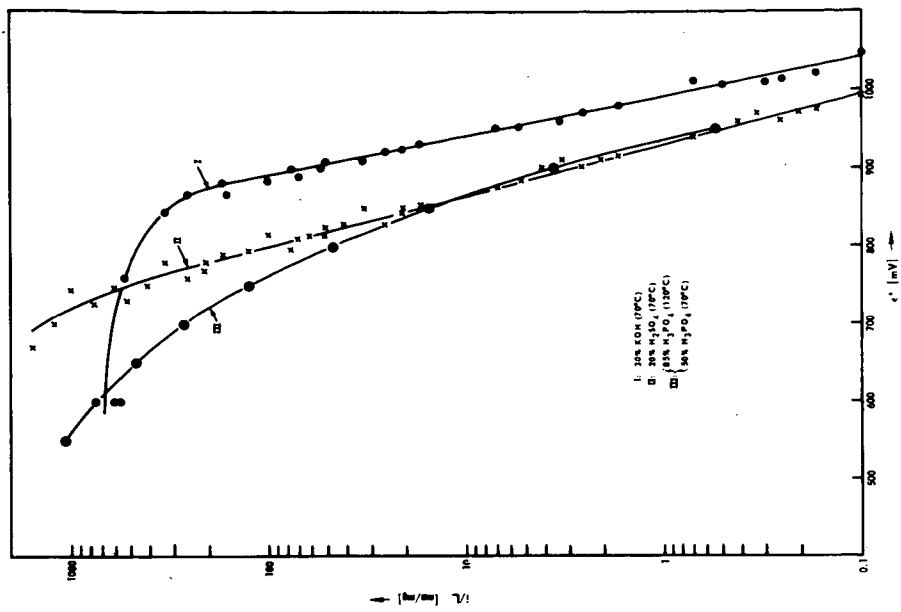

Figure 8. Polarization Curves for Oxygen Normalized to 1 mg Pt/cm^2

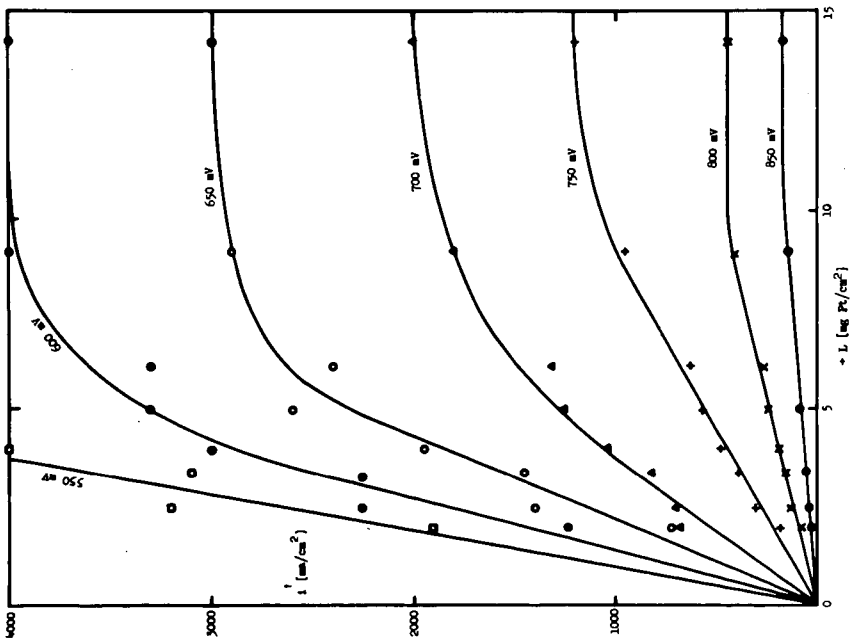

Figure 7. Performance on Oxygen 120°C, 85 W% H_3PO_4

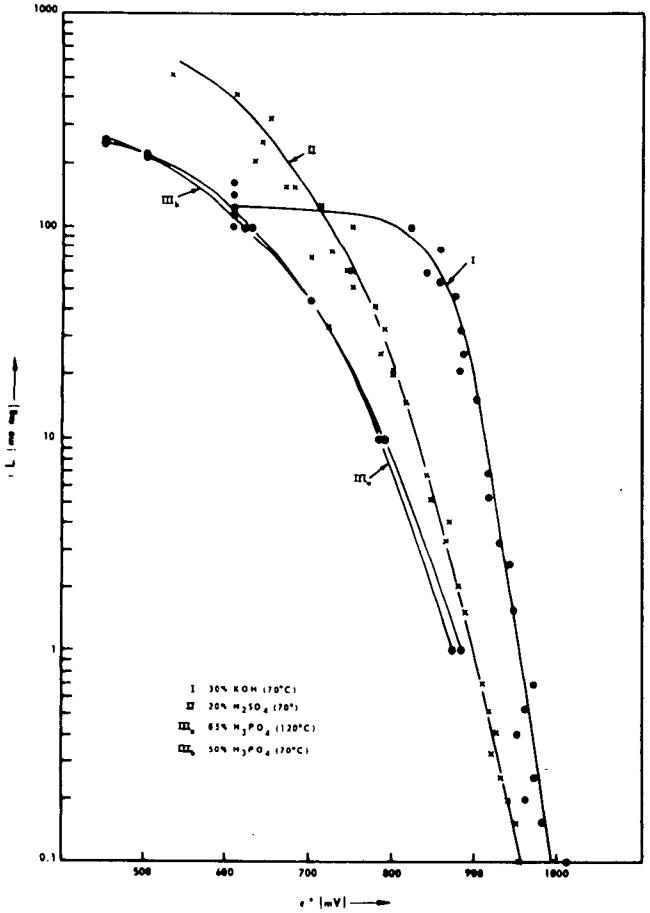

Figure 9. Polarization Curves for Air Normalized to 1 mg Pt/cm^2

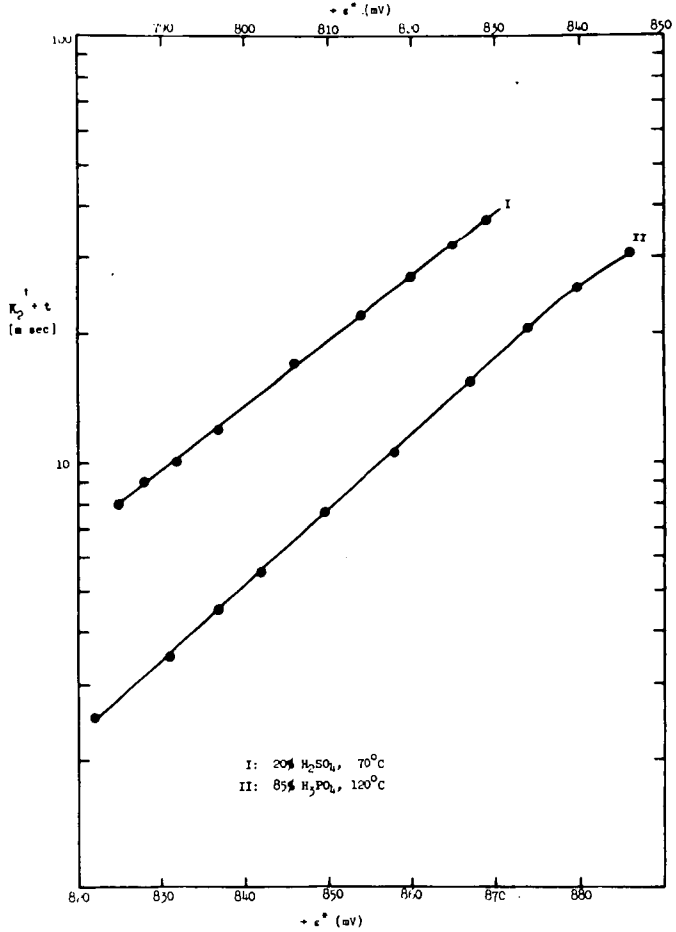

Figure 10. Determination of Tafel Parameters from Oscillographic ε-t Traces after Interrupting an External Current

SOME INFLUENCES OF STRUCTURE IN FILM-TYPE OXYGEN CATHODES

T. Katan
Lockheed Palo Alto Research Laboratory
Palo Alto, California 94304

and

E. A. Grens, II
Department of Chemical Engineering, University of California
Berkeley 94720

ABSTRACT

Measurements were taken of the performance of oxygen electrodes consisting of beds of silver spheres operating in 13.5 M KOH at 95°C. The intrinsic meniscus was positioned in a fine silver mesh, and silver spheres were added to the gas side of the mesh while constant cathodic current was applied. Classified spheres were used in sizes ranging from 14 to 156 microns in diameter, and electrode thickness was gradually increased to about 3000 microns. In these electrodes, the electrochemical reaction occurs beneath a film coating the walls of the gas-filled pores between the spheres.

Several effects can be observed when such electrodes are built up. Increased performance is generally noted until a certain thickness is obtained. For spheres with diameters of about 156 and about 86 microns, if the electrode is made thicker than 800 microns, little further improvement in performance is found. However, as successively smaller sphere sizes are used, the increase in performance expected for the increased specific surface area becomes offset by another, detracting influence. As electrode thickness is then built up beyond a certain thickness, performance is found to decrease with further increases in thickness. This effect may be an important factor in considerations of electrode design.

CATHODIC OXYGEN REDUCTION ON COBALT PHTHALOCYANINE

J. Bett, W. Vogel, K. Routsis, and S. Anderson

Advanced Materials Research and Development Laboratory
Pratt & Whitney Aircraft
Middletown, Connecticut 06457

Metal phthalocyanine complexes have been reported to have electrocatalytic activity for oxygen reduction in both acidic[1] and basic electrolytes[2] and a patent has been issued for their use in fuel cell electrodes.[3] Since the specific conductance of all phthalocyanines is very low, about 10^{-6} ohm^{-1} cm^{-1}[4] it has been the practice to disperse these compounds in conductive supports in order to utilize their catalytic activity. This renders it impossible to estimate the true specific activity of the phthalocyanine surface or to decide whether their activity is limited by their seemingly prohibitive resistivities. For example if one postulates a phthalocyanine surface which draws a current of 0.2 ma/cm^2, i.e., approximately that obtained from the reduction of oxygen on platinum at 800 mv, a current path length of 1 μ through the phthalocyanine crystal would cause an internal resistance polarization of 2 volts. Under these circumstances any polarization data obtained on phthalocyanine electrodes would reflect the effective electrical contact of the phthalocyanine crystal with the conductive support rather than the transfer resistance of oxygen reduction on the catalyst.

We have examined the electrochemical behavior and activity of a number of thin films of cobalt phthalocyanine in order to separate the resistive and charge transfer components of oxygen reduction and to evaluate the true specific activity of the phthalocyanine surface.

Experimental Part

Cobalt phthalocyanine was prepared by the reaction of cobalt metal with o cyanobenzamide at 250°C.[5] The product was purified by precipitation from concentrated sulfuric acid and sublimation under vacuum. The visible spectrum of the sublimed sample was identical to those in the literature.[6]

Several electrodes were prepared from this material:

a) CoPc was dissolved in concentrated H_2SO_4, mulled with a desired amount of Columbia Neo Spectra carbon or Shawinigan Black, and precipitated on the carbon by dilution in ice water. This resulting powder was mixed with 30% by weight of Teflon 30 dispersion and sprayed on Au plated tantalum screen. Sintering and pressing completed the electrode.

b) CoPc was sublimed onto gold foil under vacuum to form films with loadings of from 0.05 to 0.1 mg/cm^2, although of varying uniformity of thickness.

c) CoPc was adsorbed on Columbia Neo Spectra carbon from pyridine solution. Adsorption isotherms were obtained by measuring the change in concentration of CoPc in solution spectrophotometrically. Conditions were chosen under which a monolayer of phthalocyanine would form on the carbon and catalysts were prepared by filtering the carbon from the pyridine solution after equilibration. The resulting powder was evacuated at 50°C to remove the pyridine and mounted as thin layer[7] electrodes for testing.

Before the adsorption of CoPc, samples of Columbia Neo Spectra carbon (1000 m^2/g) were pretreated in three different ways. The first was heated at 420°C under oxygen to give an acid surface which, on titration with base gave 1.6 m eq/g of

surface acid species.[8] The second, evacuated at 400°C and exposed to oxygen at room temperature had a basic surface, which had 0.5 m eq/g of basic species. The third was the initial untreated Columbia Neo Spectra carbon.

These electrodes were examined variously in a floating electrode cell,[9] a conventional three compartment cell with gold counter electrode and platinum reference electrode, and as submerged gas electrodes in the manner described for the thin layer electrode.[7]

Results and Discussion

Screen Electrodes

Screen electrodes were first made by method (a) and parameters were varied to give the best possible performance. For instance mechanical mixing of the phthalocyanine and carbon gave poor results relative to a catalyst made by mulling catalyst and support in H_2SO_4. Furthermore, highest activity was displayed by a catalyst to support weight ratio of about 1:1 and the higher surface area Neo Spectra carbon (1000 m^2/g) proved superior to Shawinigan black (70 m^2/g). Data for these comparisons are given in Table I and were obtained from floating electrodes in 50% H_3PO_4.

The effect of each of these variables was such as to suggest that the best performance was achieved when maximum electrical contact was established between the catalyst and the support. Thus the high resistivity of the solid phthalocyanine appeared to limit catalytic activity.

The polarization curve for the best electrode of Table I run in half cell configuration in 30% H_2SO_4 is shown in Figure 1. Since the available surface area of the CoPc was not known, nor the contribution of internal resistance to polarization, no calculation of the intrinsic activity of the CoPc surface could be made.

Table I

W% CoPc** in Catalyst Powder	Carbon Support	OCP	O_2 reduction ma at mv*** 10	100	200
30	Sh. Bk.	755	210	---	---
50	Sh. Bk.	789	410	310	260
70	Sh. Bk.	760	345	220	---
30	Sh. Bk.*	802	148	---	---
50	N. Sp.	750	570	360	260

Films of CoPc on Gold

If the major portion of the polarization of phthalocyanine electrodes were caused by the internal resistance then the cathodic reduction of oxygen on thin films of CoPc on gold would be inversely proportional to film thickness. As is shown in Table II this effect was not observed for films of phthalocyanine sublimed onto gold foil. The current density at a given voltage appeared to be independent of film thickness. Moreover when an electronic interrupter measurement was made on the film no sharp jump characteristic of internal resistance was seen. In agreement with these observations the activation energy for oxygen reduction on this film was calculated from experiments at several temperatures to be less than 15 K cals/mole

*Mechanically mixed. All others mulled in H_2SO_4.
**Electrode contains 30% TFE.
***50 W% H_3PO_4, 70°C.

whereas the activation energy for intrinsic semi-conduction in CoPc, the expected value if conductance limits performance, has been measured as 36 K cals/mole.[4]

Table II

Oxygen Reduction on Films of CoPc of Varying Thickness on Gold

Film Thickness* ma/cm^2	O_2 Reduction** μa at 500 mv
.01	17
.05	4
.58	8

The apparently contradictory results obtained from screen electrodes and CoPc films might be reconciled if one assumed that the films of CoPc were porous and that, due to high internal resistance, oxygen reduction only took place at the bottom of the pores, where phthalocyanine was in good electrical contact with the gold foil base. Then no internal resistance would be observed although a large gas concentration polarization might be expected in the pores. The porous nature of these films was proven by electrodepositing gold and copper on them. Thus, although the plating current was kept constant no deposit was visible except towards the end of the experiment when microscopic metallic beads appeared on the surface.

The CoPc films were also investigated by cyclic voltammetry under N_2 at scan rates of 410 mV/sec. The CoPc film disintegrated rather rapidly in the electrolyte if the electrode was polarized to low potentials (E^* = 0 to 50 mv versus S.H.E. in same medium). The samples were therefore kept at $E^* \geq 300$ mv. Under the conditions used the currents were due within a few percent solely to reactions of the electrode material, i.e., CoPc.

Progressive changes which occurred on repeated cycling of a characteristic film are shown in Figure 2. We see initially (Curve A) two redox systems designated by I and II with equilibrium potentials of approximately E^*_I = 900 mv and E^*_{II} = 700 mv. The original red-purple electrode color remained the same during the first potential cycles. These curves rapidly changed during subsequent cycles, the change being the more rapid the thinner was the film. An intermediate state was reached, characterized by curve B in Figure 2, and by a clear blue color at low, and the former red-purple color at high potentials. Eventually a new couple III appeared at around E^*_{III} = 450 mv which became the dominant feature. Simultaneously the color changed to grass green (at potentials cathodic to peak III) and purple (at higher potentials) without any blue intermediate. It is probable that the reactions involved in these couples are the redox reactions of central Co ion involving the valencies 3+, 2+, 1+ and zero.[10] The measured resistance of the dry film was approximately 4000 to 5000 Ω cm^2 corresponding to a specific resistivity of $\sigma \simeq 10^8$ Ω cm. The maximum currents in Figure 2 (curve C) are 4.5 ma/cm^2 and these peaks are separated by 50 mv. The IR loss within the film therefore could not be larger than 50/2 = 25 mv. If the original resistivity were maintained during the experiment the thickness λ of the layer involved in reaction III would have to be thinner than approximately $\lambda \simeq Ra/\sigma \simeq 25/4.5 \times 10^{-8} \simeq 5$Å. A calculation based on the density of CoPc shows that a layer this thin can produce a charge of only 0.01 μ Coul/cm^2 whereas the total area within the Curve C of Figure 2 indicates that changes two orders of magnitude greater are involved (Table III). These changes, in Table III, would be consistent with the case where approximately 20% of the thickness of the CoPc film was involved in the redox reaction. One must therefore conclude that the resistivity of the CoPc breaks down as a load is applied to the electrode film and that the operating resistances of the film are lower than those measured in the dry state.

*Prepared by sublimation.
**Tafel slope approximately 160 mv.

Table III

Coulometric Behavior of CoPc Films during Cyclic Voltammetry

CoPc Loading [mg/cm^2]	Area [m Coul/cm^2]	Charge [Coul/mole CoPc]
.055	5.8	6.0×10^4
.075	5.9	4.5×10^4
.095	4.9	3.0×10^4

The electrical circuit at the CoPc/electrolyte interface has to be completed by Faradaic reaction since capacity currents would not be sufficiently large. For this role we assume H^+ ions to be the most likely reactant according to the diagram:

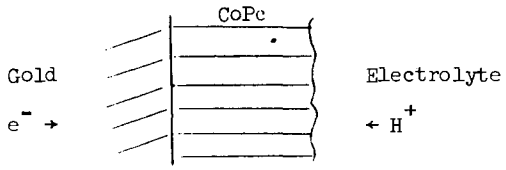

Without supply of H^+ into CoPc the reaction could not proceed even if electronic conductance were sufficient. Hence the reduction of the cobalt ion requires the formation of the protonated form of phthalocyanine (free-base). The model which emerges from these arguments, which can explain at least some of the observations is as follows: The CoPc in contact with the electrolyte acquires electronic conductivity by the passage of protons from the electrolyte however due to limited ion-conductivity only a fraction can react during a voltammetric cycle.

The catalytic activity of the CoPc films on gold is therefore a complex combination of reaction at the bottom of pores in the film and extending into the film because of the increased conductance of phthalocyanine under load. It is thus not possible to evaluate the true specific activity of the phthalocyanine surface from polarization data on these thin films.

Formation and Catalytic Activity of CoPc Monolayers

Cobalt phthalocyanine adsorbed strongly from pyridine solution onto carbon. The equilibrium concentration of phthalocyanine in solution was measured spectroscopically and the concentration on the surface of the carbon calculated by the difference. The adsorption isotherms are shown for the three different carbon surfaces in Figures 3, 4 and 5. These have the sharp elbow and saturation coverage characteristic of Langmuir adsorption and indeed the isotherms may be plotted according to the linear form of the Langmuir isotherm[11] (Figures 6, 7 and 8).

$$\frac{C_B}{C_S} = \frac{C_B}{C_M} = \frac{1}{KC_M}$$

C_B = concentration of CoPc in solution (mg/liter)
C_S = concentration of CoPc on surface (mg CoPc/mg carbon)
C_M = surface concentration at saturation coverage
K = adsorption equilibrium constant

The saturation coverages for each carbon surface were very similar, Table IV, suggesting that in strongly basic pyridine solution differences in surface species was minimized. The surface area occupied by one CoPc molecule at saturation coverage is also listed and shows that the CoPc was considerably less than close packed since

the CoPc molecule is approximately 180 $\AA^2$. It is unlikely that the very small carbon particles, < 30 $\AA$ diameter, have pores sufficiently large to occlude the CoPc molecules therefore we assume the CoPc to be dispersed on the surface of the carbon and in strong interaction with it.

Table IV

Saturation Coverage of CoPc adsorbed from Pyridine Solution on Various Neo Spectra Carbon Surfaces

Surface Pretreatment	Saturation Coverage mg CoPc/mg Carbon	Surface Area per CoPc Molecule $\AA^2$
Untreated	0.107	880
Acidic	0.135	700
Basic	0.141	670

Since CoPc is insoluble in 20% H_2SO_4 it was possible to use these preparations in electrodes for oxygen reduction. Thus the activity for oxygen reduction of monolayers of CoPc could be measured; a condition where there is no possible resistance to the passage of electrons from the conductive support to the active site and hence where internal resistance should be negligible.

The catalyst powders were mounted in thin layer electrodes[7] designed to eliminate gas concentration polarization and electrolyte IR losses. Polarization curves for oxygen reduction on phthalocyanine supported on the three different carbon surfaces are shown in Figures 9, 10, 11. The linearity of the Tafel plot and its lack of dependence on catalyst loading confirms that these data refer only to charge transfer.

The current density, plotted as ma/mg CoPc, was very nearly the same for each of the three carbon surfaces and only slightly greater than for the carbon without CoPc (Figure 12). Since the phthalocyanine was spread as a monolayer the exchange current could be calculated assuming 180 $\AA^2$ per phthalocyanine molecule. This gave a value of 4×10^{-11} amps/cm^2 for i_o and a Tafel slope of 160 mv for CoPc on the acid carbon surface. The other surfaces were not significantly different. Thus the CoPc surface is rather weakly catalytic; only slightly better than the carbon on which it is supported. The presence of different surface species under the adsorbed phthalocyanine appears to have little effect on the catalytic activity although the basic carbon surface seems to lower the activity slightly.

Polarization data for the best screen electrode made from CoPc by method (a) is also plotted on the basis of ma/mg CoPc in Figure 9 for comparison. Its lower performance points out that this electrode did not make the most efficient use of the phthalocyanine on the carbon possibly because all the phthalocyanine was not in electrical contact with the support.

Discussion

Cyclic voltammetry of the thin films of phthalocyanine showed that the resistance of the phthalocyanine decreased at cathode potentials as the oxidation state of the central ion changed. Hence despite the very high initial resistance of phthalocyanine there is probably not an important resistance contribution to cathode polarization. This behavior would imply that the activity of cobalt phthalocyanine mixed with a conductive support in a screen electrode should be close to the intrinsic activity of the available phthalocyanine. This assumption is borne out by the very similar activity of thin layer electrodes with monolayers of phthalocyanine and the screen electrodes in Figure 9.

Undoubtedly the nature of the surface in which the phthalocyanine is supported may have a large effect on its activity and therefore some support other than carbon may be found giving enhanced activity. Indeed the crystalline morphology of the phthalocyanine itself is known to affect catalytic activity of a number of phthalocyanines for the decomposition of formic acid.[12] Moreover the mechanism for the reduction of oxygen on a semi-conductor surface will certainly be complicated by changes in the electronic structure of the central metal ion. However the present study demonstrates that electronic conductance through the semi-conductor is not a limitation in the case of cobalt phthalocyanine but that the electrochemical reaction at the catalyst surface is the slow process.

References

(1) H. Jahnke, CITCE Meeting, Detroit, September 1968.

(2) R. Jasinski, Nature, 201, 1212 (1964).

(3) R. Jasinski, Canadian Patent No. 797,924 (1965).

(4) W. Felmayr and I. Wall, J. Elect. Soc., 105, 141 (1958).

(5) E. H. Moser and A. L. Thomas, "Phthalocyanine Compounds," p. 292, Reinhold, New York (1963).

(6) P. Day, H. A. Hill and M. Price, J. Chem. Soc., A, 90 (1968).

(7) W. M. Vogel and J. T. Lundquist, 158th National Meeting American Chemical Society, New York (1969).

(8) H. P. Boehm, Adv. in Cat., 16, 179 (1966).

(9) J. Giner and S. Smith, Elect. Tech., 5, 59 (1967).

(10) L. D. Rollman and R. I. Iwamoto, J.A.C.S., 90, 1755 (1968).

(11) H. Reis, "Catalysis," Vol. I, P. H. Emmett, Ed., Reinhold, New York (1961).

(12) W. Hanke, Natur wissenschafter, 52, 475 (1965).

Figure 1

OXYGEN REDUCTION ON CoPc SUPPORTED ON NEO SPECTRA CARBON IN A SCREEN ELECTRODE

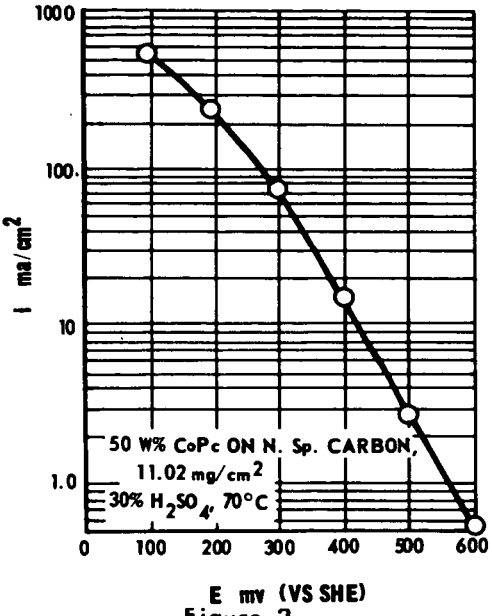

Figure 2

CYCLIC VOLTAMMETRY OF CoPc FILM SUBLIMED ON GOLD

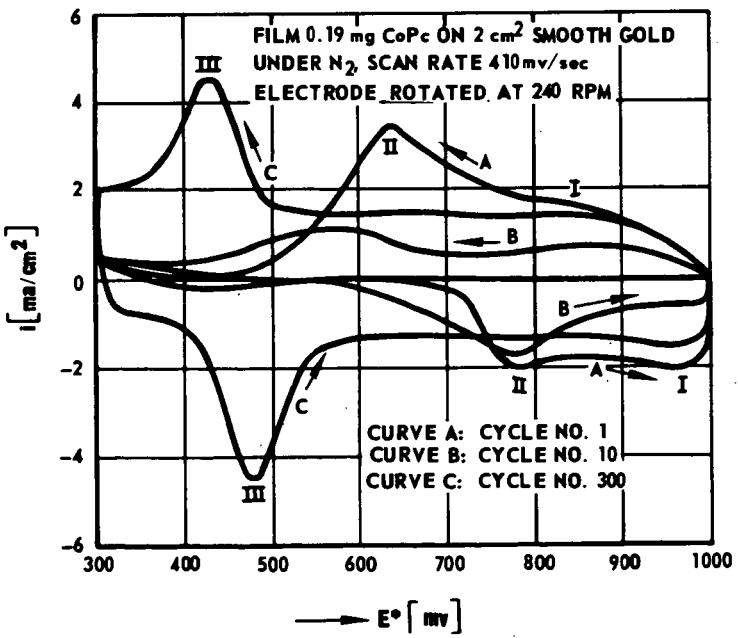

Figure 3

ADSORPTION ISOTHERM CoPc ON UNTREATED NEO SPECTRA CARBON

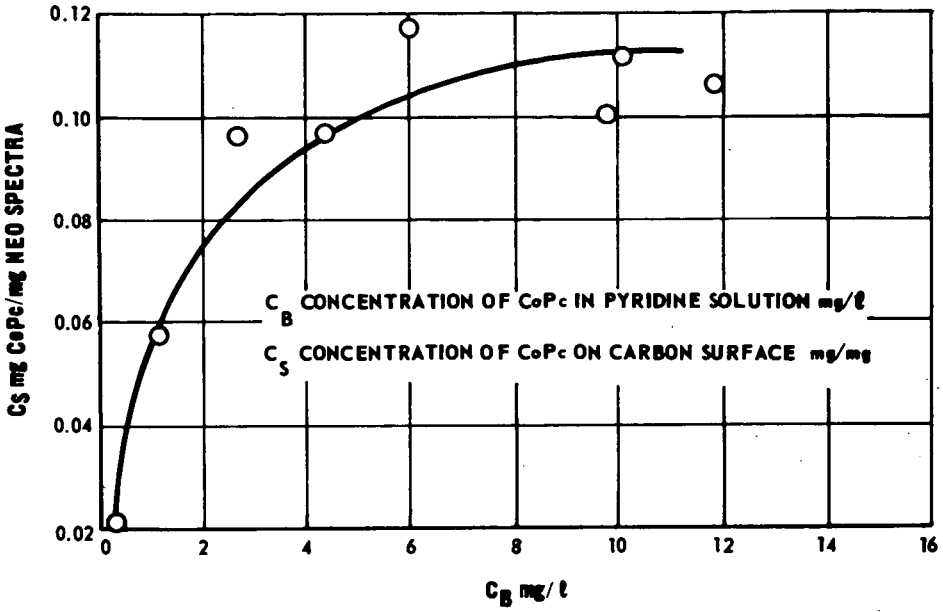

Figure 4

ADSORPTION ISOTHERM CoPc ON ACID NEO SPECTRA

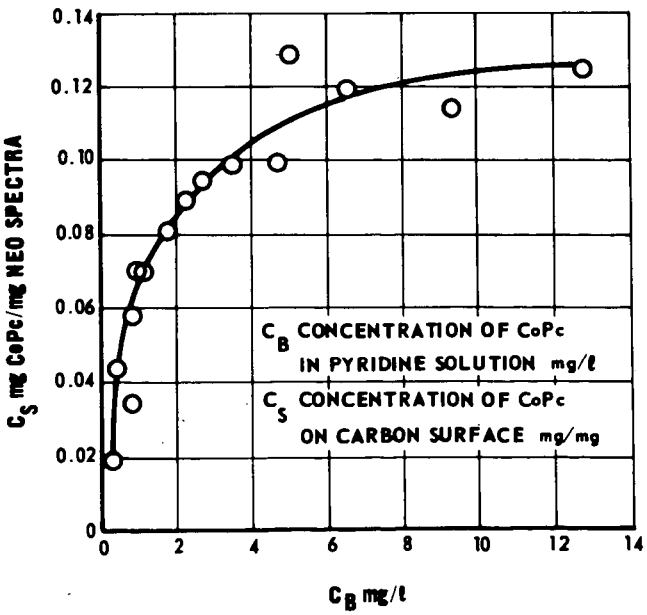

Figure 5

ADSORPTION ISOTHERM CoPc ON BASIC NEO SPECTRA CARBON

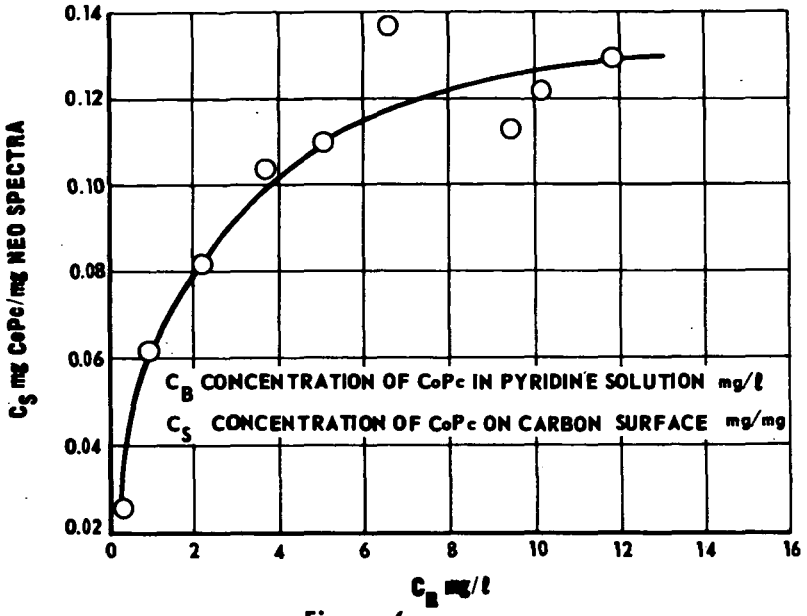

Figure 6

LANGMUIR ISOTHERM CoPc ON UNTREATED NEO SPECTRA

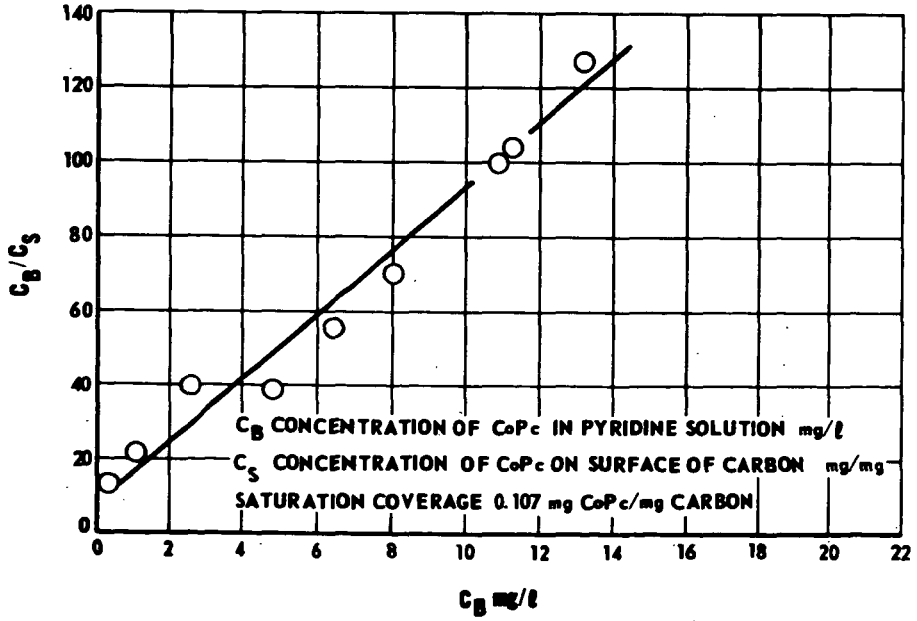

Figure 7

LANGMUIR ISOTHERM CoPc ON ACID NEO SPECTRA CARBON

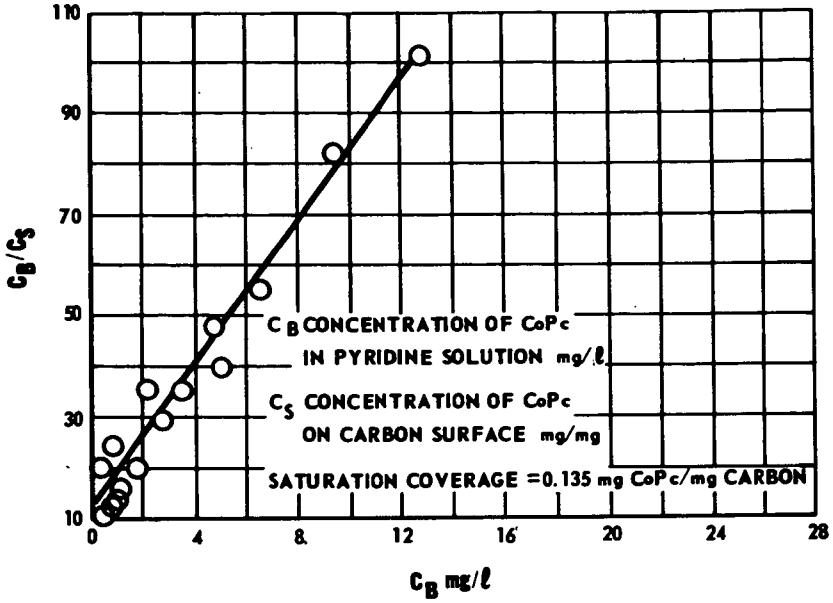

Figure 8

LANGMUIR ISOTHERM CoPc ON BASIC NEO SPECTRA CARBON

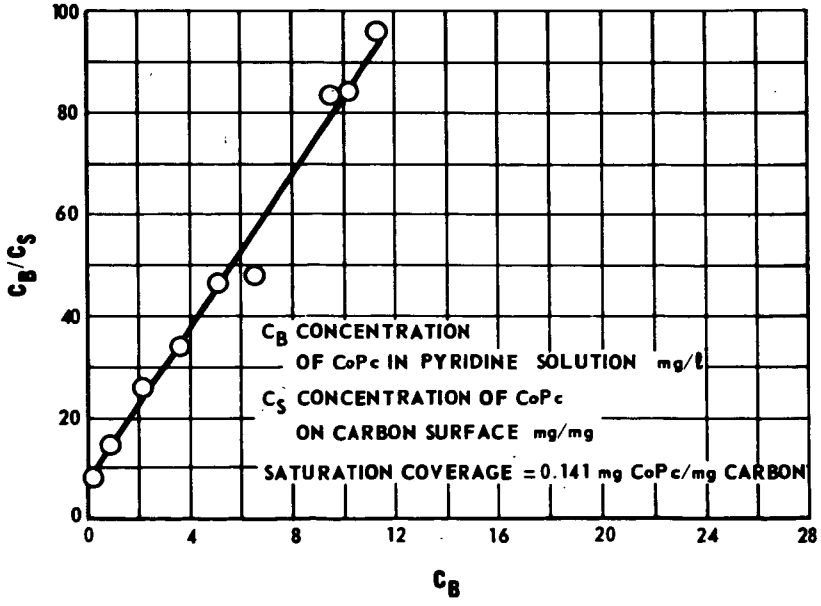

Figure 9: CATHODIC OXYGEN REDUCTION ON CARBON SUPPORTED CoPc MONOLAYERS (UNTREATED NEO SPECTRA)

50°C, 20% H_2SO_4 0.95 mg CoPc/mg NEO SPECTRA

CoPc ON UNTREATED NEO SPECTRA

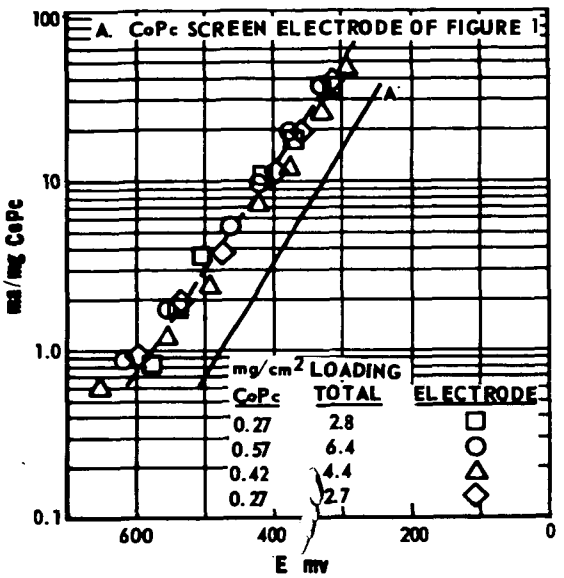

Figure 10: CATHODIC OXYGEN REDUCTION ON CARBON SUPPORTED CoPc MONOLAYERS (ACID NEO SPECTRA)

50°C, 20% H_2SO_4 0.11 mg CoPc/mg NEO SPECTRA

CoPc ON ACID NEO SPECTRA CARBON

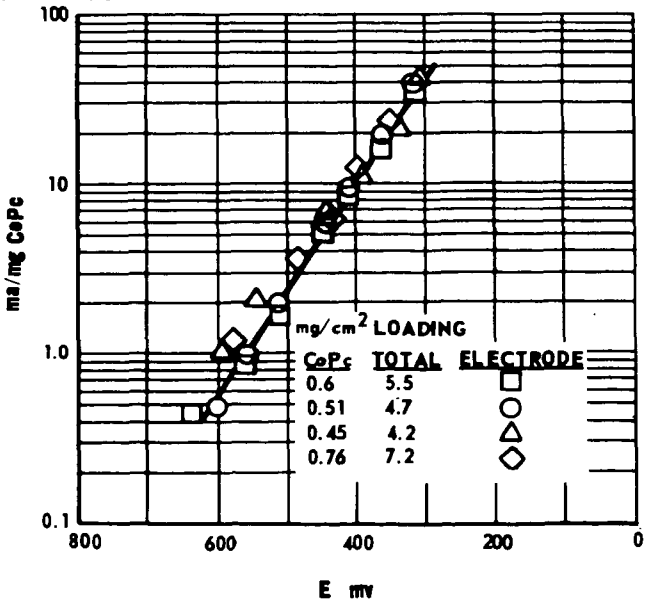

Figure 11: CATHODIC OXYGEN REDUCTION ON CARBON SUPPORTED CoPc MONOLAYERS (BASIC NEO SPECTRA)

50°C, 20% H_2SO_4

0.11 mg CoPc/mg NEO SPECTRA

CoPc ON BASIC NEO SPECTRA

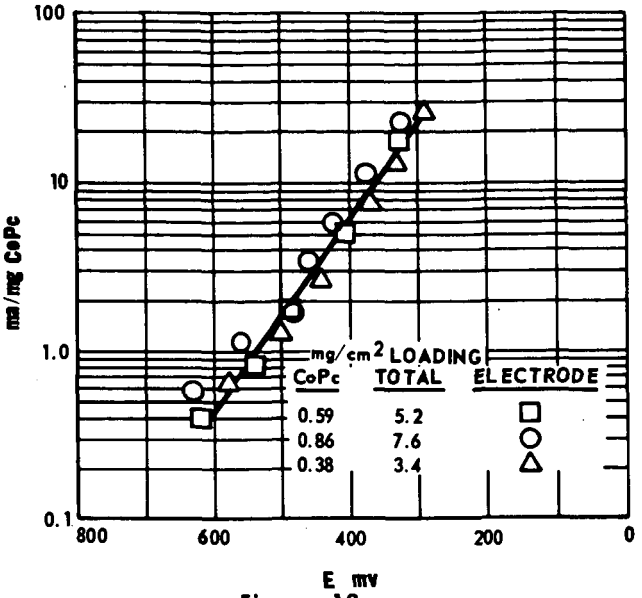

Figure 12

OXYGEN REDUCTION ON UNTREATED NEO SPECTRA CARBON WITH AND WITHOUT ADSORBED CoPc

50°C, 20% H_2SO_4

NEO SPECTRA CARBON

mg/cm² LOADING

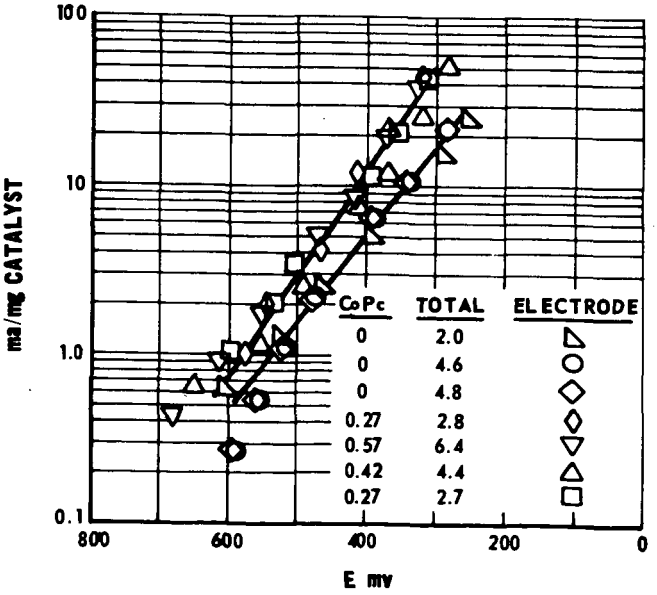

PREPARATION AND ELECTROCHEMICAL TESTING OF INTERSTITIAL COMPOUNDS AS FUEL CELL CATALYSTS

by

S. Akhtar, C.T. Grein, and D. Bienstock

U.S. Department of the Interior, Bureau of Mines,
Pittsburgh Coal Research Center, Pittsburgh, Pa.

INTRODUCTION

In March 1966, the Pittsburgh Coal Research Center of the Bureau of Mines, at the suggestion of E. Cohn of the National Aeronautics and Space Administration and funded by this organization, initiated a study of the interstitial compounds of the transition metals as fuel cell catalysts. The interest in the work was generated by a preliminary observation at Tyco Laboratories, Inc., of Waltham, Mass., that the interstitial carbide χ-Fe_2C is an active catalyst for the electrochemical reduction of oxygen. The Bureau's part in this program was to prepare cathode catalysts for alkaline hydrogen-oxygen fuel cells operating at low temperatures; the cathodic activity of these preparations was to be determined by Tyco Laboratories. The scope of the project was later enlarged by cooperative arrangement with ten other laboratories engaged in fuel cell work. The materials were made available to them for both cathodic and anodic activity tests in a variety of systems. The results obtained in two of these laboratories are presented in this paper.

The carbides of Fe have been prepared by the action CO, $CO+H_2$, or hydrocarbons on Fe (1,2,3)[1]. When $CO+H_2$ is employed, Fe is in effect carburized with a mixture of CO and hydrocarbons, since CO reacts with

---

[1] Underlined numbers in parentheses refer to items in the list of references at the end of this report.

H_2 to form hydrocarbons in the presence of reduced Fe (Fischer-Tropsch synthesis). Hydrocarbons alone do not lead to complete carbiding (3), and CO alone tends to deposit unacceptable amounts of free carbon. The action of CO on Fe is very exothermic and there is a strong tendency for the Fe to become overheated. Reaction temperature should be carefully controlled below that at which the desired carbide decomposes. H_2 in the reacting gas helps remove the excess heat and minimizes the amount of free carbon in the product.

Co_2C is prepared by the action of CO on Co (4) and Ni_3C by the action of CO on Ni (5) at 250°-280°C. In both cases, carbide formation is accompanied by deposition of free carbon, and the higher the reaction temperature, the greater the proportion of free carbon. Some features of the kinetics of the reaction of CO with Ni are presented in Fig. 1 from the published results of Eyraud (6). A fixed weight of reduced Ni was carburized with CO at different temperatures. Below 250°C, the rate of formation of Ni_3C was very slow but the product was substantially free from deposited carbon. At 285°C, the reaction was complete in about 30 hours, but Ni_3C was contaminated with free carbon. At temperatures above 300°C, large quantities of free carbon were deposited.

As with Fe, the reactions of CO with Co and Ni are strongly exothermic. However, H_2 can not be employed to dilute CO in carburizing Co and Ni; Co_2C and Ni_3C can not be prepared under conditions of Fischer-Tropsch synthesis. The contrast in this respect with Fe may be noted.

The nitrides of Fe, Co, and Ni are prepared by reacting the metals with NH_3. The phase diagram for the nitrides of Fe is shown in Fig. 2 (7); it shows the phases that are in equilibrium with N_2 at the pressures corresponding to the dissociation of NH_3. ϵ-Fe_3N-Fe_2N has the most extended range of existence. With the exception of the γ-phase, the various nitrides of Fe may all be prepared at about 350°C, the composition of the product depending on the space velocity of NH_3 and the duration of nitriding. The nitrides of Co and Ni also have been prepared by the action of NH_3 on the metals but their preparation appears to be attended by unusual difficulties (8). Temperatures no higher than 350°C and high space velocities of NH_3 are recommended. Even so, the reported successes in the preparation of these nitrides have only been in terms of "milligram" or "up to a gram" quantities.

PREPARATION OF INTERSTITIAL COMPOUNDS

The scheme for preparing the interstitial compounds of Fe, Co, and Ni is shown in Fig. 3. The first step consists of preparing finely divided metals and mixtures of metals, or alloys. Since the rate of formation of carbides and nitrides by gas-solid reactions falls off as successive layers of the products increasingly obstruct the access of the reacting gas to metal substrates, it is important to start with

fine powders of metals. Also, the preparations were intended to be tested as contact catalysts where large specific surface areas are of obvious advantage. The different methods employed for preparing finely divided metals are indicated in the scheme.

The gas-solid reactions were carried out in horizontal vycor tubes of 1-inch diameter shown in Fig. 4. The tubes were fitted with metallic end pieces which had provisions for gas inlet and outlet. Fifty to one hundred grams of solids were processed at a time. Separate thermocouples monitored the temperature of the front end, the middle, and the rear of the powder beds. Fig. 5 is a photograph of the apparatus which included furnaces, thermoregulators, gas flow meters, safety valves, and a 12-point recorder for the thermocouples.

Reactions were carried out at atmospheric pressure. The leached Raney metals were treated with hydrogen at 450°C for 10-20 hours at an hourly space velocity of 1,000-2,500 before carbiding or nitriding. The hydroxides were generally reduced in situ.

The experimental conditions employed in the preparation of the carbides are presented in Table 1. Reduced metals were always allowed to cool down to at least 160°C before CO or $CO+H_2$ was introduced. When pure CO was employed as the carburizing agent, the concentration of CO in the exit gas was monitored by a differential type infrared detector.

When the concentration of CO in exit gas fell below 80 percent, power supply to the furnace was cut off by an automated arrangement. Higher CO conversions is conducive to run away temperatures and excess carbon deposition. The temperature of the powder bed was raised slowly and in steps. Several hours were usually allowed for the temperature to come up to the final level (see columns 4 and 5 in Table 1). With Co and Ni, the tendency for sudden overheating appears at about 180°-220°C in the presence of CO. Since the carburization of Co or Ni does not ordinarily proceed at measurable rates at temperatures below 250°C, the lower temperature represents the point of onset of carbiding of the active spots on the metal powders. Column 6, Table 1, gives the results of qualitative x-ray analysis of the carburized materials. The major detectable phase is listed first. The findings were further checked by chemical analysis of the products for carbon. As concomitant deposition of some free carbon is unavoidable, the combined or carbidic carbon must be distinguished from the free carbon. In practice, it is simpler to determine the total carbon and the free carbon, and to compute the combined carbon by difference. Total carbon was determined by igniting samples in excess O_2 and scrubbing CO_2 from the stream of combustion gases in towers packed with ascarite. The towers were weighed before and after the absorption of CO_2. The free carbon was determined as follows: Samples were digested in dilute (1:3) HCl at

60°-80°C for ½ hour to drive off carbidic carbon as gaseous hydrocarbons. Free carbon is not affected by digestion with dilute HCl. The insolubles were filtered on a porous crucible, washed with hot water, and dried at 105°C. The crucible was then placed in a tube furnace and ignited in excess O_2. As before, CO_2 was scrubbed in ascarite towers. The results for total carbon and free carbon are given in columns 7 and 8, Table 1.

The experimental conditions employed for preparing the various nitrides of Fe are given in Table 2. Samples of Raney Fe were reduced with H_2 at 450°C before treatment with NH_3. The products were analyzed for nitrogen by the Kjeldahl method. When mixtures of Fe and Ag were treated with NH_3, only Fe was nitrided. All efforts to prepare nitrides of Co and Ni were fruitless.

The experimental conditions employed for the preparation of nitrocarbides and carbonitrides are given in Tables 3 and 4, respectively.

Electrocatalytic Activity of the Interstitital Compounds

As the interstitial compounds of Tables 1-4 are pyrophoric, the preparations were subjected to a process of "induction" before electrochemical investigation. Induction of a pyrophoric powder essentially consists of oxidizing the surface layer of its particles by exposing the powder to mildly oxidizing conditions; the oxide layer then provides a protective coating for the solid against further attack by oxygen. When pyrophoric powders are ordinarily exposed to air, the conditions are too drastic for the oxidation to stop at the surface layer. The powders are inducted by successive treatment with a series of solvents of increasing solubility for O_2. The powders so treated were found to develop far less heat on subsequent exposure to air and the electrodes prepared from them gave reproducible results.

The catalytic activity of the interstitial compounds were tested in the reduction of O_2 in KOH containing N_2H_4, and in the oxidation of NH_3 in 30 percent KOH.

(1) Reduction of O_2 in KOH containing N_2H_4 at room temperature[2]

The interstitial compounds were homogenized by grinding, and sieving through a 325-mesh screen in a dry box filled with nitrogen. The powders were covered with petroleum ether and then brought out in the open, where they were inducted with diethyl ether, acetone, and ethanol. 0.1 gram samples of the inducted materials were waterproofed with a teflon emulsion, cured at 200°C in N_2, mixed with equal weights of waterproofed graphite, and packed in the sample holder shown in Fig. 6. The electrolyte consisted of 10 ml. of 12 M KOH containing 0.2 ml. of 60 percent N_2H_4. For activity measurement, the electrodes were polarized against an inert nickel screen at 10 amp/ft^2 for 15 minutes, then at 20, 30, and 40 amp/ft^2 for 5 minute periods, and finally again at 10 amp/ft^2 for 5 minutes. The polarization measurements were made with a Kordesch-Marko Bridge, a Hg/HgO electrode serving as the reference electrode. The average values of the potentials are plotted against the apparent current densities in Fig. 7. It will be seen that 17N, 3CN, and 1NC are about as active as Pt-black. Duplicate experiments gave reproducible results.

---

[2] This portion of the work was done in the laboratories of the Union Carbide Corporation, Fuel Cell Department, Parma, Ohio, under the supervision of Dr. G.E. Evans.

(2) Oxidation of NH_3 in 30 percent KOH at 25°C[3]

After induction with heptane, acetone, methanol, and water, 28.3 mg of each dried material was mixed with an aqueous emulsion of 5 mg PTFE and the mixture was spread on a 1.5 cm x 1.5 cm platinum screen. The screen, with the spread, was dried in vacuum at 85°C for half an hour and then pressed at 100 psi for 2 minutes at 250°C. Anodic activities and corrosion currents were determined potentiostatically by a floating electrode technique. A dynamic hydrogen electrode (9) was employed as the reference electrode and corrosion currents were measured in N_2. The potentiostat was programmed for continuous scanning from 0 v to 1.2 v and the current-voltage curves were traced directly on an x-y recorder. If an electrode gave a corrosion current of more than 1 ma, the electrode material was considered incompatible with the electrolyte. To compare the activities per unit area of the various preparations, the electrochemically effective area of each electrode was determined by a double layer capacitance method (10). The values of equilibrium potential, exchange current, and Tafel slope were computed graphically from the current-potential data. I-R corrections were ignored since the currents were small. The results are presented in Table 5.

---

3 This part of the work was done in the laboratories of the Catalyst Research Corporation, Baltimore, Md. The principal investigators were H.J. Goldsmith, J.R. Moser, and T. Webb.

Five of the fourteen interstitial preparations tested corroded visibly on addition of NH_3 to the electrolyte. The stable electrodes gave half-cell potentials of 0.54 v-0.56 v compared to 0.58 v for Pt, and Tafel slopes of about 0.12 v compared to 0.04 v for Pt. The half-cell potentials and Tafel slopes for the unstable materials were widely scattered.

Oswin and Salomon (11) have suggested a four-step mechanism for the anodic oxidation of NH_3. Their scheme and their calculated values for the Tafel slopes of the intermediate steps are as follows:

		Calculated Tafel slope, v
(1)	$NH_3 + M + OH^- \rightarrow M\text{-}NH_2 + H_2O + e^-$	0.118
(2)	$M\text{-}NH_2 + OH^- \rightarrow M{=}NH + H_2O + e^-$	0.039
(3)	$M{=}NH + OH^- \rightarrow M{\equiv}N + H_2O + e^-$	0.024
(4)	$M{\equiv}N \rightarrow 2M + N_2$	0.010 (or ∞ at high current densities)

A comparison of the experimental values of the Tafel slope with the calculated values indicates that on Pt the rate-determining step for the oxidation of NH_3 is reaction (2), but on the stable catalysts of Table 5, the rate-determining step for the oxidation of NH_3 is reaction (1).

From a practical point of view, the anodic activities of the nine stable catalysts as measured by the exchange current per unit weight of catalysts were disappointingly low. However, it may be noted that the intrinsic activity of some of the materials, as measured by the activity per unit of surface area, is surprisingly high. If methods for preparing interstitial compounds of specific surface areas comparable to specific surface area of Pt-black could be developed, the interstitial compounds may provide fuel cell catalysts of practical value. The specific surface areas of the interstitial preparations of the present investigation were four orders of magnitude smaller than the specific surface area of Pt-black.

CONCLUSIONS

Interstitial carbides, nitrides, nitrocarbides, and carbonitrides of Fe are active in the reduction of O_2 in KOH containing N_2H_4 at room temperature. The activity of some of these preparations is comparable to that of Pt-black. Further investigation of these compounds with prototype fuel cells appears to be desirable.

None of the preparations tested showed any promise as anode catalysts in the oxidation of NH_3 in KOH.

REFERENCES

(1) Hofer, L.J.E., and E.M. Cohn. Synthesis of Cementite. J. Chem. Phys., v. 18, No. 5, May 1950, pp. 766-767.

(2) Hofer, L.J.E., E.M. Cohn, and W.C. Peebles. The Modifications of the Carbide Fe_2C; their Properties and Identifications. J. Am. Chem. Soc., v. 71, 1949, pp. 189-195.

(3) Podgurski, H.H., J.T. Kummer, T.W. DeWitt, and P.H. Emmett. Preparation, Stability, and Adsorptive Properties of Carbides of Iron. J. Am. Chem. Soc., v. 72, 1950, pp. 5382-5388.

(4) Hofer, L.J.E., and W.C. Peebles. Preparation and X-ray Diffraction Studies of a New Cobalt Carbide. J. Am. Chem. Soc., v. 69, 1947, pp. 893-899.

(5) Escoules, M., and C. Eyraud. (Kinetic Characteristics of the Reaction of Carbon Monoxide on Finely Divided Nickel.) Bull. Soc. Chim. France,No. 4, 1966, pp. 1369-1373.

(6) Eyraud, C. Kinetics and Mechanism of Solid State Reactions. Pure and Appl. Chem., v. 9, No. 3, 1964, pp. 397-407.

(7) Hansen, Max. Constitution of Binary Alloys. McGraw-Hill Book Co., Inc., New York, 1958, 2nd ed., p. 671.

(8) Rienaecker, G., and K.H. Hol. (Nitriding of Nickel.). Z. Anorg. Allgem. Chem., v. 333, 1964, pp. 291-300.

(9) Giner, J. A Practical Reference Electrode. J. Electrochem. Soc., v. 111, No. 3, 1964, pp. 376-377.

(10) McCallum, J., R.W. Hardy, and R.F. Redmond. Measurement of True Surface Area in Electrodes. Tech. Report APAPL-TR-66031, Battelle Memorial Institute, Columbus, Ohio, 1966.

(11) Oswin, H.G., and M. Salomon. The Anodic Oxidation of Ammonia at Platinum Black Electrodes in Aqueous KOH Electrolyte. Canad. J. Chem., v. 41, 1963, p. 1686.

TABLE I.- Preparation of carbides

Run no.	Charge	Carbiding gas, (hourly space velocity)	Duration of carbiding, hrs.	Temperature of carbiding, °C	X-ray analysis	Chemical analysis, weight percent: Total C	Chemical analysis, weight percent: Free C
3C	Raney Fe	$1CO+10H_2$ (3,000)	48	305	χ-Fe_2C, Fe_3O_4	4.90	3.45
9C	Reduced magnetite	CO (100)	16	190			
			24	260			
			6	320	χ-Fe_2C		
11C	Reduced magnetite	CO (100)	20	205			
			25	340	χ-Fe_2C	17.31	11.81
12C	Raney Fe	$1CO+10H_2$ (3,000)	10	240	ϵ-Fe_2C, α-Fe		
			14	240	χ-Fe_2C, ϵ-Fe_2C		
		He	12	300	χ-Fe_2C	7.6	2.2
14C	Reduced magnetite	CO (100)	20	175-325			
		He	3	500	θ-Fe_3C	7.98	5.15
27C	Raney 3Ni-1Co	CO (100)	14	170-250			
			144	250	Ni_3C	9.33	7.48
33C	Raney Co	CO (100)	28	160-250			
			72	250	Co_2C, α-Co	3.59	0.54
42C	Raney 1Ni-1Co	CO (100)	22	160-250			
			101	250	Ni(cubic), α-Co	4.25	1.11
43C	Raney 1Ni-1Ag	CO (100)	4	160-250			
			102	250	Ag(cubic)	2.14	0.16
46C	Raney 3Ni-1Ag	CO (100)	7	160-250			
			104.5	250	Ag, Ni_3C	3.44	0.22
61C	Reduced co-precipitated hydroxides of 3Ni-1Co	CO (100)	5	160-260			
			102	260		0.28	0.17

TABLE 2.- Preparation of nitrides

Nitriding gas: NH_3
Space velocity: 1,000 hr^{-1}

Run no.	Charge	Duration of nitriding, hrs.	Temp., °C	X-ray analysis	Chemical analysis, N, weight percent
1N	Reduced magnetite	6	365	ϵ-Fe_3N-Fe_2N, γ'-Fe_4N	5.92
10N	Reduced magnetite	24	350	ϵ-Fe_3N-Fe_2N	7.94
11N	Reduced, coprecipitated 3Fe-1Ag	25	355	ϵ-Fe_3N-Fe_2N, Ag	4.85
14N	Raney Fe	24	355	ϵ-Fe_3N-Fe_2N	9.61
17N	Raney Fe	12	355	ϵ-Fe_3N-Fe_2N	9.12
18N	Raney Fe	24	295	ζ-Fe_2N, ϵ-Fe_3N-Fe_2N, γ'-Fe_4N	9.8
19N	Reduced magnetite	24	350	ζ-Fe_2N, ϵ-Fe_3N-Fe_2N, γ'-Fe_4N	7.77
20N	Raney Fe	7.5 48	350 300	ζ-Fe_2N, γ'-Fe_4N, ϵ-Fe_3N-Fe_2N ϵ-Fe_3N-Fe_2N	9.95
21N	Reduced magnetite	5	250	γ'-Fe_4N, ϵ-Fe_3N-Fe_2N	5.93

TABLE 3.- Preparation of nitrocarbides

Space velocity of NH_3: 1,000 hr^{-1}

Run no.	Charge	Duration of nitriding the carbide, hrs.	Temperature of nitriding the carbide, °C.	X-ray analysis	Chemical analysis, weight percent		
					N	Total C	Free C
1NC	3C (χ-Fe_2C, Fe_3O_4)	28	355	ϵ-Fe_3X-$Fe_2X(C,N)$, Fe_3O_4	5.65	2.98	2.06
2NC	9C (χ-Fe_2C)	24	355	χ-$Fe_2X(C,N)$, ϵ-Fe_3X-$Fe_2X(C,N)$	2.26	11.76	5.93
15NC	27C (carbided 3Ni-1Co)	48	260	$Ni_3X(C,N)$	1.01	9.30	6.38
28NC	42C (carbided 1Ni-1Co)	48	260	α-Co, Ni	1.01	3.84	1.11

TABLE 4.- Preparation of carbonitrides

Space velocity of CO: 100 hr^{-1}

Run no.	Charge	Duration of carbiding the nitride, hrs.	Temperature of carbiding the nitride, °C.	X-ray analysis	Chemical analysis, weight percent		
					N	Total C	Free C
3CN	14N (ϵ-Fe_3N-Fe_2N)	3 7.5	180-350 350	ϵ-Fe_3X-Fe_2X(C,N)	8.49	4.02	0.88
4CN	18N (ζ-Fe_2N, ϵ-Fe_3N-Fe_2N, γ'-Fe_4N)	11	175-350	ϵ-Fe_3X-Fe_2X(C,N)	9.25	3.23	0.81
5CN	19N (ζ-Fe_2N, ϵ-Fe_3N-Fe_2N, γ'-Fe_4N)	11	190-350	ϵ-Fe_3X-Fe_2X(C,N)	7.43	2.74	3.20
6CN	11N (ϵ-Fe_3N-Fe_2N, Ag)	3 7	225-350 350	ϵ-Fe_3X-Fe_2X(C,N), Ag			
9CN	21N (γ'-Fe_4N, ϵ-Fe_3N-Fe_2N)	0.5 3.5	200-250 250	γ'-Fe_4X(C,N)			

TABLE 5.- Oxidation of NH_3 in 30% KOH at 25 °C

Catalyst (composition)	Exchange current ma/g	Exchange current $\mu a/cm^2$	Tafel slope, V	Equilibrium potential, V
Pt	883	4.24	0.04	0.58
33C* (Co_2C, α-Co)	106	21.6	0.04	0.22
43C (carbided 1Ni-1Ag)	60.1	4.40	0.08	0.68
46C* (Ag, Ni_3C)	42.4	10.5	0.08	0.24
28NC* (nitrocarbided 1Ni-1Co)	28.3	0.968	0.10	0.32
27C* (carbided 3Ni-1Co)	14.1	2.0	0.12	0.26
12C (χ-Fe_2C)	3.54	107	0.17	0.55
15NC (nitrocarbided 3Ni-1Co)	3.53	0.507	0.23	0.56
21N (γ'-Fe_4N, ε-Fe_3N-Fe_2N)	3.15	42.6	0.12	0.56
61C (carbided 3Ni-1Co)	2.80	7.0	0.11	0.54
18N (ζ-Fe_2N, ε-Fe_3N-Fe_2N, γ'-Fe_4N)	2.47	29.9	0.12	0.56
20N (ζ-Fe_2N, ε-Fe_3N-Fe_2N, γ'-Fe_4N)	1.66	23.2	0.13	0.56
1NC [ε-FeX-Fe_2X(C,N), Fe_3O_4]	1.37	14.3	0.12	0.54
5CN [ε-Fe_3X-Fe_2X(C,N)]	1.13	20.7	0.26	0.55
4CN [ε-Fe_3X-Fe_2X(C,N)]	0.99	6.45	0.11	0.56

*The catalysts marked with an asterisk dissolved in the electrolyte when NH_3 was added.

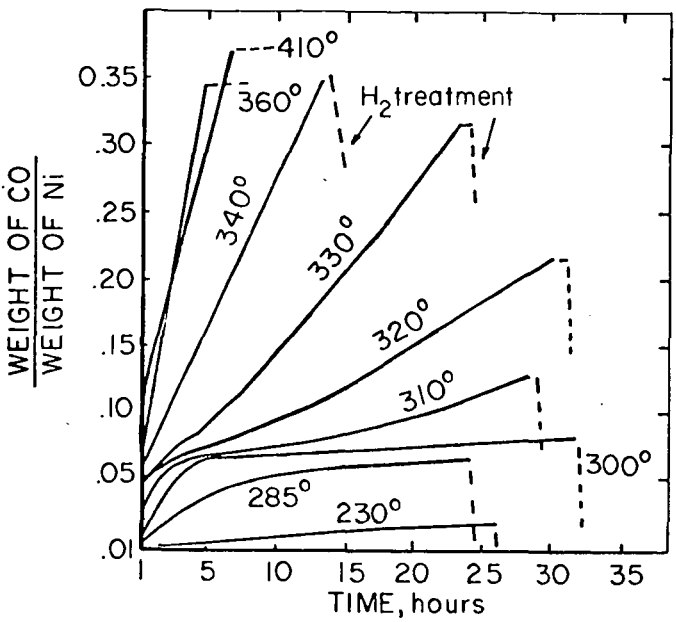

Figure 1.- Carburization of Ni with CO at different temperatures.

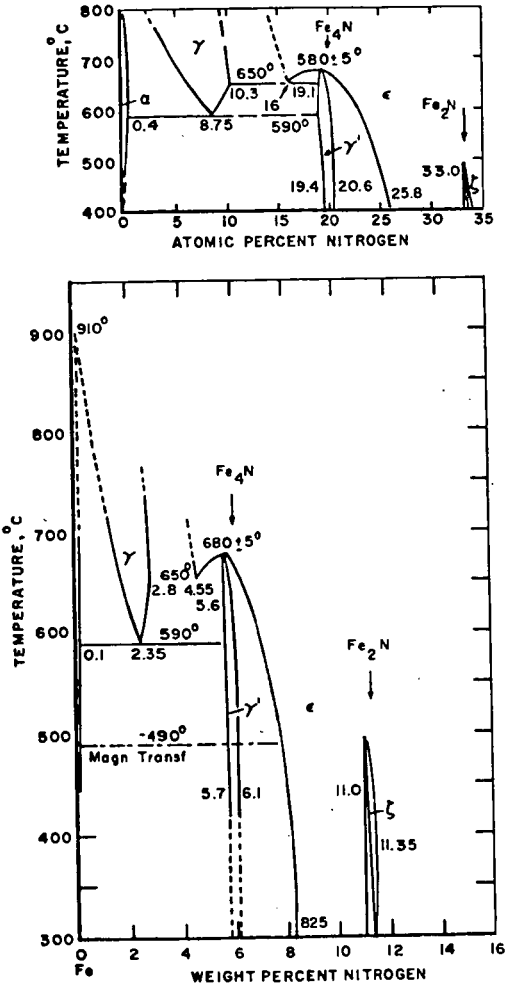

Figure 2.- Fe-N system in NH_3 (7).

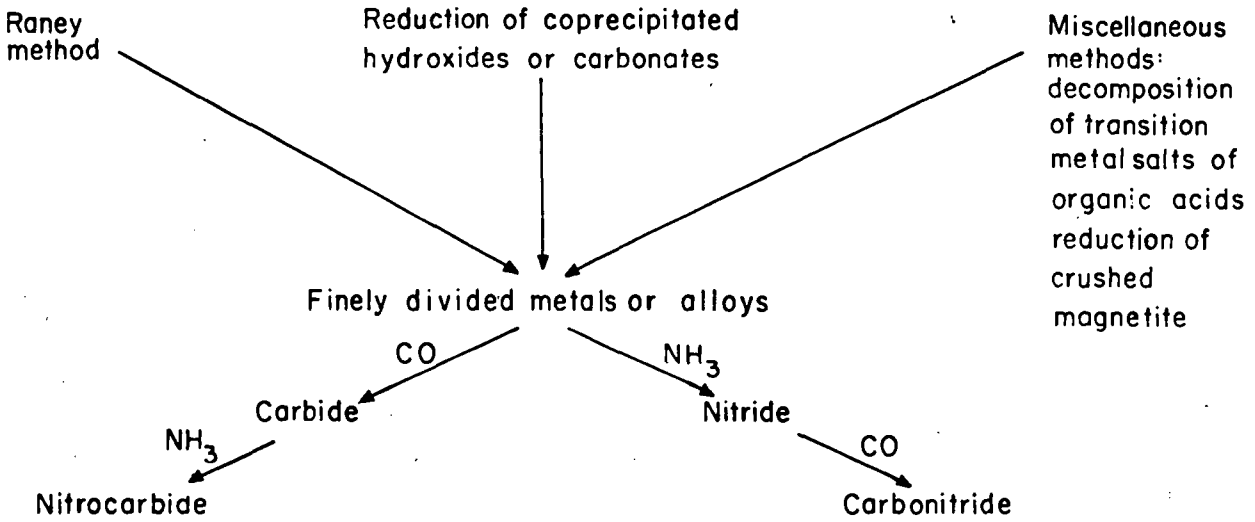

Figure 3.- Preparation of the interstitial compounds.

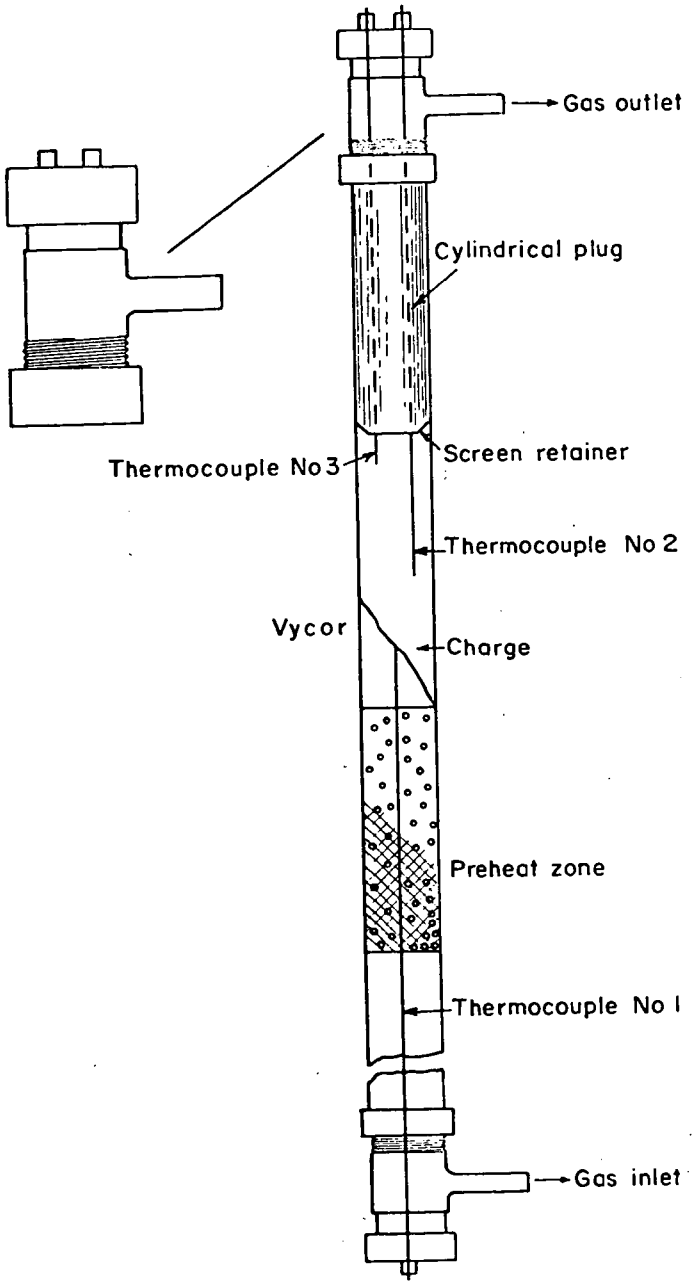

Figure 4.- Vycor reaction vessel.

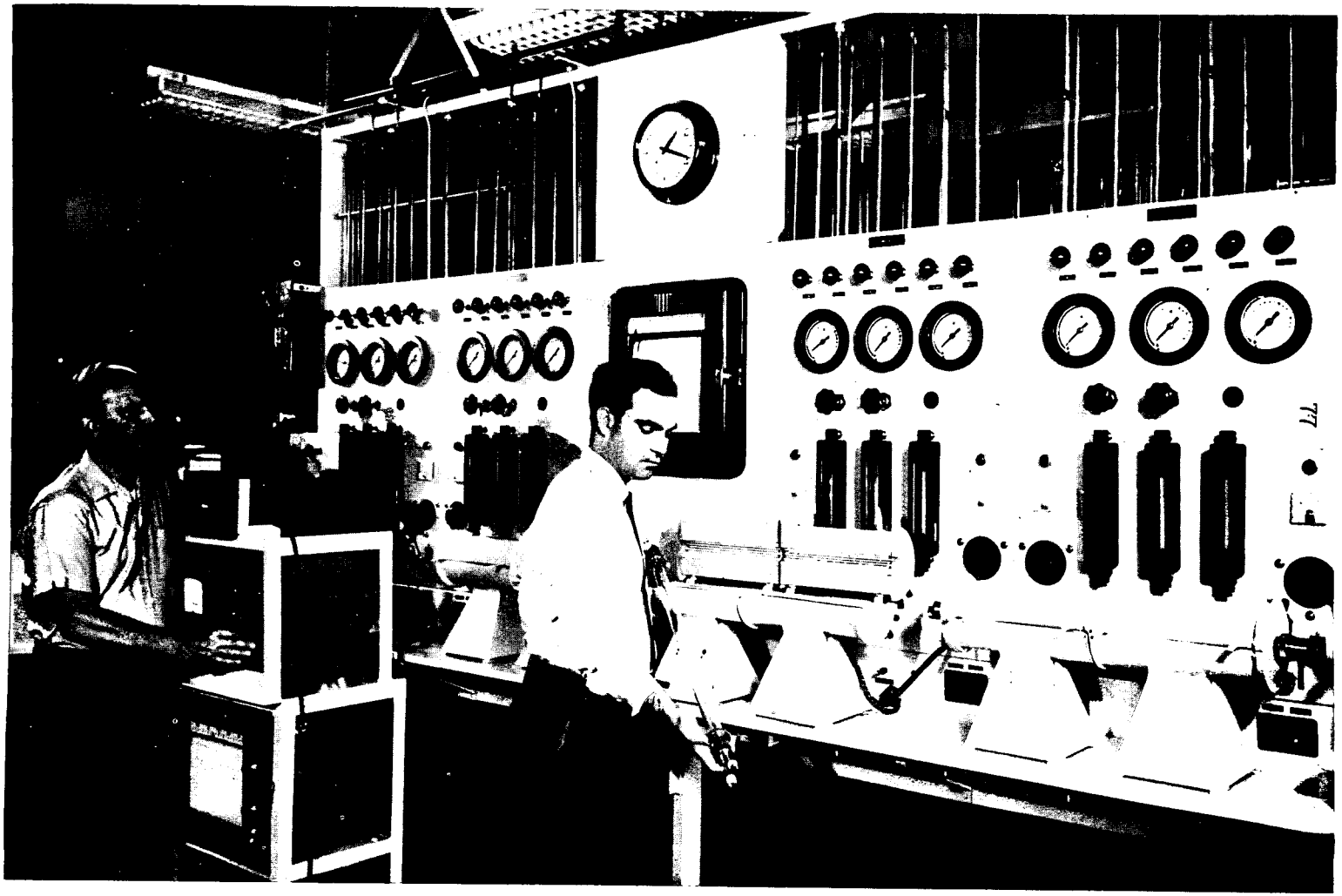

Figure 5.-Units for preparing interstitial compounds by gas-solid reactions

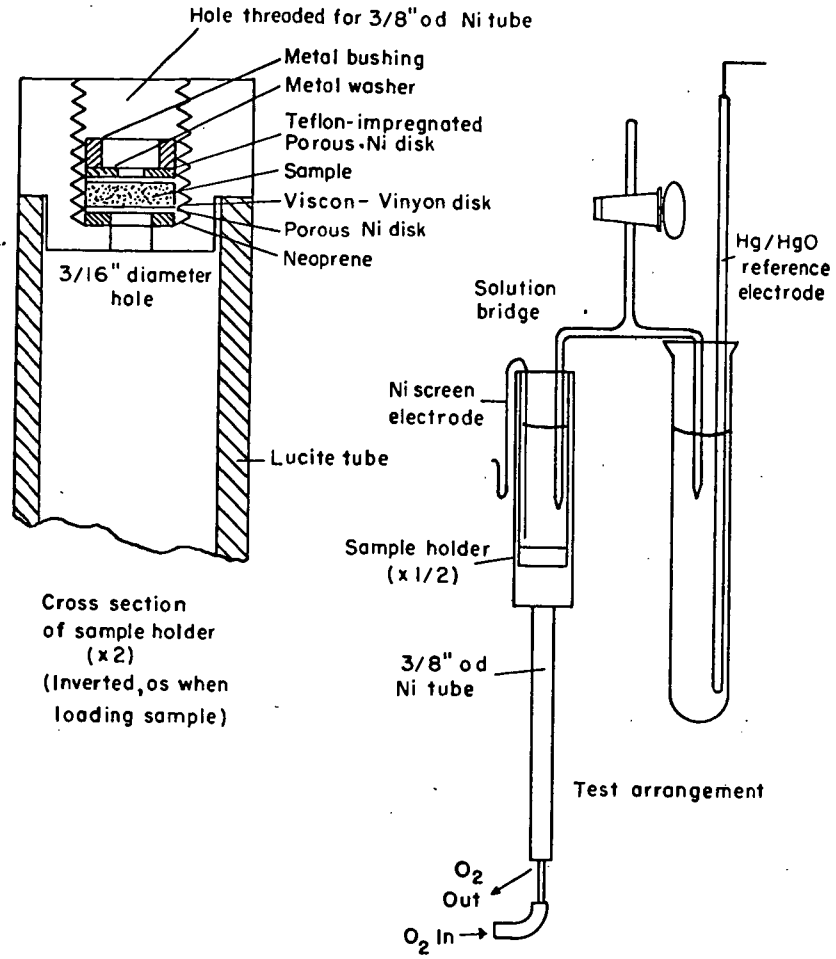

Figure 6.- Test cell.

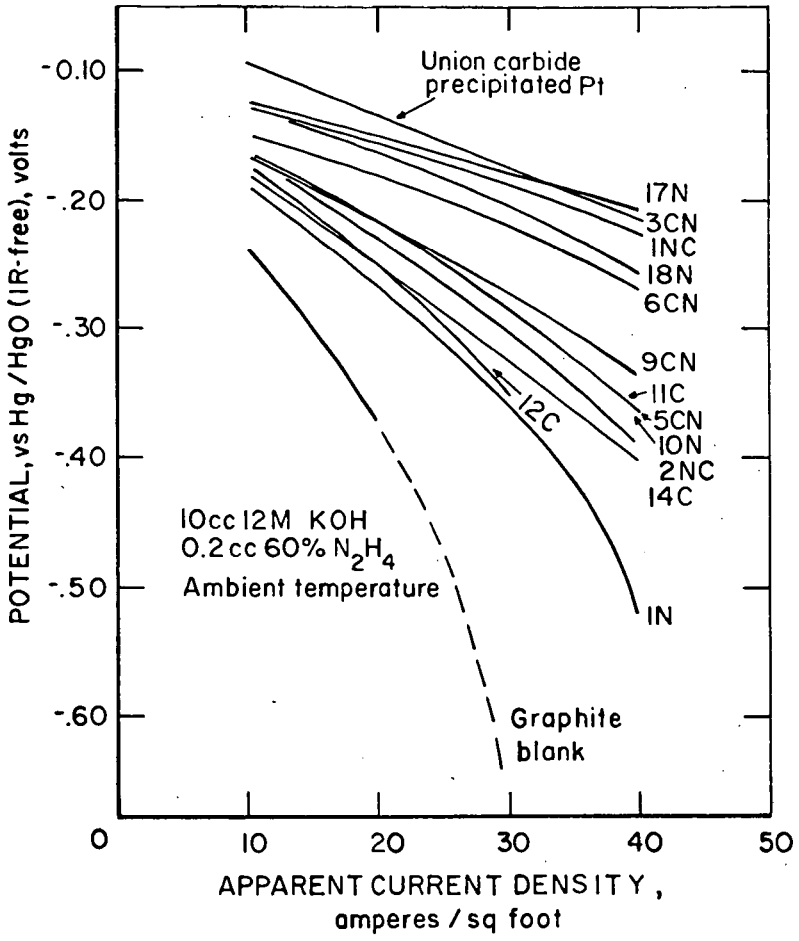

Figure 7.- Cathodic activity of homogenized, inducted materials in the reduction of O_2 in 12M KOH containing N_2H_4.

KINETICS OF REACTIONS ON SILVER AND NICKEL OXYGEN ELECTRODES IN ALKALINE SOLUTIONS

N.A.Shumilova, V.S.Bagotzky, G.V.Zhutaeva, N.D.Merkulova, G.P.Samoilov, E.I.Khrushcheva, V.Yu.Filinovsky

Institute of Electrochemistry, Academy of Sciences of the U.S.S.R., Moscow.

ABSTRACT

Although the oxygen electrode has been the object of numerous studies, it remains as yet a limiting factor in the operation of hydrogen-oxygen fuel cells. In fact, whereas the hydrogen electrode operates under reversible conditions, for real oxygen electrodes it has not been possible to obtain a low enough polarization during the oxygen ionization reaction. Therefore, for an oxygen reaction it is extremely important not only to choose a proper catalyst, but also to find the optimum conditions of the occurrence of the oxygen ionization reaction. In view of a complicated stepwise nature of this reaction, the presence of competing parallel reactions, the formation of hydrogen peroxide as an intermediate product in particular, in order to create effective and stable oxygen electrodes it is necessary to study the mechanism of this reaction, the kinetics of its separate steps and to find the optimum conditions of its occurrence.

In the present paper we have studied the operation of oxygen electrodes in alkaline solutions by means of the disk-ring electrode, using silver and nickel as electrode

materials. The oxygen ionization reaction on silver and nickel in alkaline solutions occurs simultaneously by two mechanisms; by direct reduction to hydroxyl ions and with the formation of hydrogen peroxide as an intermediate product, which can be further electrochemically reduced to water and decompose catalytically to form molecular oxygen and water. We have measured partial currents and the rate constants of the individual steps of oxygen reduction reactions, allowing for the possibility of a catalytic hydrogen decomposition, and found the dependences of these partial currents on the electrode potential and its oxidation state. Particular attention has been given to the process of further reduction of hydrogen peroxide.

The analysis of the data on the kinetics of the individual steps of oxygen ionization reaction can serve as an important subsidiary means for the assessment of the suitability of a metal for use as a material for oxygen electrodes of fuel cells, in which hydrogen peroxide formation is undesirable.

ADSORPTION AND ANODIC OXIDATION OF HYDROGEN ON TUNGSTEN CARBIDE ELECTRODES

Harald Böhm

AEG-TELEFUNKEN Forschungsinstitut
Frankfurt am Main

So far the anodic oxidation of hydrogen has mainly been performed in fuel cells working with an alkaline electrolyte. The drawbacks of an alkaline cell - carbonate formation and poisoning of the electrocatalysts - are however sufficiently well known.

Fuel cells working with an acid electrolyte avoid these difficulties. Noble metals however are needed as electrocatalysts. The resulting main disadvantages are the high inherent cost and the sensitivity of platinium against CO.

Our aim therefore was the utilisation of non-noble metal catalysts for the anodic oxidation of commercial, impure hydrogen in an acid fuel cell.

Four years ago we discovered that tungsten carbide is a useful electrocatalyst / 1 /. WC had so far been known in engineering as a refractory material with hard wearing properties. Catalytic properties had not until then been attributed to this substance. In view of its excellent acid resistance and good electrical conductivity we have prepared gas diffusion electrodes from WC-powder. On these electrodes, arranged in a conventional half-cell with 2 N H_2SO_4 as an electrolyte, we have measured the anodic hydrogen oxidation.

The first figure shows the results of the triangular voltage sweep measurements. With argon only at a potential exceeding 700 mV against a H_2 reference electrode in the same solution according to Giner /2/ commences the oxidation of the WC. With hydrogen higher current densities are achieved which are attributable to the anodic oxidation of hydrogen. Stationary measurements too - as in Figure 2 - show the hydrogen consumption rate. The results for different temperatures provide an activation energy in the range of 5.5 to 7.6 kcal/mol.

These measurements were taken on a gas diffusion electrode which was manufactured from a commercial quality of WC powder. But to exclude secondary effects such as porosity etc. measurements are best made with smooth WC electrodes. Such electrodes are obtained by carburizing 20µm thick tungsten foils with lampblack at temperatures of 1500-1600°C. A thicker sheet would not yield a full carburization effect. At these smooth electrodes the oxidation and adsorption of hydrogen was measured in a thermostatically controlled cell. Again a half-cell assembly was chosen with a platinized platinum electrode as the reference electrode, and 2N H_2SO_4 as the electrolyte. The hydrogen was streamed through a frit. (Fig. 3)

Only low current densities are observed at these smooth WC electrodes for the anodic hydrogen oxidation. At 20 $\mu A/cm^2$ the limiting current density is already found to occur. This is rather a low value compared to smooth platinum electrodes. The exchange current density for the H_2/H^+ reaction at WC is also very low, 0,4 $\mu A/cm^2$.

We have determined the kinetics of hydrogen adsorption under open circuit conditions by plotting the charging curves. For this

purpose the electrode is subjected to a loading cycle as is illustrated in Figure 4. First the electrode was kept at +400 mV where practically no H_2 adsorption takes place. Thereafter the electrode is placed into a potential-free state, and during this period of time t_{ad} hydrogen is being adsorbed. When this period has elapsed the whole amount of adsorbed hydrogen is oxidized by one rectangular current impulse; the adsorbed quantity of hydrogen is determined from the potential curve. By selecting various lengths of t_{ad} the maximum adsorbable hydrogen amount and the kinetics of the adsorption process may be determined.

A noticeable H_2 adsorption on the WC electrodes only occurs after several anodical impulses when the electrodes assume potentials of 800 to 1000 mV. It must therefore be assumed that adsorption does not directly proceed on the WC surface but rather on a thin oxide layer formed during the anodic impulse duration.

The maximum adsorbable hydrogen volume is not reproducible employing various smooth WC electrodes. The values found lay between 7 and 32 $\mu C/cm^2$. The platinum electrode in contrast yielded 570 $\mu C/cm^2$.

The adsorption process kinetics also differ between WC and Pt electrodes. This process may be characterized by the Langmuir equation:

$$\frac{d\theta}{dt} = k c_{H_2} (1 - \theta)^n$$

$$\log \frac{d\theta}{dt} = \log K + n \log (1 - \theta)$$

where θ represents the degree of coverage - θ is arbitrarily equated with unity for the maximum adsorbable H_2 amount - k is the rate constant, c_{H_2} the hydrogen concentration within the electrolyte, and n is the order of reaction with regard to the free surface sites.

Figure 5 shows log $d\theta/dt$ plotted over log $(1 - \theta)$. The slope of the curve and hence of the reaction order n are found to be unity for platinum, for tungsten carbide however two. The slope is very well reproducible for the diverse WC electrodes.

With platinum one surface site is needed, i.e. the adsorption of the H_2 molecule determines the rate of the reaction; with WC and reaction order 2, however, two surface sites are needed. The rate determining step here is the dissociation of the H_2 molecule:

$$H_{2ad} \longrightarrow 2\ H_{ad}$$

The two H atoms are then adsorbed on two surface sites; only with higher fractional coverages will values below 2 be found. With largely occupied surfaces also the adsorption of the H_2 molecule tends to determine the reaction rate.

In spite of the low exchange current density and the low adsorption capacity for hydrogen at smooth WC electrodes, higher current densities may also be attained with WC electrodes manufactured in a suitable process and under the right conditions. Carburization must then be carried out at as low a temperature as is possible with short reaction times. Another precondition is a small particle size.

A proven carburizing method is the reaction of tungsten powder (0,2 µ particle size, with CO at temperatures lying below 1000°C. This process takes place inside a rotating furnace tube; this yields uniform products.

Thin gas diffusion electrodes are manufactured from a thus prepared WC powder, and then the current-voltage characteristics are plotted for the anodic hydrogen oxidation.

In the Table Fig. 6 below the results are shown for a test series carried out at the flow rate of 5 l CO/h. The current density at U_H = 100 mV and the various phases are represented for different carburizing times and temperatures.

At 700°C and even prolonged reaction periods the tungsten powder fails to become fully carburized. But at 800° or at 900°C and within 6 or 8 hours a pure WC is produced. It is of interest to note here that the reaction proceeds via the phase $\alpha - W_2C$, while at 700°C no $\alpha - W_2C$ could be detected. The current densities are higher for the shorter reaction times; however with longer reaction times the catalytic activity drops. This is due to the precipitation of carbon on the catalyst surfaces.

The carbon content and hence the stoichiometry of the tungsten carbide are of great significance for the catalytic activity. Figure 7 shows the carbon content of the WC and the current density plotted against the reaction period, for a reaction temperature maintained at 800°C. By increasing the reaction period, the carbon content increases and exceeds the stoichiometric equivalent. The activity (current density), however, shows a peak. In Figure 8 the activity is plotted against the carbon content for the WC catalysts produced by CO carburization. It can be seen that all results lie within the region between the two curves. Because of the widely differing reaction conditions a range is obtained rather than a characteristic curve. This range, however, shows a distinct maximum. The WC catalysts develop their highest catalytic activity for a carbon content of 5.9 to 6.0 % wt. (theoretical value 6.12 %).

Figure 9 represents a current-voltage characteristic for the anodic oxidation of hydrogen which has been gained at such a sub-stoichiometric material. Current densities of 100 mA/cm^2 are obtained at a polarization of 260 mV.

Noteworthy is that such WC electrodes work on impure hydrogen without any risk of poisoning. Therefore it is possible to operate fuel cells with tungsten carbide anodes consuming unpurified steam reforming gas as their fuel source.

REFERENCES

/ 1 / French Pat. 1.436.504 (1966)

Deutsche Offenlegungsschrift 1.496.176 (1969)

H.Böhm, F.A.Pozzi: Wiss.Ber.AEG-TELEFUNKEN 41 (1968), 46 - 49

/ 2 / J.Diner: J.Electrochem.Soc. 111 (1964), 376

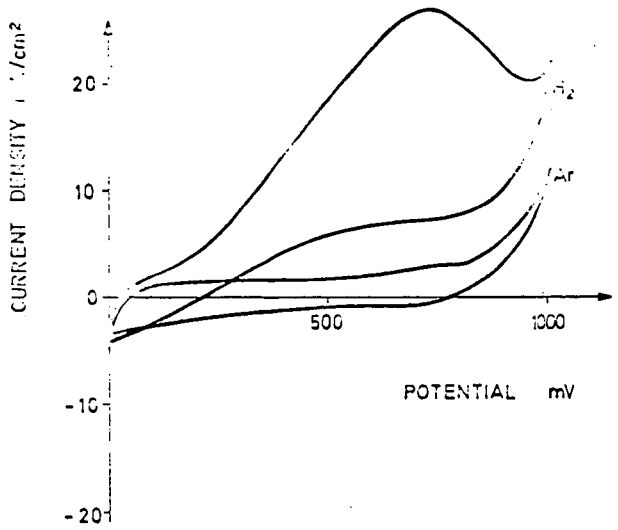

Fig. 1: Potentiodynamic current-potential curves at a WO gasdiffusion electrode, sweep speed 0,1 V/min

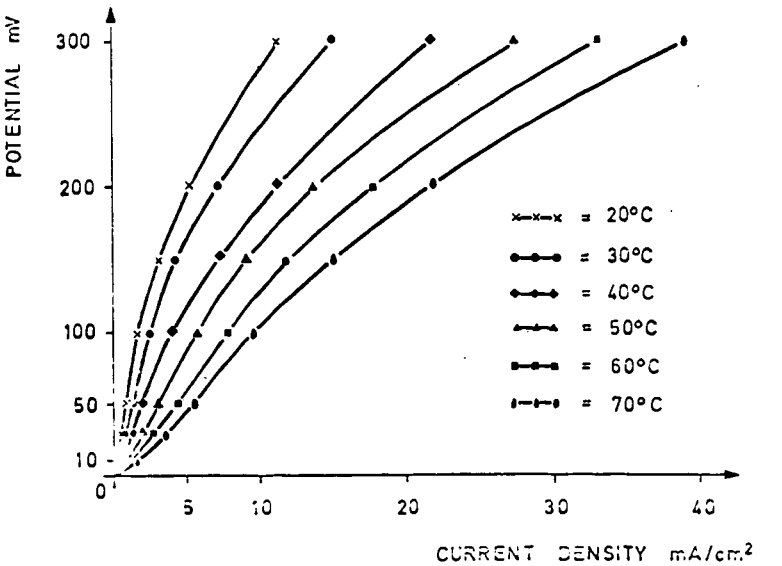

Fig. 2: Current-potential characteristics for the anodic oxidation of hydrogen at gasdiffusion electrodes prepared from commercial WO

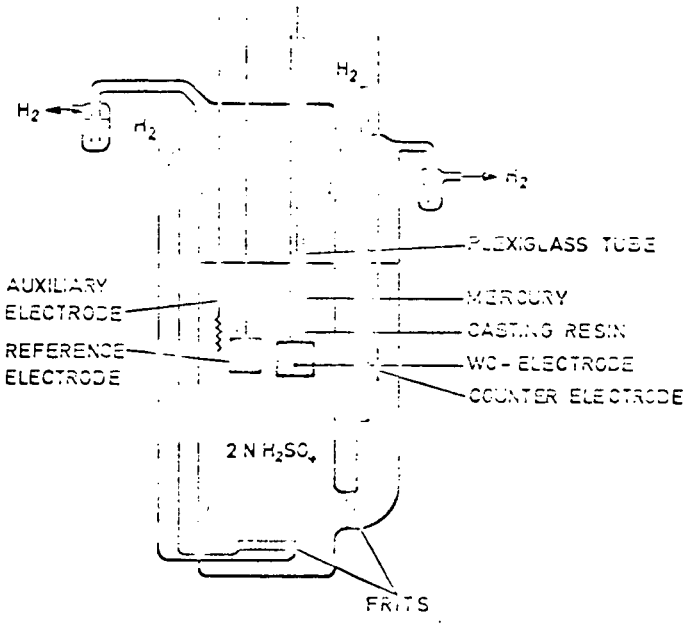

Fig. 3: Schematic diagram of cell

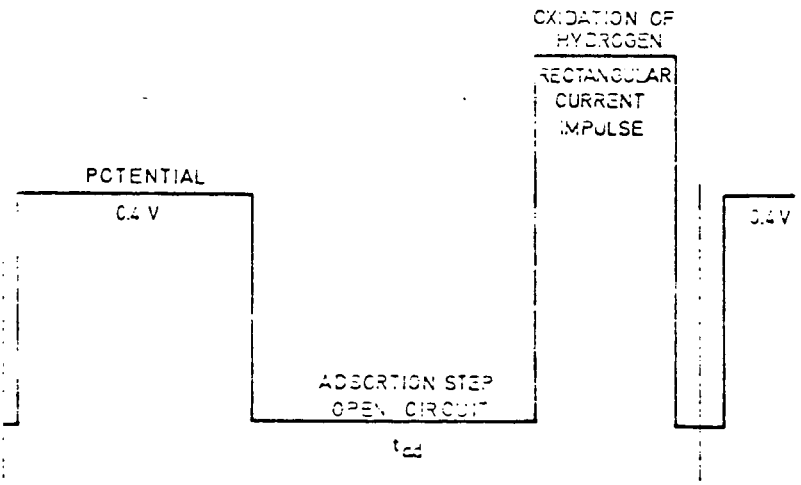

Fig. 4: Loading sequence for the hydrogen adsorption measurement

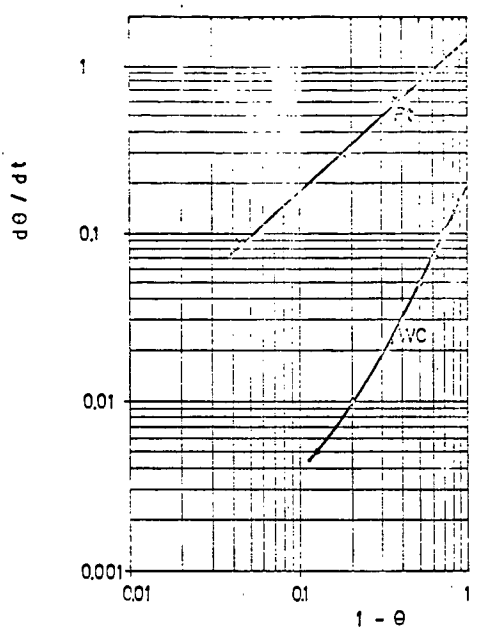

Fig. 5: log $\frac{d\theta}{dt}$ vs. log $(1 - \theta)$
for the adsorption of H_2 on Pt and WC at open circuit conditions

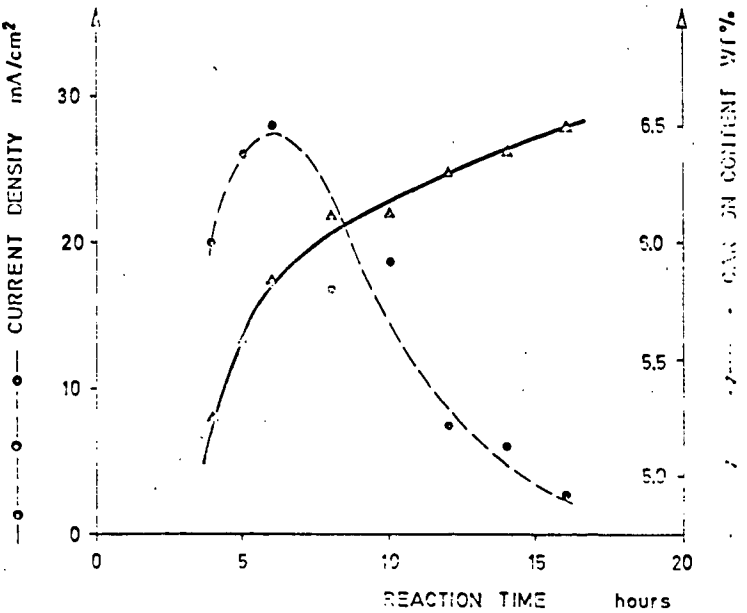

Fig. 7: Effect of carburizing time on the carbon content and on the current density (reaction temperature 1000°)

Reaction time hours	Reaction temperature 700°C	800°C	900°C
4	WC, W 24 mA/cm^2	WC, α-W_2C, W 20 mA/cm^2	WC, α-W_2C, W 6 mA/cm^2
6	WC, W 24 mA/cm^2	WC 27 mA/cm^2	WC, α-W_2C 14 mA/cm^2
8	WC, W 22 mA/cm^2	WC 16 mA/cm^2	WC 22 mA/cm^2
10	WC, W 15 mA/cm^2	WC 19 mA/cm^2	WC 19,5 mA/cm^2
12	WC, W 12 mA/cm^2	WC 6 mA/cm^2	WC 16 mA/cm^2
14	WC, W 12 mA/cm^2	WC 6 mA/cm^2	WC 14 mA/cm^2
16	WC, W 6 mA/cm^2	WC 2 mA/cm^2	—

Current densities were measured at U_H = 100 mV against the hydrogen electrode in the same electrolyte

Fig. 6: Effect of carburizing time and temperature on the catalytic activity of WC

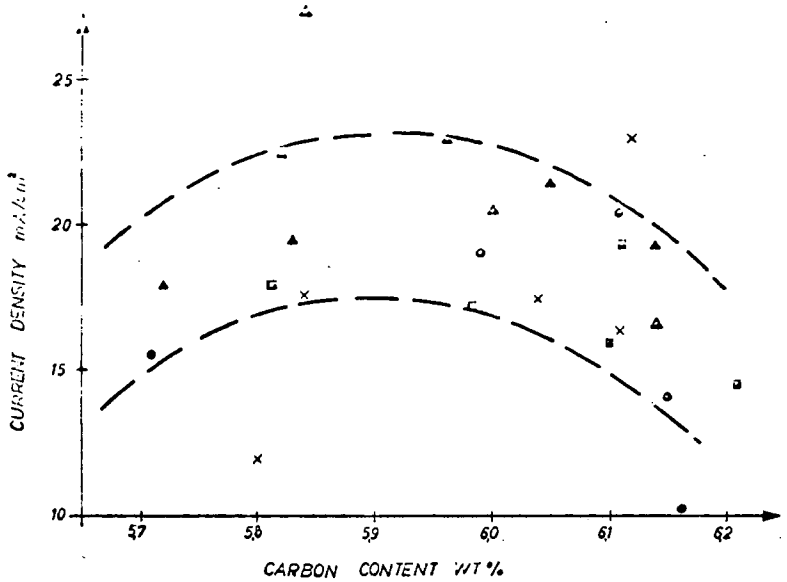

Fig. 8: Relationship between the current density at $U_H = 100$ mV and the carbon content of the tungsten carbide catalysts

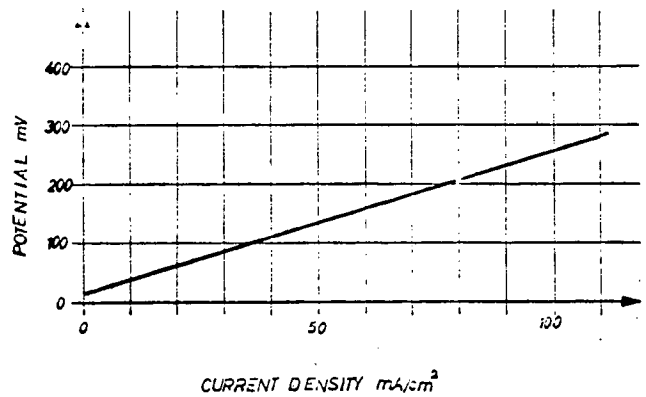

Fig. 9: Performance of a tungsten carbide anode with hydrogen

REACTION MECHANISMS OF THE HYDRAZINE ELECTRODE

M. Barak and G.R. Lomax

Electric Power Storage Limited
Manchester, England.

1. Introduction

The overall reaction at the hydrazine electrode is:-

$$N_2H_4 + 4OH^- \rightarrow N_2 + 4H_2O + 4e$$

Pavela[1] suggested that the mechanism involves the anodic oxidation of hydrogen derived from the decomposition of hydrazine, i.e.

$$N_2H_4 \rightarrow 2H_2 + N_2 \quad \text{and} \quad H_2 + 2OH^- \rightarrow 2H_2O + 2e$$

Alternatively, Szpak[2] et al concluded that at the hydrazine electrode the hydrazine molecule is systematically degraded through various radicals, e.g.

$$N_2H_3^{\bullet} \qquad N_2H_2^{*} \qquad N_2H^{*}$$

to finally produce nitrogen gas.

The reversible electrode potentials calculated from Gibbs Free Energy data for the Pavela and Szpak mechanisms are respectively 0.000V and -0.33V, against a hydrogen electrode in the same solution. The reported values for the open circuit potential of the hydrazine electrode are in the range -0.03V + -0.16V[3][4][5]. Consequently it has been suggested[6] that the observed open circuit potential of the hydrazine electrode is a consequence of the oxidation of hydrazine(1) proposed by Szpak[2] and the electrolysis of water (2).

$$N_2H_4 + 4OH^- \rightarrow N_2 + 4H_2O + 4e \qquad E^\circ = -0.33V \quad (1)$$

$$4H_2O + 4e \rightarrow 2H_2 + 4OH^- \qquad E^\circ = -0.00V \quad (2)$$

No conclusive data has been published however, on the nature of the reactions occurring on hydrazine electrodes working under the conditions encountered in fuel cells. A study was therefore made of the reactions occurring on the hydrazine electrode by investigating the reaction products and the discharge curves associated with a typical working electrode. This paper describes the results obtained on an uncatalysed sintered nickel electrode, worked under conditions where the fuel concentration was strictly controlled with respect to the current being drawn from the system.

2. Experimental

2.1 Apparatus

The apparatus is shown schematically in Fig. 1. The electrode A, diameter 5.7 cm was secured in the wall of the electrolyte cell B, by the Acrylic cover C. The gaseous reaction products were removed from the cell by the ports D and E. Ammonia which was produced at high current densities was removed from the effluent gas by a standard solution of hydrochloric acid in the scrubber F. The flow rate and the composition of the gas passing from the scrubber were respectively measured on the bubble flow meter G and a gas chromatograph.

The fuel mixture of hydrazine hydrate in 7M potassium hydroxide solution was contained in the reservoir H. The fuel mixture was forced from the reservoir H through the capillary J to the chamber K at the rear of the electrode. The fuel flow was controlled by varying the nitrogen gas pressure applied to the tank H and its flow rate was determined from the differential pressure L developed across the capillary J. The fuel mixture flowed through the test electrode into the cell B, and the excess liquid that accumulated in the cell was drained away via the tube N. The cell B was contained in a water jacket maintained at 60°C. The current flowing between the test electrode A and the auxiliary electrode P was controlled by the resistance Q and measured by the ammeter R. The potential of the electrode A was measured against a mercury mercurous oxide half cell S on the valve voltameter T then the results were transposed to the potential against a hydrogen electrode in the same electrolyte.

2.2 Procedure

An electrode 5.7 cm diameter was cut from 70% porous, 0.08 cm thick, sintered nickel plaque. The electrode was cathodised for five minutes in 10% sulphuric acid solution and thoroughly washed in distilled water. After securing the electrode in the cell wall, the interior of the box was filled with a 7M solution of potassium hydroxide containing various concentrations of hydrazine hydrate.

When the cell electrolyte attained a constant temperature of 60°C the fuel mixture was fed to the electrode at a predetermined flow rate. The working potential of the electrode and the analysis of the effluent gas were determined for current densities between 0 and 500 $mA.cm^{-2}$ at various flow rates and concentration of fuel.

3. Results

3.1 Gaseous Evolution from a Working Hydrazine Electrode

The gases evolved from a working hydrazine electrode were analysed and the results are shown in Table 1 where the respective flow rates of nitrogen and hydrogen are quoted at various current densities when the fuel concentration was 1.5M and its flow rate was 30 $ml.min^{-1}$.

Table 1

Gas Evolution for a Working Hydrazine Electrode

Working Potential	Current Density	Nitrogen	Hydrogen	Nitrogen Calculated from the Current + H_2 Evolved
V	$mA.cm^{-2}$	$ml.min^{-1}$	$ml.min^{-1}$	$ml.min^{-1}$
-0.075	50	6.46	4.78	5.03
-0.066	100	5.7	2.0	6.29
-0.050	150	7.6	0.2	8.0
-0.035	200	11.4	0.1	10.65
-0.025	250	15.5	0	13.2
+0.030	300	20.25	0.25	16.1
+0.038	350	20.3	0.4	18.7
+0.045	400	23.8	0.73	22.56
+0.050	450	30.5	1.80	24.7
+0.055	500	29.2	3.4	28.1

A graph of the increase in working potential with current density is shown in Fig. 2. Similarly, Fig. 3 shows the working electrode potential plotted against hydrogen evolution expressed for convenience as $\log_{10} H_2$ evolved on closed circuit.

The experimental technique used for quantitative measurements of hydrogen evolution was not capable of detecting the small amounts of gas evolved within the potential range -0.035V to +0.030V. The observed results plotted in Fig. 3 however, appear to suggest a relationship between the $\log_{10} H_2$ evolved on closed circuit and the working potential, which graphically follows a parabolic curve. This curve, shown in Fig. 3, was therefore extrapolated to pass through a minimum, and it is interesting to note that the potential of the minimum coincided with current density inflexion x shown in Fig. 2.

3.2 Effect of Fuel Flow Rate on a Hydrazine Electrode

When the flow rate of 0.5M fuel through the electrode was varied, the inflexion in the discharge characteristic shown in Fig. 2 was found to be dependent upon the rate at which fuel mixture passed through the system. Table 2 shows the correlation between fuel flow rate and the inflexion current density.

Table 2

The Effect of Fuel Flow Rate

Fuel Flow Rate	Inflexion Current Density
$ml.min^{-1}$	$mA.cm^{-2}$
37	140
56	200
78	250
140	385
220	550

3.3 Effect of Fuel Concentration on a Hydrazine Electrode

At 30 $ml.min^{-1}$ the concentration of the fuel passing through a working hydrazine electrode was varied between 0.5M and 4.0M. The inflexion in the discharge characteristics observed in previous experiments was found to be dependent upon the fuel concentration as shown in Table 3.

Table 3

The Effect of Fuel Concentration

Hydrazine Concentration	Inflexion Current Density
M	$mA.cm^{-2}$
0.5	90
1.0	190
2.0	390
4.0	>500

4 Discussion

All the experiments on working hydrazine electrodes produced an inflexion in the discharge characteristic as the potential of the electrode passed through zero on the hydrogen scale (Fig. 2). The points of inflexion were shown to depend upon the availability of fuel, either in terms of concentration or flow rate. If the polarisation curve in Fig. 2 is plotted in terms of potential against $\log_{10}$ (current density) shown in Fig. 4, then it can be seen that the graph displays two distinct

straight Tafel lines A and B. These lines together with the inflexion observed in Tables 2 and 3 suggest that the electrode can work via two mechanisms. As the theoretical and observed nitrogen evolution rates agree within experimental error it was concluded that the measured evolutions of hydrogen and nitrogen were faradaically consistent with the currents drawn from the working electrode. This justifies the conclusions drawn from Fig. 3 which shows that the evolution of hydrogen was at a minimum in the region of zero potential and it is probable that the mechanism changed at this point.

Susbielles and Bloch[6] have suggested that the observed open circuit potential of the hydrazine electrode is a mixed potential arising from the direct oxidation of hydrazine and the electrolysis of water. In this case the hydrogen evolution should increase as the potential of the hydrazine electrode becomes more negative relative to the hydrogen electrode. Conversely when the hydrazine electrode is at zero volts on the hydrogen scale there should be no nett evolution of hydrogen. The results in Fig. 3 show that at zero potential the hydrogen evolution appears to pass through a minimum, and that it increases directly with increases in the negative potential. This would suggest that the potential is a consequence of two simultaneous reactions which occur in the region negative to the hydrogen electrode. The negative potentials however, exclude the possibility of the hydrazine electrode working via the thermochemical reaction

$$N_2H_4 \rightarrow 2H_2 + N_2$$

and the electrochemical reaction

$$H_2 + 2OH^- \rightarrow 2H_2O + 2e$$

This leaves the more probable mechanism involving the direct oxidation of hydrazine

$$N_2H_4 + 4OH^- \rightarrow N_2 + 4H_2O + 4e$$

associated with the simultaneous evolution of hydrogen by the electrolysis of water

$$4H_2O + 4e \rightarrow 2H_2 + 4OH^-$$

The rate equation for electrochemical processes is

$$i = i_o \exp\left[-\frac{nF}{RT}\,\alpha\,\eta\right]$$

where i = Current density ($A.cm^{-2}$) supporting an overpotential η (V)
i_o = Exchange current ($A.cm^{-2}$)
n = Number of electrons passed
F = Faradaic equivalent
R = Gas Constant
T = Temperature ($^\circ K$)
α = Exchange coefficient

The terms i_o, n, F, R, T and α are constants provided the concentration of reactants remain constant. Under these circumstances the rate equation is simplified to,

$$i = K_1 \exp\left[-K_2\eta\right]$$

where K_1 and K_2 are constants. The relationship between the current i_N and the overpotential η_N associated with the direct oxidation of hydrazine becomes,

$$i_N = K_{1_N} \exp\left[-K_{2N}\eta_N\right]$$

Similarly the current i_H associated with the electrolysis of water is,

$$i_H = K_{1H} \exp \left[-K_{2H}\eta_H\right]$$

The ratio of the currents for both the reactions can be expressed as

$$\log \frac{i_N}{i_H} = A + K_{2H}\eta_H - K_{2N}\eta_N \qquad (3)$$

but the relationship between η_N and η_H is

$$\eta_N = 0.33 - \eta_H$$

Therefore the expression (3) above becomes of the form

$$\log \frac{i_N}{i_H} = B + C\eta_H$$

where B and C are constants.

It can be seen that if at negative potentials on the hydrogen scale, the reaction involving the direct electrochemical oxidation of hydrazine occurs simultaneously with the electrolysis of water on a working hydrazine electrode, then the ratio $\log \frac{i_N}{i_H}$ should be proportional to the overpotential η_H. Values of i_N, i_H and η_H were therefore evaluated from the negative region of Table 1 and the results are shown in Fig. 5. It can be seen that the overpotential η_H was proportional to $\log \frac{i_N}{i_H}$ indicating that the hydrogen evolution was an electrochemical process arising from the electrolytic decomposition of water.

As the evolution of hydrogen at negative potentials is an electrochemical process governed by the rate equation

$$i_H = i_o \exp \left[-\frac{nF}{RT} \alpha_H \eta_H\right]$$

it can be seen that at zero overpotential the hydrogen evolved would be equivalent to the exchange current i_o. Now Fig. 3 shows that the term $\log_{10} H_2$ evolved at closed circuit would pass through a minimum value as the potential passes through zero. It was therefore possible to calculate the hydrogen evolution at zero potential and this was found to be 0.616 $ml.min^{-1}$, which is equivalent to a current $I = 8.85 \times 10^{-3}$A. The exchange current for this reaction was estimated[7] at $i_o = 4 \times 10^{-7} A.cm^{-2}$. The active area of the hydrazine electrode was therefore calculated from the ratio

$$\frac{I}{i_o} = 2.21 \text{ m}^2$$

A typical hydrazine electrode with a superficial area of 16 m^2 would weigh 3.2 g. The active area to weight ratio would therefore be 0.7 $m^2.g^{-1}$. This result agrees closely with the value of 0.66 $m^2.g^{-1}$ calculated from porosity measurements on sintered nickel plaques.

Thus the application of the rate equation to the electrochemical reactions

$$N_2H_4 + 4OH^- \rightarrow N_2 + 4H_2O + 4e$$
$$\text{and } 4H_2O + 4e \rightarrow 2H_2 + 4OH^-$$

produces a result that theoretically correlates with the observed values of electrode

active area, and the proportional relationship between $\log \frac{i_N}{i_H}$ and the overpotential η_H at negative potentials below 0.0V. It was concluded therefore that the working potential of a hydrazine electrode in the region negative to zero on the hydrogen scale, is a consequence of two competing electrochemical reactions, the oxidation of hydrazine and the decomposition of water.

The reactions occurring in the region positive to zero on the hydrogen scale on a working hydrazine electrode were far more complex. Fig. 3 shows that as the working potential of the hydrazine electrode increased above zero, there was a net increase in hydrogen evolution. This phenomena was associated with the straight line Tafel plot B shown in Fig. 4. The results show that it is not possible to correlate this increase in the hydrogen evolution with the reactions proposed by either Pavela[1] i.e.

$$N_2H_4 \rightarrow 2H_2 + N_2 \quad \text{and} \quad H_2 + 2OH^- \rightarrow 2H_2O + 2e$$

or Szpak[a] i.e.

$$N_2H_4 + 4OH^- \rightarrow N_2 + 4H_2O + 4e$$

The evolution of ammonia in this region has been detected on many occasions and it is probable that a number of partial oxidation processes are involved. The dependence of the inflexion current density on the mass transfer of hydrazine to the reaction interface would suggest that diffusion processes were occurring (Tables 2 and 3) but further work will be required to identify these reactions.

References

1. Pavela, Suomen Kemistilehti, 30B, 240, 1957.
2. Szpak, Stonehart and Katan, Electrochimic Acta 10, 563, 1965
3. Gillibrand and Lomax, 'Batteries', Ed. Collins, D.H. Pergamon Press, 1963.
4. Baker and Eisenberg, Abstract 45, Extended Abstracts Electrochem. Soc., Boston, September, 1964
5. Jasinski, Electrochem. Technology, May-June, 1965, p. 129-132
6. Susbielles and Bloch, Compt. Rend Acad. Sci. Paris, 255, 685, 1962.
7. Bockris, Modern Aspects of Electrochemistry, Butterworths, 1954, p. 199.

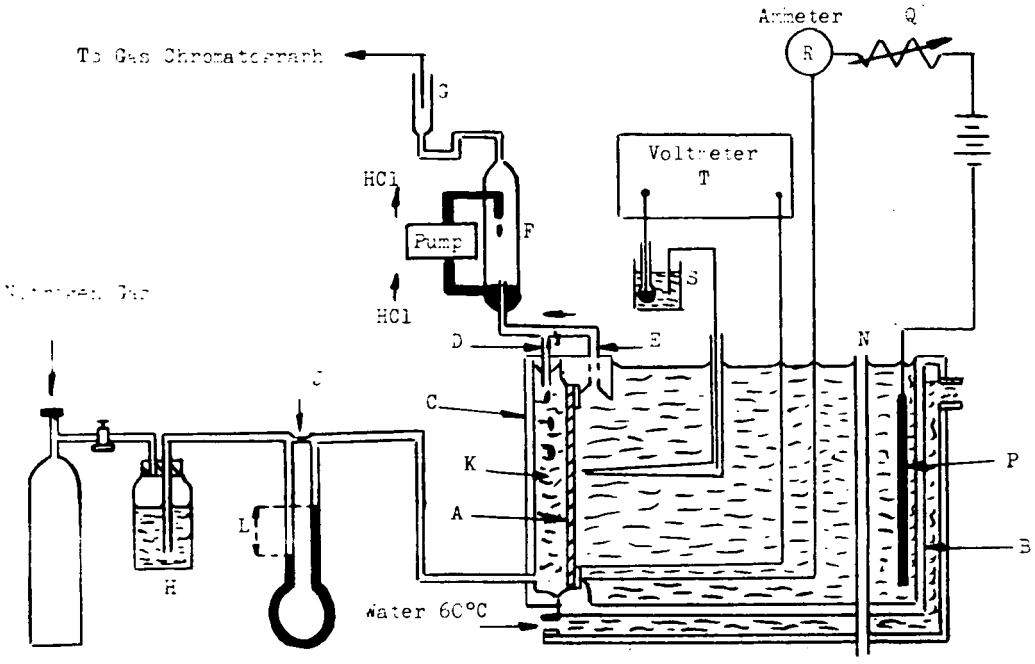

Fig. 1 Apparatus for Investigation on Single Electrodes

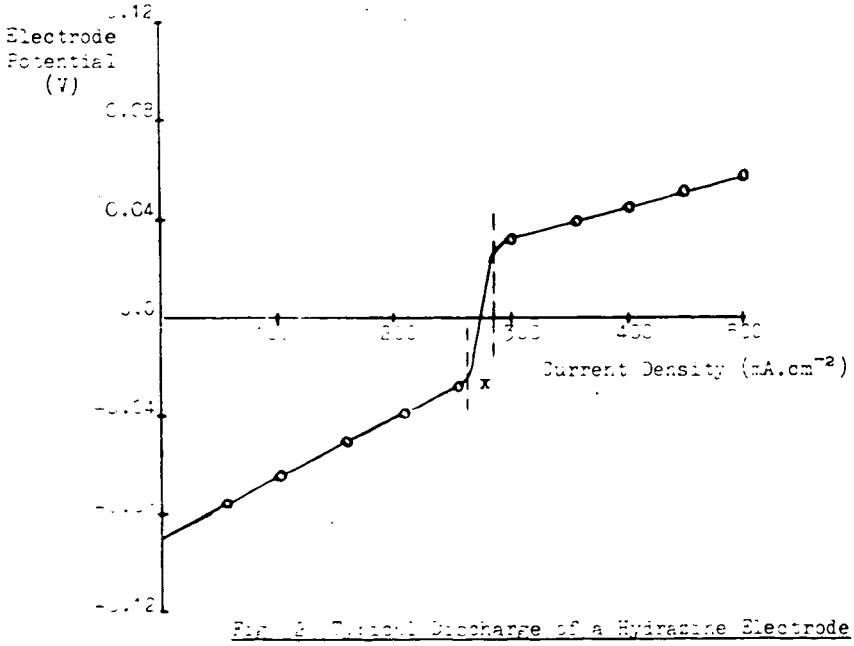

Fig. 2 Typical Discharge of a Hydrazine Electrode

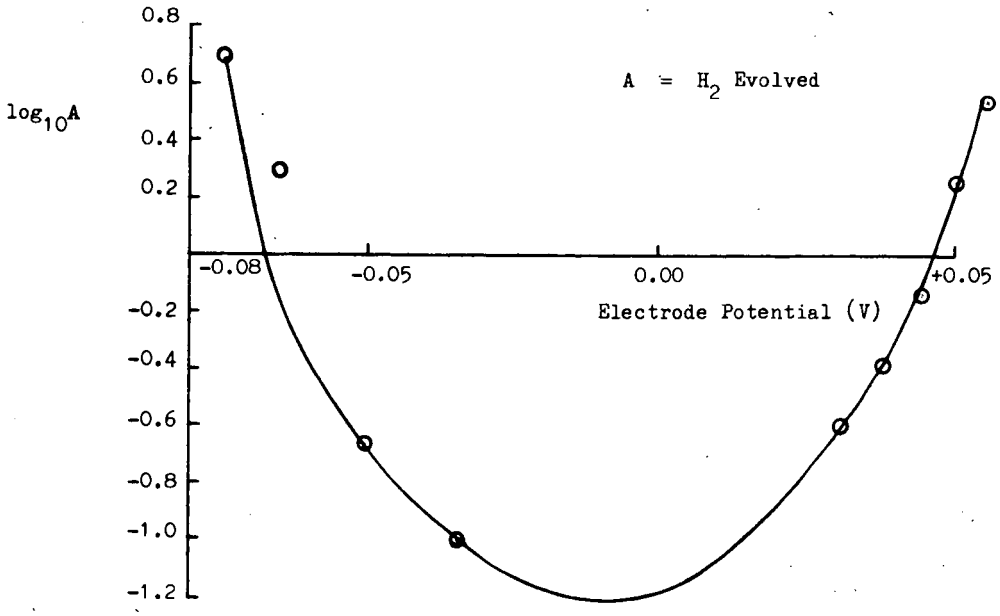

Fig. 3 Hydrogen Evolution from a Hydrazine Electrode

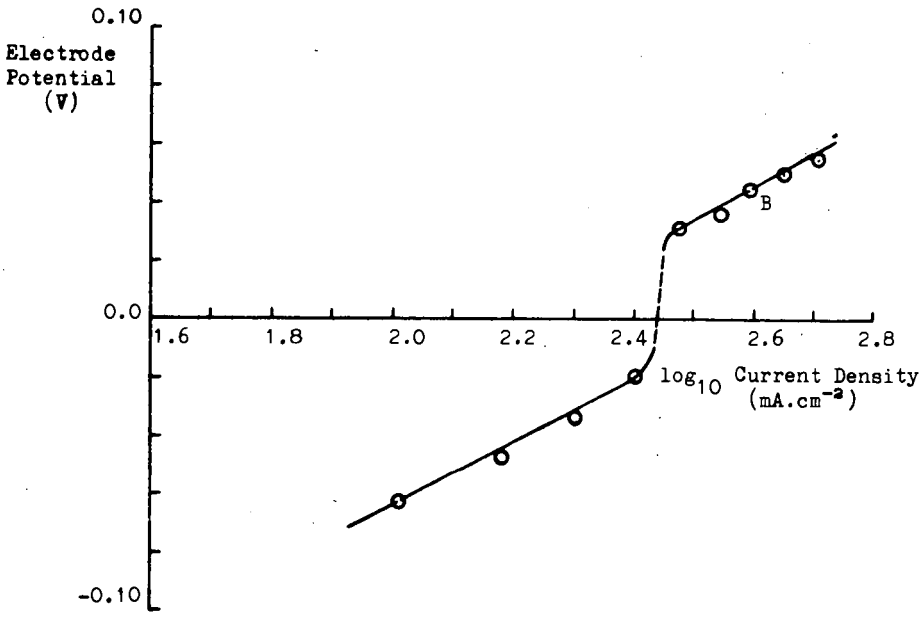

Fig. 4 Tafel Plot for a Working Hydrazine Electrode

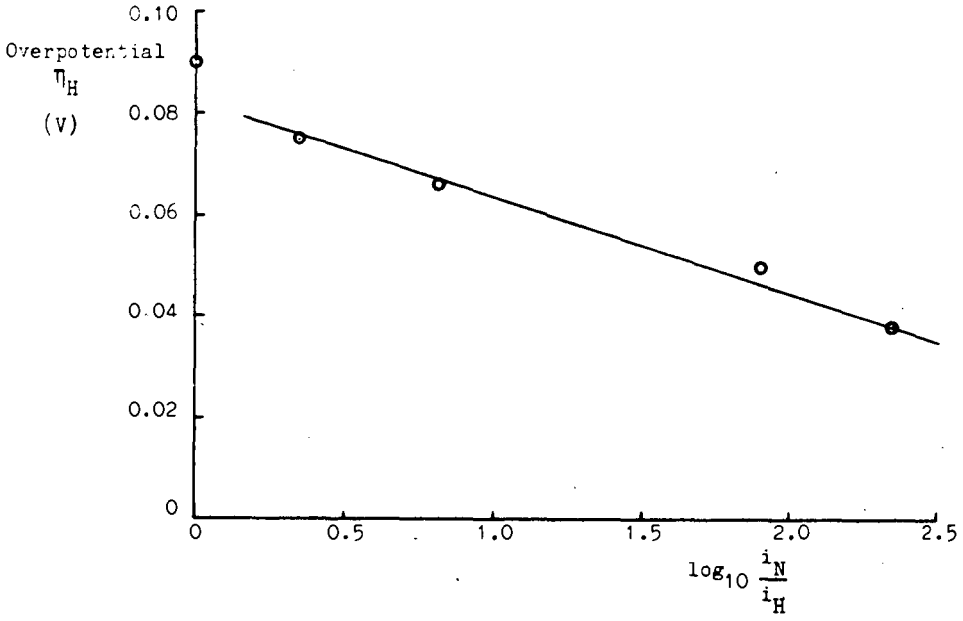

Fig. 5 Relationship Between Overpotential, η_H and $\log_{10} \frac{i_N}{i_H}$

ON THE PERFORMANCE OF WC ELECTRODES UPON OXIDATION OF HYDROGEN, HYDRAZINE, AND FORMALDEHYDE

H. Binder, A. Köhling, and G. Sandstede

Battelle-Institut e.V.
Frankfurt am Main, Germany

1. Introduction

For wide application of fuel cells other than in space technology the one with an acid electrolyte will probably play the predominant part. We could show that in sulfuric acid hydrogen and carbon monoxide can be oxidized simultaneously at high current densities and temperatures below 100 °C at electrodes with pre-sulfurized platinum as the catalyst (1) (2).

However, the price of platinum, even if used in small amounts, is prohibitively high for the very broad application of fuel cells in everyday life. In the attempt to replace platinum a variety of substances has been investigated and proposed as a catalyst for a cell with an acid electrolyte. They did, however, not prove satisfactory. Some of them, e.g. $CoMoO_4$, are not even stable against the attack of sulfuric acid. The activity claimed for several other substances was presumably due to the presence of traces of platinum in the product used as the catalyst in a fuel-cell electrode. So far, we have only found tungsten carbide (WC) to be catalytically active, which has recently been described as a catalyst for the oxidation of hydrogen in acid electrolyte (3). The present paper deals with the preparation and the improvement of tungsten carbide electrodes at which not only hydrogen but also hydrazine and even organic substances can be anodically oxidized at considerably high current densities.

2. Preparation of Electrodes

Tungsten carbide which can serve as a catalyst has to be finely divided. Unfortunately, the commercially available substances generally do not meet this requirement. Tungsten carbide with a large surface area can be obtained, e.g., by precipitation from the gas phase or by the carburization of finely divided tungsten powder with carbonaceous gases (CO or CH_4). We pre-

pared the tungsten carbide required for our investigations by firing an intimate mixture of tungsten powder and soot at a temperature between 1100 °C and 1300 °C in a hydrogen atmosphere.

During the firing process sintering takes place and the resultant product can be used directly as an electrode provided that the starting mixture contained a pore-forming substance and was compressed to disks. Such an electrode is appropriate for the oxidation of fuels dissolved in the electrolyte or may even serve as a bubbling electrode for the oxidation of gaseous substances, such as hydrogen.

When using hydrogen as fuel, we usually prefer an electrode with polyethylene as a binder backed with a wet-proofing layer made from PTFE, as has been described elsewhere (4).

The best performance is achieved with electrodes containing a tungsten-carbide preparation whose carbon content is somewhat smaller than that corresponding to the stoichiometric value. An excess of carbon considerably decreases the catalytic activity of the product.

3. Electrochemical Measurements

3.1 Half-Cell Arrangement

For the electrochemical measurements we used the half-cell arrangement described in detail elsewhere (5), with an autogenous hydrogen electrode in the same electrolyte at the same temperature as the reference electrode. For use as a bubbling electrode the disks were fixed in a plexiglass ring by means of an adhesive and fitted in a specially designed electrode holder. Immersed electrodes were fixed by a tantalum wire loop. The electrolyte - 2N H_2SO_4 - was saturated with pure argon in order to exclude the influence of air. In most cases the measuring temperature was 70 °C.

3.2 Corrosion and its Effect on the Activity

In sulfuric acid free from oxygen corrosion of WC is negligibly small at open-circuit potential or even up to a potential of 300 mv. Between 300 and 500 mv a corrosion current is observed during periodic potentio-dynamic measurements (Fig. 1). After some sweeps this corrosion current starts to decrease and after some hours the corrosion has discontinued. While corrosion takes place the evolution of a gas is observed which means that part of the carbon contained in the carbide is oxidized to give carbon dioxide.

After cessation of corrosion, i.e., when the passive state is reached, the current density achieved with hydrogen is smaller than at the beginning of the experiment. Fig. 2 shows the decrease in activity for an electrode which has been corroded at a potential of 700 mv during 16 hrs. In this case the current density has decreased by about 20 per cent of the initial value.

It has never been observed that such a disactivated electrode can be reactivated by hydrogen gas applied to the electrode, not even at open-circuit potential; the inactive layer can be removed, however, by other means, e.g. by a treatment in potassium hydroxide solution.

A considerable increase in the activity instead of a disactivation is observed, however, when anodic corrosion takes place in the presence of a reducing agent, e.g., hydrogen bubbling through the electrode. Hence the activity of a WC electrode increases slowly during its operation as an anode for the oxidation of hydrogen. Such a slow increase in activity takes several days until a final state is reached where no further activation is observed. More defined results are obtained with a solution of hydrazine sulfate in the sulfuric acid electrolyte at a potential of about 600 to 700 mv maintained by means of a potentiostat. A period of some hours is sufficient to achieve optimum activity. In general the current density at a given potential can be increased up to twice its initial value.

Instead of hydrazine, formaldehyde dissolved in the electrolyte can be used as the reducing agent for the activation process. The reason why the application of a dissolved reducing agent is more effective than the application of hydrogen may be seen in the fact that a dissolved fuel can in any event reach those parts of the inner surface area of the electrode which are reached by the electrolyte, whereas in the case of hydrogen the pore-size distribution and the varying porosity may restrict the expected activation to only a small part of the inner surface area. An electrode which has been activated in the manner just described does not undergo further corrosion up to a potential of, say, 0.7 v, not even in the absence of any fuel.

Fig. 3 shows the current-potential plots obtained with an activated WC electrode under steady-state conditions upon hydrogen oxidation. At a potential of 300 mv and a temperature of 90 °C a current density of 160 ma/cm^2 is measured with this type of a sintered bubbling electrode. At a temperature of 25 °C the current density is reduced to 35 ma/cm^2. From the dependence of the current density on the temperature a mean value of 5.8 kcal/mole is derived for the activation energy at a potential of 300 mv.

A surprising observation is the fact that hydrazine is oxidized at a WC electrode at considerable densities, whereas it is not decomposed at open-circuit potential. Fig. 5 shows galvanostatic current-voltage plots obtained with hydrazine in 2N H_2SO_4 at a temperature of 70 °C. At a potential of 400 mv a current density of 80 ma/cm^2 is achieved under these conditions. Moreover, the figure clearly shows the influence of activation described above.

On the other hand, polarization is very high upon oxidation of hydrazine in sulfuric acid. The periodic potentiodynamic plot of Fig. 6 reveals that oxidation starts only at a potential of about 200 mv. This may be due to the fact that hydrazine sulfate is formed in the sulfuric-acid electrolyte so that a higher activation energy is required. Hence the performance of hydrazine on WC is somewhat improved by using a sulfuric-acid electrolyte with a concentration smaller than 2N, since in this case the solubility of hydrazine is greater. The best performance is achieved in a solution of hydrazine sulfate in water as the electrolyte.

Much more interesting than the oxidation of hydrazine appears the oxidation of formaldehyde. Fig. 7 shows that with formaldehyde a current density of about 60 ma/cm^2 can be achieved at a potential of 400 mv, and that the oxidation starts already at the potential of the hydrogen electrode.

The current density depends largely on the concentration of formaldehyde in the electrolyte, as is shown by Fig. 8.

Unfortunately, oxidation of formaldehyde nearly stops at the stage of formic acid, which is only slowly oxidized. At a potential of 200 mv and a temperature of 70 °C a current density as low as 1 ma/cm^2 is observed (Fig. 9). Even at 90 °C the oxidation rate is small compared with that of formaldehyde. An interesting feature in the oxidation of formic acid at 90 °C is the observation that it is dehydrogenated at the WC electrode under open-circuit conditions. At low current densities the oxidation of hydrogen evolved in the decomposition is the rate-determining step; at higher current densities the rate of dehydrogenation is insufficient, and direct oxidation of formic acid has to take place. This new process requires a higher potential. The maximum current density is reached at a potential of about 400 mv, as is shown by the peak in the periodic potentiodynamic current-voltage plot (Fig. 10).

Acetaldehyde, too, is oxidized at WC. Fig. 11 shows that a current density of about 20 ma/cm^2 is measured at a potential of 400 mv in periodic potentio-dynamic investigations. Under steady-state conditions the current density decreases to about 10 ma/cm^2 (Fig. 12). In the potential range considered, the oxidation stops completely at the stage of acetic acid. This means that at WC electrodes acetic acid can be formed from acetaldehyde in an electrochemical reaction, a process which might be of interest to the chemical industry.

With propionaldehyde only small current densities are observed, which are even smaller in the case of other aldehydes.

Neither alcohols, not even methanol, nor carboxylic acids other than formic acid can be electrochemically oxidized at WC electrodes in sulfuric acid.

4. Conclusions

Our investigations show that WC is an interesting new electrocatalyst at which not only hydrogen but also a variety of other substances can be oxidized. From our findings we conclude that the activation process described in this paper is due to the formation of tungsten oxides other than WO_3 with an oxidation number smaller than six, for instance tungsten bronzes of the type H_xWO_3, first reported by Glemser and Naumann (6). These bronzes are considered as activators of platinum catalysts in the oxidation of carbon monoxide (7). Thus it might be the combination of such a bronze with WC as the carrier which gives rise to the good performance observed. We hope that these results will help us in our efforts to replace platinum as a catalyst even for the direct electrochemical oxidation of methanol or hydrocarbons.

Acknowledgement: This work is part of a program for a group project and we greatly appreciate the sponsors' permission to publish these results.

Literature

(1) H. Binder, A. Köhling and G. Sandstede, Advanced Energy Conversion 7, 77(1967)

(2) H. Binder, A. Köhling and G. Sandstede, Paper presented at the 5th Biannual Fuel Cell Symposium of the ACS in Chicago, Fall 1967, Advances in Chemistry Series, in press

(3) H. Böhm and F.A. Pohl, Wissenschaftliche Berichte, AEG-TELEFUNKEN, 41, 46(1968); Paper presented at the "Troisièmes Journees Internationales d'Etude des Piles à Combustible", Brussels, June 1969

(4) H. Binder, A. Köhling, W. Kuhn, W. Lindner and G.Sandstede, Chemie-Ing.-Technik 40, 171(1968); French Pat.1537403(1967)

(5) H. Binder, A. Köhling and G. Sandstede, Chemie-Ing.-Technik 40, 543(1968); Advan.Chem.Ser. 47, 269(1965)

(6) O. Glemser and K. Naumann, Z.Anorg.Allg.Chemie 265, 288(1951)

(7) B.S. Hobbs and A.C.C.Tseung, Nature 222, 558(1969)

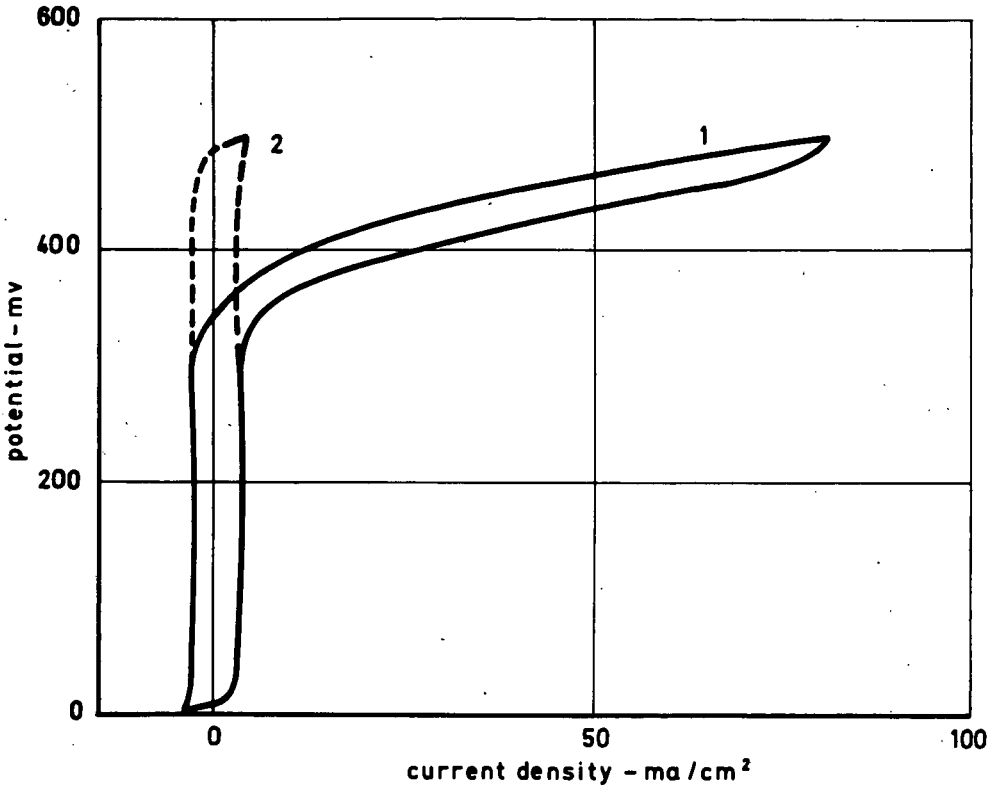

Fig. 1 Corrosion of WC in 2N H_2SO_4 at Anodic Potentials in the Absence of Reducing Agents at 70 °C. Periodic Potentiodynamic Current-Potential Plots; dU/dt = 40 mv/min.

Curve 1: Initial State
Curve 2: Final (Passive)State

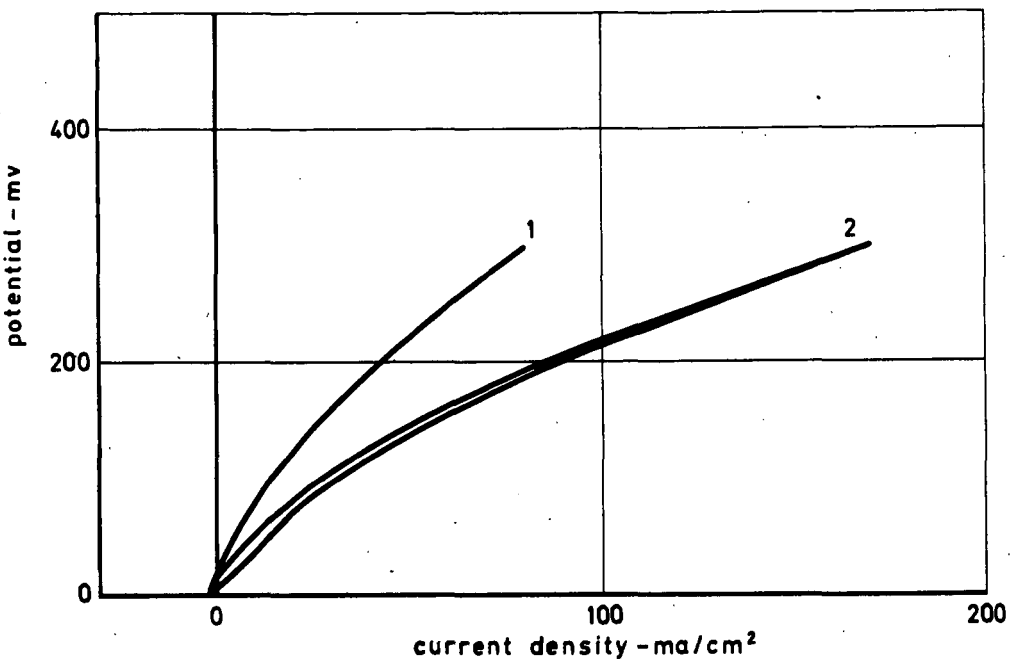

Fig. 2 Oxidation of Hydrogen at a WC Electrode in 2N H_2SO_4 at 70 °C. Periodic Potentiodynamic Current-Potential Plots; dU/dt = 100 mv/min.

Curve 1: Initial State
Curve 2: After Activation at a Potential of 650 mv in the Presence of Hydrogen

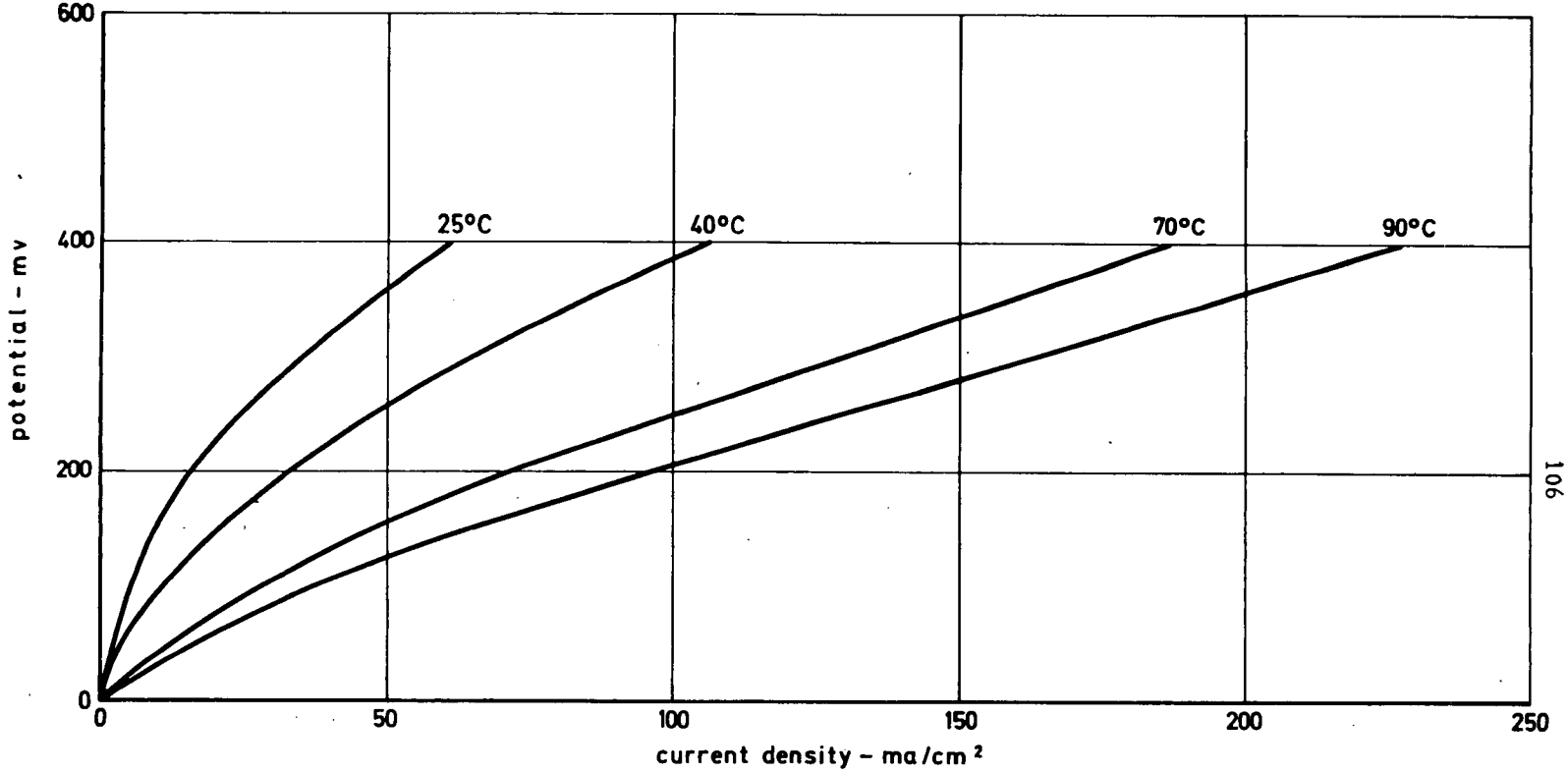

Fig. 3 Effect of Temperature on the Rate of Hydrogen Oxidation at a WC Electrode in 2N H_2SO_4 under Steady-State Conditions

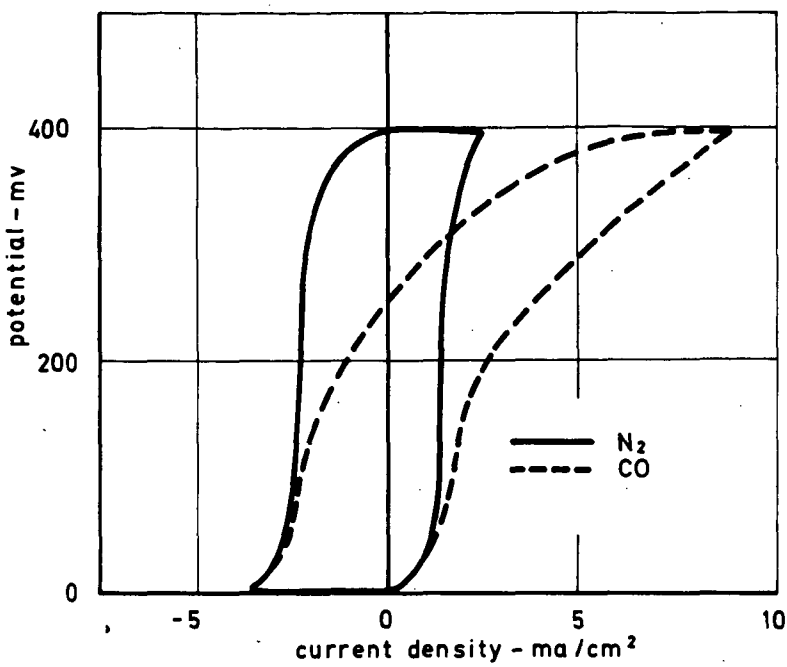

Fig. 4 Oxidation of Carbon Monoxide at a WC Electrode in 2N H_2SO_4 at 70 °C. Periodic Potentiodynamic Current-Potential Plots; dU/dt = 40 mv/min.

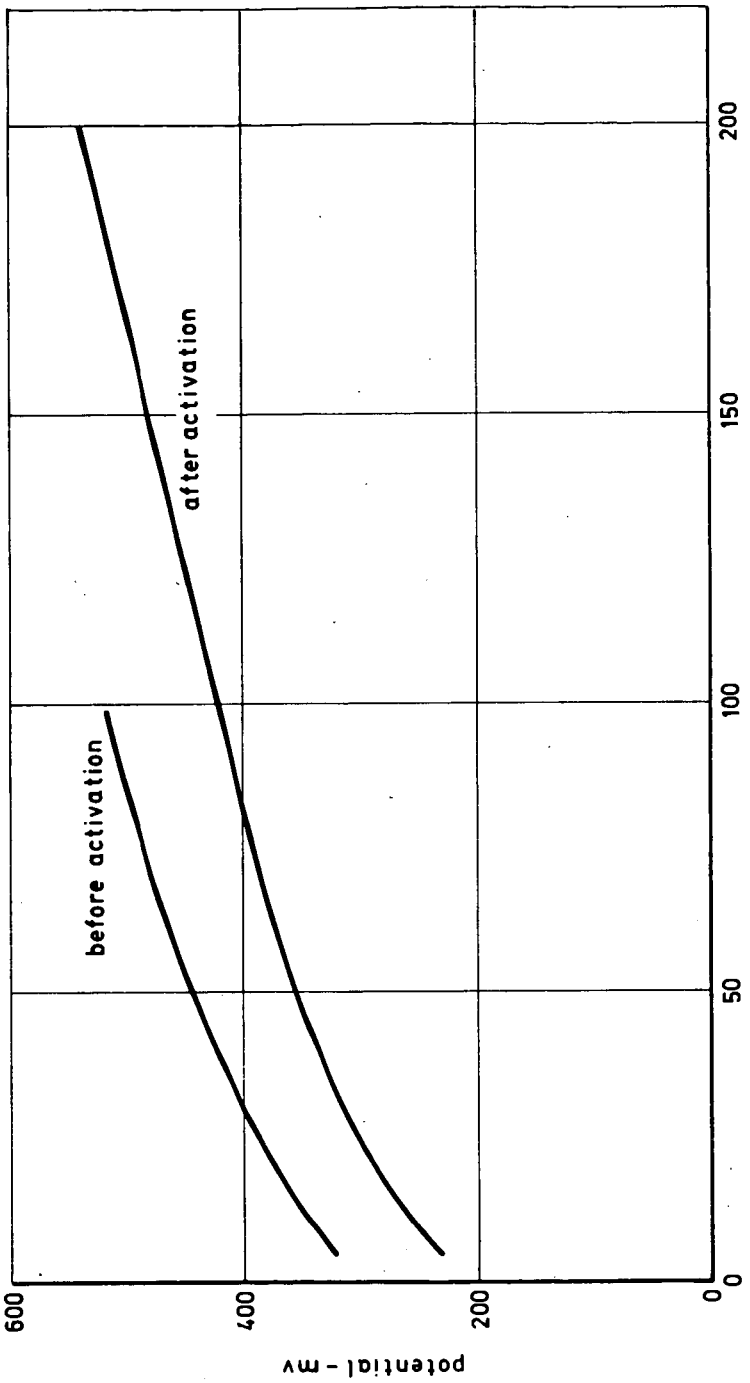

Fig. 5 Oxidation of Hydrazine at a WC Electrode in 2N H_2SO_4 at 70 °C under Steady-State Conditions

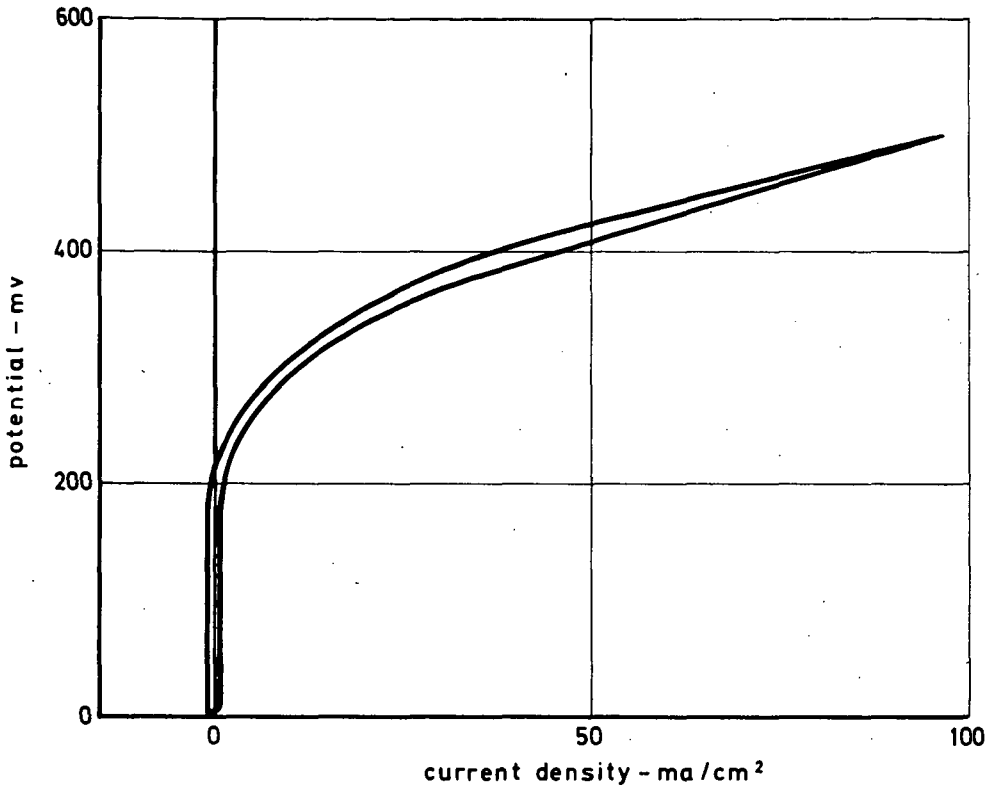

Fig. 6 Oxidation of Hydrazine at a WC Electrode in 2N H_2SO_4 at 70 °C. Periodic Potentiodynamic Current-Potential Plot; dU/dt = 100 mv/min

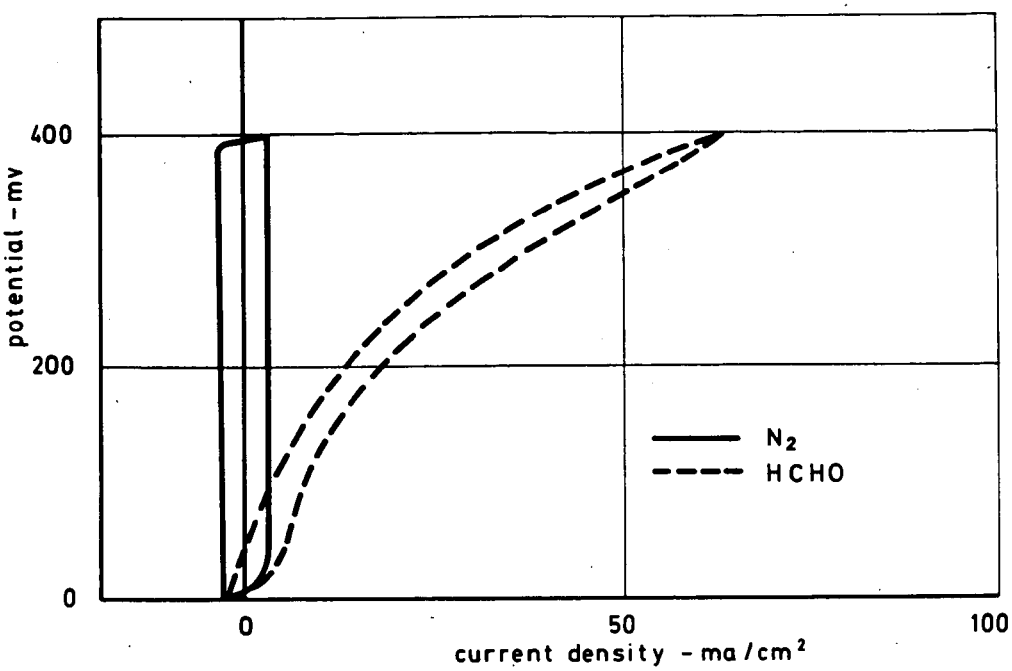

Fig. 7 Oxidation of Formaldehyde at a WC Electrode in 2N H_2SO_4 at 70 °C. Periodic Potentiodynamic Current-Potential Plot; dU/dt = 100 mv/min

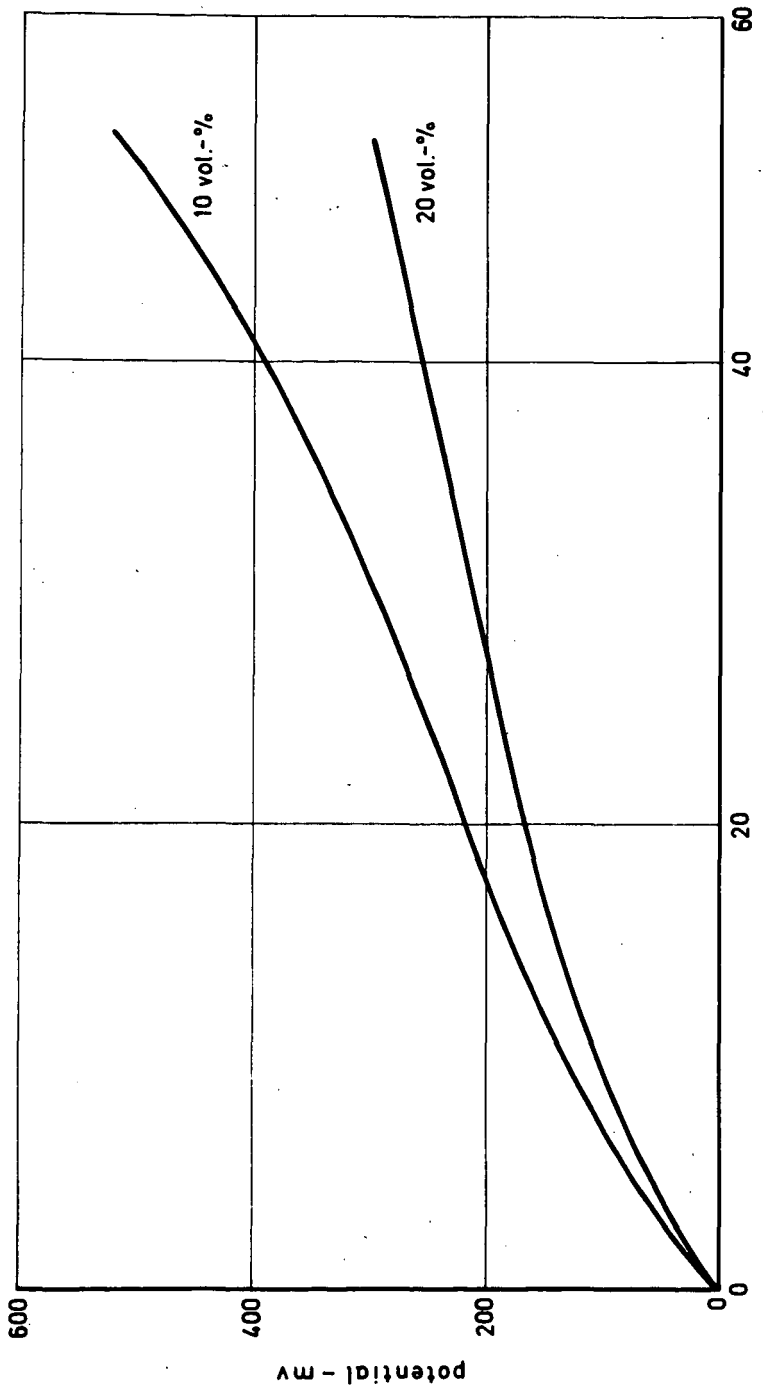

Fig. 8 Effect of Formaldehyde Concentration on the Performance of a WC Electrode in 2N H_2SO_4 at 70 °C under Steady-State Conditions

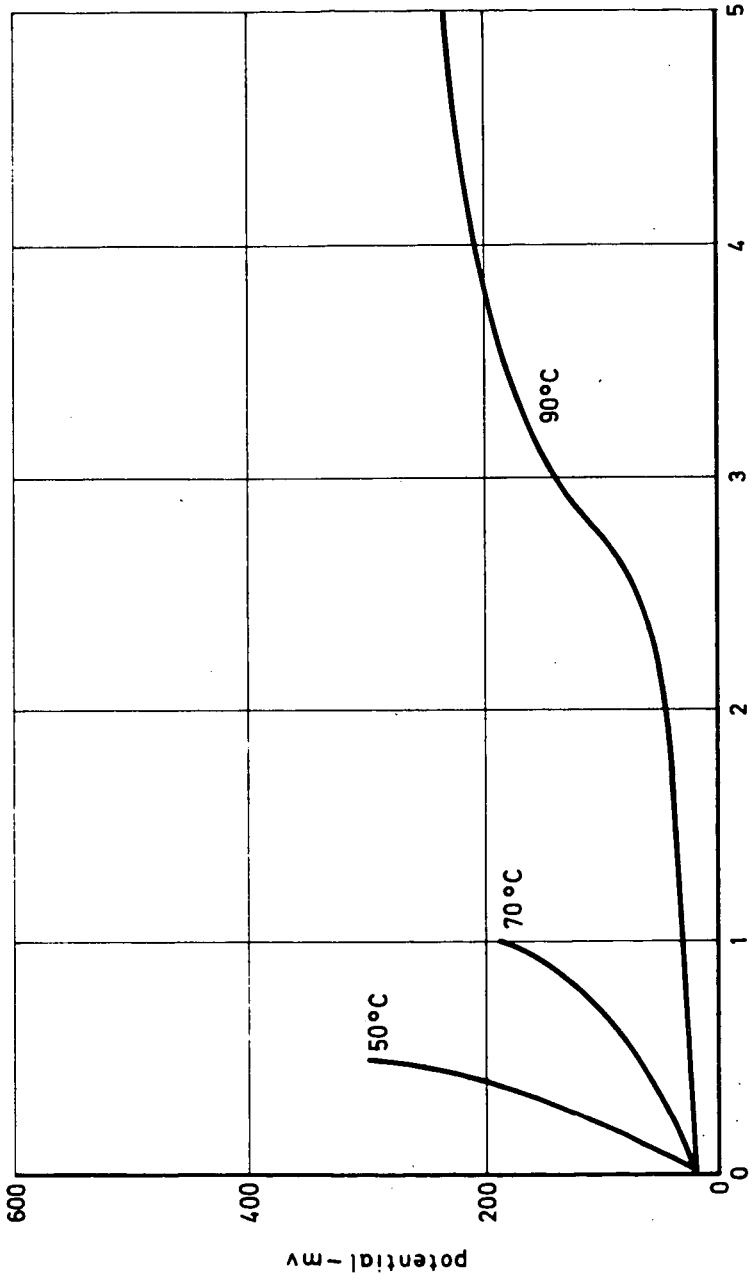

Fig. 9 Effect of Temperature on the Rate of Formic Acid Oxidation at a WC Electrode in 2N H_2SO_4 under Steady-State Conditions

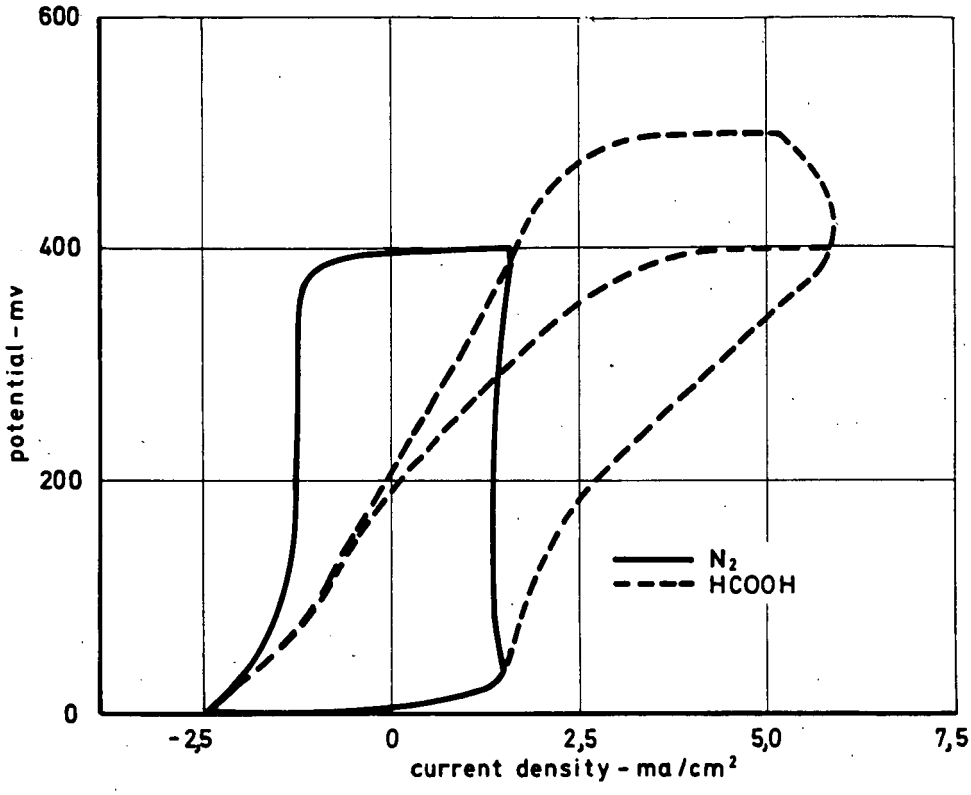

Fig. 10 Effect of an Intermediate from Formic Acid Oxidation on the Performance of a WC Electrode in 2N H_2SO_4 at 70 °C. Periodic Potentiodynamic Current-Potential Plots; dU/dt = 40 mv/min

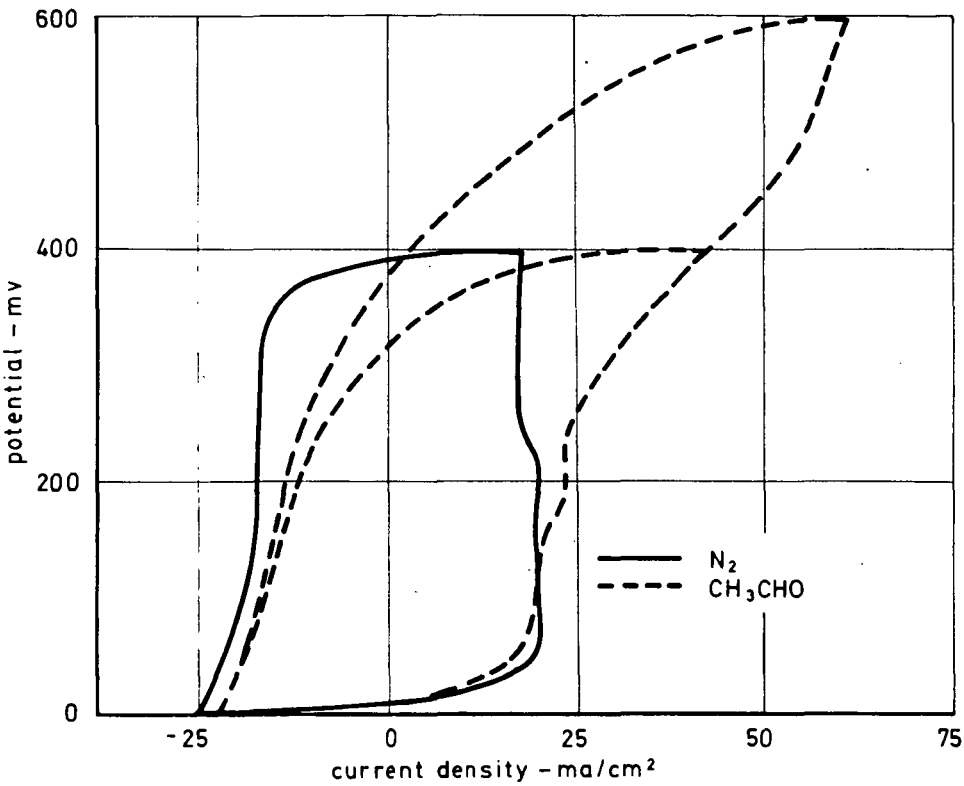

Fig. 11 Oxidation of Acetaldehyde at a WC Electrode in 2N H_2SO_4 at 70 °C. Periodic Potentiodynamic Current-Potential Plots; dU/dt = 100 mv/min

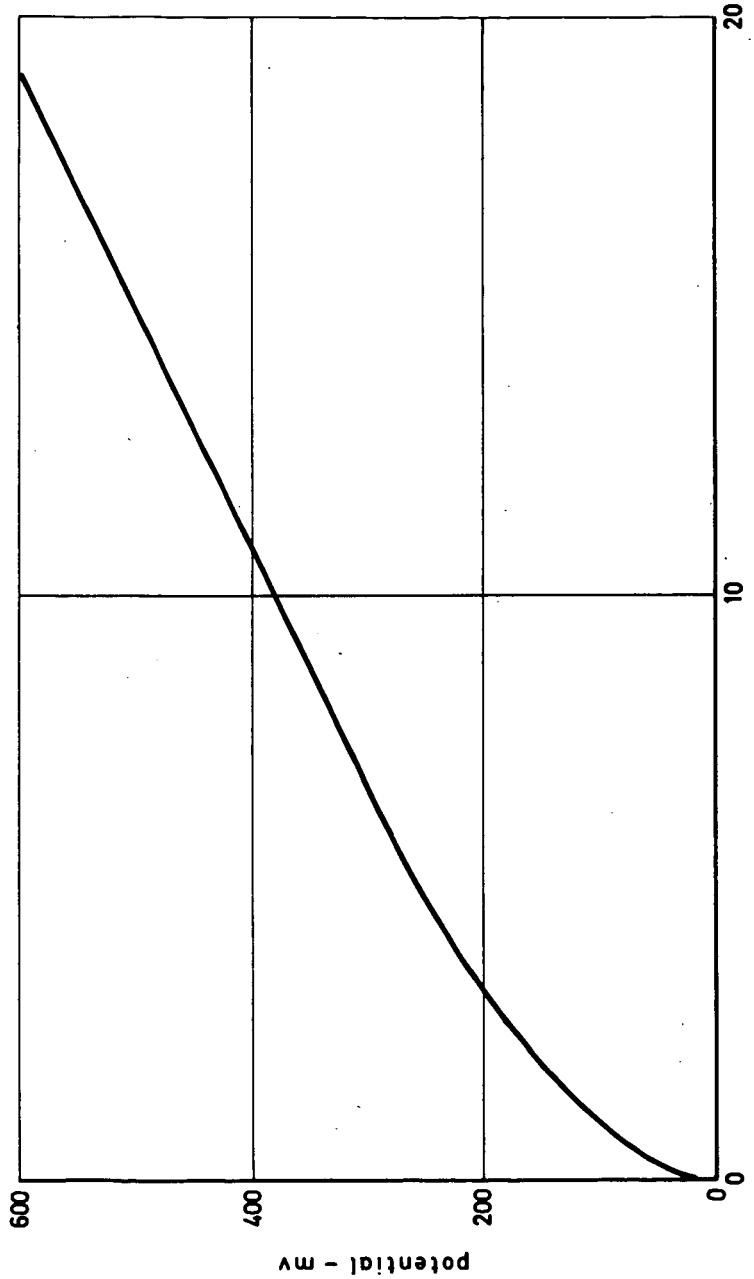

Fig. 12 Oxidation of Acetaldehyde at a WC Electrode in 2N H_2SO_4 at 70 °C under Steady-State Conditions

THE EFFICIENCY OF HYDRAZINE-PEROXIDE FUEL CELLS

H. B. Urbach and R. J. Bowen

Naval Ship Research and Development Laboratory
Annapolis, Maryland

INTRODUCTION

Hydrazine fuel cells may be a contender in some future applications of fuel-cell power (reference 1). However, the precise evaluation of the hydrazine fuel cell relative to other cells requires a knowledge of their realizable experimental coulombic efficiencies. The inefficiencies characteristic of hydrazine fuel cells are caused largely by self decomposition of the hydrazine, cross diffusion of hydrazine and oxygen through the porous structure of the cell, and by bleed of oxygen from the cell. A sample evaluation of such coulombic inefficiencies is made in this report based upon laboratory analysis of a single 6-in by 6-in cell employing platinum catalyzed fuel cells. The revelancy of the data is quite general. However, the specific assignment of numerical values of efficiency to other systems should only be employed with the knowledge that considerable variation exists not only between different commercial systems but within individual systems.

DESCRIPTION OF THE EQUIPMENT

Mechanical Features of the Experimental Apparatus

High ambient pressures were developed in a pressurized system

similar to that shown in Figure 1. The pressure chambers were 5-in and 9-in diameter steel vessels rated at 15,000 and 30,000 psi respectively. Pressurization of the system was achieved with high pressure argon and oxygen compressed with air-driven compressors. Cells of 15 cm^2 (circular) and 232 cm^2 (6-in by 6-in square) were employed. The hydrazine-electrolyte mixture was circulated past the anode with a magnetically coupled centrifugal impeller for the small cell with a pressure-equilibrated submersible centrifugal pump in the large cell. The electrolyte flow was monitored with a turbine flow meter (FI).

Electronic Components of the Experimental Apparatus

Polarization data were obtained by programming the current sweep of a 50-amp Kordesch-Marko-type current interrupter and gate (reference 2), recording sequentially by means of a stepping switch, the anode, cathode and cell potential (including cell potential corrected for ohmic losses).

Fuel Cell Components

The anodes were commercially supplied pressed teflon-platinum

powders on gold-plated nickel screens with platinum loadings of 9 mg/cm^2. The cathodes were the same except that the platinum loadings were 40 mg/cm^2. The electrolyte was fixed in a .030-in asbestos matrix. The electrolyte contained in the asbestos was in contact with the hydrazine-electrolyte mixture circulated behind the anode through the pores of the electrode. These pores permitted convection and/or diffusion of oxygen and nitrogen depending upon the differential pressure (indicated by the differential pressure gage DF in Figure 1) maintained between anolyte and catholyte compartments by the differential pressure regulator within the pressure vessel.

EXPERIMENTAL RESULTS

The major sources of the inefficiencies in the hydrazine-oxygen fuel cell are derived from self-decomposition of the fuel, cross diffusion of the oxidant and fuel, and from bleed of the oxidant. The experimental data on self-decomposition are indicated in Figure 2. The arrows indicate the rate of gas evolution during increasing or decreasing load. Gas evolution rates include both hydrogen and nitrogen evolution. The dashed line increasing with load represents only the theoretical nitrogen evolution discussed below. The ascending solid line is the straight line parallel to the theoretical line of nitrogen evolution which best approximates the experimental points. The descending solid line has the same absolute value of slope. The points show a fall-off in gas evolution which approaches a minimum at approximately 128 ml/min-ft^2 almost 67% of the open circuit approximation of 200 ml/min-ft^2.

Figure 3 represents the cross diffusion of hydrazine from the anolyte through the anode and cell matrix to the cathode where the hydrazine is oxidized to water and nitrogen. The cross diffusion is measured by analysis of the evolved gases rather than by electrochemical analyses as in reference 1. The diffusion is dependent upon the applied load as well as the hydrazine concentration. The equivalent hydrazine loss is given in ml/min-ft^2 for water-saturated nitrogen at 25° C and in equivalent amp/ft^2. Gas volumes are always water-saturated at 25° C in all graphs and tables.

The most significant fact relative to efficiency is that the cross diffusion losses of hydrazine decrease rapidly with load. At low concentrations of hydrazine the ratio of cross-diffusion losses at open circuit and at load is much higher than the ratio at high concentrations of hydrazine. For example, at 1% hydrazine the ratio is approximately 20 whereas at 3% the ratio is approximately 4.5.

Table I contains the raw data used to calculate efficiency in subsequent figures. Figure 4 illustrates the effect of experimental bleed rates on the cell potential at various loads. The cell potential is logarithmically dependent upon the bleed rate within the experimental limits of study. However, the logarithmic dependence is not uniform with current density, exhibiting increasing slope with the load. Thus bleeds rates effect increased cell output most strongly at high loads.

DISCUSSION

Self-Decomposition Losses

Experimental gas-evolution data for hydrazine decomposition have

been reported in the open literature (reference 2). It is possible to rationalize the shape of the experimental curves. If it is assumed that the mechanism of self-decomposition of hydrazine proceeds according to the following half cell and overall reactions:

$$N_2H_4 + 4OH^- \longrightarrow N_2 + 4H_2O + 4e \qquad (1)$$

$$4H_2O + 4e \longrightarrow 2H_2 + 4OH^- \qquad (2)$$

$$N_2H_4 \longrightarrow 2H_2 + N_2 \qquad (3)$$

then as the potential of the electrode becomes more anodic, reaction (2) will be suppressed while reaction (1) is accellerated. For every four equivalents of charge one mole of nitrogen will be produced and 2 moles of hydrogen will be consumed. Thus:

$$V_n = V_n^o + \frac{K I}{4} \qquad (4)$$

$$V_h = V_h^o - \frac{K I}{2} \qquad \text{for } I \leq 2V_h^o / K \qquad (5)$$

where V_n and V_h are the volumes in liters of nitrogen and hydrogen produced per min-ft^2, V_n^o and V_h^o are the volumes produced under open circuit conditions, K is (298/273) (22.4 x 60)/96,500 and I is the current density in amp/ft^2. When the current density exceeds $2V_h^o / K$, V_h vanishes. The total gas production rate, V_t, is given by the sum of Equations (4) and (5). Recognizing from Equation (3) that $2V_n^o$ equal V_h^o we obtain:

$$V_t = 3V_n^o - \frac{K I}{4} \qquad \text{for } I \leq 2V_h^o / K \qquad (6a)$$

$$V_t = V_n^o + \frac{K I}{4} \qquad \text{for } I \geq 2V_h^o / K \qquad (6b)$$

Thus, the slope of the descending portion of the gas evolution curve at

low current densities is equal in absolute value to the slope of the ascending curve. The minimum occurs when the two branches of the curves in Equations (6) are equal whence, at the minimum,

$$I_{min} = 4V_n^o / K \qquad (7)$$

and

$$V_{t_{min}} = 2V_n^o \qquad (8)$$

Thus at the minimum, the total volume of gas should correspond to 67% of the open circuit gas evolution. Furthermore, the slopes of the ascending branch of the curve should be KI/4, in agreement with the theoretical value indicated by the dashed curve. These conclusions are closely approximated in Figure 2 and in the results of reference 2.

There is one area of divergence between theory and results. In previous studies (unpublished) analytical data on gas evolution indicate that not all of the hydrogen is consumed. This result would suggest that some self-decomposition does not occur at the electrodes but on insulated metallic or catalytic surfaces which cannot accomodate electrochemical discharge of the evolved hydrogen.

Thus the current of minimum gas evolution at approximately 15.5 amp/ft^2 in Figure 2 might normally be expected to correspond with the current of self-decomposition indicated by the back-extrapolated (to zero) ascending branch of the curve which indicates 20 amp/ft^2. The difference, 4.5 amp/ft^2 (corresponding to 1.5 amp/ft^2 since only a third of this gas should be nitrogen) might reasonably be interpreted as self-decomposition

on insulated metal surfaces.

Cross Diffusion Losses

The results of Figure 3 may be compared with previous studies of cross diffusion reported in reference 1. The data of reference 1 were obtained by a potentiostatic analysis of hydrazine under open circuit conditions. The present data, interpolated to 30° yield a cross-diffusion loss of approximately 9.5 amp/ft^2 in good agreement with the value of 8 amp/ft^2 obtained from Figure 3 (at 3% hydrazine) considering the differences in the experimental conditions.

The significant features of the data in Figure 3, namely that losses arising from cross diffusion decrease with load, arise from the fact that under load the available hydrazine is more rapidly consumed. Most interesting is the fact that the cross-diffusion loss at lower concentrations of hydrazine is significantly less than half the loss at higher concentrations. In particular, for example, at the 80-amp load, the loss at 2% hydrazine is only 35% of the loss at 3%.

The possibility that cross diffusion of oxygen decreases with load is suggested by these results.

Bleed Losses

The data of Figure 4 represent not only bleed losses, but cross diffusion of hydrazine. The nitrogen which is observed in the oxygen bleed was originally part of the hydrazine which was transported by diffusion from the anolyte flowing past the backside of the anode through the asbestos separator. Convection plays no role in the transport of this

hydrazine because the pressure gradient in the cell is normally against the direction of hydrazine flow.

The logarithmic dependence of the cell potential on oxygen bleed rate suggests that the cathode potential is exhibiting a Nernst-like response to the oxygen concentration which therefore should be linearly related to the bleed rate. While logarithmic proportionality may exist the slopes of the curves do not correspond to expected values for typical Nernst behavior. In addition, the slopes change with current density indicating more complex relationships.

Hydrazine Fuel Requirements

A formulation of fuel requirements is simply stated if it is assumed that there are only four significant elements of fuel-cell inefficiency, the diffusion of hydrazine to the cathode, D_n, the diffusion of oxygen to the anode, D_o, the bleed of oxygen from the cathode space, B, and the self decomposition of hydrazine, S. The weight per kw-hr of hydrazine, W_n, in terms of the weight per kamp-hr, M_n (0.663 lb/kamp-hr for pure hydrazine) is

$$W_n = \frac{M_n}{E}\left(\frac{I + D_n + D_o + S}{I}\right) \qquad (9)$$

where E is the cell output potential. The oxygen bleed term does not enter into the expression for fuel requirements.

In Table I the compilation of raw laboratory data, losses have been expressed in amp/ft^2 for consistency. The loss due to diffusion of oxygen, D_o, (see column 3 which contains the sum of D_o and

S) is obtained from Figure 5 which is reproduced from reference 1. The value of D_o is 1 amp/ft^2 corresponding approximately to the cross diffusion of 4500 psi and 50° C. The value of the self decomposition term, S, is 1.5 amp/ft^2 and is derived from Figure 2 in accordance with the discussion above. The average values for the cross diffusion of hydrazine, D_n, namely, 5.75, 3.7 and 3.8 amp/ft^2 were obtained experimentally and deviate from the values 7.8, 5.5 and 2.6 interpolated from Figure 3 and corrected for temperature. The results of Figure 3 represent a separate independent study at 30° C. The disparities result from aging processes and from difficulties associated with maintaining constant oxygen bleed, hydrazine diffusion rates, and differential pressures in a dynamic system. The results of Figure 3 exhibit a larger fall-off in the cross-diffusion rate as load increases than is apparent from column 2 of Table I. In fact according to Table I, the average cross diffusion, D_n, is slightly higher at 80 amp/ft^2 than at 40 amp/ft^2. Figure 3 indicates that such behavior is anomalous. The data of Table I represent measurements over a period of several hours in contrast with the data of Figure 3. Thus, they may represent changes in the differential pressure between anode and cathode spaces which modify the diffusion processes by superposition of convective flow patterns.

In the following analysis, the values of hydrazine diffusion, D_n, employed in subsequent calculations are those listed in Table I. The inconsistency described in the previous paragraph color the results of

the following analyses to the extent of +4% to -2% in the most discrepant cases. The discrepancy is on the conservative side in the most likely operating ranges.

Columns 6 and 7, the hydrazine fuel requirement calculated by use of Equation 9 are plotted as a function of the bleed rates in column 8 in Figure 6. The immediate conclusion to be drawn is that the oxygen bleed rate within the range of 1 to 5 amp/ft^2 does not change the fuel requirement by more than 1.5% and is therefore not the most significant factor in hydrazine fuel requirements.

Peroxide Requirements

A formulation of peroxide requirements is given in Equation 10. The weight per kw-hr of peroxide, W_o, in terms of the weight of peroxide required per kamp-hr, M_o, (1.398 lb/kamp-hr for 100% peroxide) is

$$W_o = \frac{M_o}{E} \left(\frac{I + D_o + D_n + B}{I} \right) \qquad (10)$$

The self-decomposition term, S, in Equation (9) is replaced by the bleed rate, B, in Equation (10). The value of D_o has again been arbitrarily set at 1 amp/ft^2 corresponding to the cross diffusion at 4500 psi and 50^o C. The values of D_n and B are taken directly from the measured raw data of Figure 4. See Table II for a compilation of the input raw data and calculated values of weights per kw-hr. The required weights are plotted against bleed rate in Figure 7. The significant fact again is that at current densities where operation is likely because of high efficiency, the bleed rate is essentially negligible in effect between 1 and 4 amp/ft^2.

Fuel-Oxidant Requirements

Figure 8 indicates that fuel-oxidant requirements per kw-hr (derived from Figures 6 and 7) exhibit broad minima with respect to oxygen bleed rate. The significant conclusion, as before, is that the oxygen bleed rate is **not** a significant factor at operating current densities such as 40 amp/ft^2 or greater which would be desirable for reasonable coulombic efficiency.

Figure 9 represents the specific fuel-oxidant requirements per kw-hr under varying load as determined by Figure 8. The effect of bleed rate is again seen to be small compared to the effect of load. In contrast with behavior observed in hydrogen-oxygen fuel cells, the specific fuel-oxidant requirements decrease with load until approximately 80 amp/ft^2. Increase in specific fuel-oxidant requirements probably increases above 80 amp/ft^2 where life characteristics of hydrazine fuel cells represent an uncertain area. Assuming acceptable life characteristics, maximum energy density appears to occur between 60 and 90 amp/ft^2. However, at least up to 80 amp/ft^2, the specific energy density of the tested cells does not exhibit a maximum when trade-off analyses are made involving the operating power of fuel cells and the power efficiency of fuel and oxidant.

Coulombic Efficiencies

Figures 10 shows that the coulombic efficiency of the peroxide (oxygen) cathode is a function of bleed rate exhibiting a maximum for high current densities in the neighborhood of 1 amp/ft^2. On the other hand, Figure 11

shows that the coulombic efficiency of the hydrazine anode is essentially independent of oxygen bleed rate over the range studied. Figures 12 and 13 show again that load rather than bleed is the significant overall factor in coulombic efficiency as in specific energy requirements.

SUMMARY

The coulombic efficiency and specific material requirements per energy unit of a hydrazine-peroxide single cell was studied. Electrodes were a commercially supplied variety prepared from pressed powdered platinum and teflon powders in 6-in. by 6-in. squares. Analysis of the gas evolution at hydrazine anodes indicates that at high loadings the self-decomposition losses of hydrazine may be negligible. Cross diffusion of hydrazine (and possibly oxygen) decrease rapidly with load. Bleed rates effect increases in cell potential most strongly at high loadings.

Hydrazine requirements decrease only slightly with bleed rate. On the other hand, peroxide requirements increase with bleed rate although at high loads the increase is small. Combined fuel-oxidant requirements per energy unit show broad minima with respect to bleed rate. At high current densities the fuel-oxidant requirements are essentially independent of bleed rate. However, they are strongly dependent upon load. Maximum energy density and coulombic efficiency may occur between 60 and 90 amp/ft^2.

The results are peculiar to the particular system studied. In any

systems analysis, numerical assignment of efficiencies should be based upon experimental evaluation of the fuel cell modules actually contemplated for application.

As a result of the increase of coulombic efficiency with load at least up to 80 amp/ft^2 no maximum may be expected when trade-off analyses are made involving the operating power density of fuel cells and the coulombic efficiency of fuel and oxidant consumption.

ACKNOWLEDGEMENTS

This work is part of a program of research sponsored by the Naval Ship Systems Command under the cognizance of Bernard Rosenbaum. The authors are pleased to acknowledge encouragement and discussion with John H. Harrison, Head of the Fuel Cell Branch of the U. S. Naval Ship Research and Development Laboratory, Annapolis.

The opinions or assertions made in this paper are those of the author(s) and are not to be construed as official or reflecting the views of the Department of the Navy or the naval service at large.

GLOSSARY OF SYMBOLS

B = Bleed loss of oxygen in amperes per square foot

D_n = Diffusion loss of hydrazine in amperes per square foot

D_o = Diffusion loss of oxygen in amperes per square foot

E = Cell potential in volts

I = Current density in amperes per square foot

K = A constant

M = Mass requirements per kiloampere-hour

M_n = Wt of hydrazine-water mix per kiloampere hour

M_o = Wt of peroxide-water mix per kilowatt hour

S = Self-decomposition loss of hydrazine

V_h = Volume of hydrogen in liters produced per minute per square foot

V_n = Volume of nitrogen in liters produced per minute per square foot

V_t = Volume of all gases in liters produced per minute per square foot

W_n = Wt of hydrazine-water mix per kilowatt hour

W_o = Wt of peroxide-water mix per kilowatt hour

REFERENCES

1. R. J. Bowen, H. B. Urbach, D. E. Icenhower, D. R. Gormley and R. E. Smith, "The Hydrazine-Oxygen Fuel Cell at Ambient Deep Sea Pressures", NSRDC Report 2671, February 1969. Published for the Intersociety Energy Conversion Engineering Conference in "IECEC '68 Record" by the Institute of Electrical and Electronics Engineers, Inc., New York, 1968.

2. V. S. Daniel'-Bek and G. V. Vivitskaya, Elektrokhimiya, 3, 8 (1967).

TABLE I - FUEL REQUIREMENTS

I Amp/ft^2	D_n Amp/ft^2	$D_o + S$ Amp/ft^2	$\frac{I + D_n + D_o + S}{I}$	E Volt	Wt (100%) (.663) lbs/kw-hr	Wt(90%) lbs/kw-hr	B Amp/ft^2	Coulombic Efficiency
20	5.7	2.5	1.410	.895	1.045	1.161	.3	.7092
20	5.8	2.5	1.415	.899	1.004	1.159	.9	.707
20	5.8	2.5	1.415	.907	1.034	1.149	1.8	.707
20	5.7	2.5	1.410	.907	1.031	1.146	2.8	.7092
20	5.7	2.5	1.41	.910	1.027	1.141	5.5	.709
40	3.5	2.5	1.15	.849	.898	.998	.3	.870
40	3.5	2.5	1.15	.858	.889	.988	.8	.870
40	3.7	2.5	1.155	.865	.885	.984	1.6	.8658
40	3.5	2.5	1.15	.864	.882	.980	2.1	.870
40	3.5	2.5	1.15	.869	.877	.974	4.5	.870
80	3.8	2.5	1.079	.838	.854	.949	1.1	.927
80	3.4	2.5	1.074	.846	.842	.935	2.7	.931
80	4.2	2.5	1.084	.849	.846	.940	2.9	.923

TABLE II - PEROXIDE REQUIREMENTS

I	D_{n+B}	$\frac{I + D_o^* + D_{n+B}}{I}$	E	$\frac{(1.398)}{\text{Wt/kw-hr}}$ 100%	Wt/kw-hr	B	Coulombic Efficiency
20	6	1.35	.895	2.109	2.343	.3	.741
20	6.7	1.385	.899	2.158	2.393	.9	.722
20	7.6	1.43	.907	2.204	2.45	1.8	.699
20	8.5	1.475	.907	2.273	2.526	2.8	.678
20	11.2	1.61	.910	2.473	2.748	5.5	.621
40	3.8	1.12	.849	1.844	2.05	.3	.893
40	4.3	1.13	.858	1.841	2.046	.8	.885
40	5.3	1.156	.865	1.868	2.076	1.6	.865
40	5.6	1.165	.864	1.885	2.094	2.1	.858
40	8.0	1.225	.869	1.971	2.190	4.5	.816
80	4.9	1.074	.838	1.792	1.991	1.1	.931
80	6.1	1.089	.846	1.80	2.00	2.7	.918
80	7.1	1.101	.849	1.813	2.014	2.9	.908

* D_o is chosen as the value at 50°C and 4500 psi, namely 1. amp/ft^2.

TABLE III - FUEL-OXIDANT REQUIREMENTS

I Amp/ft^2	Fuel Wt per kw-hr	Oxidant Wt per kw-hr	Total Wt per kw-hr (100%)	Total Wt per kw-hr (90%)	B
20	1.045	2.109	3.154	3.504	0.3
20	1.044	2.158	3.202	3.558	0.9
20	1.034	2.204	3.238	3.598	1.8
20	1.031	2.273	3.304	3.671	2.8
20	1.027	2.473	3.50	3.889	5.5
40	.898	1.844	2.742	3.047	0.3
40	.889	1.841	2.73	3.033	0.8
40	.885	1.868	2.753	3.059	1.6
40	.882	1.885	2.767	3.074	2.1
40	.877	1.971	2.848	3.164	4.5
80	.854	1.792	2.646	2.94	1.1
80	.842	1.80	2.642	2.936	2.7
80	.846	1.813	2.659	2.954	2.9

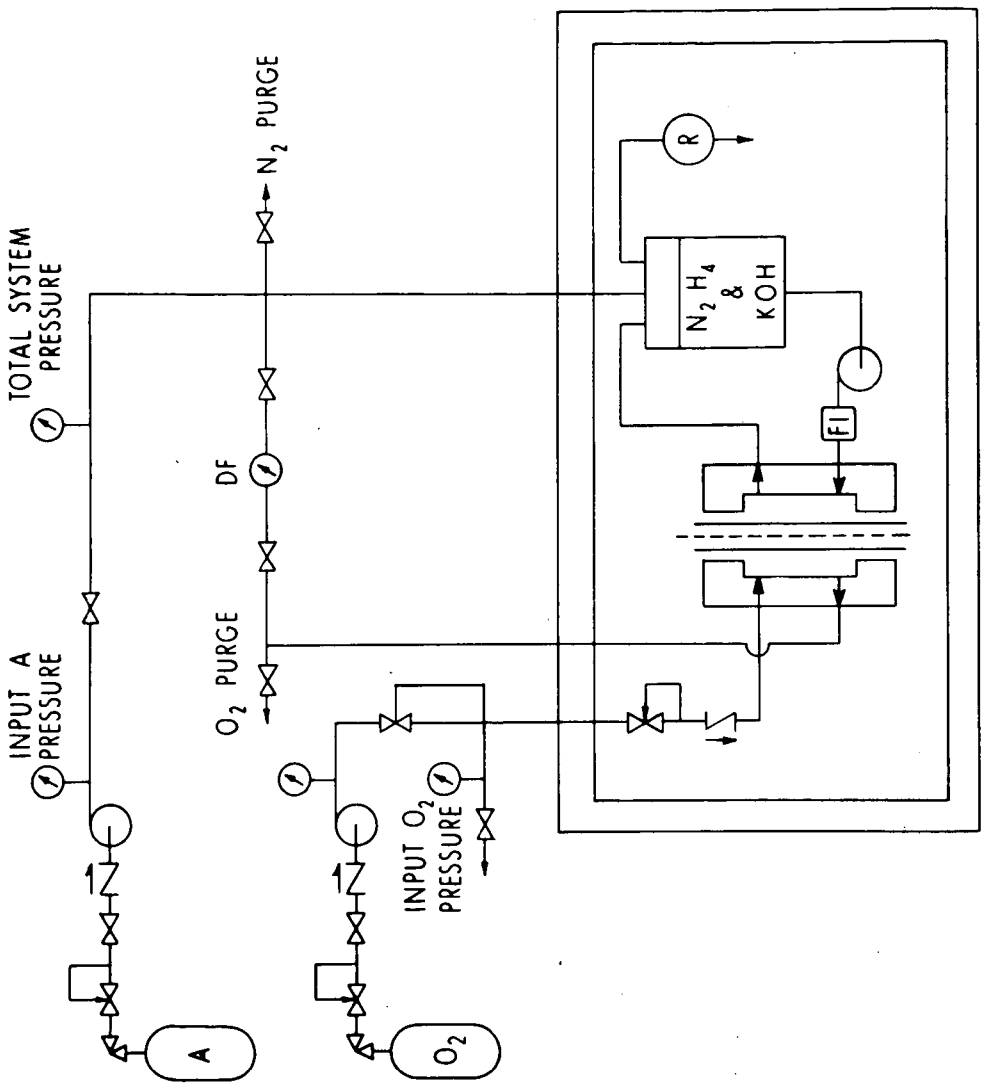

Figure 1 - Experimental apparatus for studying fuel cells under pressure.

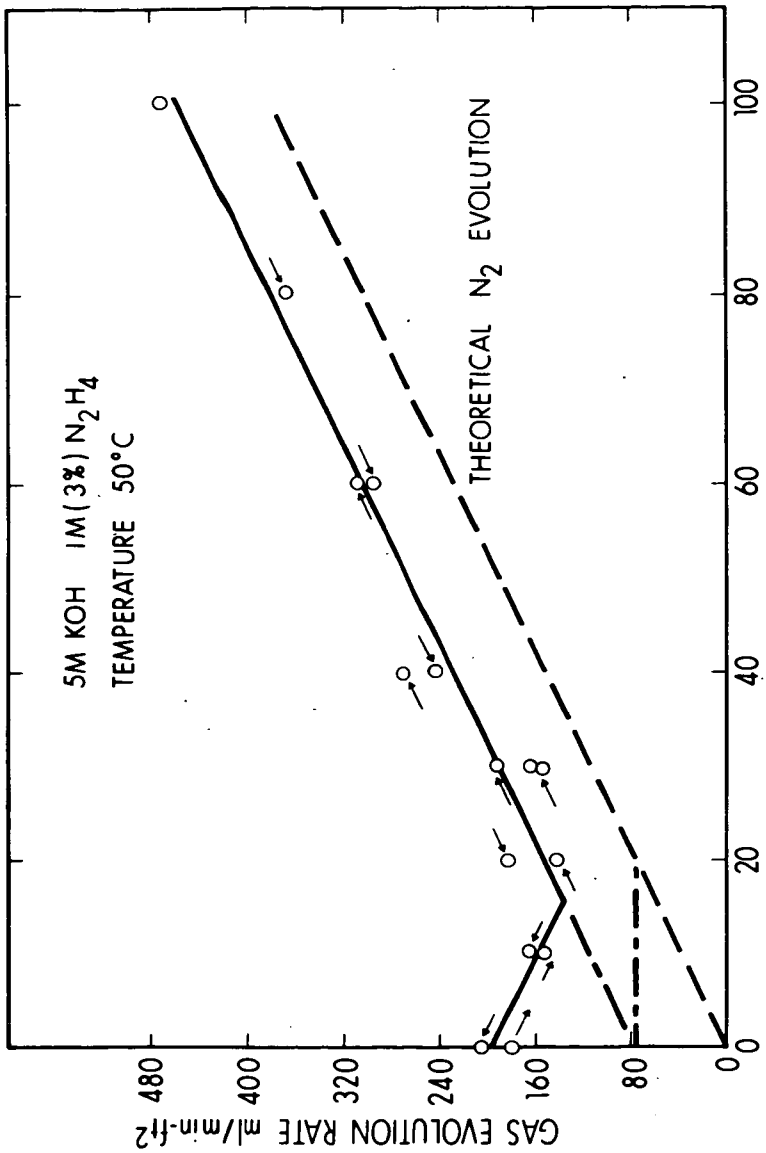

Figure 2 - Gas evolution at platinum-teflon anodes (platinum loading is 9 mg/cm^2) exposed to hydrazine.

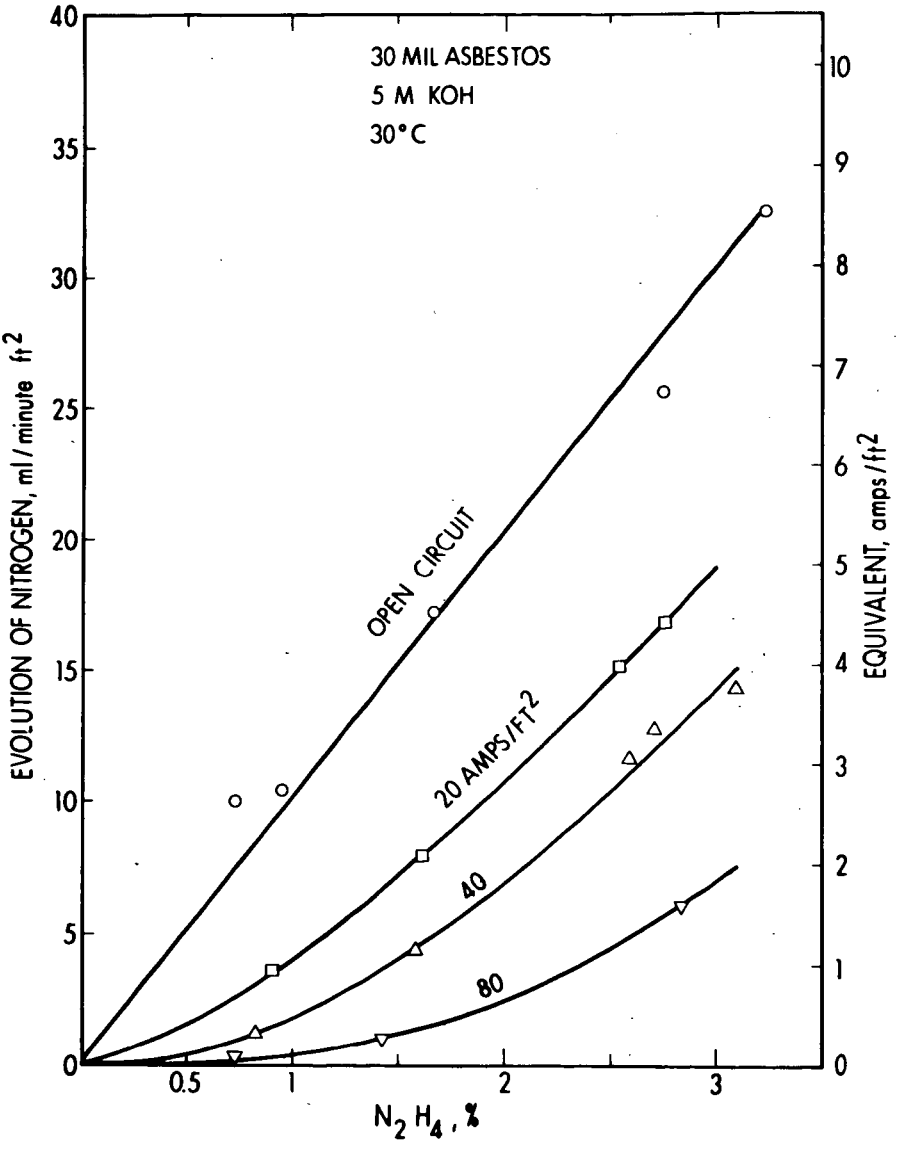

Figure 3 - Effect of hydrazine concentration and load on nitrogen evolution at a platinum anode.

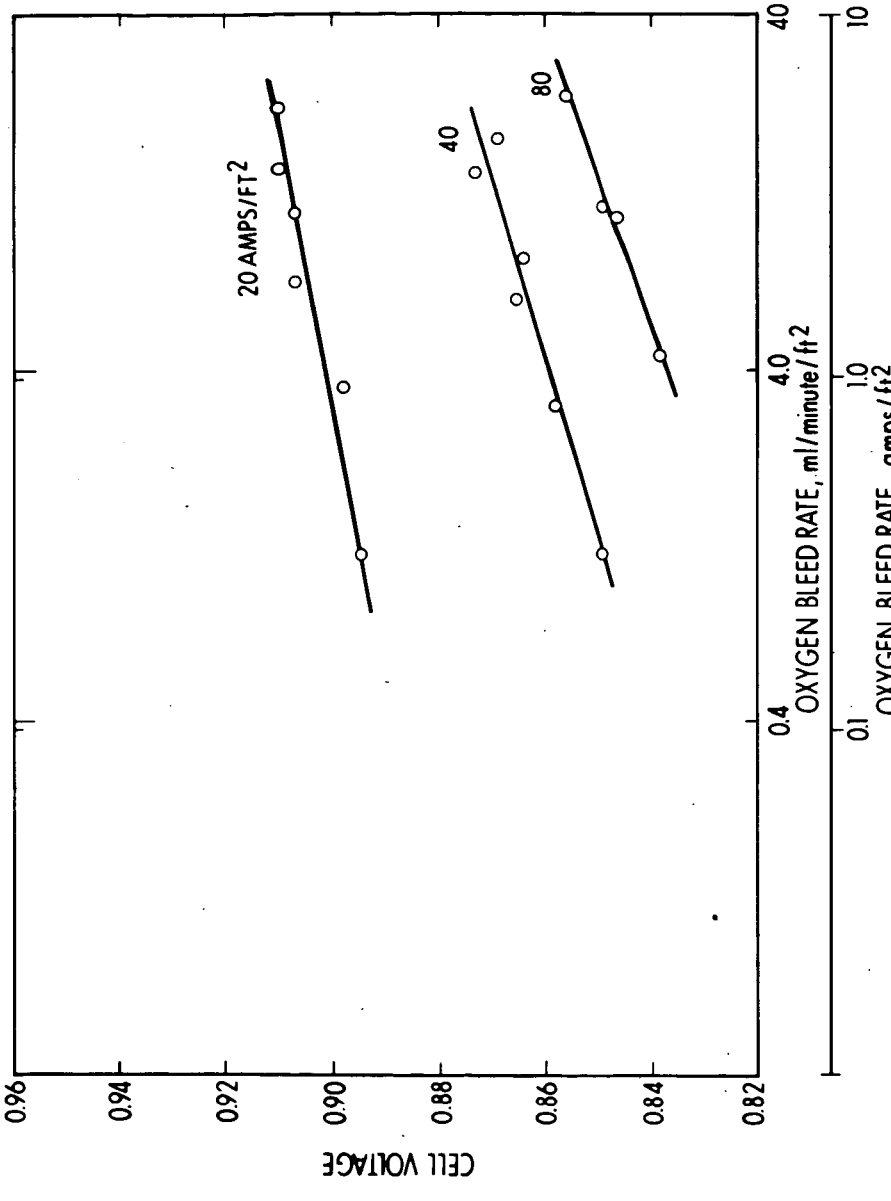

Figure 4 - Effect of load and oxygen bleed rate on the output potential of a hydrazine-oxygen cell.

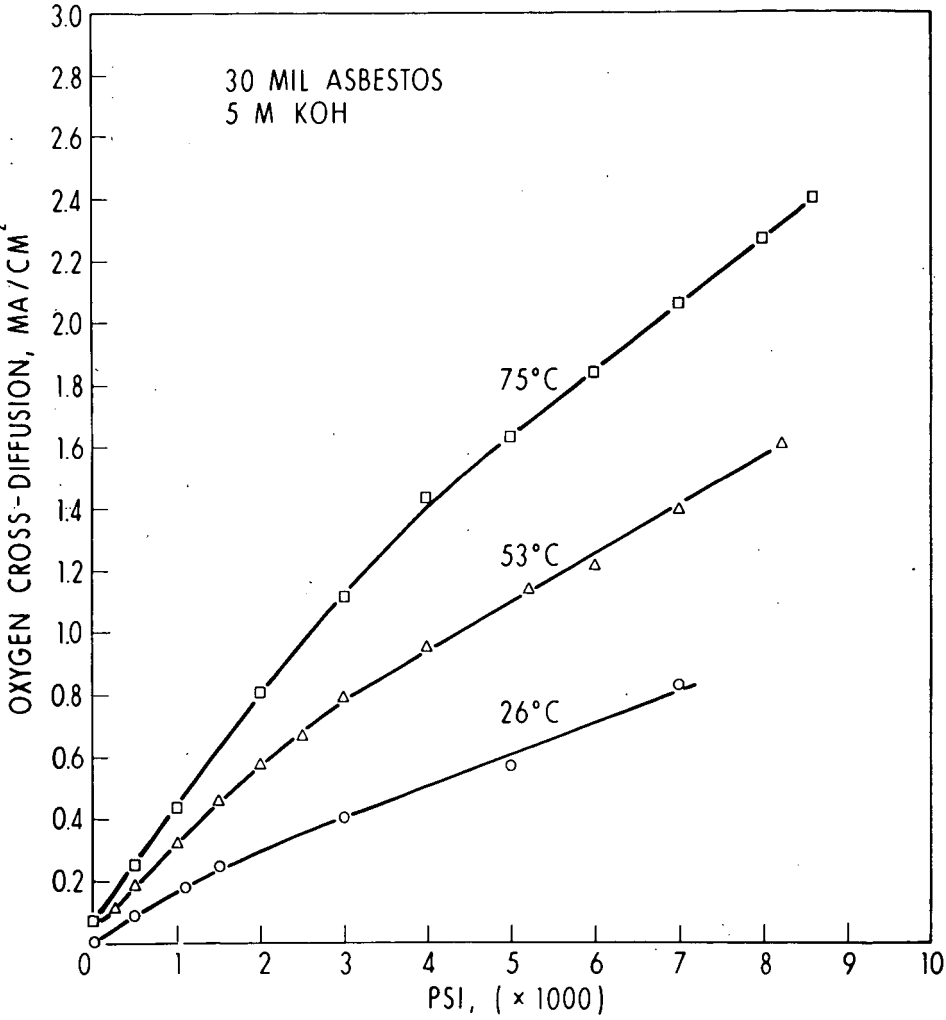

Figure 5 - Effect of pressure on the cross diffusion of oxygen through an asbestos separator in a hydrazine-oxygen cell.

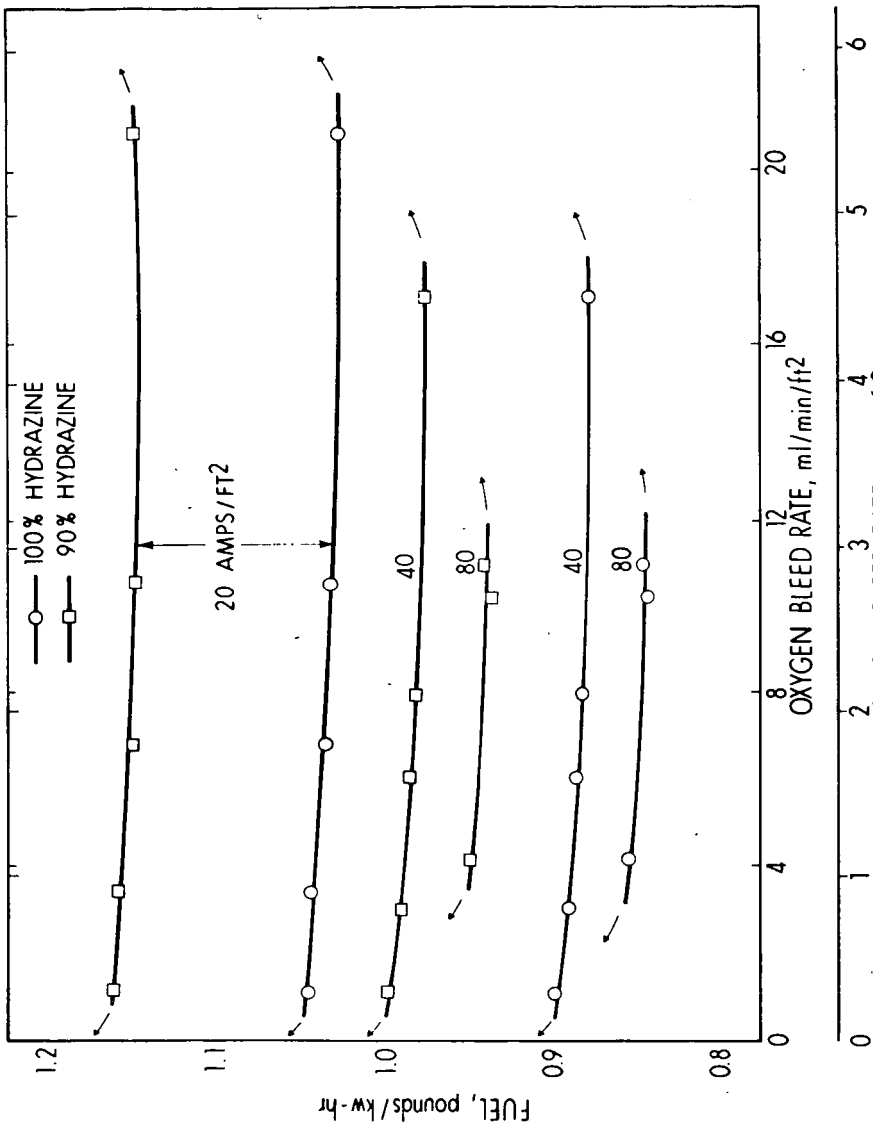

Figure 6 - Effect of oxygen bleed rate on the hydrazine fuel requirements per kw-hr.

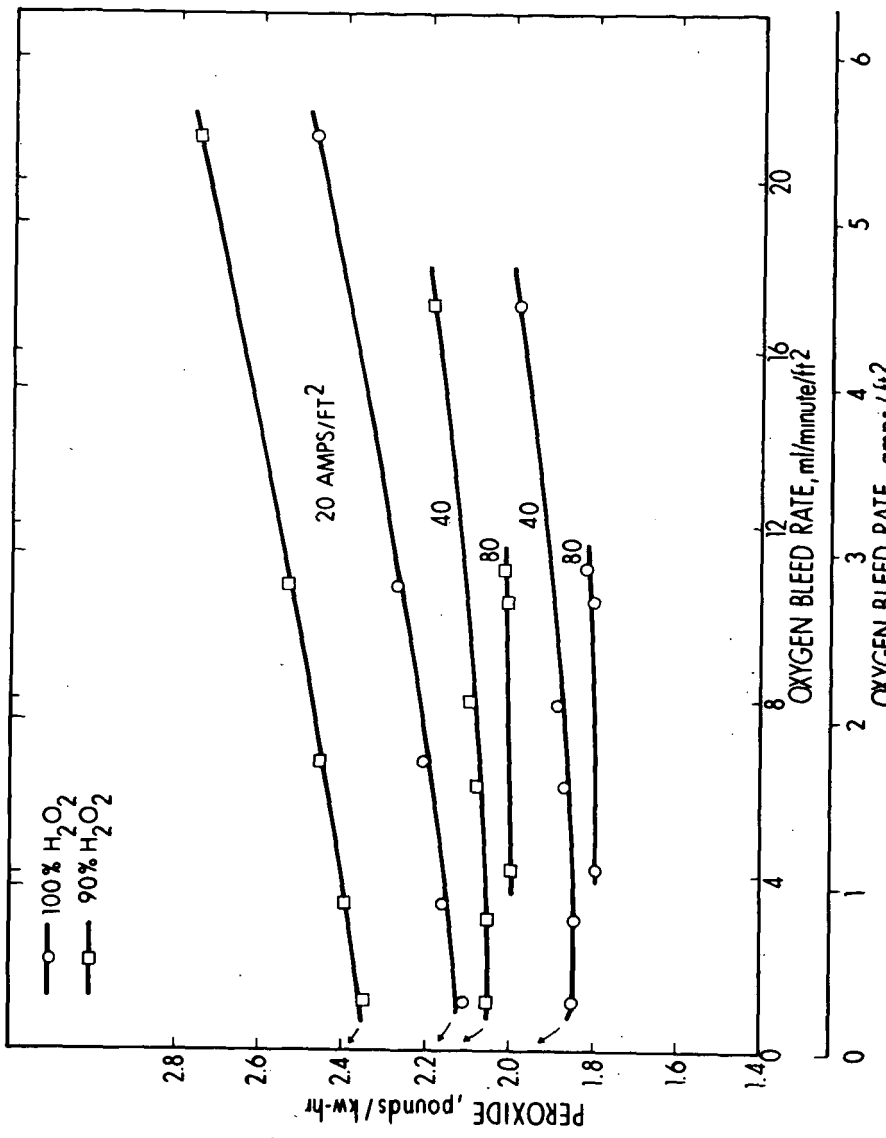

Figure 7 - Effect of oxygen bleed rate on peroxide requirements per kw-hr.

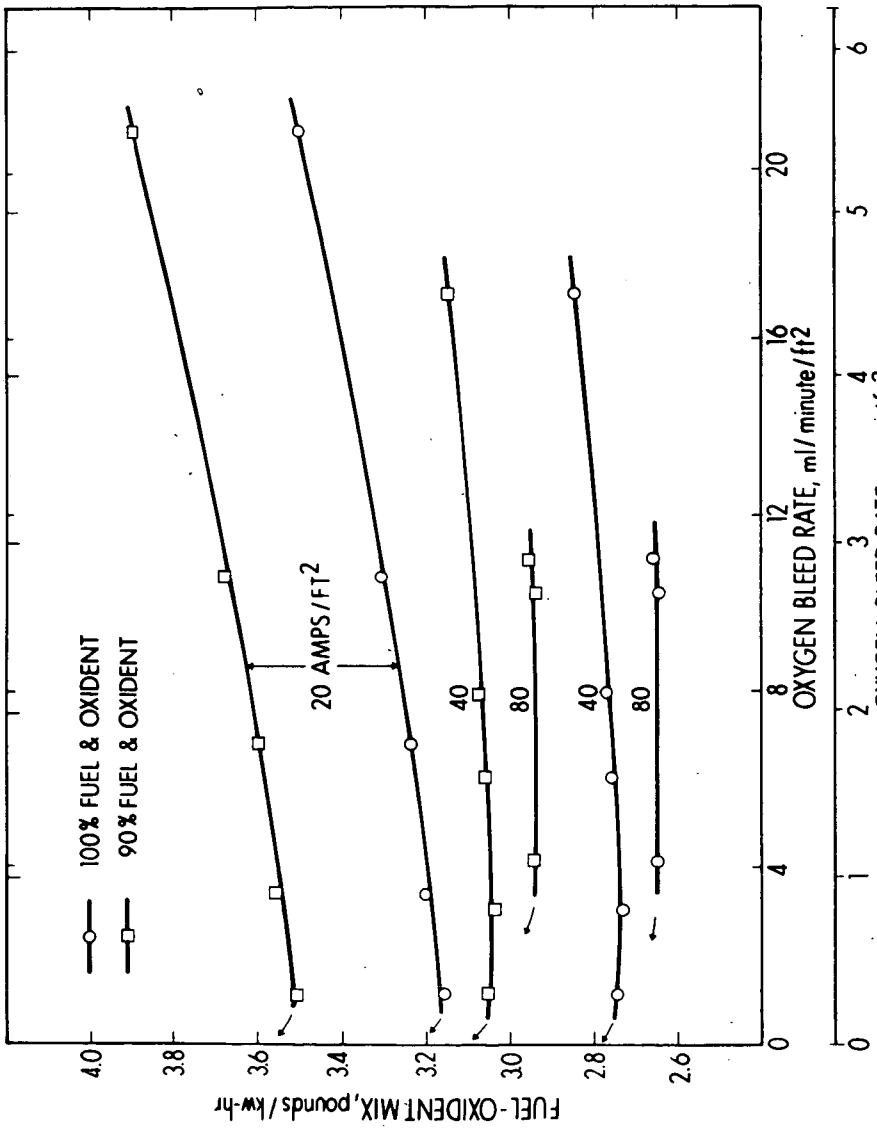

Figure 8 - Effect of oxygen bleed rate on hydrazine-peroxide requirements per kw-hr.

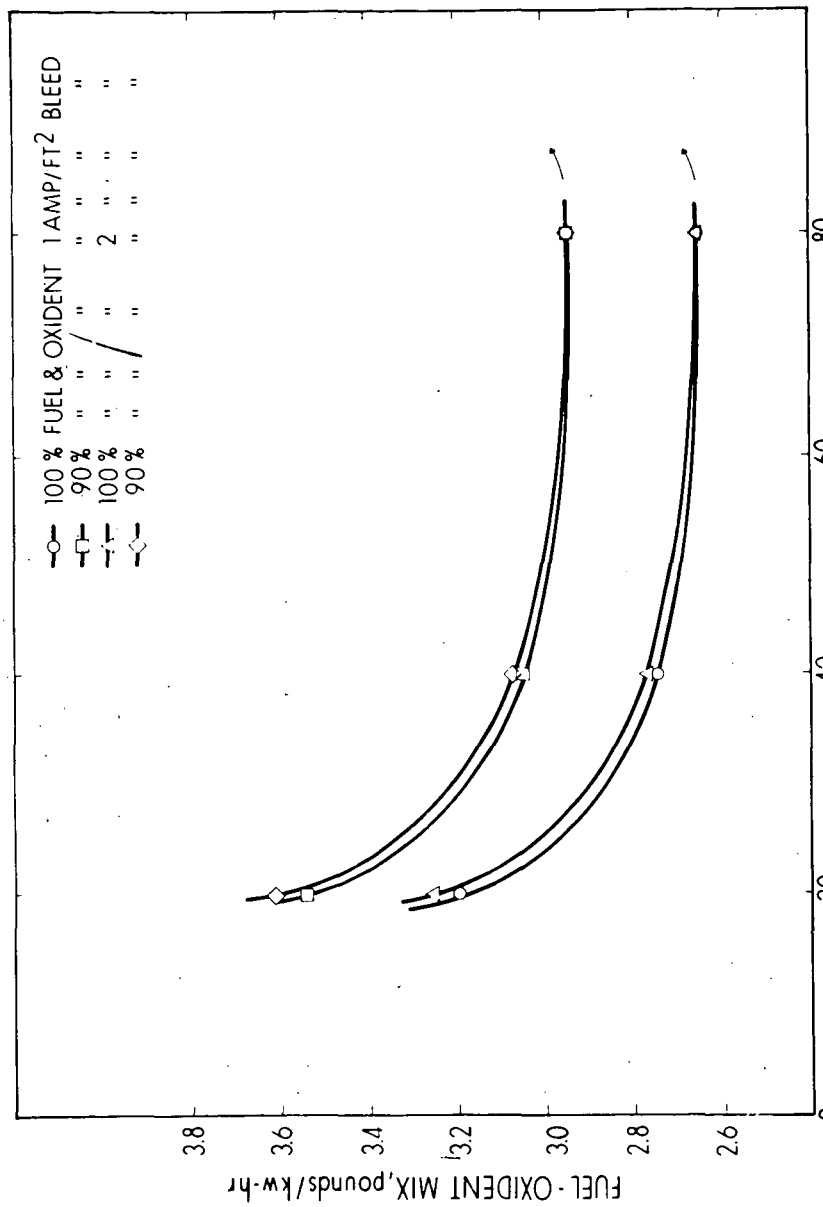

Figure 9 - Effect of loading on the hydrazine-peroxide requirements per kw-hr.

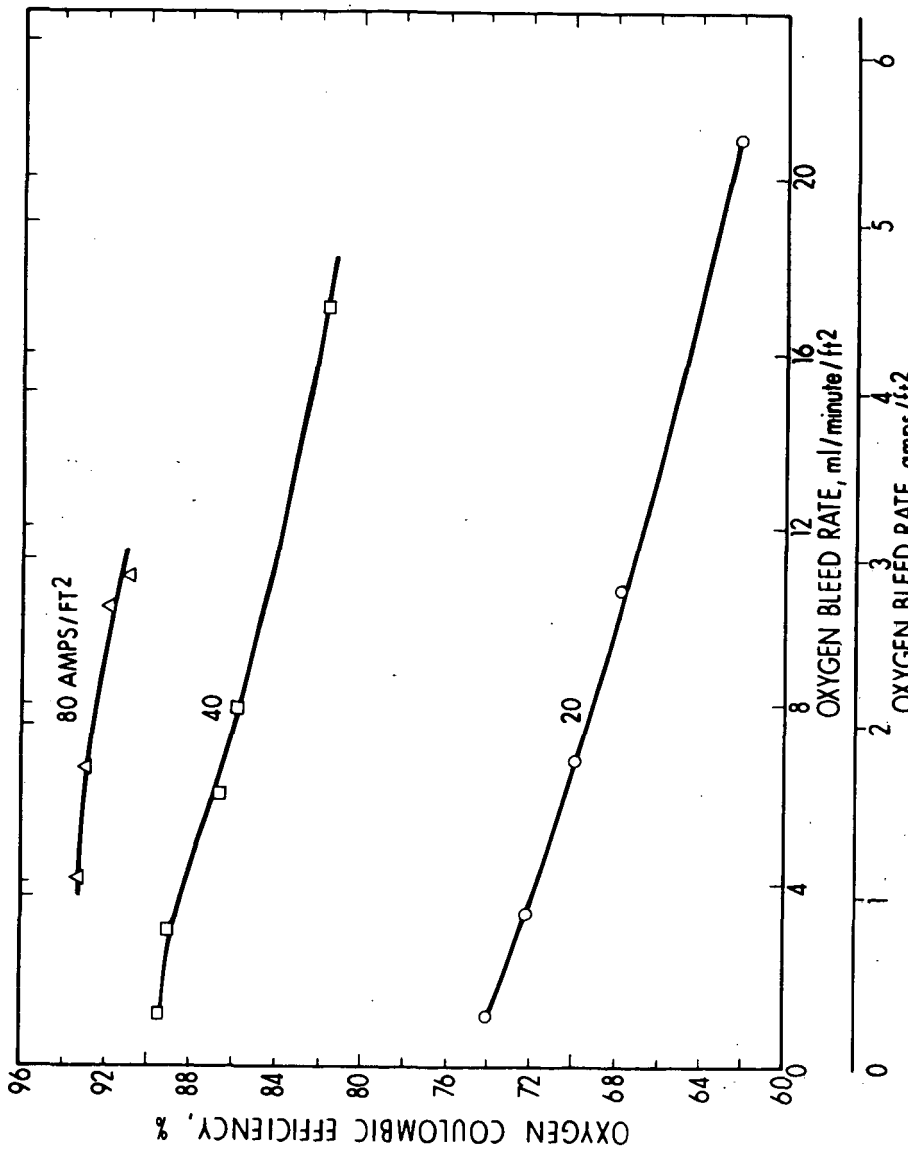

Figure 10 - Effect of oxygen bleed rate on the coulombic efficiency of cathodic oxygen or peroxide consumption.

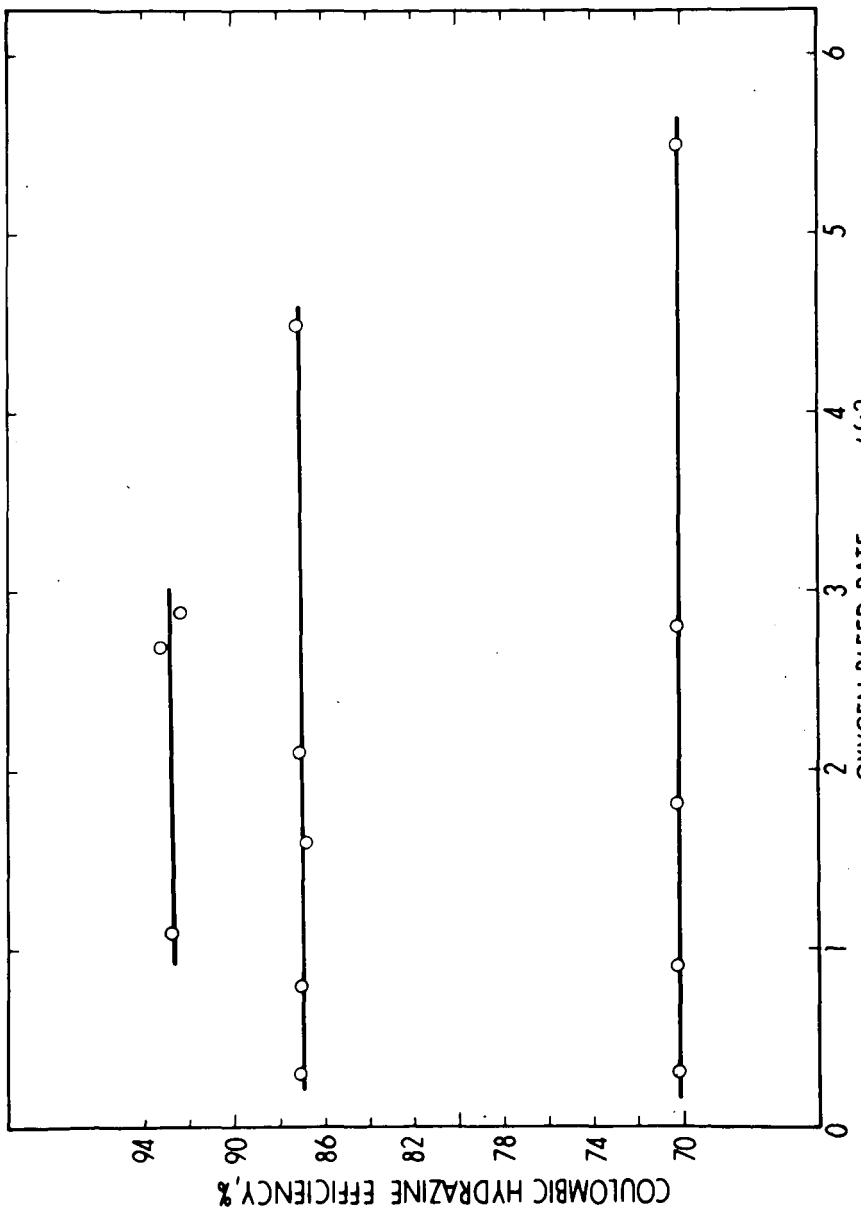

Figure 11 - Effect of oxygen bleed rate on the coulombic efficiency of anodic hydrazine consumption.

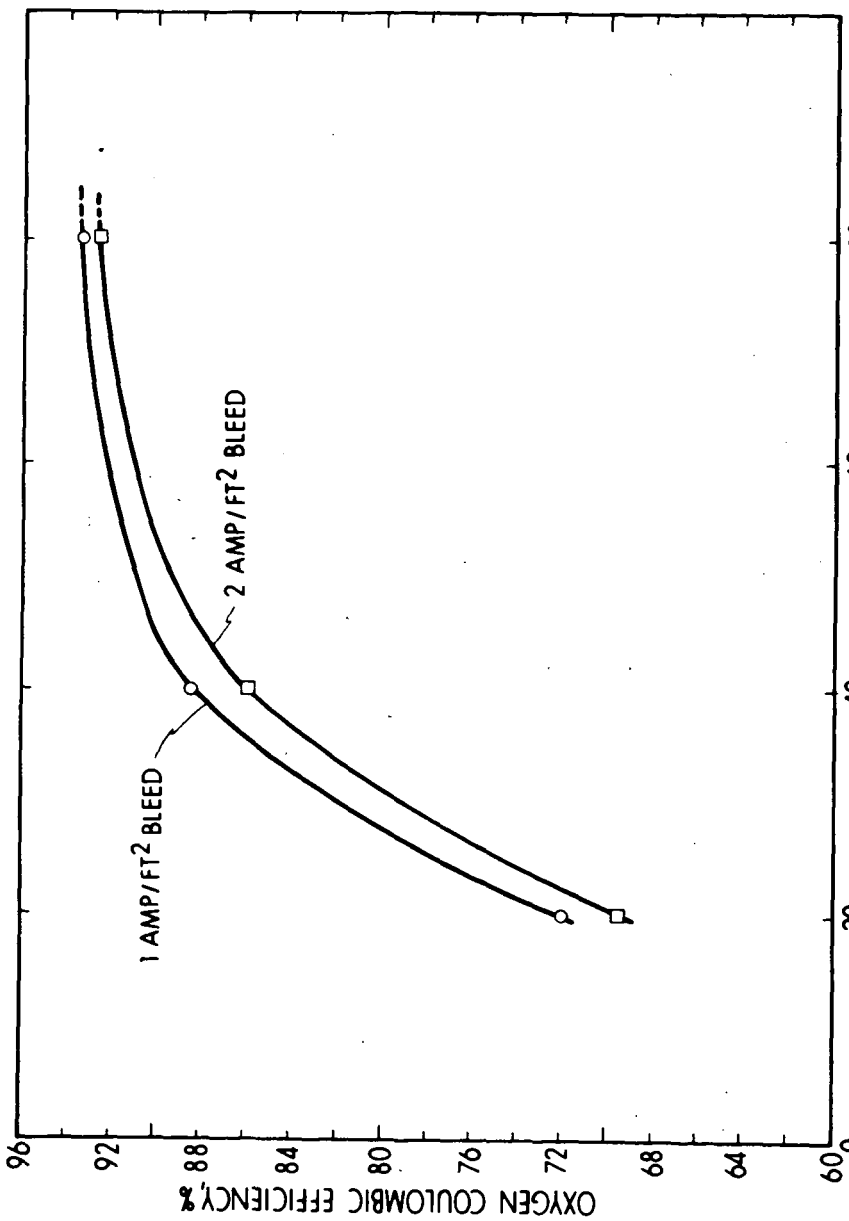

Figure 12 - Effect of loading on the coulombic efficiency of cathodic oxygen or peroxide consumption.

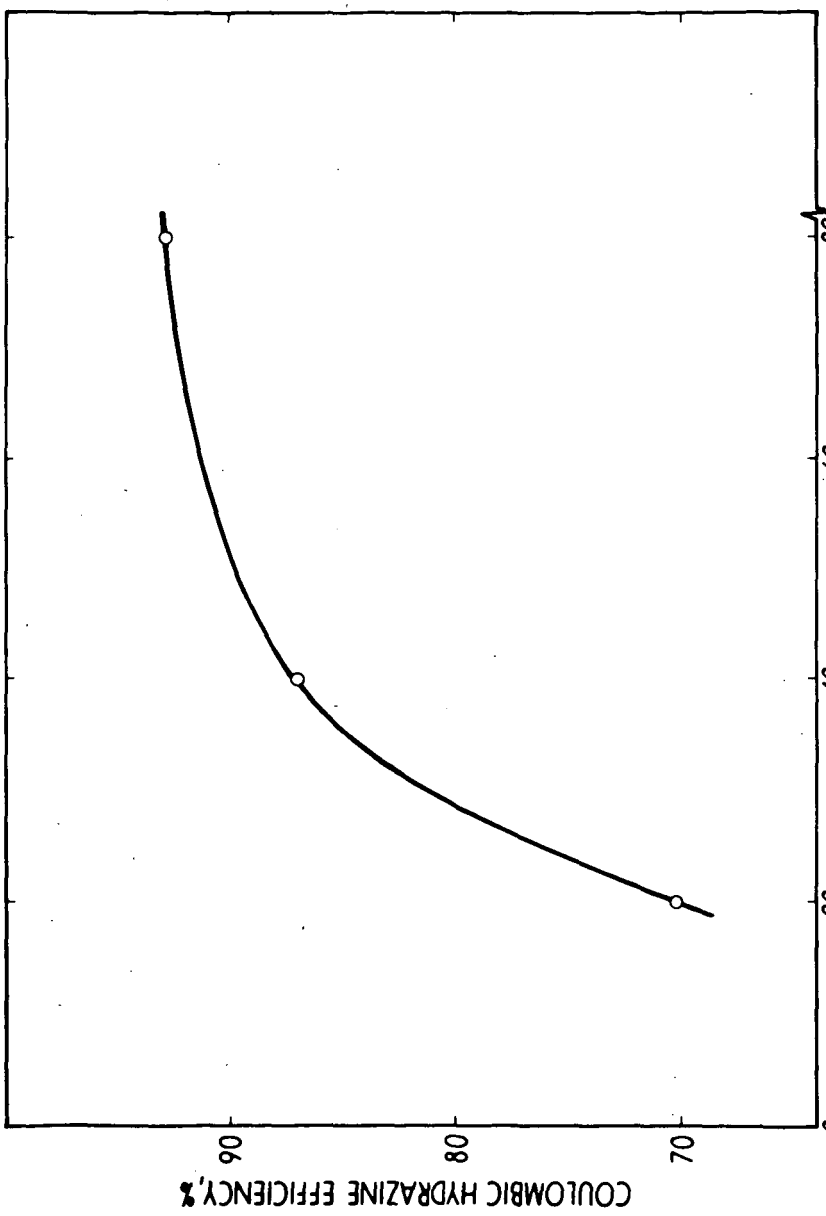

Figure 13 - Effect of loading on the coulombic efficiency of anodic hydrazine consumption.

ELECTROCATALYSIS IN THE NICKEL-TITANIUM SYSTEM

Eduard W. Justi, Henning H. Ewe, Adolf W. Kalberlah, Nikolaus M. Saridakis, and Martin H. Schaefer

Institute of Technical Physics, University of Braunschweig
Braunschweig, West Germany

1. INTRODUCTION

Europe offers no economic chances for application of fuel cells in military or space technology and therefore, all efforts are focussed to eventual applications in civilian technique. This has been the reason why Justi, Scheibe, and Winsel (1) have postulated from their beginnings in the early fifties to avoid principally rare metal electrocatalysts when publishing their double skeleton katalyst ("DSK") system of fuel cells. To achieve the necessary high catalytic activity of base metal catalysts operating at ambient temperature they have introduced into electrochemistry for the first time Raney type microskeleton catalysts supported by inactive macroskeleton electrodes. Raney nickel in hydrogen anodes, and Raney silver oxygen (air) cathodes or similar structures are now widely used even in other countries for fuel cells operating with alkaline electrolytes at ambient temperature and low pressure. In the meantime Justi et al. (2) have investigated various other base metals concerning their abililty as electrocatalysts and focussed their present interest to titanium which appears attractive for its low specific weight and huge hydrogen storage capacity, up to the nonstoichiometric hydride $TiH_{1.65}$.

Unfortunately titanium is corroding in alkaline electrolytes by formation of irreducible impermeable TiO_2 (rutile) coating layers thus excluding application in our fuel cell system. Moreover the above mentioned huge hydrogen storage capacity cannot be used efficiently by adsorbing hydrogen at moderate temperatures and subsequent desorption at high temperatures. For by this method of storing hydrogen about one half of the free energy of combustion of hydrogen would be wasted, as we have calculated by applying a Carnot cycle on experimental data such as temperatures, pressures, heat content, and heats of sorption. Therefore the goal of the present work is to combine the good catalytic and storing properties of nickel and titanium, and to avoid the disadvantageous ones, both for fuel cell and for accumulator electrodes. Of course this cannot be done simply by mixing both metals and thus averaging their various properties. However nickel and titanium are forming some intermetallic compounds stable by relatively high energies of formation (about 8000 cal/mole) with quite differing properties. These compounds and their

alloys may offer a chance of finding out electrocatalysts with really new and possibly favourable performance. To find this assertion plausible look at the complicated structure of the elementary cell of Ti_2Ni crystal containing 96 atoms (fig. 1) and offering at least 3 different distances between Ti-Ti, Ni-Ni, and Ni-Ti atoms, an increased tendency towards covalency between Ti and Ni atoms, and a corresponding variety of hydrogen binding energies (3).

2. DIAGRAM OF STATE OF THE BINARY SYSTEM Ti-Ni AND SCOPE OF PRESENT WORK

According to the well known diagram of state (4) Ti and Ni form the intermetallic compounds Ti_2Ni, TiNi, and $TiNi_3$, out of which we have investigated Ti_2Ni and TiNi. As the left side of fig. 2 shows, Ti_2Ni forms an eutecticum with ß-Ti. Therefore, all alloys containing less than 33.3 at-% Ni have finely dispersed Ti corroding in lyes and forming the above mentioned thick layer of irreducible TiO_2. This is the reason why we have focussed our efforts to the interval between Ti_2Ni and TiNi, this is from 33.3 to 50 at-% Ni. The diagram of state shows that cooling down a melt of e. g. 43 at-% Ni starts with precipitation of TiNi thus enriching the residual melt with Ti. Continued cooling causes increased segregation of TiNi, until at 1015°C Ti_2Ni is formed by peritectic reaction of TiNi and the residual melt. A typical example of such a peritectic structure is shown in the micrograph fig. 3 at 250 times linear magnification. The rounded off parts of the structure are the residuals of primarily precipitated TiNi grains surrounded by peritecticly formed Ti_2Ni.

For our experiments we have chosen several alloys with different contents of Ti_2Ni and TiNi. Concerning the TiNi-rich alloys a difficulty arises because TiNi is extremely hard and tough and can neither be rolled nor powdered. The nickel richest composition we were able to mill contained 53.6 at-% Ti and 46.4 at-% Ni. In this case the TiNi grains are prevailing but are surrounded completely by the brittle Ti_2Ni-regions, a circumstance of importance for our results to be reported.

3. STORAGE OF CATHODICALLY EVOLVED HYDROGEN

First of all we would like to learn if and how this alloy will accept cathodically evolved hydrogen. For this purpose we have pressed and sintered DSK electrodes consisting of 3 gramms of the particular Ti_2Ni-TiNi alloy with grain sizes from 35 to 150 microns, and 6 gramms copper with grain sizes below 6 microns as a soft macroskeleton preventing formation of cracks caused by volume increase of hydrogen accepting titanium. This circular electrodes of 40 mm diameter, corresponding to twice 12 sq. cm geometric surface were charged first with 5 mA cathodically in 6m KOH at ambient temperature. Fig. 4 shows the potentials of several specimens thus measured vs. reversible hydrogen potential as function of the charge accepted. The potentials start rather negative

and subsequently become somewhat more positive. This transient positive sign of potential may be explained by supposing an autocatalytic mechanism (5), this means the primarily accepted hydrogen will favour subsequent entering of H-atoms. Probably this effect is caused by enlargement of the crystal lattice facilitating the inclusion of additional hydrogen until complete saturation.

Next diagram fig. 5 shows the slow anodic discharge of same electrodes at same current strength. There are striking differences between charging and discharging capacities. This difference may be called "irreversible capacity" or "first hydrogen" and is plotted in fig. 6 vs. Ni content of each specimen and one may conclude that only Ti_2Ni will bind the hydrogen so strongly. In this connection let us remember the complicated structure of the Ti_2Ni crystal cell (fig. 1) offering a variety of interatomic distances and thus binding energies. More precise measurements, taking into account an initial corrosion of Ti_2Ni have shown that one molecule of Ti_2Ni may trap irreversibly about two hydrogen atoms. However, concerning the storage capacity of the system Ti-Ni mainly hydrogen dischargeable in the region of reversible hydrogen potential - this is up to 200 mv against reversible hydrogen - is of practical importance. These reversible capacities are plotted vs. Ni-content of each alloy in fig. 7, and one may see that they decrease with Ni-content linearly, so the useful capacity is composed additively of those of the pure compounds Ti_2Ni and TiNi. Only the values of the Ti_2Ni richest compositions are deviating from this linearity. Micrographs have shown that these deviations may be caused by insufficient breaking of alloys containing only a few grain boundaries. Therefore, we have feeled justified to calculate the specific capacities of the pure compounds Ti_2Ni and TiNi by linear extrapolation of these measuring values of the alloys. Thus the specific useful capacity of pure Ti_2Ni amounts to 0.26 , and that of pure TiNi to 0.245 amp. hrs/gramm. This means, that each molecule of Ti_2Ni may store about 1.5 , and each molecule of TiNi about 1 H-atom in a reversible way, and this hydrogen may be called "second hydrogen".

According to our hope mentioned in our introduction the reversible specific capacity is rather high, but there are several other important points of view for the evaluation of an accumulator electrode, such as fast charge acceptance, high discharging rate, aging properties and so on. Ti_2Ni offers excellent fast discharge performance, for the capacity decreases but little on discharge rates down to 15 minutes ("4 C"). In contrast to Ti_2Ni, the capacity of TiNi decreases with increasing discharge rate, what may be explained by slower diffusion of H-atoms within the TiNi crystal lattice.

To evaluate the cycling performance we have checked the above mentioned specimens by automatic cycling at a six hours rate (C/6) within a potential interval from -30 to + 200 mv vs. reversible hydrogen electrode in the same electrolyte 6m KOH at room temperature. The discharge capacity of Ti_2Ni rich electrodes degraded to 50% after 45 cycles already, whereas TiNi rich specimens, e. g. 53.6 at-% Ti and

46.4 at-% Ni reached this deterioration but after 300 cycles.

One may conclude that it is mainly Ti_2Ni which is responsible for aging of the alloys. This result could be confirmed directly by microscopic inspection of polished and etched specimens containing 57 at-% Ti and 43 at-% Ni, and comparing a virgin sample with another after 180 cycles. Fig. 8 demonstrates that TiNi grains remain unaffected, whereas the surrounding Ti_2Ni regions became completely black under cycling. The information given by light microscopy have encouraged us to apply larger magnifications using an electron microscope and in addition to elucidate the structure and composition by electron beam probe. Fig. 9a corroborates at 1000x linear magnification that TiNi grains remain unchanged. Fig. 9b shows a monochromatic photo of the nickel X-ray radiation and indicates that the surface of TiNi grains is enriched in nickel. In contrast, the original Ti_2Ni phase has lost most of its nickel. Fig. 9c is a monochromatic picture of Ti radiation and shows that Ti atoms are distributed rather homogeneously. Fig. 9d proves an enrichement of potassium atoms in the areas of former Ti_2Ni grains. Another analysis has disclosed an enrichement of about 20% oxygen there, and both K and O atoms must have entered from electrolyte.

However, the decrease of useful capacity of TiNi rich alloys under cycling cannot be explained by Ti_2Ni oxidation only, for the capacity of TiNi grains should remain unaltered. According to fig. 8 the TiNi grains are surrounded by peritecticly formed Ti_2Ni respectively the impermeable coating layers formed by its oxidation, preventing the access of hydrogen.

4. HYDROGEN ADSORPTION FROM GASEOUS PHASE

After the adsorption of cathodically evolved hydrogen by various Ti-Ni compounds we have studied the corresponding acceptance from gaseous molecular hydrogen. For this purpose we used electrodes with the data mentioned above. These electrodes were now provided with an additional fine pore copper coating layer, and after being fitted in a conventional gas tight half cell arrangement with 6m KOH as electrolyte, hydrogen was admitted at pressure of 2 atmospheres to the active side of the electrode. In fig. 10 is plotted the hydrogen consumption Q(t) measured in amp. hrs equivalents per gramm alloy containing 64 at-% Ti and 36 at-% Ni, vs. time t in hours. The saturation value is about 0.44 amp. hrs/gramm, this is as much as from cathodically evolved hydrogen (cf. fig. 4). The adsorption velocity $\dot{Q}(t)$ of hydrogen is obtained by differentiating Q(t), and is also plotted in fig. 10 vs. time. As one may see, the adsorption starts very slowly following an exponential function and reaching its maximum after 7.5 hours. This dependence on time may be explained by an autocatalytic mechanism similar to the course of potential during the first cathodic charging as described above, cf. fig. 4.

By this arrangement we have checked all our alloys and confirmed that they are able to adsorb molecular hydrogen from the gaseous phase. Hydrogen adsorbed in this way may also be discharged electrochemically and therefore, this alloy is suitable as electrocatalyst in H_2 anodes.

5. HYDROGEN ANODES

However, for application of said Ti-Ni compounds and alloys as catalysts in hydrogen anodes, adsorption of molecular hydrogen does not suffice; in addition is deciding the voltage amperage performance. For this purpose we have made circular gas diffusion electrodes of 40 mm diameter consisting of an active layer containing 3 gramm Ti-Ni compounds alloy with grain size below 60 microns, 6 gramm electrolytic copper as macroskeleton and 1.5 gramm Na_2CO_3 with grain size below 75 microns as filler. This active layer was coated by 2 gramm of copper as fine pore coating layer and hot pressed at 400 °C under 8 tons. Among the various compositions of active materials, the Ti_2Ni rich mixtures were hydrogenated before hot pressing to prevent subsequent formation of cracks under hydrogen adsorption.

These electrode specimens were operated both as cathodes or anodes in an hydrogen atmosphere of 2 atm at room temperature. Fig. 11 shows the current polarization performance for both directions of processing and a slope of 3.5 to 6 ohm. cm^2, and this differential resistance compares unfavourably with good Raney nickel DSK electrodes reaching values below 1.5 ohm. cm^2. To specify the reason for this insufficient performance we have first measured the current density as function of temperature and plotted in an Arrhenius diagram delivering a linear correlation between logarithm of amperage and inverse operating temperature with a slope corresponding to 4 to 5.5 kcal/mole, rather independent on Ti_2Ni to TiNi ratio and equalling those of good Raney nickel. Therefore, the inner surface became suspicious to be insufficient. In fact, BET measurements have disclosed that the inner surface of TiNi rich alloys is less than 1 sq. m/gramm, this is only 1 percent of our Raney nickel.

6. OUTLOOK

Although our investigations into the electrocatalytic properties of alloys of intermetallic Ti-Ni compounds have not yet yielded a technical progress we are finding it encouraging that intermetallic compounds are offering a new variety of potential electrocatalysts, in addition to the hitherto applied metallic elements. Moreover the electron beam probe has proved to be a very useful tool in analyzing electrode structures and in fact we have quite recently succeeded in increasing the inner surface of the tough compound TiNi and reached the cathodic and anodic performances shown in the last diagram (fig. 12) equalling the values of good Raney nickel. So one may hope to make a breakthrough in this way.

ACKNOWLEDGMENTS

We should like to express our gratitude to Professor O. Rüdiger, director of the Krupp Central Research Institute, Essen, for preparing

the alloys and for stimulating discussions. The authors wish also to thank their sponsors, Siemens AG in Erlangen, and Varta AG in Frankfurt, West Germany, for their support and permission to publish this work.

REFERENCES

(1) Justi, E., Scheibe, W., and Winsel, A.: DBP 1 019 361 (1954); Brit. Pat. 806 644; US Pat. 2 928 891 (1954).

(2) Justi, E. W., and Winsel, A. W., "Cold Combustion - Fuel Cells", Fr. Steiner Publ., Wiesbaden, Germany, (1962); J. Electrochem. Soc. 108, 1073 (1961).

(3) Yurko, G. A., Barton, J. W., and Parr, J. Gordon, Acta Cryst. 12, 909 (1959).
Kubaschewski, O., Trans. Faraday Soc. 54, 814 (1958).
Hume-Rothery, W., and Coles, B. R., Advances in Physics 3, 149 (1954).
Pauling, L., J. Amer. Chem. Soc. 69, 542 (1947).

(4) Hansen, M., "Constitution of Binary Alloys", McGraw-Hill Book Co., New York, (1958).

(5) Kalberlah, A. W., and Winsel, A. W., Z. Elektrochem., Ber. Bunsenges. physik. Chem. 68, 250 (1964).

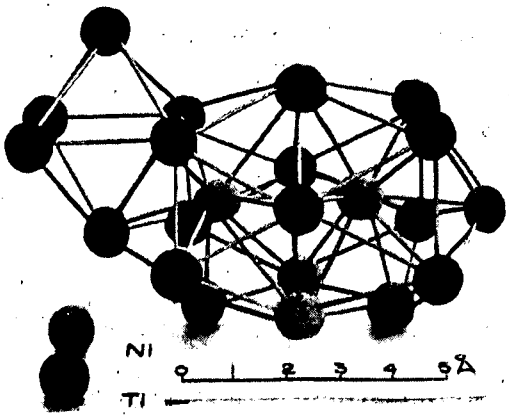

Fig. 1. Representative portion of Ti_2Ni cell.

Fig. 3. Photomicrograph of Ti-Ni alloy with 43 atomic per cent nickel. Etched in a mixture of 2 cm^3 HF, 2 cm^3 HNO_3 and 96 cm^3 water.

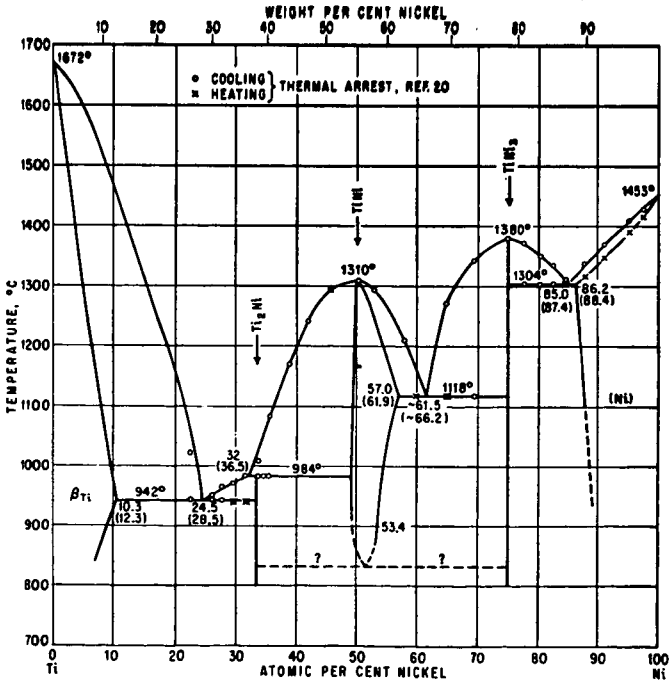

Fig. 2. Titanium-nickel phase diagram

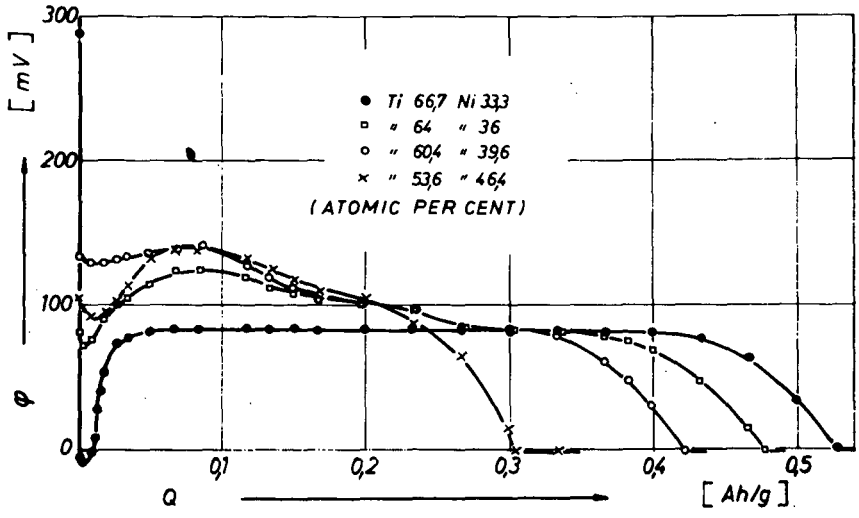

Fig. 4. Potential φ vs. hydrogen electrode in the same electrolyte of four electrodes with various Ti-Ni alloys as function of electric charge Q (in amp. hours per gramm Ti-Ni alloy) during the first galvanostatic kathodic charging process with 5 mA.

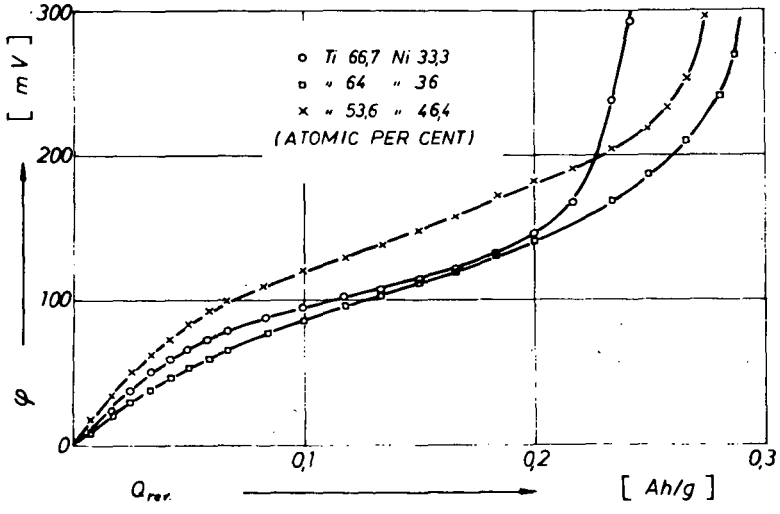

Fig. 5. Potential-charge plots of three electrodes during first anodic discharge with 5 mA following the cathodic charge of Fig. 4.

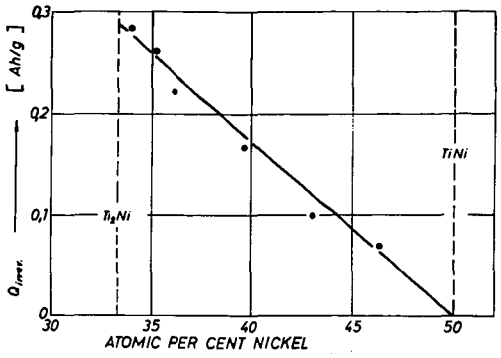

Fig. 6. Irreversible hydrogen storage capacity $Q_{irrev.}$ of one gramm Ti-Ni alloy vs. its composition.

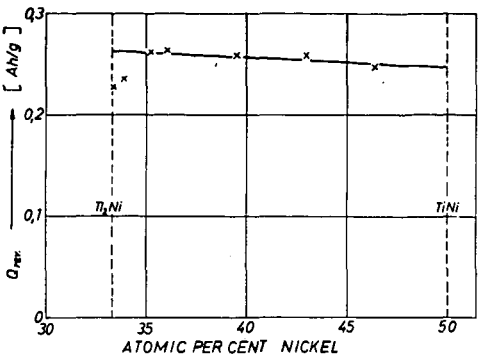

Fig. 7. Reversible hydrogen storage capacity $Q_{rev.}$ of one gramm Ti-Ni alloy vs. its composition.

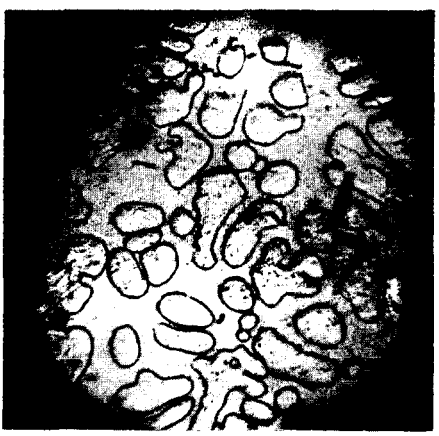

Fig. 8a.

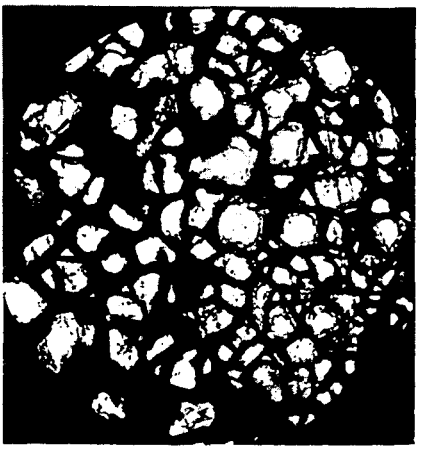

Fig. 8b.

Photomicrographs of Ti-Ni alloy grains (43 atomic per cent nickel), showing TiNi surrounded by Ti_2Ni

a) before any electrochemical treatment

b) after 180 charge discharge cycles, etching, cf. Fig. 3.

Fig. 9. Electron microprobe analysis of a Ti-Ni alloy grain (43 atomic per cent nickel), after 180 charge discharge cycles.

Fig. 9a. Electron image

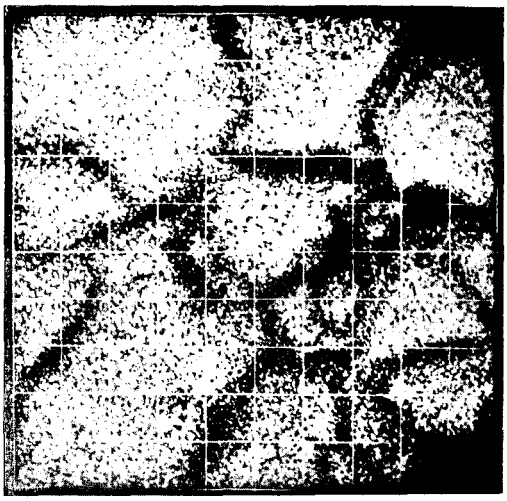

Fig. 9b. Distribution of Ni

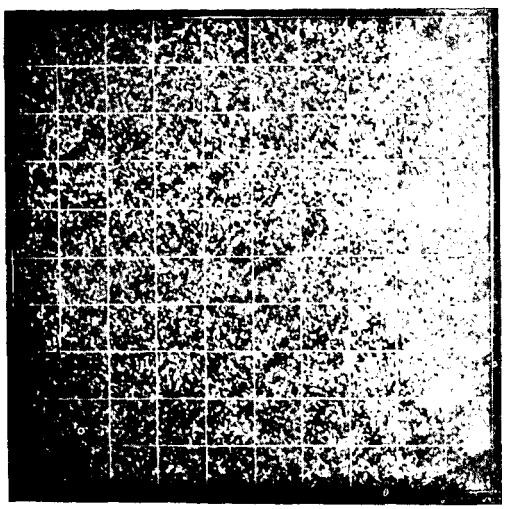

Fig. 9c. Distribution of Ti

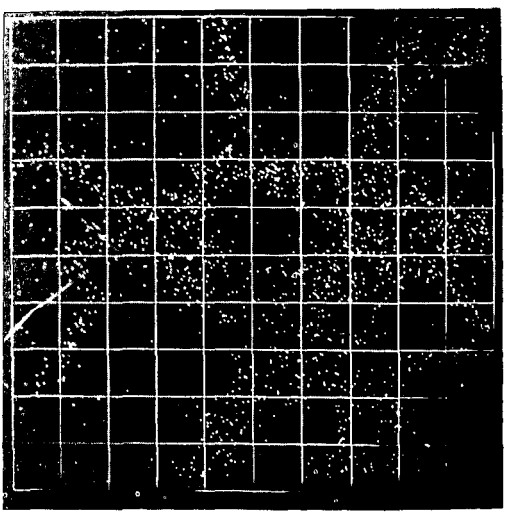

Fig. 9d. Distribution of K

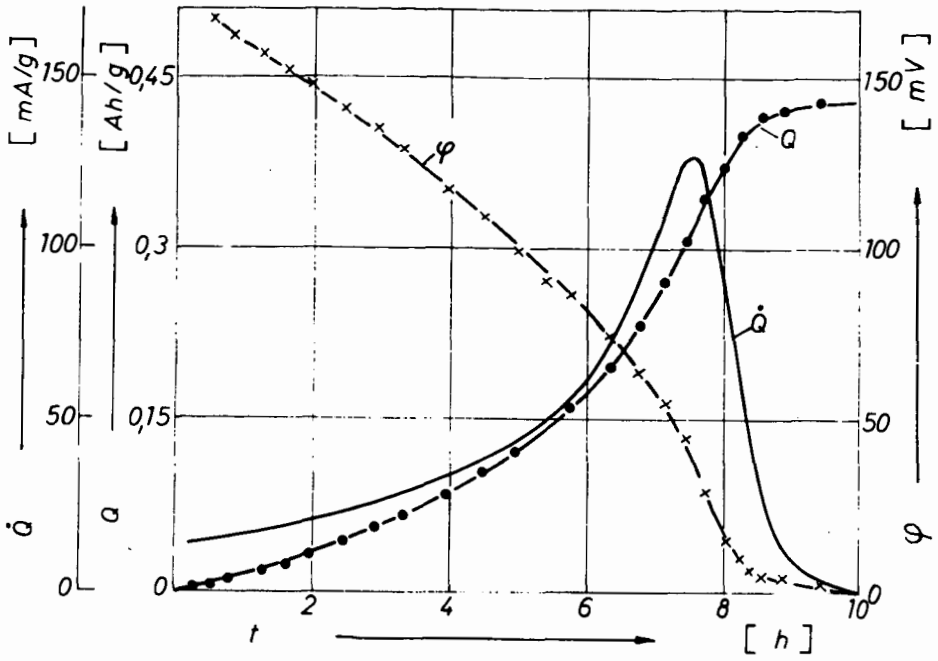

Fig. 10. First acceptance of hydrogen from the gasphase by an electrode with Ti-Ni alloy. Electrode potential φ against hydrogen electrode in the same electrolyte, accepted amount Q of hydrogen (expressed in Ah per gramm alloy) and influx $\dot{Q}$ of hydrogen in mA per gramm vs. time t in hours, 22°C.

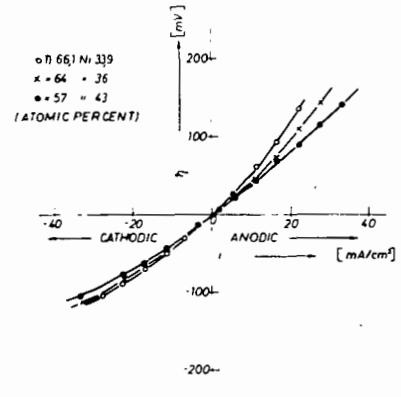

Fig. 11. Polarization-current density plots of three hydrogen electrodes with different Ti-Ni alloys as catalyst.

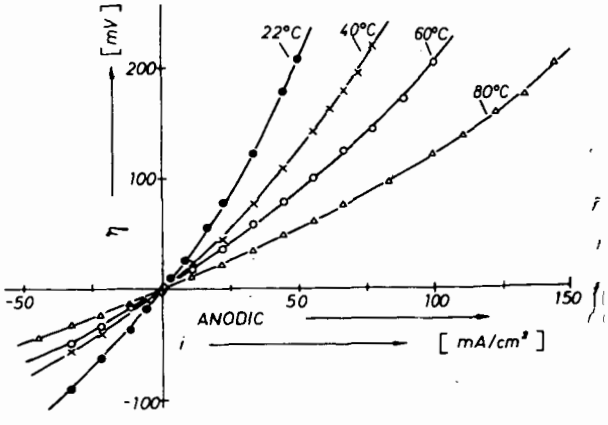

Fig. 12. Polarization-current density plots of a hydrogen electrode with TiNi as catalyst at different temperatures. Hydrogen pressure: 2 atmospheres.

157

ANODE-CATALYST PROMOTED REACTIONS OF REFORMED HYDROCARBON FUEL CELL FEEDS

D. K. Fleming, S. S. Randhava, and E. H. Camara

Institute of Gas Technology
Chicago, Illinois 60616

INTRODUCTION

The purpose of this study was to investigate the reactions of anode feed mixtures over candidate anode catalyst combinations. Previous work indicated that some of the catalysts suggested for CO-tolerant anodes were active in promoting chemical reactions of carbon monoxide with other constituents in the normal anode fuels. A program was initiated to determine if these reactions could occur at the operating temperature of the fuel cell with catalysts which had been formulated into fuel cell anodes with Teflon binder. The relative extent of these reactions could illustrate the mechanism of carbon monoxide tolerance in electrodes and indicate the formulations required for improved anodes.

The methanation of carbon monoxide with hydrogen was one of the major reactions expected.

Methanation of CO: $CO + 3H_2 \rightleftharpoons CH_4 + H_2O$ (1)

This reaction is the reverse of the reforming reaction and, according to free energy considerations, should proceed to the right at lower temperatures.

CO Shift: $CO + H_2O \rightleftharpoons CO_2 + H_2$ (2)

Another expected reaction is the CO shift. Equilibrium considerations dictate that the steady-state concentration of CO is about 1700 ppm at 150°C, if the H_2O/CH_4 ratio fed to the reformer is 2.5. With dry fuel, the equilibrium carbon monoxide concentration is higher by a factor of 10. There is an electrochemical equivalent of this reaction in which the product hydrogen is directly oxidized. This reaction may take place in an operating fuel cell because the hydrogen formed is adsorbed on the electrocatalysts.

Methanation of CO_2: $CO_2 + 4H_2 \rightleftharpoons CH_4 + 2H_2O$ (3)

Reaction 3 indicates the direct methanation of carbon dioxide and is the sum of Reaction 1 and the reverse of Reaction 2. However, this reaction need not occur stepwise with the formation of free carbon monoxide.

Other chemical reactions are also possible; however, these reactions have little likelihood of occurring at the fuel cell operating temperature and the C-H-O composition employed.

In this paper only the relative strength of the anode catalysts for enhancing these reactions is presented. No attempt is made to relate to the CO tolerance of operating fuel cell anodes, except in general terms with known past histories of anode performance.

Catalyst Selection

All of the anode catalysts used in this study were manufactured by American Cyanamid Co. according to its standard techniques, but with the noble metal constituents specified below. The noble metal loading in all electrodes was 5 mg/sq cm; the oxide admixture proportions followed the supplier's standard specifications. In mixed catalysts the weight proportions were evenly divided

between the constituents. The catalysts were not analyzed for precise composition; rather, the compositions requested from the supplier are discussed below.

The anode catalysts tested were —

- Platinum: This is the standard fuel cell catalyst and was used as a basis of comparison for the other materials.
- Ruthenium: This material is known to be active for the methanation reaction (Equation 1) when deposited on alumina. It provides the basis of comparison for platinum-ruthenium mixtures (1, 2, 4, 7).
- Rhodium: Pure rhodium is known to be slightly active in promoting the methanation reaction (2, 4) and provides a basis for comparison with platinum-rhodium mixtures.
- Platinum-Rhodium: This is the standard Type-BA catalyst manufactured by American Cyanamid and mentioned in its basic patent by Ziering, L. K. (8). Studies of this electrode were also conducted by McKee et al. (5).
- Platinum-Rhodium + WO_3: This is Cyanamid's Type-RA anode; it is discussed in the Ziering, L. K., patent (8) and by R. G. Haldeman (3), also of American Cyanamid Co.
- Rhodium + WO_3: Although not a standard anode catalyst, excellent carbon monoxide tolerance was claimed for this combination in the Ziering, L. K., patent (8) of American Cyanamid Co.
- Platinum-Ruthenium: This is the basic mixture used by General Electric Company: Several papers have been published on its carbon monoxide tolerance (4, 7).
- Platinum-Ruthenium + WO_3: This combination was selected because of the high activity of the platinum-ruthenium and the beneficial effects of the addition of WO_3 in other catalysts.
- Ruthenium + WO_3: This catalyst combines the best features of the ruthenium and the WO_3 admix, without the dilution effect of the platinum.
- Platinum + WO_3: This was a basic reference catalyst to determine the effects of the oxide constituents with a relatively inert base. This electrode combination exhibits carbon monoxide tolerance according to Niedrach and Weinstock (6).
- Platinum-Rhodium + MoO_2: Molybdic oxide was a constituent in the original precursor of the Type-RA electrode and was studied in this program to determine the effects of the MoO_2 admix.
- Platinum-Ruthenium + MoO_2: This combination was chosen to determine the effects of the molybdic oxide admixture upon the relatively active platinum-ruthenium noble metal base.

Palladium was not tested because it is relatively inert and iridium-containing electrodes could not be supplied. Variation of the noble metal proportions was not attempted in this study; varying concentrations of the oxide admixture were not available.

Table 1 lists the catalyst combinations used and the logical divisions according to systems and admixtures.

Table 1. CATEGORIZATION OF CATALYSTS TESTED

	Metals	Mixed Metals	Admixed Catalysts	
			WO_3	MoO_2
Rhodium System	Pt		Pt + WO_3	
		Pt-Rh	Pt-Rh + WO_3	Pt-Rh + MoO_2
	Rh		Rh + WO_3	
Ruthenium System	Pt		Pt + WO_3	
		Pt-Ru	Pt-Ru + WO_3	Pt-Ru + MoO_2
	Ru		Ru + WO_3	

Experimental Equipment and Techniques

The reactors for this work were standard fuel cell hardware, indicated schematically in an exploded view in Figure 1. Stainless steel and tantalum end-plates were tested and found inert for these reactions. The flow configurations in the 2 x 2 inch test cells were checked for uniformity by smoke tests. These electrodes were placed against a Teflon backup sheet and the available area of the electrode was determined by the opening in the frame gasket, identical to a standard fuel cell compartment gasket. Tantalum, expanded-metal screens were used to fix the location of the electrode.

The flow pattern of this reaction, with the reactant gas passing through a thin, wide chamber with one catalyzed wall, is not ideal. However, this is the configuration used in most fuel cells, and the equipment was set up to relate to operating fuel cells.

The tests were operated with dry electrodes; that is, an acid-soaked matrix was not present behind the electrode. The acid was omitted to avoid the effects of variable electrode drowning, gas dissolution rates, equilibrium shifts due to water at the electrodes, variable acid concentration with drying out of the cell, and other effects that would alter the rate and/or the reproducibility of the reactions. The results presented, however, are useful in relating the relative activity of the catalysts – a factor which is not grossly affected by the presence of an electrolyte. However, in an operating fuel cell, the electrode operates at fixed potentials with respect to the electrolyte: This potential may shift the equilibrium due to the effect upon the free energy change.

The experimental apparatus is indicated schematically in Figure 2. In the flow system either standard fuel gas or a zero gas (for calibrating the instrument) is admitted to the system through a pressure regulator and block valve. The gas passes through a flow-indicating rotometer and a flow regulator which control a constant, downstream flow rate, regardless of the upstream pressure. The gas then flows either to the test cell or to a bypass. Leaving the system, the gas goes either to a bubble flowmeter or to the gas analysis train. The bubble flowmeter is used to adjust the flow controller for each run. The gas analyzing equipment is calibrated with a zero and a standard gas at the beginning of each run. In a given test, when the cell temperature stabilized, as controlled by a proportional temperature-indicating controller and verified by a strip-chart temperature recorder, the bypass valve is closed and the gas fed to the cell for several minutes to establish steady-state conditions. The carbon monoxide and methane contents in the effluent gas are then recorded as a function of temperature.

The gas compositions are determined by sensitive infrared analyzers calibrated for the detection of carbon monoxide and methane. The first unit in the analysis train is a Lira Model 200, manufactured by Mine Safety Appliances,

Pittsburgh, Pa. It has three carbon monoxide ranges with full-scale sensitivities of 100, 500, and 5000 ppm CO. Although the lower range is direct reading, non-linearity exists in the upper two ranges so that calibration curves are required. When used with these curves, the Lira IR analyzer continuously monitors the carbon monoxide concentration in the flowing gas stream with an estimated accuracy of 2% of full scale. The analyzer used for methane determination is a Lira Model 300, which has greater electronic drift so the absolute values of the methane concentrations are not as accurate: This unit has a single range of 0-6000 ppm methane.

The gas flow rate used in most of this work was 300 cu cm/min. This rate was chosen because it is near the lower range of the gas analyzing equipment. Lower flows are time-consuming, and this standard flow rate indicates the relative performances of the catalysts. For comparative purposes, this flow rate is approximately equivalent to 30 times the stoichiometric equivalent for 1-ampere current drain from this size cell, or 10 times the stoichiometric flow rate for 100 A/sq ft current density. The average residence time in the cell is approximately 3/4 second.

The primary feed gas was a simulated reformer product:

Hydrogen	79.7%
Carbon Dioxide	20%
Carbon Monoxide	0.3%

Gas of this composition may be expected after reforming and shifting reactions with a high H_2O/CH_4 ratio in the feed to the reformer. This gas composition was chosen because it is a possible fuel cell feed and is near the mid-range of the gas analyzing equipment in concentration.

In some tests, a reference gas containing 80% hydrogen and 20% carbon dioxide was used. This gas determines the effect of a carbon monoxide-free feed. Most of the tests were run with dry feed, although some were operated with 57°C dew point humidification to check the effect of moisture on the reaction.

PRESENTATION OF RESULTS

Interpretation of the Data

The relative capabilities of these catalysts in promoting the reactions are determined by the change in the CO and CH_4 concentrations in the effluent gas stream. Any increase in the CH_4 concentration is indicative of Reactions 1 or 3. If an increase in CH_4 concentration is accompanied by a corresponding decrease in the CO level, then Reaction 1 takes place.

A decrease in the CO concentration could mean either Reaction 1 or 2 occurs. As discussed above, a corresponding increase in the CH_4 level indicates Reaction 1. Any increase in CO content, without a change in the CH_4 level, indicates the reverse of Reaction 2.

The effluent from some rhodium-containing catalysts first shows a decrease in the CO content, with a corresponding increase in CH_4. At higher temperatures, both the CO and CH_4 levels increase: This is interpreted as simple methanation of carbon monoxide at lower temperatures, followed by the reverse CO shift and continued methanation at higher temperatures. However, the methanation capabilities of the catalyst are weak, so the net CO content increases.

Metals – Rhodium System

Figures 3 and 4 present the carbon monoxide and methane concentrations in the effluent from fuel-cell-type reactors containing "metal-only" catalysts. In the rhodium system, the electrode containing only platinum exhibited a slight reduction in the CO concentration (Figure 3) at higher temperatures; the platinum-rhodium electrode was similarly inert. A pure rhodium electrode showed a carbon monoxide generation of about 50-100 ppm above 225°C. In Figure 4, the platinum exhibited a methane generation which was not significant. Again, the platinum-rhodium was inert. The pure rhodium electrode, however, showed a definite methane generating capability.

In summary, the platinum and platinum-rhodium electrodes are essentially inert in the temperature range studied. The pure rhodium is a weak methanation catalyst, probably forming CH_4 from CO: It is also slightly active in promoting the reverse CO-shift reaction.

Metals – Ruthenium System

The performance of the ruthenium system metals is presented in Figures 3 and 4. As indicated above, the platinum reference electrode is almost inert; however, the pure ruthenium one is a definite methanation catalyst. The carbon monoxide concentration in the effluent from this electrode decreased rapidly at temperatures between 150° and 175°C. Similarly, the methane concentration in the effluent rose as the CO concentration decreased, indicating that the carbon monoxide was being methanated. At temperatures greater than 175°C, the methane concentration continued to increase; the graphs do not present enough evidence to indicate if carbon dioxide was being methanated directly, or if carbon monoxide was being formed from carbon dioxide and hydrogen by a reverse CO shift, while the high methanation capabilities of the electrode maintained a low CO concentration. At higher temperatures, the CO concentration in the effluent tended to increase slightly. This is in accordance with the equilibrium consideration.

The platinum-ruthenium mixed electrode also exhibited methanation capabilities (Figures 3 and 4) but the effect took place at a higher temperature. This indicates that the catalytic strength of the platinum-ruthenium electrode is not as great, probably because of the dilution effect of the platinum upon the ruthenium.

In summary, in the ruthenium system, the platinum electrode is inert, but the ruthenium electrode is active in promoting the selective methanation of the carbon monoxide. When the CO had been consumed, additional methane was still generated, indicating either a direct methanation of carbon dioxide, or activity for the reverse CO-shift reaction followed by enough activity for the CO-methanation reaction that the carbon monoxide concentration was maintained at a low level. The platinum-ruthenium electrode behaves similarly to the ruthenium electrode, although at higher temperatures.

Effect of Additives – Ruthenium System

Figures 5 and 6 present the CO and CH_4 concentrations from three platinum-ruthenium electrodes. One of these electrodes contained no admixtures, another contained tungstic oxide, and the third contained molybdic oxide. These graphs indicate that the tungstic oxide admix significantly improves the methanation capabilities of this electrode, dropping the temperature of reaction to about 150°C. The molybdic oxide admix, however, had no significant effect upon the electrode's methanation capabilities; it may even have decreased this activity at the higher temperature, as indicated in Figure 6. However, the MoO_2 admix did cause an increase in the CO concentrations at elevated temperatures (Figure 5), indicating that this electrode is active in promoting the reverse CO-shift reaction when used in conjunction with platinum-ruthenium.

Figures 7 and 8 show the CO and CH_4 concentrations in a series of ruthenium-containing electrodes, both with and without tungstic oxide admix. These graphs indicate that the Pt-Ru + WO_3 is even more active for the methanation reaction than the pure ruthenium electrode; the Ru + WO_3 is more active yet. In contrast, the Pt + WO_3 anode exhibits the same degree of inactivity as the pure platinum electrode.

Summarizing, tungstic oxide exhibits a definite synergistic effect in promoting the methanation reaction when used in conjunction with ruthenium-containing electrodes. Molybdic oxide admix may have a slight depressing effect upon the methanation reaction, but promotes the reverse CO-shift reaction.

Effect of Admixes – Rhodium Systems

The CO and CH_4 concentrations from three platinum-rhodium electrodes are given in Figures 9 and 10. One of the electrodes contains no admix, another contains tungstic oxide, and the third contains molybdic oxide admix. These graphs indicate that the tungstic oxide admix promotes the generation of methane. At temperatures less than 175°C, the methane apparently is formed from carbon monoxide, because the decrease in the CO concentration is equal to the increase in the CH_4 concentration. At elevated temperatures, the CH_4 concentration continues to increase: The CO concentration also increased, indicating catalytic activity for the reverse CO-shift reaction.

The molybdic oxide admix, however, promotes very little decrease in the CO concentration at lower temperatures, but apparently promotes the reverse CO-shift reaction at higher temperatures. In Figure 10, the amount of methane generated with the molybdic oxide admix is relatively high. This may be due to direct methanation of carbon dioxide. As indicated earlier, the platinum-rhodium electrode without admix is relatively inert.

Figures 11 and 12 present the CO and CH_4 concentrations for the family of rhodium-containing electrodes both with and without WO_3 admix. As indicated earlier, platinum, platinum-rhodium, and platinum + WO_3 are relatively inert; the pure rhodium electrode has slight activity for the methanation and reverse CO-shift reaction. However, with the addition of tungstic oxide, the activity of the platinum-rhodium electrode for the methanation and CO-shift reactions increases significantly. These graphs also illustrate the one irregularity which has been observed: The pure Rh + WO_3 electrode is not as active for the methanation or CO-shift reactions as the Pt-Rh + WO_3 catalyst. This effect may be real or due to an irregular catalyst sample.

Summarizing, tungstic oxide admix exhibits a definite synergistic effect in promoting the methanation and reverse CO-shift reactions when used in conjunction with rhodium-containing catalysts. However, pure platinum plus tungstic oxide is relatively inert. Molybdic oxide admix apparently promotes only the reverse CO-shift reaction, although it may have an effect on the direct methanation of carbon dioxide with platinum-rhodium based catalyst.

Effect of CO-Free Feed

Figures 13 and 14 present the carbon monoxide and methane concentrations in the effluent from a Pt-Ru + WO_3 electrode with both the standard feed gas containing 3000 ppm CO and with a CO-free feed. Apparently, the methane-generating capability of this catalyst is greater with a CO-free feed: No carbon monoxide is generated with this catalyst. At temperatures in the range of 125°-150°C, significant CH_4 is generated without apparent CO in the effluent. This is the range (with the 3000 ppm CO feed) where the CO concentration decreases and the CH_4 concentration increases in an apparent steady-state condition. The new data indicate that methane may be generated from carbon dioxide without an independent

CO intermediate. Earlier data indicated that free CO would be present in the indicated temperature range during the selective methanation of the carbon monoxide. However, with the CO absent from the feed, the carbon dioxide can methanate directly and apparently reacts at a lower temperature when CO is absent from the feed.

Figures 15 and 16 present carbon monoxide and methane concentrations for a platinum-rhodium + tungstic oxide electrode combination, both with and without carbon monoxide in the feed. Figure 15 indicates that the activity of this catalyst for the CO-shift reaction is constant; Figure 16 indicates the variation in the methane-producing capabilities of the electrode with the feedstock. Again, more methane is generated from a CO-free feed. Similar to the ruthenium-containing electrode, methane is generated in a temperature range where the CO/CH_4 ratio is much lower than was required for the 3000-ppm CO feed. Therefore, it appears that the CO_2 is methanating at lower temperatures, but, as the temperature increases, CO also methanates as the two lines of Figure 16 merge.

With the feed containing 20% hydrogen and 20% carbon dioxide, the direct methanation of carbon dioxide is indicated for both Pt-Ru + WO_3 and Pt-Rh + WO_3 electrodes. The methane generated at any temperature is greater than experienced with CO-containing fuels when selective methanation of the carbon monoxide is experienced before methanation of the carbon dioxide. With the rhodium-containing electrode, activity for the reverse CO-shift reaction was still evident as carbon monoxide was formed at higher temperatures. In this case, the methane-generating capabilities from the two feed streams became similar at elevated temperatures with higher CO concentrations, indicating methanation of the carbon monoxide generated.

Effect of Moisture

Several tests were made with the fuel gas humidified to 57°C; the dew point if the H_2O/CH_4 ratio fed to the original hydrocarbon reformer was 2.5. The water concentration in the feed caused the effects expected from equilibrium considerations. It reduces the methane generated over the catalysts in Reaction 1 and the CO generated by the reverse CO-shift Reaction 2. Extensive tests with moisture in the feed were not run because they did not aid in the general purpose of the program – determining the relative catalytic activities of candidate anodes in the reformed fuel mixtures.

Effect of Gas Flow Rates

Earlier work had shown that the methanation reaction was sensitive to contact time. Figure 17 presents the methanation capability of a pure ruthenium catalyst electrode as a function of flow rate. The temperature at which the majority of the carbon monoxide is methanated decreases from 160° to 130°C as the flow rate is decreased from 500 to 100 cu cm/min. These data indicate that, at flow rates normally employed at the fuel cell anode, the temperature of the reaction decreases so that significant methanation may occur. This is particularly true in the case of the CO-containing fuel in the pores of the electrode as longer residency time would be expected in this case.

Figure 18 presents a similar set of curves for the variation in the CO consumed, with the flow rate for a platinum-rhodium plus tungstic oxide electrode. In this case, the methanation capability of the electrode is improved with lower flow rates, enough to partially offset the CO-increasing tendency of the CO-shift reaction at higher temperatures. Again, significant chemical reactions could occur at the fuel cell operating temperature; the lowest flow rate on this graph is still stoichiometrically equivalent to over 300 A/sq ft.

CONCLUSIONS

Noble metal catalysts formulated into fuel cell anodes maintained their activity for the methanation reaction. Particularly, ruthenium-containing electrodes exhibited significant methanating capabilities; pure rhodium electrodes showed some methanation activity. Therefore, the Teflon waterproofing is not a significant deterrent to the reaction, nor is the alumina support used in granular methanation catalysts necessary for the reaction.

Ruthenium-containing electrodes are active for the production of methane. If carbon monoxide is present in the fuel, it is selectively converted to methane before the carbon dioxide reacts. If the feed is CO-free, CH_4 is generated directly from CO_2 in greater quantities than if CO was present. The ruthenium-containing electrodes appear to be inactive for the generation of CO from CO_2, although this effect could be masked by the CH_4-generating capability of the material.

Rhodium-containing electrodes are much less active for the generation of CH_4 from CO and CO_2, but the reactions still take place. Pure rhodium electrodes appear to be relatively inactive for the generation of CO from CO_2.

All the reactions tested were sensitive to flow rate, indicating that reaction time is an important parameter in the equipment configuration used.

The addition of molybdic oxide appears to enhance the production of CO from CO_2 with both rhodium- and ruthenium-containing electrodes. It has slight effect upon the CH_4 generating capabilities, except, perhaps, causing some production of CH_4 from CO_2 with Pt-Rh electrodes.

The addition of WO_3 to the electrode has a definite synergistic effect for every catalyst combination tested, except pure platinum. With the ruthenium-containing electrodes, the methanation capabilities were significantly improved. The methanation capabilities were also improved with the rhodium-containing electrodes; in addition, this constituent improved the generation of CO from CO_2 with the rhodium catalyst family.

ACKNOWLEDGMENT

The work reported in this paper was supported under subcontract from Pratt & Whitney Division, United Aircraft Corporation under the gas industry's TARGET program and whose support and permission to publish are gratefully acknowledged. In addition, the efforts of D. Hegyi in the collection of the data are appreciated.

1. Baker, B.S., Meek, J., Khan, A.R. and Linden, H.R., "Process for Generation of Hydrogen From Liquid Hydrocarbons for Use in Acid Fuel Cells," U.S. Patent Application Serial No. 461,298 (1965) June 4.

2. Baker, B.S., Huebler, J., Linden, H.R. and Meek, J., "Process for Selective Removal of CO From a Mixture of Gases," U.S. Patent Application Serial No. 701,036; continuation filed (1968) January 10.

3. Haldeman, R.G., "Electrode-Matrix Materials," Proc. 21st Annual Power Sources Conf. 1-3 Red Bank, N.J., PSC Publications Committee (1967).

4. McKee, D.W., "Interaction of Hydrogen and Carbon Monoxide on Platinum Group Metals," J. Catalysis 8, 240-49 (1967) July.

5. McKee, D.W., Niedrach, L.W., Paynter, J. and Danzig, I.F., "Electrocatalysts for Hydrogen/Carbon Monoxide Fuel Cell Anodes. Part II. The Platinum-Rhodium and Platinum-Iridium Systems," Electrochem. Technol. 5, 419-23 (1967) September-October.

6. Niedrach, L.W. and Weinstock, I.B., "Performance of Carbon Monoxide in Low-Temperature Fuel Cells Containing Oxide Catalysts," Electrochem. Technol. 3, 270-75 (1965) September-October.

7. Niedrach, L.W., McKee, D.W., Paynter, J. and Danzig, I.F., "Electrocatalysts for Hydrogen/Carbon Monoxide Fuel Cell Anodes. Part I. The Platinum-Ruthenium System," Electrochem. Technol. 5, 318-23 (1967) July-August.

8. Ziering, L.K. (assigned to American Cyanamid Co.), "Rhodium Catalyst and Fuel Cell," U.S. 3,357,863 (1967) December 12.

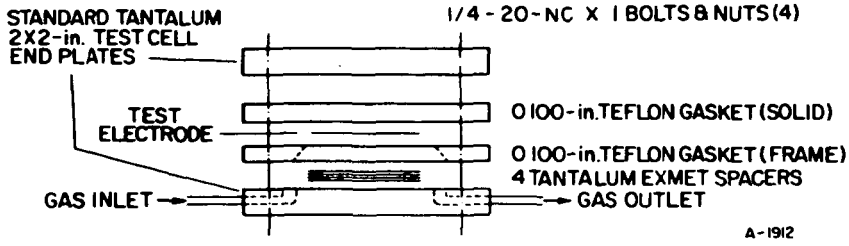

Figure 1. EXPLODED VIEW OF REACTOR

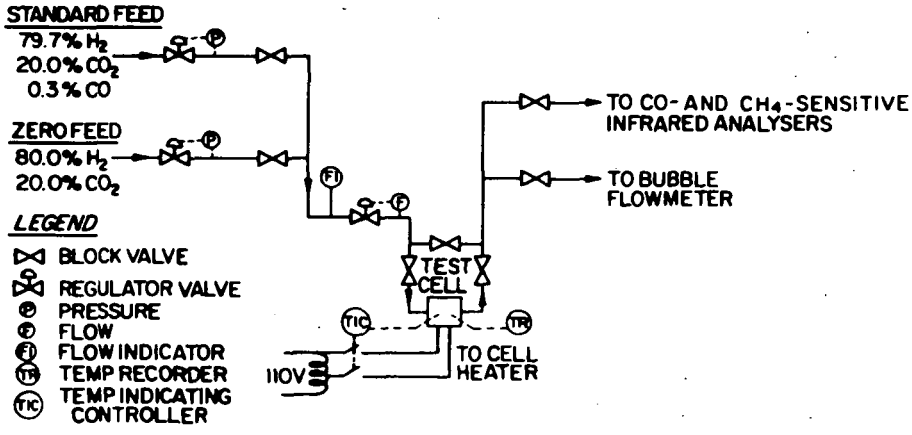

Figure 2. SCHEMATIC FLOW DIAGRAM OF EXPERIMENTAL SETUP

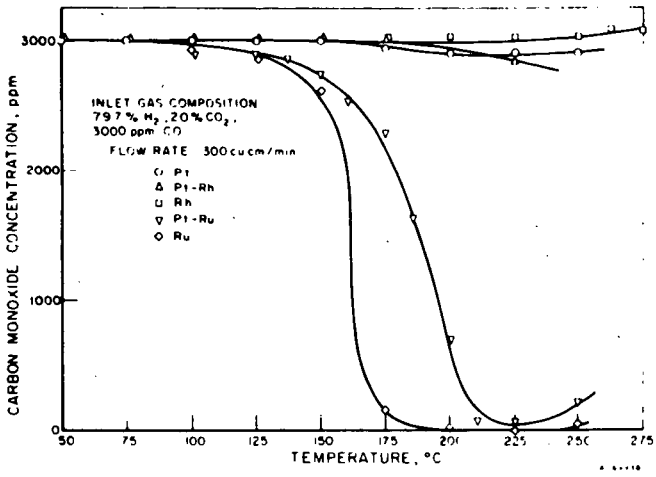

Figure 3. CARBON MONOXIDE IN EFFLUENT FROM METAL CATALYSTS

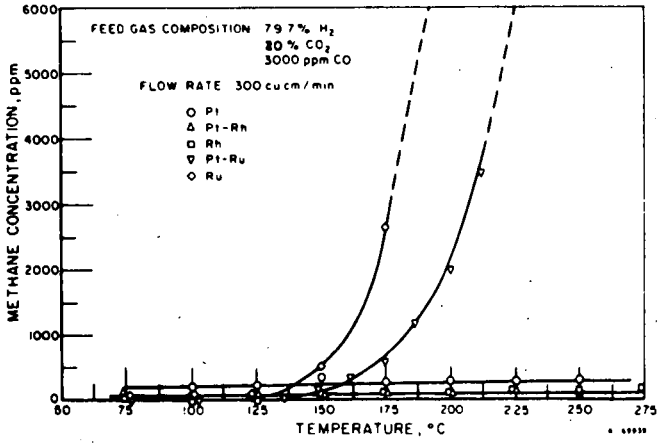

Figure 4. METHANE IN EFFLUENT FROM METAL CATALYSTS

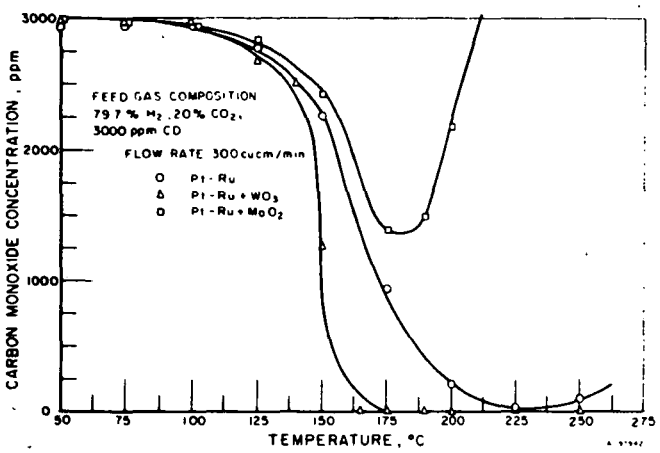

Figure 5. EFFECT OF ADMIX ON CARBON MONOXIDE IN EFFLUENT FROM Pt-Ru CATALYSTS

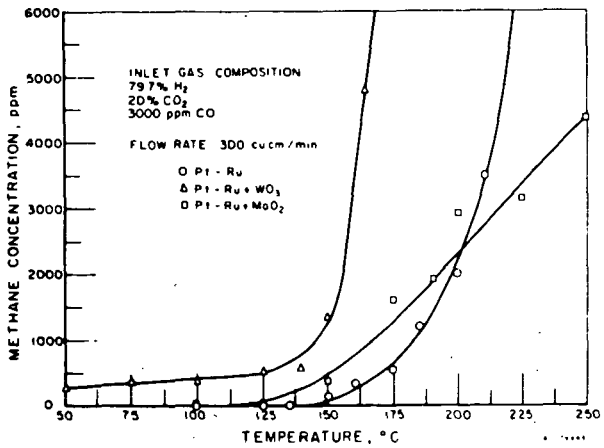

Figure 6. EFFECT OF ADMIX ON METHANE IN EFFLUENT FROM Pt-Ru CATALYSTS

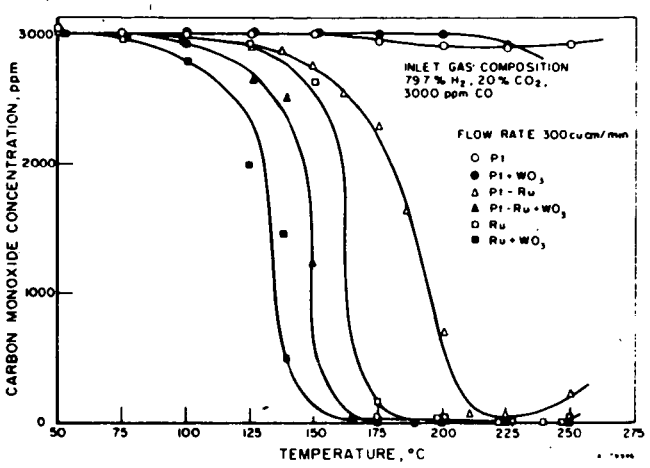

Figure 7. EFFECT OF WO_3 ADMIX ON CARBON MONOXIDE IN EFFLUENT FROM Ru-SYSTEM CATALYSTS

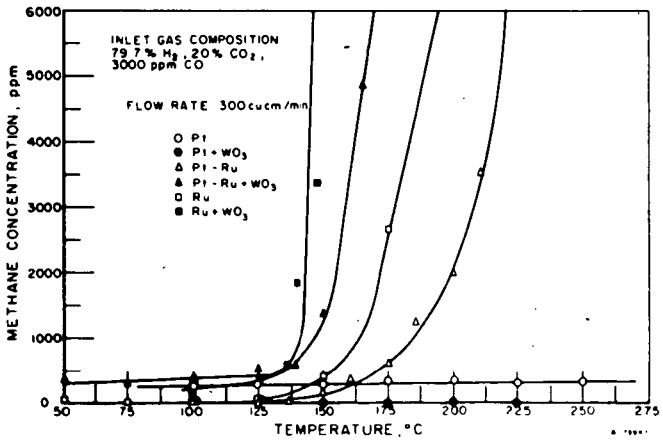

Figure 8. EFFECT OF WO_3 ADMIX ON METHANE IN EFFLUENT FROM Ru-SYSTEM CATALYSTS

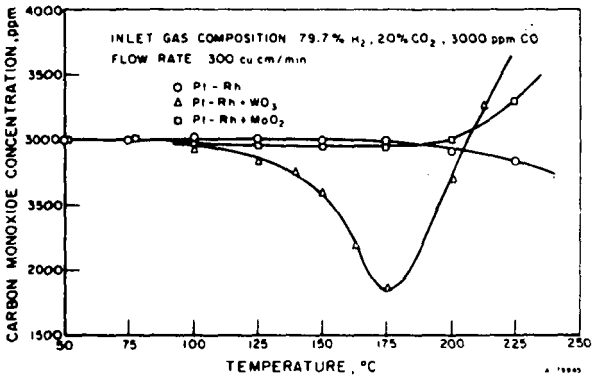

Figure 9. EFFECT OF ADMIX ON CARBON MONOXIDE IN EFFLUENT FROM Pt-Rh CATALYSTS

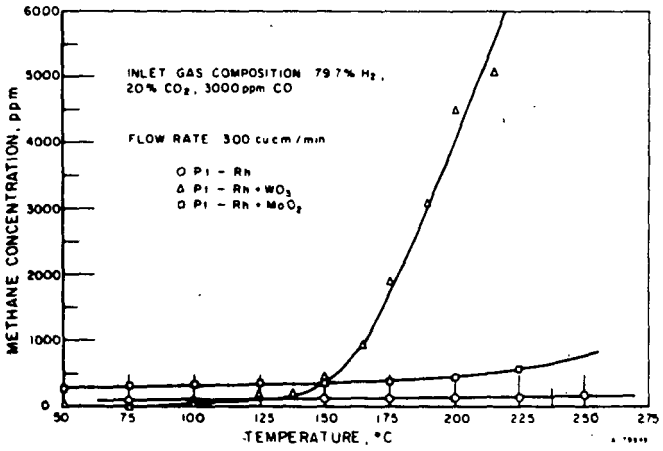

Figure 10. EFFECT OF ADMIX ON METHANE IN EFFLUENT FROM Pt-Rh CATALYSTS

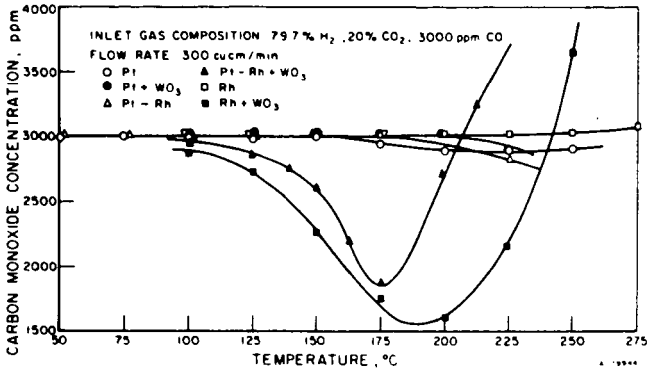

Figure 11. EFFECT OF WO_3 ADMIX ON CARBON MONOXIDE IN EFFLUENT FROM Rh-SYSTEM CATALYSTS

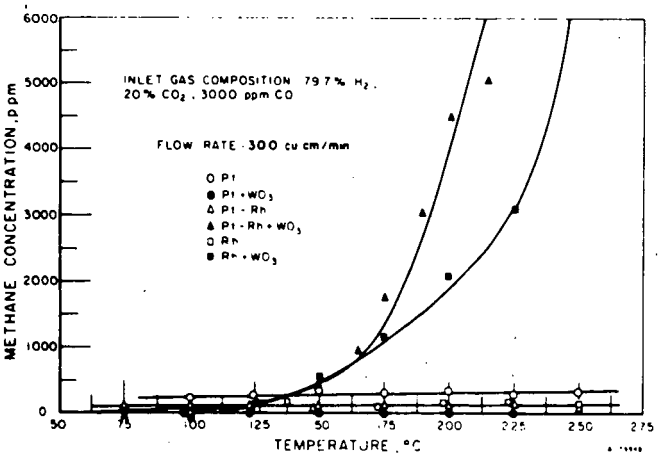

Figure 12. EFFECT OF WO_3 ADMIX ON METHANE IN EFFLUENT FROM Rh-SYSTEM CATALYSTS

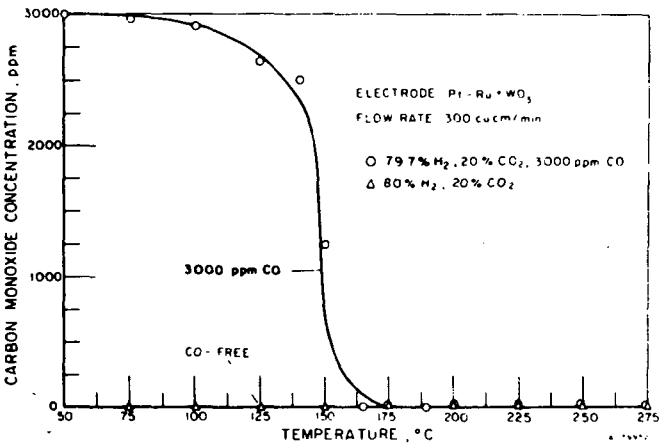

Figure 13. CARBON MONOXIDE IN EFFLUENT FROM Pt-Ru + WO_3 CATALYST WITH 3000-ppm CO AND CO-FREE FEEDS

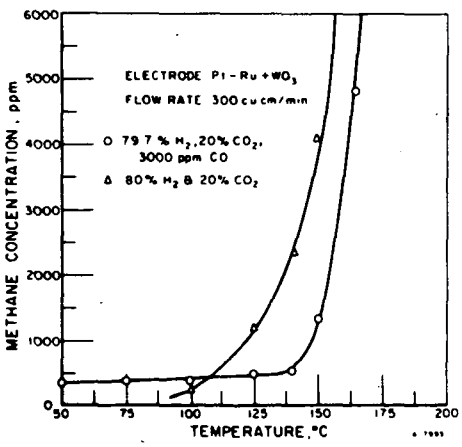

Figure 14. METHANE IN EFFLUENT FROM Pt-Ru + WO_3 CATALYST WITH 3000-ppm CO AND CO-FREE FEEDS

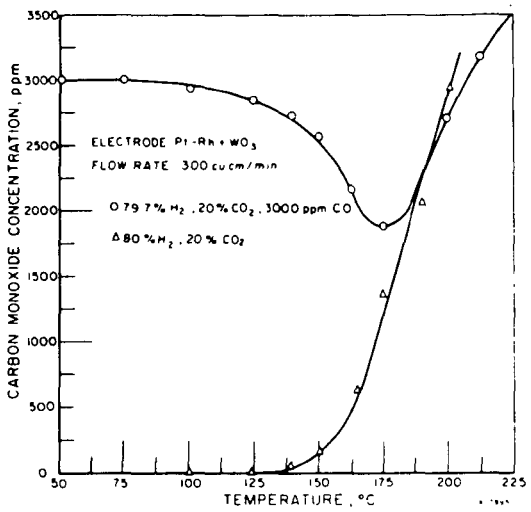

Figure 15. CARBON MONOXIDE IN EFFLUENT FROM Pt-Rh + WO_3 CATALYST WITH 3000-ppm CO AND CO-FREE FEEDS

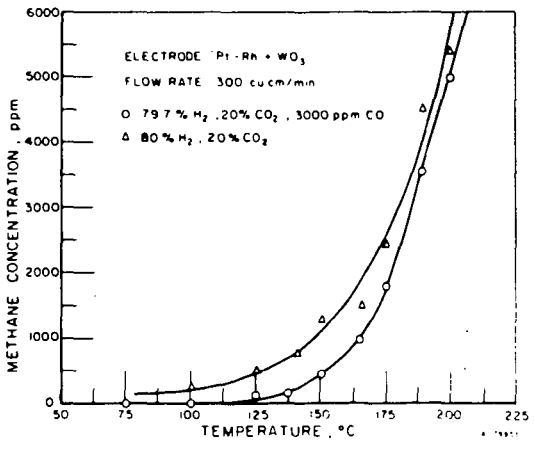

Figure 16. METHANE IN EFFLUENT FROM Pt-Rh + WO_3 CATALYST WITH 3000-ppm CO AND CO-FREE FEEDS

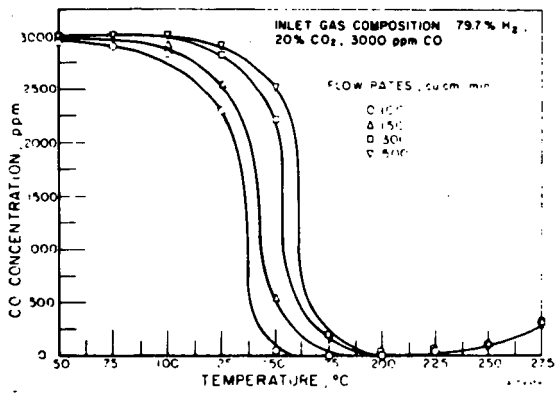

Figure 17. CARBON MONOXIDE IN EFFLUENT FROM Ru CATALYST AS A FUNCTION OF FLOW RATE

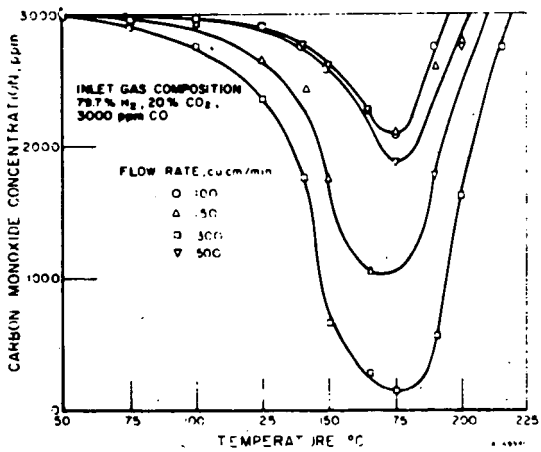

Figure 18. CARBON MONOXIDE IN EFFLUENT FROM Pt-Rh + WO_3 ELECTRODE AS A FUNCTION OF FLOW RATE

ON THE DEPENDENCE OF THE CATALYTIC ACTIVITY OF PLATINUM ON SIZE AND ORIENTATION OF THE CRYSTALLITES

V. S. Bagotzky, Yu. B. Vassiliev, A. M. Skundin, V. Sh. Palanker, I. I. Pyshnograeva, O. A. Khasova, and L. S. Kanevsky

Academy of Sciences of U.S.S.R.
Moscow V-71

ABSTRACT

The influence of structural factors upon the activity of platinum catalysts for different reactions was investigated. Processes of electrolytic hydrogen and oxygen evolution, anion and methanol adsorption and methanol oxidation were used as model reactions.

It was shown that for methanol oxidation the catalytic activity of platinized platinum, referred to unit true surface, is appreciably lower, than that of smooth platinum. Investigations on monocrystalline platinum have shown that on different crystal faces the isotherms for hydrogen adsorption are similar. Neither is there a difference as regards the oxygen adsorption isotherm and the kinetics of oxygen and bromine adsorption. However, there is a appreciable change in the rates of methanol adsorption (involving dehydrogenation of the methanol molecule) and of the oxidation of organic residues on the surface. On the (111) face with the greatest density of surface atoms the rate constants (referred to one surface atom) exceed the relevant constants on other faces 3-6 times. An analogous effect can be observed for hydrogen and oxygen evolution. The values of the activation energy remain unchanged, the density of the surface atoms affecting mainly the preexponential factor. Annealing of polycrystalline platinum or preliminary mecanical deformation do not affect the adsorption and catalytic properties of the surface.

On a smooth carbon surface (glassy carbon covered with nonporous pyrolytic carbon) low quantities of platinum microcrystallites were deposited electrolytically. The surface concentration was low enough to prevent overlapping. The hydrogen evolution rate depends on the crystal size and on the mean distance between crystallites on the surface. For small crystallites (i.e. for high specific surface areas) and for small amounts of crystallites on the surface the reaction rate exceeds 5-7 times the rate on smooth platimum.

DISTRIBUTION OF CURRENT CONVERSION IN POROUS GAS ELECTRODES

Karl Joachim Euler

VARTA
Frankfurt/Main, Germany

§ 1 Introduction, Problems

During the past years, the phenomena of current conversion in porous gas electrodes of finite thickness have been investigated very thoroughly by a great number of authors (2, 3, 4, 5, 6, 7, 8, 9). The main attention in recent papers was paid to the investigation of the current conversion in the nearest neighbourhood of thriphase zones, i.e. nearest to the liquid - gas meniscus in a single pore of the working electrode, see below § 5. However, this is only one of several important factors, responsible for the distribution of current conversion inside electrodes of finite thickness. In the following paper, plaine porous gas electrodes consisting of at least two layers, having different pore diameters, are examined. To this kind of electrodes, the gas is fed through one surface, and the liquid electrolyte adheres the other electrode surface. Thickness is supposed to be finite but small with regard to the lateral dimensions, and the use of electrolyte repellent agents may be generally excluded*).

§ 2 General Theory.

In most cases, the complicated theory of tri-phase electrodes can be reduced to the better known (9, 12)

*) Please see § 7

theory of porous two-phase electrodes. Figure 1 shows the geometry of a semi-infinite porous double layer oxygen electrode, made of metal powder. The electronic conductivity of the electrode matrix is supposed to be high, to such a degree, that the voltage drop in the electron path can be neglected. In the cover layer, the narrow pores are filled completely with electrolyte, and no electrical conversion of ions to electrons proceeds therein. Thus, the cover layer acts as simple resistor in the electric analogue, having no influence on the spatial distribution of current conversion inside the working layer.

When we regard, for instance, a hydrogen anode in alkaline electrolyte, the electrochemical gross reaction may be written

$$H_2 + 2\ OH^- \longrightarrow 2\ H_2O + 2\ e^-.$$

Since "metabolism waste" water is formed, which must be removed from the working layer, either migrating in the liquid phase, or diffusing, as steam, into the hydrogen supply system. Because the water lowers the ionic conductivity inside the electrode, its effect approximatively can be taken into consideration, under steady state conditions, by introduction of a somewhat elevated ionic resistivity $\bar{\varrho}_i$, see § 8.

§ 3 Special Transport Function Θ

Consequently, only two transport phenomena remain to be considered, the ion resistivity, and the gas friction inside the narrow pores, hereafter called "gas resistivity". Two-phase electrodes, up to now have been treated as an electrical network. Mechanical characteristics, like diffusion constant D of gases, pressure drop, and channel geometry must be transferred into adequate electrical magnitudes.

Using the Einstein equation $D = b\,kT/e$, immediately a gas resistivity ϱ_g can be defined:

$$1/\varrho_g = nN\,b\,e = D\,nN\,e^2/kTf,$$

$N\ [cm^{-3}]$	carrier density	$D\ [cm^2/s]$	diffusion constant
n	number of elementary charges per carrier	$kT/e \approx 25$ mV	at room temperature
		$f \approx 4$	geometrical factor, including porosity, tortuosity, etc.
$b\ [cm^2/Vs]$	"physical" mobility		
$e = 1{,}601 \cdot 10^{-19}$ As			

To be exact, the Einstein equation applies only to conductors having equal mobilities b_+ and b_- of carriers of both signs. Here, H^+ and OH^- ions are involved, the mobilities of which differ considerably. However, only an estimate is necessary in the framework of this investigation, as become evident here below.

Inserting figures as follows:

$0{,}1 < D < 1$ cm^2/s valid for gases at room temperature under nearly atmospheric pressure

$N \approx 5{,}3 \cdot 10^{19}$ cm^{-3} { room temperature, pressure 2 kp/cm^2

$n = 1$; $e = 1{,}601 \cdot 10^{-19}$ As ; $f \approx 4$;

$kT/e = 25{,}3$ mV

we get $0{,}01 < \varrho_g < 0{,}1$ ohm·cm.

On the other hand, the ionic resistivity inside the working layer can be estimated easily, and, in addition, has been measured by Holthusen (11). Porosity is around 50 pct., and about 15 pct. thereof are filled with electrolyte, 6 n KCH at 60 °C. Taking into consideration a tortuosity factor of 1,5 , the final ionic resistivity can be calculated to $\varrho_i \approx 20$ ohm·cm. This result agrees well with Holthusens measurements.

When comparing gas and ionic resistivities, we find, that $\varrho_g \ll \varrho_i$. Thus, beneath electronic resistivity ϱ_e, also ϱ_g can be neglected.

Out of the theory of two-phase electrodes, we take

$$\theta(z^*) = \frac{a \cosh[\alpha S z^*] + c \cosh[\alpha S(1-z^*)]}{(a+c)\sinh[\alpha S]} \alpha S. \qquad \text{(eq.1)}$$

$a = \varrho_i/A$; $c = \varrho_g/A$; $\alpha^2 = (\varrho_i+\varrho_g)\varepsilon$; $\varepsilon = i/\psi$;

A [cm^2] area; ψ [mV] border overvoltage; i [mA/cm^2] current density.

Since equation 1 implies diffusion constant D and ion mobility b, we call Θ the "Special Transport Function" of this type of porous gas electrode. Because $\varrho_i > \varrho_g$ or $a > c$, the above written equation 1 can be simplified

$$\Theta_i(z^*) = \frac{\cosh\left[\sqrt{\varrho_i\varepsilon}\ S\ z\right]^*}{\sinh\left[\sqrt{\varrho_i\varepsilon}\ S\right]}\ \sqrt{\varrho_i\varepsilon}\ S, \qquad \text{(eq. 2a)}$$

or, introducing $C = \sqrt{\varrho_i\varepsilon}\ S$

$$\Theta_i(z^*) = \frac{C}{\sinh C}\ \cosh\left[C\ z^*\right], \qquad \text{(eq. 2b)}$$

the shape of this function being given in figure 2. $\Theta_i(z^*)$ is analogous to $\Theta(z^*)$ the approximative special transport function, neglecting gas resistance.

To let $\Theta(z^*)$ or $\Theta_i(z^*)$ become effective and evaluable, we have to introduce adequate values of boundary overvoltage ψ, or overvoltage parameter g, respectively. Under steady state conditions, i.e. a constant current density i flowing to or from the electrode, there may exist a factor of 10 or 100 between gas concentration (or activity) in the gas phase and electrolyte. Thus,

we are led to the conclusion, that a small "diffusion" potential ψ will occur across the boundary, similar to phenomena often observed on semiconductors. Using as approximation simply the Nernst equation $\psi = \frac{kT}{ze} \ln f_2/f_1$, wherein f_2 and f_1 devote the hydrogen activity within electrolyte and gas phase, respectively, we have to expect 15 to 60 mV in oxygen electrodes *), and 60 to 120 mV in hydrogen electrodes, respectively. Inserting current density i between 10 and 100 mA/cm^2, the range of possible values, in which $g = i/\psi$ must be comprised, is $0{,}1 < g < 10$. Figure 2 exhibits a set of special transport function, equation 2b, using as parameters $\varrho_i = 20$ ohm·cm, $0{,}1 < g < 10$, and electrode thickness S = 1 mm.

§ 4 Statistical Distribution of Active Sites

With the special transport function $\Theta(z^*)$, the porous electrode has been described as homogeneous and isotropic continuum. The active sites, or, in other words, working grains of incorporated catalyst are supposed to be evenly distributed, and its activity shall not depend on z^*. From observations made at a great number of electrodes, we know, that there exists a certain statistic distribution $Y(z^*)$ of active sites, depending on grain density statistics, grain size statistics, spatial distribution of active procedure, flooding of pores and on poisoning after a prolonged period of work. However, in general $Y(z^*)$ may

*) depending on electrode mechanism, i.e. reversible oxygen electrode, or formation of H_2^-

be regarded as even, $Y_o(z^*) \approx 1$. This approximation holds fairly well during the first year of use under rated load. Later on, expressions like $Y_t(z^*) \approx 1 - (mz^*)^q$, therein m depending on time, $0 < m < 1$, and $q > 1$, fit better. To avoid unadequate mathematical difficulties, we limit the study here to the behaviour of electrodes having active sites evenly distributed, $Y(z^*) = Y_o(z^*) \approx 1$.

§ 5 Current Distribution in a Single Pore

More than 100 years ago, already Sir Grove (1), had some insight into the import role of the tri-phase boundary as current generating zone of gas electodes. However, not earlier than during the past years, several authors tried to solve the problem of current conversion spatial distribution in these tri-phase zones, see for instance (3,4,5 and 6). The resulting distribution functions $\Phi(v)$ are with respect to a co-ordinate v along the single pore, or perpendicular to a single conversion zone.*) The origin v has to be imagined in the top of the meniscus, or simply centered to each individual conversion zone. z^* (or z) and v include an angle ψ depending on the geometrical situation of each site, see figure 3.

*) This treatment is not restricted to "pore" geometry, but can be easily applied to every geometry, just inserting as d the characteristic distance.

The distribution ϕ (v) depends considerably on geometrical and physical assumptions, e.g. pore or film geometry, gas diffusion across liquid or solid phase, surface migration of gas atoms, creeping of electrolyte, electrochemical reaction, rate determining step, nature of wastes formed etc. However, as global characteristics, the simple rule can be regarded as generally valid in nearly all cases, that ϕ (v) differs from zero only in a small interval $\pm \Delta$ v on both sides of the co-ordinate origin, and Δ v being comparable to the characteristic "pore diameter" d. Consequently, each individual conversion site can approximately be treated as a small differential volume, perhaps as small cube or sphere, the diameter s of which is a little bit larger than the pore diameter d. In our special case, d is of the order of magnitude of 30 /um, and therefore small when compared with electrode thickness S.

§ 6 Combination of Θ, Y and ϕ

Combining the aforementioned distributions, we get for <u>one</u> single conversion site

$$dJ/J = \Theta(z^*)\ Y(z^*)\ \phi\ (v)\ dv. \qquad \text{(eq.3)}$$

Therein, ϕ (v) is the distribution inside a single site, $Y(z^*)$ represents the probability, that sites are

located in a certain depth interval from z^* to z^*+dz^*, and $\Theta(z^*)$ indicates the fraction dJ of the overall current J converted in the zone z^* to z^*+dz^*. Since the problem, in fact, is to indicate the conversion profile inside the whole working layer , we have to integrate equation 3, taking into consideration the angle φ between the co-ordinates v and z^*. However, we restricted ourselves to $Y = Y_o(z^*) \approx 1$ and to such electrodes, whose thickness $S > d$ allows to approximate the individual sites as small point-like spheres. Then the influence of Φ and φ degenerates simply to a factor, which furthermore can be taken into account by normalizing the distribution with respect to the current J of the entire electrode. Thus, we get finally the spatial distribution of current conversion in the working layer of a semi-infinite, porous gas diffusion electrode

$$dJ(z^*)/J = \Theta_i(z^*)\, dz^* = \frac{C}{\sinh C} \cosh [C\, z^*]\, dz^*; \quad \text{(eq.4)}$$

Expression 4 do not depend on electrode area A, therefore dJ/J can be taken, at will, as current, or current density. In most practical cases, the columetric current load of the eletrode will be the favourized, because mostly obvious magnitude

$$\frac{di(z^*)}{i\, dz^*} = \frac{dJ(z^*)}{J\, dz^*} = \frac{C}{\sinh C} \cosh [C\, z^*]. \quad \text{(eq.5)}$$

to be measured in mA/cm^3.

§ 7 Penetration Depth

Since the current conversion in the electrodes under consideration is described by monotonous functions without maxima or minima, it may be useful, to define a penetration depth in the absolute z-scale

$$\cosh\left[\sqrt{\varrho_i g}(S-\tau)\right] = \frac{1}{e}\cosh\left[S\sqrt{\varrho_i g}\right],$$

e: basis of natural logarithms.

As easily event, this expression loses its sense, if $\cosh C < e$. Therefore, we let rise the electrode thickness S to very high values, than we are able to replace $\cosh[z \gg 1] \approx \frac{1}{2}\exp z$, and we get $\tau \approx -1/\sqrt{\varrho_i g}$. Table 1 contains calculated penetration depths in the ranges of g and ϱ_i here of interest.

Table 1 Penetration depth τ of conversion current in the working layer of a semi-infinite porous gas diffusion electrode, as function of boundary overvoltage parameter g and ionic resistivity ϱ_i.

g $(\text{ohm}^{-1}\,\text{cm}^{-3})$	specific ion resistivity ϱ_i (ohm·cm) 20	30	40	50	60	80
	penetration depth τ (mm)					
o,1	7,o2	5,73	4,95	4,45	4,o4	3,51
o,2	5,oo	4,o8	3,53	3,17	2,89	2,50
o,5	3,15	2,57	2,22	2,oo	1,82	1,58
1	2,25	1,84	1,59	1,42	1,3o	1,13
2	1,58	1,29	1,12	1,oo	o,91	o,79
5	1,oo	o,82	o,71	o,63	o,58	o,5o
1o	o,7o	o,57	o,5o	o,44	o,4o	o,35
2o	o,5o	o,41	o,35	o,32	o,29	o,25

In the working layer of manufactured sintered nickel electrodes penetration depth has been found between o,6 and o,9 mm. These results refer to electrodes of different design, both oxygen cathodes and hydrogen anodes, containing fine divided silver metal, and Raney nickel as catalysts, respectively. Having in mind, that under steady load the mean ion resistivity $\bar{\varrho}_i$ appears somewhat elevated above 20 ohm·cm*), the measured penetration depths agree fairly well with the results given in table 1. Consequently, the experimental range of g, has to be assumed to about $5 < g < 10$, i.e. the upper limit of the

*) see § 9.

range indicated in § 3. The reason probably for it, is, that the border overvoltage ψ really is somewhat lower, than evaluated from the normal Nernst equation. However, already Nernst (12) pointed out clearly, that "diffusion" potentials can be much lower, depending on the mobility quotient and on the sign of the second term within the brakes in a straight forward equation indicated also by Nernst:

$$\psi = - \frac{kT}{ne} \frac{b_+ - b_-}{b_+ + b_-} \left[\ln \frac{f_2}{f_1} + B(\sqrt{f_2} - \sqrt{f_1}) \right]. \qquad \text{(eq.5)}$$

wherein b_+ and b_- are the mobilities of positive and negative ions, f_1 and f_2 are hydrogen activities in the gas phase and the electrolyte, and B is a constant, the magnitude and sign of which depend on the mutual interaction of ion strength, activity factors, and electrophoresis. Assuming $b_+ = 33 \cdot 10^{-4}$ and $b_- = 18 \cdot 10^{-4}$ cm^2/Vs, the mobility quotient equals $\approx$ o,3 . When we approximate $B \approx 0$, then we finally find numerical values of ε up to 30 $ohm^{-1} cm^{-3}$.

§ 8 Carbon Electrodes

Instead of multiple hydrophilic layers having different porse size, gas phase and electrolyte can be throughout separated by impregnating uniform porous electrodes with electrolyte repellent agents. This is effected, preferably on carbon electrodes, by adding solid hydrocarbons, nitrobenzene, synthetic rubber, silicones, polyethylene (PE)

or even polytetrafluoro-ethylene (PTFE). Schumacher and Heise (13) showed already, that "hydrophobic" monolayer electrodes can be manufactured only either not completely electrolyte repellent but correctly working, or, on the other side, completely hydrophobic but not properly suited to their electrochemical duties.

During the past years, very thin triple layer carbon electrodes have been developed by Kordesch (14). These electrodes consist of a sintered nickel foil as substrate, about o,18 mm in thickness, and completely water repellent by addition of some PTFE. On this supporting sheet, a coarse carbon layer is sprayed, composed of 50 pct of carbon powder and 50 pct PTFE and PE. This inner, so-called "backing" carbon layer incorportes no catalyst. Its thickness is about o,25 mm. Finally, the electrode is covered by a third layer, consisting of 75 pct of carbon and 25 pct ~~PTFE~~ PTFE, having also about 2 mg/cm^2 of platinum black as catalyst. The thickness of this upper, so-called "active" carbon layer is about o,13 mm.

The large amounts of electrolyte repellent agents incorporated in the two under layers, holds them free of electrolyte.. However, in the upper layer, the PTFE acts preferably as binding agent and, therefore, this active layer is partly filled with electrolyte. This kind of

electrodes are designed for a very low gas pressure, less than o,1 kp/cm^2 gage. Therefore, already the very thin film of electrolyte, adherent to the outer surface of the electrode avoid gas losses.

In principle, multilayer, partly hydrophobic electrodes obey the same theory as hydrophilic two-layer arrangements. Only a thorough study of the parameters is required in those cases.

Since the active layer exhibit a thickness of no more than o.13 mm, we are led to the conclusion, that, in hydrophobic carbon electrodes ϱ_i and/or g must be higher, than in hydrophilic nickel sintered electrodes. In fact, both assumptions are reasonable. Electrolyte films on a partly repellent substraten often will be interrupted. Therefore, the main ion resitivity of the electrolyte network becomes substantially higher, than on hydrophilic materials. In carbon electrodes, the reaction gases are fed to the converting sites through very narrow slits and channels in the solid material rather than dissusion across liquid films. Thus, the activity between gas phase and electrolyte, in this type of electrode differs certainly less, than in hydrophilic ones. Consequently, the overvoltage ψ , as caused by this difference must be lower, $g \sim 1/\psi$ must be higher.

Thus, it seems likely, that gas restivity ϱ_g and electron resistivity ϱ_e remain small as compared to ion resistivity ϱ_i , $\varrho_e \ll \varrho_i$ and $\varrho_g \ll \varrho_i$. Since exact values of porosity, pore diameter, and fraction of pores filled have not been published, a quantitative comparison with the theory cannot yet be accomplished.

§ 9 Non-uniform Ion Resistivity

In a recent paper (15), it has been shown, that "strange"*) types of current distributions occur in porous electrodes, if ion and electron resistivities do not remain homogeneous, but depend on thickness co-ordinate z^* . Under steady state conditions, in hydrogen anodes water is formed, and in oxygen cathodes water is consumed. Thus, concentration profiles $K(z^*)$ occur, which influences ion conductivity. The "zero current" electrolyte exhibit nearly the ion resistivity minimum, and any change in concentration K will, therefore, cause an increase of ion resistance ρ_i. However, the exact concentration -and therefore also resistivity- profile is so far not yet known.

However, the influence of resistance profiles $\rho_i(z^*)$ can be studied without exact knowledge of their magnitude, simply by putting different oblique profiles into the electrical analogues. As a first series, we took linear concentration profiles $K(z^*)$:

$$K(z^*) = K_1 - K_2(1-z^*) \quad , \; z^* = z/S \qquad \text{(equ. 6a)}$$

having different constants K_2. In figure 4, the influence of three linear concentration profiles on current distribution is given.

*) i.e. distributions exhibiting a maximum inside the electrode, instead of a broad minimum as in "common" distributions

Table 2

Concentration profile parameters in figure 4

curve No. in fig.4	type of profile	KOH concentration $K(z^*)$ in pct. of weight at $z^* = 0$	at $z^* = 1$
(1)	const.	27	27
(2)	linear	13,5	27
(3)	linear	4,5	27
(4)	linear	o,27	27

In general the influence even of very steep concentration profiles is not very important. Therefore, figure 4 to 6 are given in a logarithmic scale. Indicated is the relative fraction of current converted in a thin sheet Δz = o,1 mm of the electrode, given in pct. of the entire electrode current. As become evident, the concentration profile lowers the current distribution near the gas side of the electrode, i.e. near $z \approx 0$. In other words, the penetration depth has been decreased.

In order to verify this result, as a second series, we also took some other ion resistivity profiles into the analogue. The result indicated in figure 5 does not differ considerably from the influence of linear concentration profiles, as is evident when comparing fig. 4 and 5.

Table 3

Concentration profiles of figure 5

curve No in fig.5	type of profile	KOH concentration $K(z^*)$ in pct.of weight at $z^* = 0$	at $z^* = 1$
(1)	const.	27	27
(2)	linear	4,5	27
(3)	exp.	4,5	27
(4)	tgh	o,5	26

Exponential and tgh profiles are given by

$$K(z^*) = K_1 \quad \exp\left[-K_2(1-z^*)\right] \qquad \text{(equ. 6 b)}$$

and

$$K(z^*) = \frac{K_1}{2} + K_3 \quad \text{tgh}\left[K_4\left(\frac{1}{2} - z^*\right)\right]. \qquad \text{(equ. 6 c)}$$

As main result, we can state, that concentration profiles in the electrolyte do not cause unusual distributions of the current conversion in porous triphase electrodes. Especially, "strange" distributions do not occur here.

§ 10 Non-uniform Overvoltage

In order to replenish the results, in figure 6 the influence of overvoltage profiles on current distribution in porous triphase electrodes is shown, either having

uniform ion resistivity (curve 2), either in combination with exponential concentration profiles (curve 3). Already in (14) it was explained, that overvoltage profiles influences the distribution of current conversion much less, than resistivity profiles do. The profile chosen here is very steep; a nine-fold increase of overvoltage over a distance of only 1 mm, is completely out of the range to be ever expected in manufactured electrodes. Therefore, it can be affirmed, that also in porous triphase electrodes, the influence of realistic overvoltage profiles remains small. Even taking steep overvoltage profiles into consideration, no uncommon distributions occur in those triphase electrodes under consideration.

Table 4

Concentration and overvoltage profiles in figure

curve No in fig.6	KOH concentration $K(z^*)$ (pct. of weight)			overvoltage (z^*) (relative units)		
	type of profile	at $z^*= 0$	at $z^*= 1$	type of profile	at $z^*= 0$	at $z^*= 1$
(1)	const.	27	27	const.	1	1
(2)	const.	27	27	linear	9	1
(3)	exp.	4,5*)	27	linear	9	1

*) the same concentration profile as curve (3) in figure 5

Conclusion

The treatment of current conversion and its distribution inside the working layer of porous gas electrodes -tri-phase electrodes- can be substantially simplified by reducing the problem to the much better known theory of porous electrodes. The only condition ist, that electron resistivity can be neglected, as it is the case for instance in all practical fuel cell electrodes. To realize this theory, gas supply can be characterized by a "gas resistivity" to be measured in electrical units.

The distribution of current conversion can be found out as the product of three main factors, the special transport function Θ, the current distribution in a single current generating site, and the site statistics. The first of these factors governs the conversion behaviour at least of sintered metal electrodes. As a principal result of the work reported here, following the rules mentioned above, monotonous distribution curves can be given. A penetration depth can be defined, having the order of several tenth of a millimeter. The results agree with practical experience. By introducing concentration and/or overvoltage profiles, the theory can be further developed. As special result, no "strange" distributions occur under these conditions.

Références :

1. R. Grove : On a Gaseous Voltaic Battery, Phil. Mag. 21 (1842) pp. 417 - 420

2. L. G. Austin : Fuel Cells, NASA S P - 120, Washington, D. C., pp. 303 - 321, 1967

3. A. Borucka and J. N. Agar : An Electric Analogue for Meniscus Gas Electrodes, Electrochimica Acta 11 (1966) pp. 603-624

4. E. Justi and A. Winsel : Kalte Verbrennung - Fuel Cells, Franz-Steiner-Verlag, Wiesbaden, 1962, pp. 88 - 94

5. A. Winsel : Statistisches Modell einer Gasdiffusionselektrode, Advanced Energy Conversion 3 (1965) pp. 677 - 708 and 5 (1965)pp.173-181

6. F. G. Will : Electrochemical Oxydation of Hydrogen on Partially Immersed Platinum Electrodes, Journ. Electrochem. Soc. 110 (1963) pp. 145 - 151

7. M. Bonnemay, C. Bernard, G. Bronoël, D. Doniat, E. Levart, G. Pesleerbe et A. A. Pilla : Etude expérimentale des électrodes poreuses. Les piles à combustible, ouvrage collectif, Paris 1965, p. 103 à 125

8. R. Buvet : Origine des phénomènes de polarisation dans les électrodes poreuses. Les piles à combustible, ouvrage collectif, Paris 1965, p. 27 à 46

9. I. Gurevich and V. S. Bagotskij: Porous-Electrode Polarization, Electrochimica Acta 12 (1967) pp. 593 - 614

10. H. Holthusen: Untersuchungen über Knallgaszellen in Eloflux-Anordnung, Diploma Thesis, Technical University Braunschweig, Fed. Rep. Germany, Dec. 15, 1966, to be published soon

11. see for instance J. Euler and W. Nonnenmacher: Stromverteilung in porösen Elektroden, Electrochimica Acta 2 (1960) pp. 268 - 286

12. W. Nernst: Über die elektromotorische Wirkung der Ionen, Z. f. physikalische Chemie 4 (1889) pp. 129 - 181

13. E. A. Schumacher and G. H. Heise: The Alkaline Cell with Copper Oxide or Air Depolarization, Journ. Electrochem. Soc. 99 (1952) pp. 191 C - 196 C

14. K. Kordesch: Thin Carbon Electrodes, Proc. 21st Annual Power Sources Conference, Fort Monmouth 1967, pp. 14 - 16

15. K. J. Euler: Anomale Verteilung der Stromkonversion im Inneren poröser Zweiphasenelektroden, Electrochimica Acta, under press

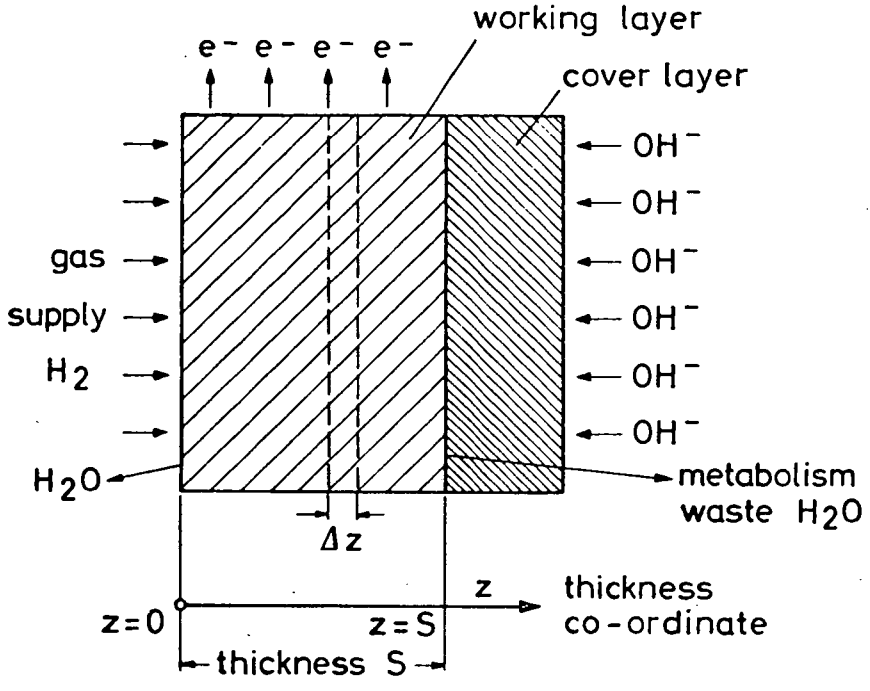

Figure 1

Geometry of the semi- infinite porous double layer electrode investigated here.

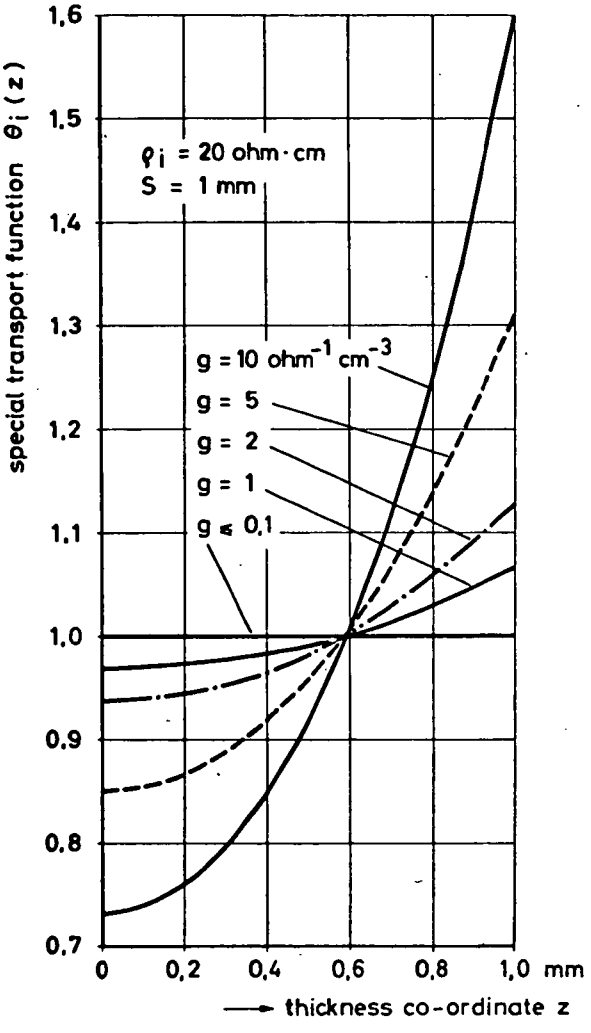

Figure 2

Shape of special transport functions $\Theta_i(z^*)$ in working layers of porous gas electrodes, equation 2 a or 2 b.

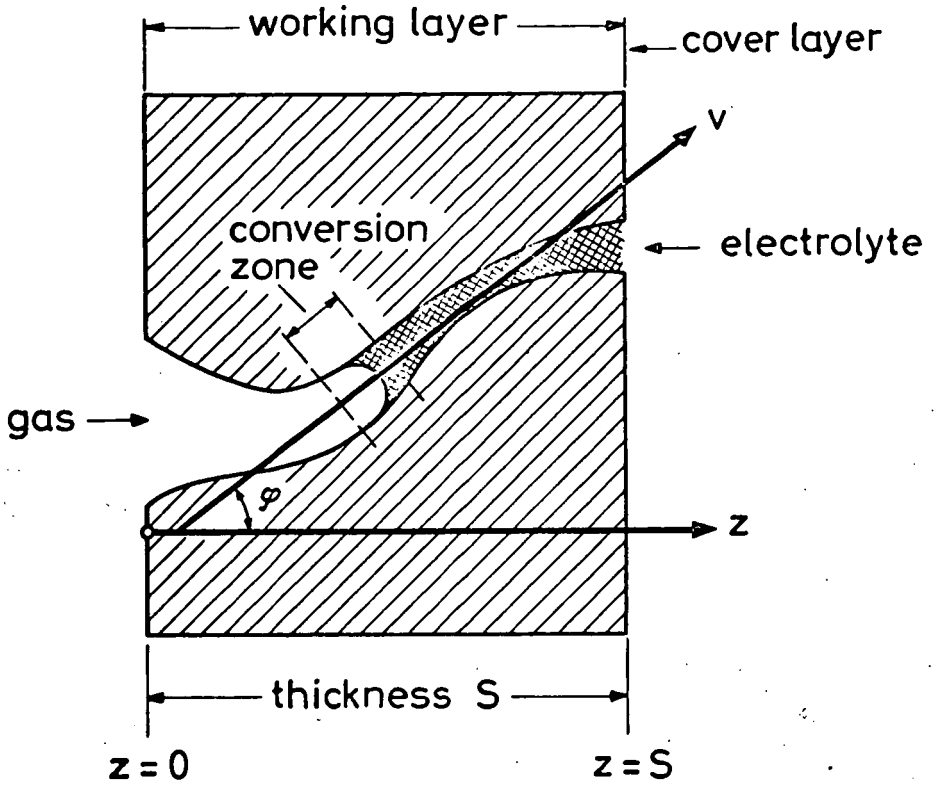

Figure 3

Relations between electrode co-ordinate z and individual site co-ordinate v. $z^* = z/S$.

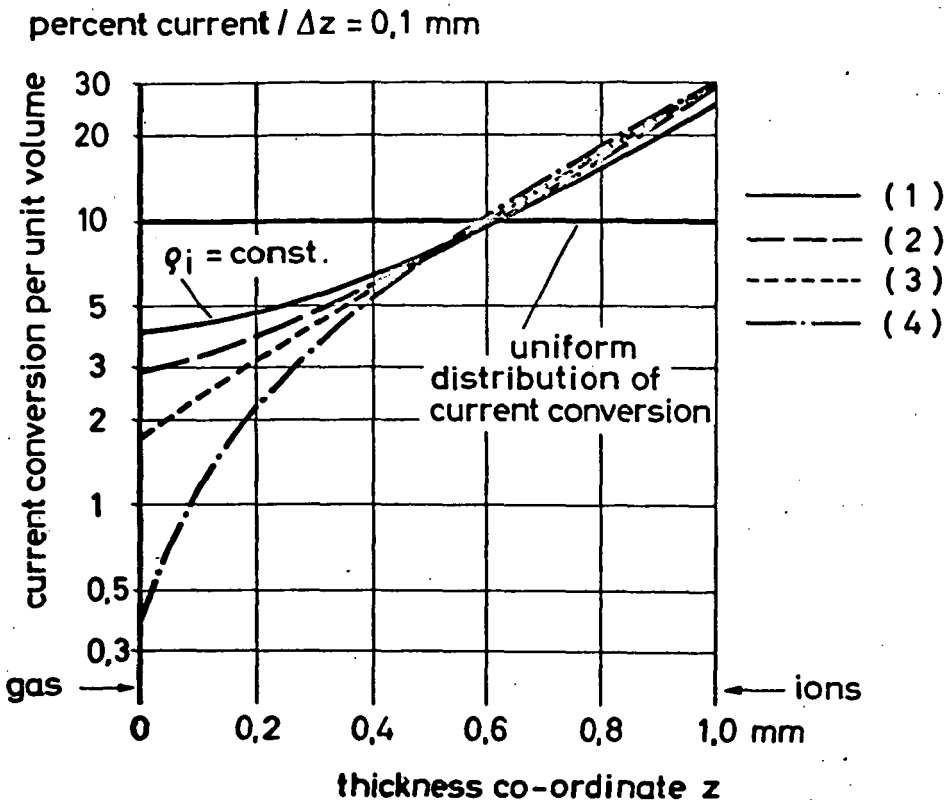

Figure 4

Influence of linear concentration profiles K(z) on current distribution in porous triphase electrodes. Thickness of working layer S = 1 mm, overvoltage parameter g = 10 $ohm^{-1}cm^{-3}$. Concentration profile parameters are given in table 2.

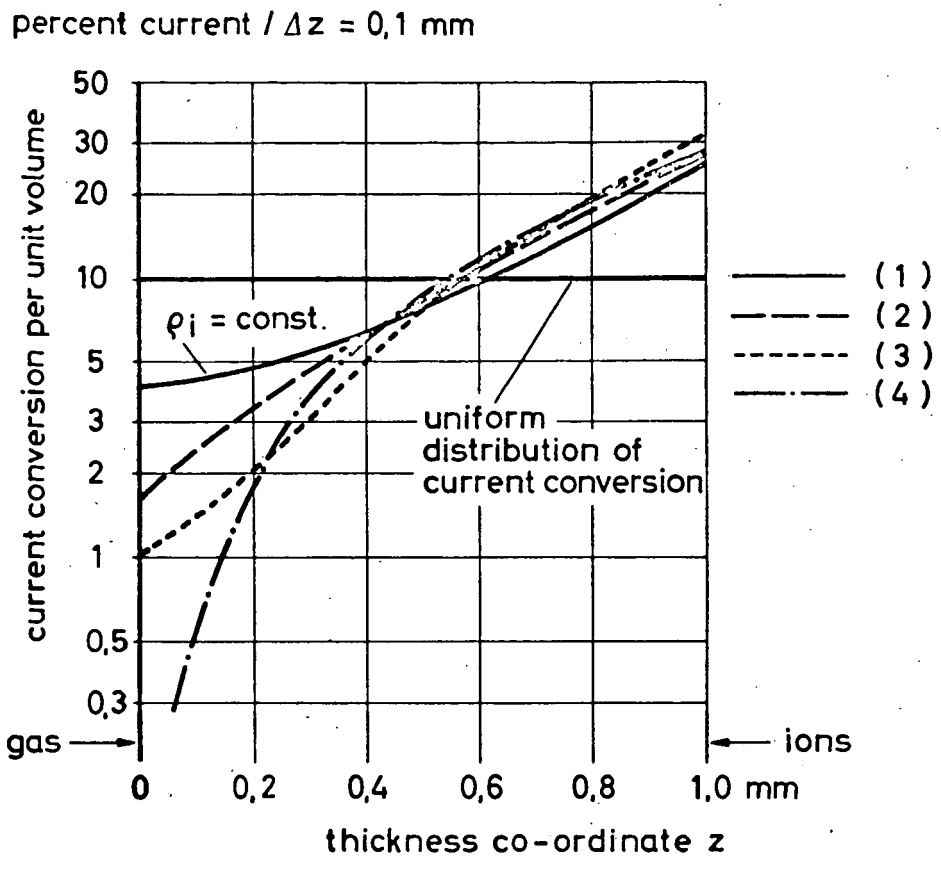

Figure 5

Influence of different shape of the concentration profile K(z) on current distribution in porous triphase electrodes. Thickness of working layer S = 1 mm, overvoltage parameter ε = 10 $ohm^{-1}cm^{-3}$. Concentration profiles are given in table 3.

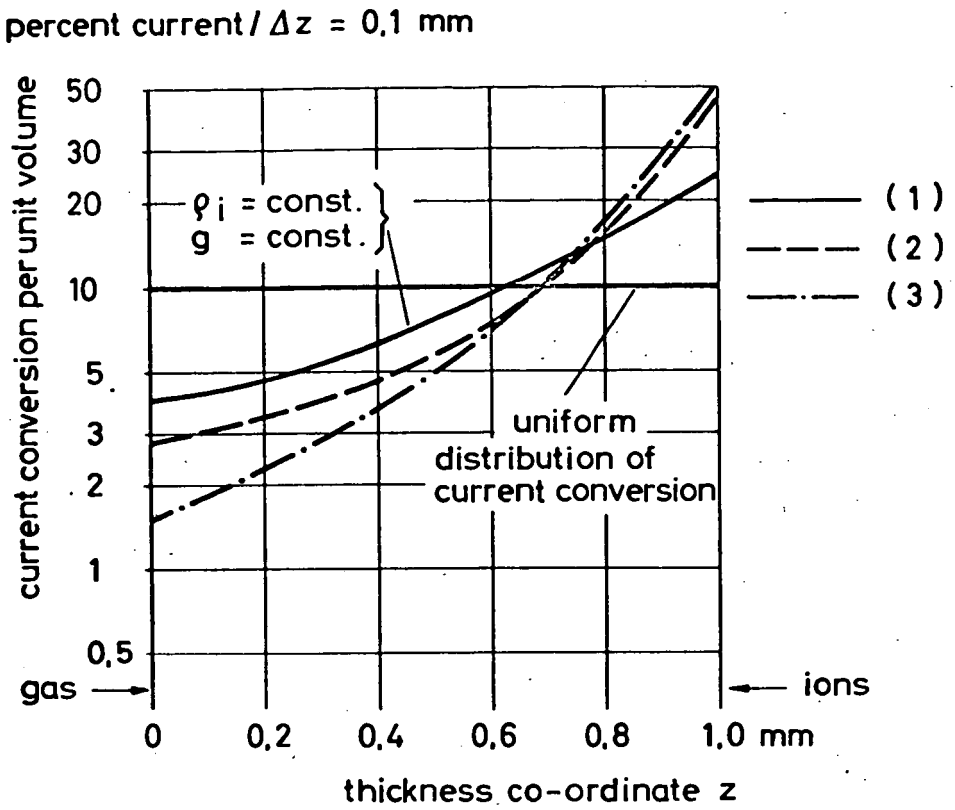

Figure 6

Influence of a linear overvoltage profile $\psi(z)$ on current distribution in porous triphase electrodes. Thickness of working layer S = 1 mm, parameters indicated in table 4.

ADSORBED RESIDUES FROM FORMIC ACID AND FORMATE ION GENERATED UNDER STEADY-STATE POTENTIOSTATIC CONDITIONS

Sigmund Schuldiner and Bernard J. Piersma*
Naval Research Laboratory, Washington, D. C. 20390

INTRODUCTION

When a clean platinum electrode is exposed under open circuit conditions to formic acid or sodium formate solutions there is a rapid dehydrogenation reaction followed by a much slower interaction of adsorbed H atoms with formic acid or formate ions to give molecular hydrogen and free radicals (1, 2). The free radicals formed by this reaction and by the initial dehydrogenation reactions interact with the surface and each other to form residues which then hinder further dehydrogenation. Upon potentiostating the Pt electrode, one would expect that any atomic hydrogen formed by dehydrogenation would be readily oxidized. A previous steady-state potentiostatic study (3) on the anodic oxidation of formic acid and hydrogen in formic acid and formic acid + sulfuric acid mixtures showed that even though the initial rates of oxidation for formic acid and hydrogen in such solutions could be quite high, there is a gradual decrease in rates until at steady-state, the reaction rates would be considerably reduced. Evidently, the formation of free radicals also occurs under potentiostatic conditions and the resulting residue can affect the rates of oxidation of both formate species and hydrogen.

* Permanent address, Eastern Baptist College, St. Davids, Pa.

The present investigation was for the purpose of determining the steady-state potential vs. coverage relationship of the organic residue on Pt in formic acid and formate ion solutions, both under helium and hydrogen saturated conditions. The amount of residue was determined by a high current density anodic galvanostatic pulse. Such charging curves show an increase in the number of $\mu coul/cm^2$ required to form a monolayer of adsorbed oxygen atoms on the surface of the Pt electrode ($Pt\text{-}O_{ad}$). This increase beyond the 420 + 36 $\mu coul/cm^2$ required to form a monolayer of $Pt\text{-}O_{ad}$ on a clean Pt electrode plus double layer charging, respectively (4) was attributed to oxidation of the organic residue on the electrode. Such measurements only show the number of coulombs of charge required to oxidize adsorbed organic material plus water. Unreactable species on the surface may not be oxidized by the anodic galvanostatic pulse, but may be desorbed. Unreactable species which are chemisorbed may cause an increase in overvoltage for the formation of oxygen atoms. Because of the complexity of interpretation of the anodic charging curves and because qualitative identification of the organic residues or of the oxidized or desorbed products is an extremely difficult problem in itself, it is not possible, at the present time, to associate the amount of charge actually determined by this technique to specific reactants, reactions, or products. Therefore, in such a case the use of such terms as degree of surface coverage have little real meaning. Hence, in this study the number of electrons generated in the atomic oxygen adsorption region (from ~0.9 to 1.8 v), after subtracting the monolayer contribution due to $Pt\text{-}O_{ad}$ + double

layer, is expressed as q_{org} and solely represents the amount of charge used to remove the organic species adsorbed on the Pt surface at specific, steady-state anodic potentials.

EXPERIMENTAL

The solutions investigated were: (a) 1 M HCOOH + 1 M H_2SO_4 (pH $\approx$ 0), (b) 1 M HCOOH + 1 M HCOONa (pH = 3.5), and (c) 1 M HCOONa (pH = 7.9). The formic acid was reagent grade, the H_2SO_4 was ultrapure (E. Merck, Darmstadt). Measurements were made in both helium- and hydrogen-saturated solutions (see ref. 2 for details of experimental techniques). The Pt working electrode potentials were controlled with a Wenking 61RS potentiostat, galvanostatic pulses (1-2 amp/cm^2) were applied with either an Electro-Pulse 3450C or 3450D pulse generator and traces were photographed from a Tektronix 547 oscilloscope with a 1A1 plug-in. The circuitry used and the fast switching between potentiostatic and galvanostatic control were as previously described (5).

The time required to reach steady-state conditions, in most cases, required at least 14 hours. Fig. 1 gives two examples of the q_{org} relation with time. Curve (a) for the 0.1 M HCOOH + 1 M H_2SO_4 in H_2-saturated solution is the only data obtained for this solution. Even though, in many cases, there was little change in q_{org} within the first 5 minutes, the steady-state values after a sufficient length of time showed considerably larger amounts of charge were required to remove the organic residue which slowly formed on the surface.

All potentials are referred to the reversible hydrogen electrode in the same solution (RHE). The temperature was 25 ±1°C.

RESULTS

Steady-state, potentiostatic polarization curves for formic acid and formic acid + sulfuric acid mixtures were published previously (3). Fig. 2 and 3 show the polarization behavior for 1 M HCOOH + 1 M HCOONa and 1 M HCOONa solutions. Both curves show hysteresis effects similar to those in other formic acid solutions (3). There are some important differences, however. In the 1 M HCOOH + 1 M HCOONa (He-saturated) solution (Fig. 2), on the decreasing potential arm, the current densities extend beyond the values found for the increasing potential arm at potentials of about 1.0 v. In the 1 M HCOONa solution (Fig. 3), there is a similar increase in current densities for decreasing potentials in H_2-saturated solution which extends from 1.0 to 0.1 v.

Fig. 2 shows a passivation effect for both He-and H_2-saturated 1 M HCOOH + 1 M HCOONa at about 1.4 v. This is well above the potential water can be oxidized to form Pt-O_{ad}. Fig. 2 further shows that in the presence of an oxidizable anion passivation does not occur at the relatively low potentials (vs. RHE) found in solutions containing inert anions (3, 6, 7). A slight passivation effect in He saturated 1 M HCOONa (Fig. 3) occurs at about 1.5 v but this also is well above the potential at which water can be oxidized

to form Pt-O_{ad}. In H_2-saturated 1 M HCOONa there is a slight decrease in oxidation rate at potentials positive to 1.0 v and a marked activation on the decreasing potential arm starting at about the same potential. However, these effects clearly show that the formation of oxygen species on Pt do not affect the retardation of the oxidation of formic acid or formate ion below 1.4 v. This verifies previous conclusions (3, 6, 7) that passivation effects in the presence of easily oxidized hydrogen or organic species is not due to the formation of oxygen species from water which retard the oxidation of H_2 and/or formates.

Fig. 4, 5, and 6 show the effects of the steady-state, potentiostatic adsorbed residue found in formic acid and formate ion solutions. The q_{org} values in Fig. 4, 1 M HCOOH + 1 M H_2SO_4 in both He and H_2-saturated solution, start at about 450 μcoul/cm^2 at open-circuit and go to maximums of about 525 to 575 at 0.5 v. If one would assume a monolayer coverage of the residue, then a little over two electrons per Pt site (210 μcoul/cm^2 = 1 electron per Pt site) would be required to oxidize the residue. Contrasting these results with those of Breiter (8), Brummer and Makrides (9), Brummer (10), Minakshisandaram et al. (11), and Urbach and Smith (12), the amount of charge required to strip the adsorbed residue is more than twice the amount found by those investigators. It should be remembered, however, that we have measured the steady-state values, and as can be seen in Fig. 1, this can be about twice the values found for the coverages at the short adsorption times used in references (8-12). In addition, although the general shape of the curves in Fig. 4 are similar to those in (8-11), the details are quite different. For example, instead of the plateau found (8-11)

a linear increase in q_{org} with potential up to a maximum at about 0.5 v was found. The drop in q_{org} was also less abrupt. It is obvious that the residue formed under steady-state conditions is quite different from the one adsorbed on the surface after only short times. The adsorption results of Urbach and Smith (12) showed peaks at about 0.2 and 0.8 v and were different from the results of other workers (8-11) and to those shown here. However, Urbach and Smith determined coverage from radiometric measurements of tagged formic acid and were, in fact, determining the concentration of adsorbed tagged carbon rather than the concentration of adsorbed oxidizable species. It is possible also that the differences found by the various workers are due to the differences in the constantly changing composition of the surface species. This can be seen from Fig. 1, curve (a) where the initial 2.5 to 5 minute results gave q_{org} of 140 to 180 μcoul/cm^2 or, on the basis of 210 μcoul/cm^2 for fraction of surface coverage, $\theta = 1$, a θ of about 0.7 to 0.9 is obtained.

The q_{org} found in 1 M HCOOH + 1 M HCOONa in He- and H_2-saturated solutions are shown in Fig. 5. In H_2-saturated solution the relationship between q_{org} and potential is similar to the sulfuric acid case (Fig. 4) except that the drop in q_{org} is less at potentials above 0.5 v. In He-saturated solution, however, the character of the residue must be quite different since the q_{org} runs considerably higher than in sulfuric acid solutions. In this case q_{org} runs as high as 775 μcoul/cm^2 or about 3.7 electrons per Pt site. Such a high value of q_{org} appears to indicate that the organic residue which

is oxidized consists of complex molecules with oxidizable sites which extend several atomic distances away from the surface.

The complexity of the potential vs. q_{org} relation shown in Fig. 6 makes analysis virtually impossible. There are some similarities between the peaks and valleys for the He- and H_2-saturated solutions, but the most obvious difference is the fact that in He-saturated solution the adsorption behavior is both more complex and q_{org} can rise to substantially higher peak values. The 0.95 v value of 925 μcoul/cm^2 is equivalent to 4.4 electrons per Pt atom.

DISCUSSION

The most obvious effect of hydrogen in the solutions investigated is that the measured q_{org} is substantially lower at essentially all potentials. In H_2-saturated solutions, the open-circuit potentials were the equilibrium hydrogen potentials, even though the charging curves taken under steady-state conditions showed no visible hydrogen oxidation region. It appears that the trace amounts of hydrogen present on the electrode were sufficient to maintain the equilibrium hydrogen reaction at open-circuit (2). Some of the hydrogen from the H_2 can associate with the surface and/or organic residue on the surface affecting the structure and composition of this residue. Previously reported work (13) has indicated that atomic hydrogen at potentials negative to 0.3 v can interact with CO_2 which then prevents oxidation of this hydrogen at potentials below 0.9 v with a high amplitude galvanostatic pulse.

The interaction of hydrogen with formic acid and formate ion is much more complex, but it is apparent that the presence of hydrogen does affect the character of the steady-state organic residue.

Another factor which apparently also has a strong effect on the character of the organic residue is the pH. This can be especially seen for the He-saturated solutions shown in Fig. 4, 5, and 6 where the interfering effect of hydrogen is minimized. At potentials below 0.7 v, q_{org} decreases as the pH increases. This indicates that the structure of the adsorbed organic residue is in a higher oxidation state as the pH increases. This and the fact that the pH 7.9, 1 M HCOONa solution (Fig. 6) is more sensitive to potential indicates that in the more alkaline solution the adsorbed species may be more in the nature of adsorbed anions or simple dipoles rather than complex molecules. The lower pH adsorption is less dependent on potential and significant desorption does not occur below 0.5 v.

Further evidence for the pH effect on the structure can be seen from the He-saturated potentiostatic polarization curves shown in Fig. 2 and 3. The higher pH results (Fig. 3) show a limiting current density at 2.5×10^{-5} amp/cm^2 from 0.7 to about 1.2 v followed by a range of increasing oxidation rates with increasing potential. The hysteresis effect in the decreasing potential arm is relatively small. This and the data in Fig. 6 (which shows a strong coverage dependence on potential) indicates that the oxidation of formate ion itself is rate-determining and is not limited by the

amount or character of the organic residue on the surface. At potentials above 1.2 v, the surface is essentially free of the organic residue and the rate of oxidation gradually increases as the potential is increased to about 1.5 v. This implies that the oxidation mechanism of formate gradually changes at about 1.2 v. Perhaps, a mechanism involving a water oxidation intermediate has some affect on the reaction rate at potentials above 1.2 v.

In Fig. 3 there really is no pronounced passivation on the increasing potential arm for the He-saturated solution. It also is significant that in H_2 saturated solution, the organic residue only slightly passivates the H_2 oxidation component to the oxidation rate of the formate itself on the increasing potential arm above 1.0 v. In fact, there only is a little difference between the H_2- and He-saturated solutions from 0.7 to 1.6 v on the increasing potential arm. On the other hand, for the decreasing potential arm there is a significant activation effect which reaches a maximum at 0.7 v. The hysteresis at potentials below 1.0 v in H_2-saturated solution show increased activity for hydrogen oxidation. This and the decreasing potential increased activity shown in Fig. 2 are the first times such increases have been noted in the various formic acid, formate, sulfuric acid, and alkali solutions investigated here. Although these points were repeatedly checked and critical points kept potentiostated at a given value for three to four days, it is likely that very slow changes in reaction rate may still be occurring and that eventually a return to the values on the potential increasing curve would be obtained. It is difficult to see how this could be otherwise.

Contrasting the behavior in 1 M HCOONa with that in 1 M HCOOH + 1 M HCOONa (Fig. 2) important differences are noticeable. In the first place, Fig. 2 shows little difference in the behavior in He-and H_2-saturated solutions except in the potential range from open circuit to about 0.9 v. At lower potentials the current densities are higher in the presence of H_2. The increased reaction rates for both the data shown in Fig. 2 and 3 are due to the contribution of H_2 oxidation which is faster in this potential range than is the oxidation of formate species. The fact that the net oxidation rate in Fig. 2 reaches a peak of about 7×10^{-3} amp/cm^2 at about 1.4 v is of interest because this rate of oxidation is 3.5 times faster than the maximum rate of oxidation of hydrogen in sulfuric acid solution (6). The pronounced passivation which occurs at higher potentials can be explained by adsorbed oxygen atoms generated by the oxidation of water. The marked hysteresis for the decreasing potential arm indicates the strong effect of dermasorbed oxygen atoms on the reaction rates.

CONCLUSIONS

A limitation to the use of organic fuels for low temperature fuel cell applications is the formation of organic residues primarily from the free radicals which are generated at the surface. To better understand these residues it is necessary to study their formation, to characterize their electrochemical behavior, and to determine their chemical composition. Transient electrochemical studies which primarily avoid the effects of these

residues and which deal only with the reactions of the original species in solution on a clean electrode must be carried out on rigorously controlled surfaces characterized in a meaningful way. The rates of the various processes occurring on a clean surface may be controlled and separated in certain instances. However, the character of the surface is constantly changing and of real import from both a fundamental and practical viewpoint is the steady-state behavior.

The work reported here shows that at low polarization potentials the rates of fuel oxidation are strongly retarded by the organic residues formed on the surface. This most likely occurs by removing sites at which dehydrogenation of the organic material can take place (2). Dehydrogenation appears to be the desired process which can produce easily oxidizable H atoms which are the effective fuel at low polarization. It appears that oxidation of carbon itself can readily occur at higher potentials, but this reaction would be of no obvious value for fuel cell operation. Dissociation of organic fuels to atomic hydrogen also implies that full low temperature oxidation of the fuel to CO_2 and H_2O would not be practicable in many cases, and that a large part of the chemical energy of the fuel could not be utilized in the generation of electricity.

Some degree of control of the organic residue results from the presence of molecular hydrogen and by changing the pH. Both increased pH and hydrogen lower the number of coulombs of charge required to oxidize the organic residue and allow higher anodic current densities at low polarization potentials.

Activation of a Pt electrode by anodic charging appears to have long-time effects on increasing the rate of fuel oxidation. This effect is most pronounced in H_2-saturated 1 M HCOONa.

REFERENCES

1. J. Fahrenfort, L. L. Van Reyen, and W. M. H. Sachtler, in "The Mechanisms of Heterogeneous Catalysis" ed by J. H. de Boer, pp. 23-48, Elsevier, Amsterdam, 1960.
2. S. Schuldiner and B. J. Piersma, J. Catalysis. ___, ,(1969)
3. S. Schuldiner, J. Electrochem. Soc., ___, ,(1969)
4. S. Schuldiner and R. M. Roe, J. Electrochem. Soc. 110, 332 (1963).
5. T. B. Warner and S. Schuldiner, J. Electrochem. Soc. 114, 359 (1967).
6. S. Schuldiner, J. Electrochem. Soc. 115, 362 (1968).
7. S. Schuldiner, J. Electrochem. Soc. 115, 897 (1968).
8. M. W. Breiter, Electrochim. Acta 8, 457 (1963).
9. S. B. Brummer and A. C. Makrides, J. Phys. Chem. 68, 1448 (1964).
10. S. B. Brummer, J. Phys. Chem. 69, 562 (1965).
11. N. Minakshisandaram, Yu. B. Vasil'ev, and V. S. Bagotskii, Elektrokimya 3, 193 (1967)
12. H. B. Urbach and R. E. Smith, submitted to J. Phys. Chem.
13. B. J. Piersma, T. B. Warner, and S. Schuldiner, J. Electrochem. Soc. 113, 841 (1966).

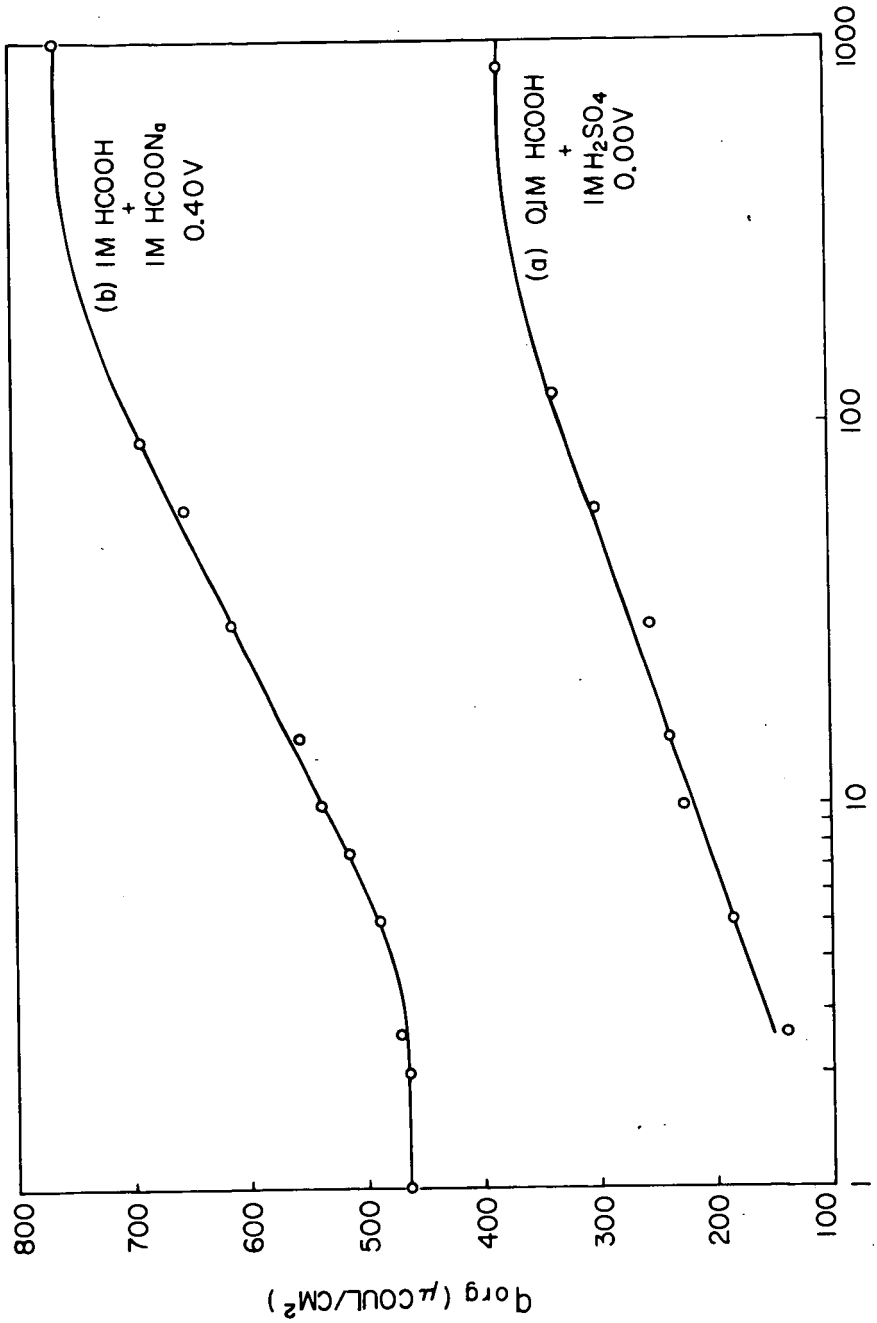

Fig. 1. Typical build-up of organic residue with time.

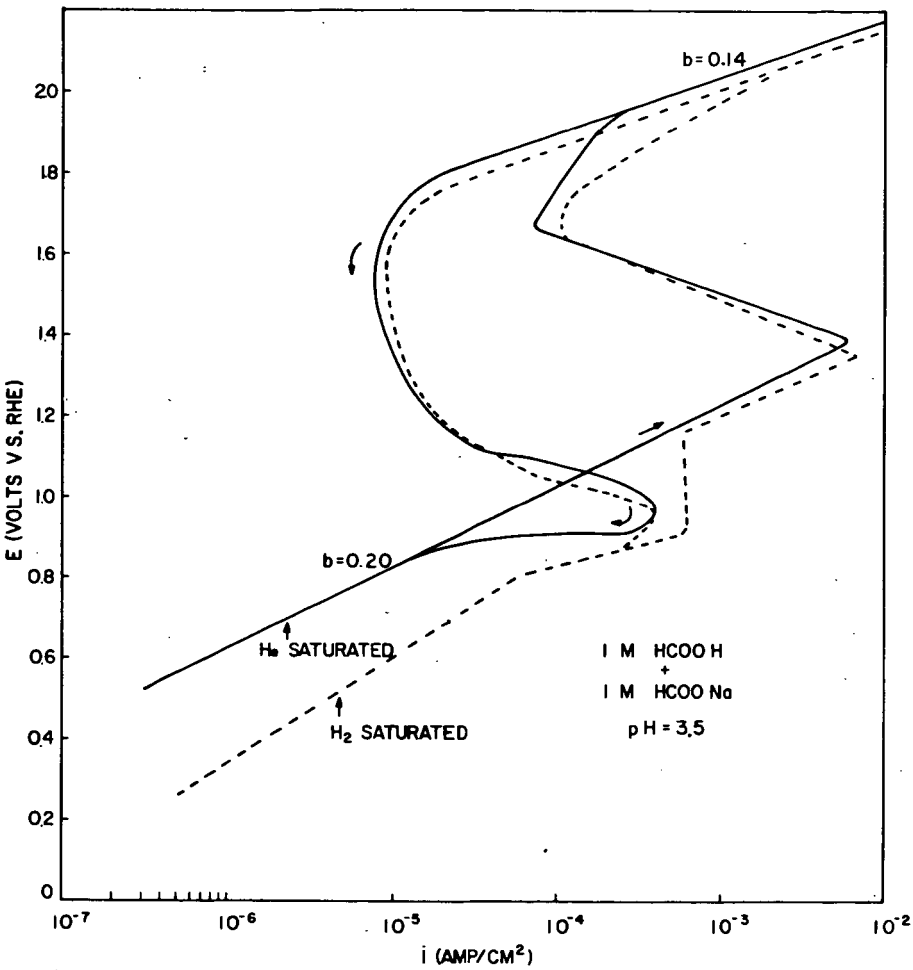

Fig. 2. Steady-state potentiostatic current density vs. potential relation in 1 M HCOOH + 1 M HCOONa.

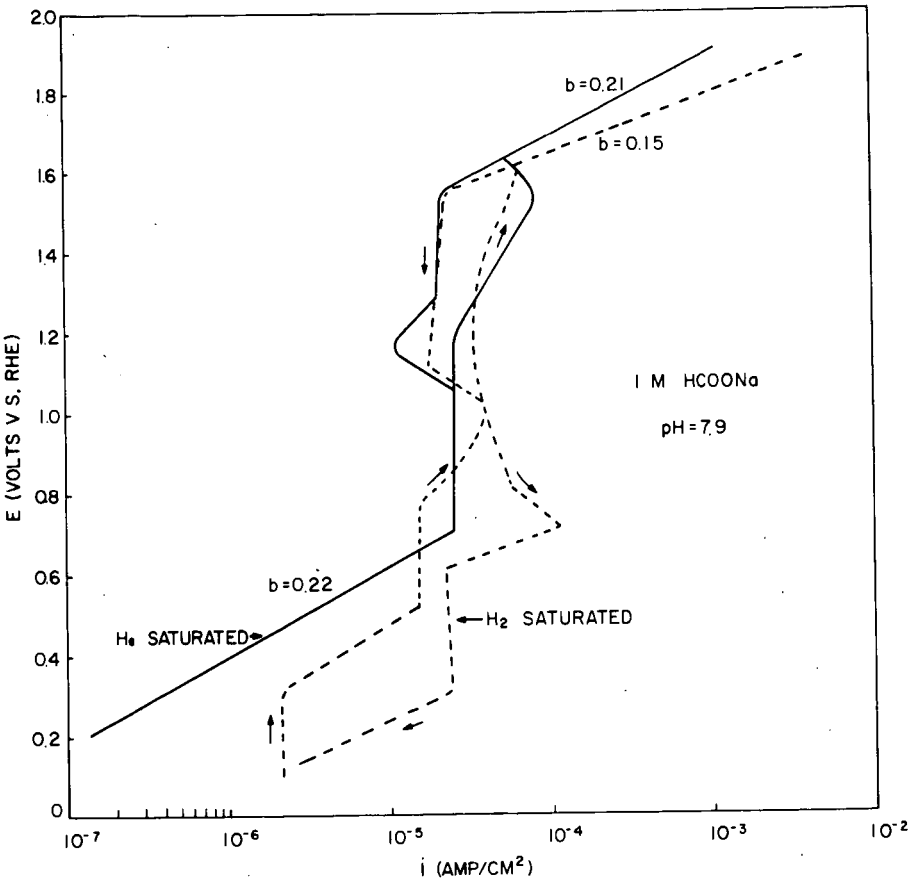

Fig. 3. Steady-state potentiostatic current density vs. potential relation in 1 M HCOONa.

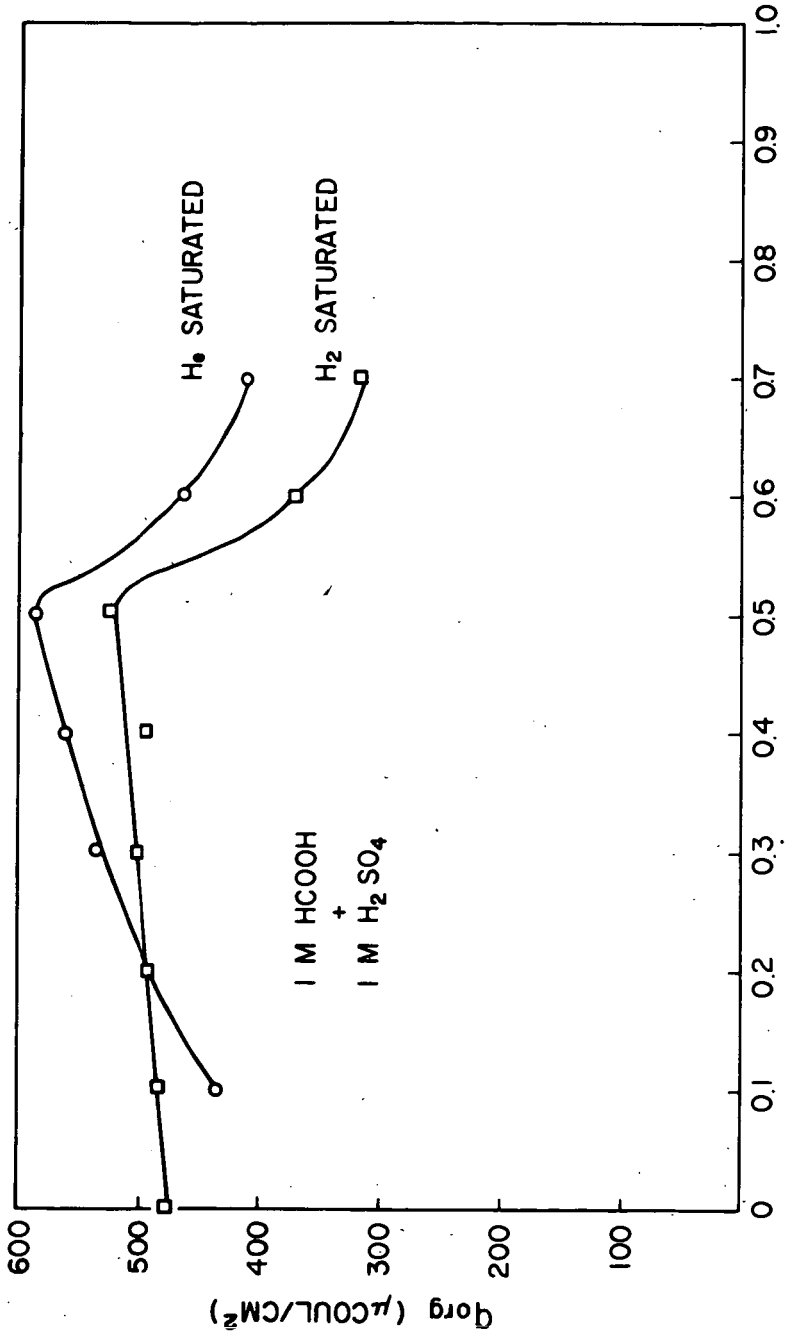

Fig. 4. Steady-state dependence of amount of charge, q_{org}, required to oxidize organic residue at set potentials; 1 M HCOOH + 1 M H_2SO_4.

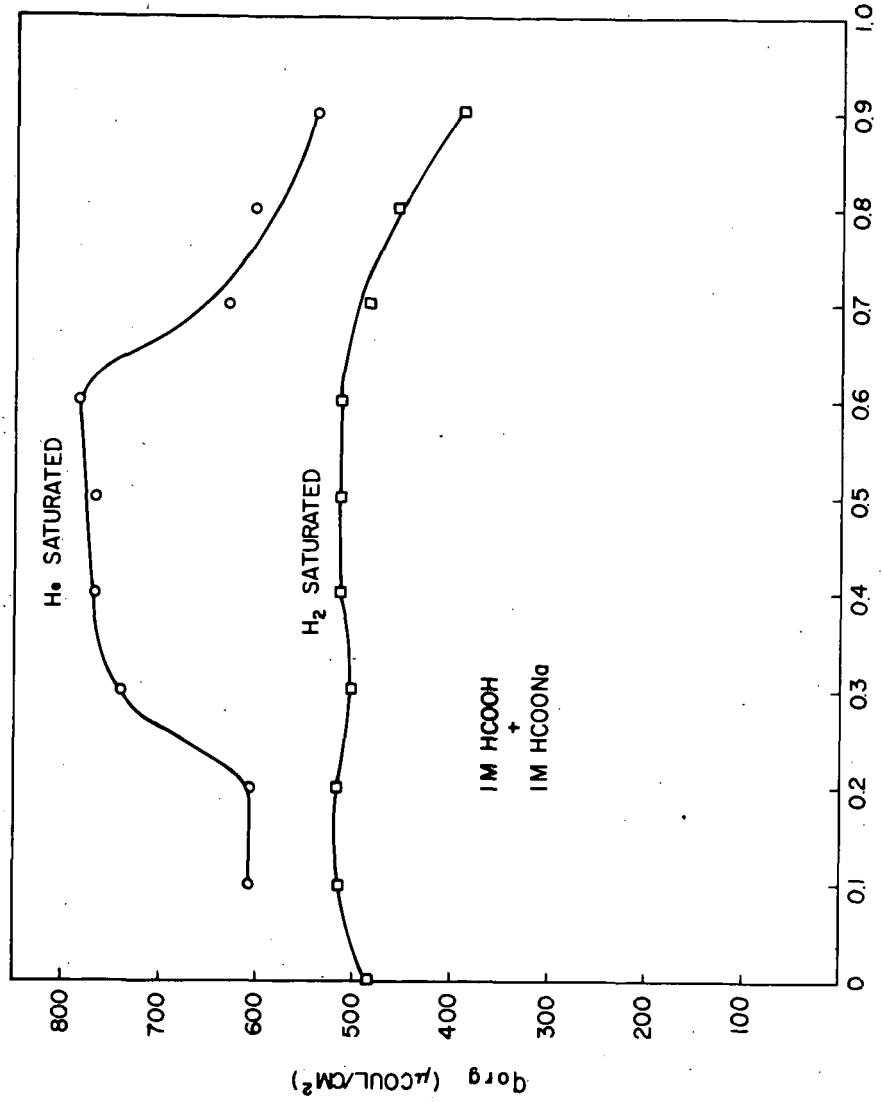

Fig. 5. Steady-state dependence of amount of charge, q_{org}, required to oxidize organic residue at set potentials; 1 M HCOOH + 1 M HCOONa.

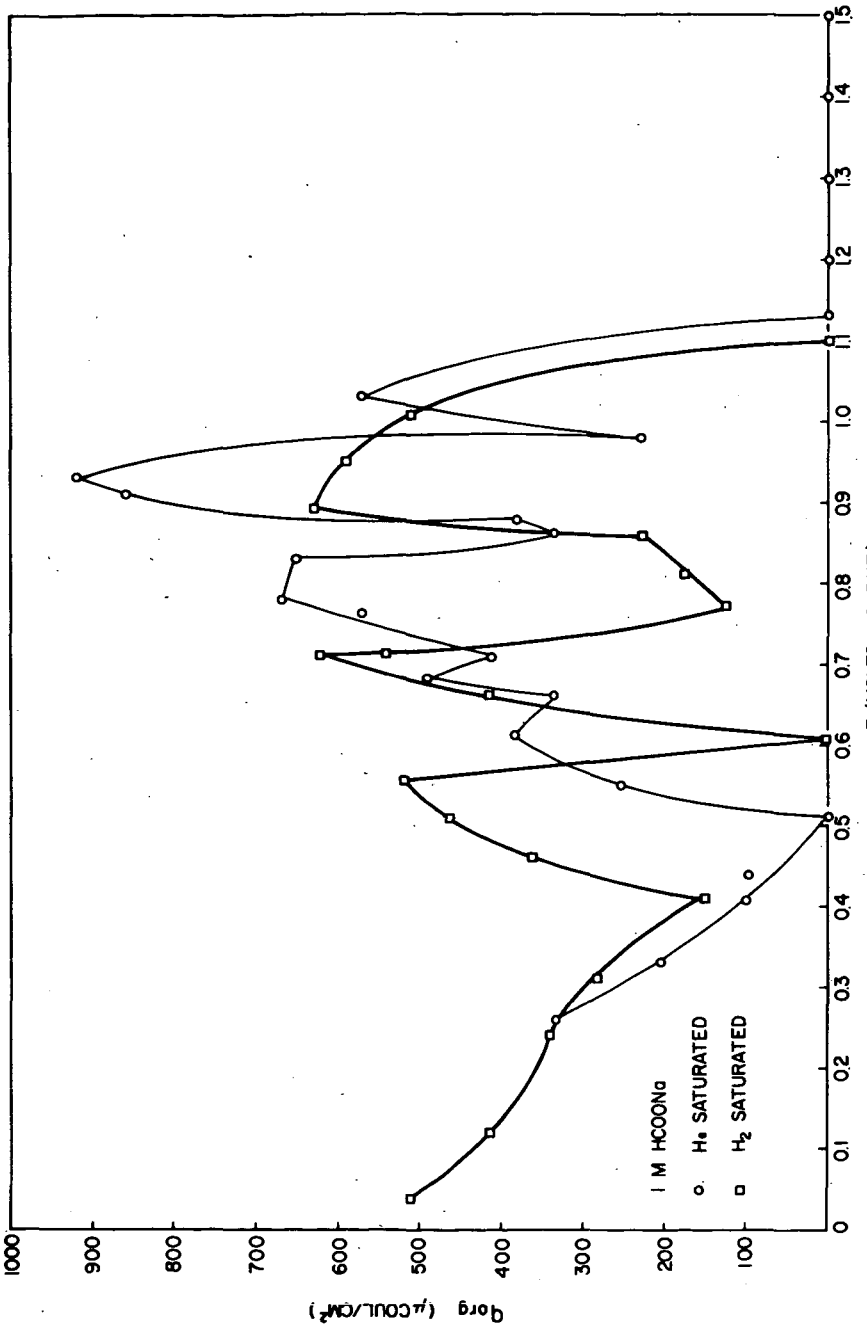

Fig. 6. Steady-state dependence of amount of charge, q_{org}, required to oxidize organic residue at set potentials; 1 M HCOONa.

FUNDAMENTAL STUDY OF ADSORPTION OF HYDROCARBONS ON PLATINUM ELECTRODE

M.BONNEMAY, G.BRONOËL, D.DONIAT and J.P.PESANT

Laboratoire d'Electrolyse
du C. N. R. S.

I. INTRODUCTION.

The purpose of this report is to present the results obtained by a selective method of analysis of adsorption in connection with the study of the kinetics of fixation of hydrocarbons on smooth platinum. The principle involved and the experimental equipment used in this method have been described in a number of articles [1-2] and we will not go into them further at this time. However, we have considered it appropriate to emphasize the basic differences existing between the method used by us and those which were selected by other authors dealing with the same subject. These differences should in fact be kept in mind in comparing our results with those previously published.

II. BASIC CHARACTERISTICS OF THE SELECTIVE METHOD FOR THE STUDY OF ADSORPTION.

The study of adsorption processes is usually carried out from an analysis of the shape of the isothermal curves, that is to say the curves representing the variation of electrode coverage θ as a function of the concentration of substances in the medium under consideration. This method is not very appropriate when the concentrations are very weak, because all isothermal curves are practically straight in cases of low concentration. That is the case with hydrocarbons the solubility of which is rather low in aqueous solutions.

On the other hand, the analysis of curves representing the variation of the coverage as a function of adsorption time makes it easier to reveal and differentiate the various adsorption mechanisms involved, even for low concentrations. That is because the curve submitted to analysis always shows a well marked curvature, which facilitates identification by theoretical kinetic functions.

In connection with their research in adsorption kinetics, some authors have also resorted to the analysis of the coverage development curves as a function time. However, in all cases the standard procedures are characterized by the fact that the electrode is polarized during the adsorption phase and that the coulometric measurement of the coverage takes place in the medium containing the adsorbable substances. As for this last point, it can be admitted that the degree of error committed is small since the duration of the phase during which the coulometric measurement is effected is a very short part of the duration of the adsorption phase. But on the other hand, the presence of a faradic current causes more serious trouble. In fact, under these circumstances the total adsorption kinetic, that is to say the development of the electrode coverage, depends not only on the characteristic constants of the elementary processes of adsorption and desorption, but also on the constants characteristic of the charge transfer. In fact :

$$\frac{d\theta}{dt} = \vec{V} - \overleftarrow{V} - \frac{i}{nF} \qquad (1)$$

in which

$\frac{d\theta}{dt}$ is the coverage velocity of the electrode,

$\vec{V}$ and $\overleftarrow{V}$ are, respectively, the adsorption and desorption velocities, and

$\frac{i}{nF}$ is the faradic term.

The result is that the experimental curves characteristic of the variation of the coverage as a function of the adsorption time, obtained by these methods, depends on the value of the overall charge transfer terms which in turn depend on the overvoltage applied. Thus, the differences observed between the curves taken at more than one adsorption potential are difficult to exploit. Moreover, the passage of a faradic current, which is never a negligeable one, is accompanied by the formation of various reaction products the adsorption of which on the electrode and the chemical reactivity of which with the adsorbate may change considerably the adsorption kinetics under study.

A second disadvantage is linked with the fact that in the method generally used the kinetics of mass transfer actions and in particular of diffusion cannot always be considered rapid in relation to the phenomena under study. Therefore, the analysis of the curves representing the adsorption imply the consideration of a term characteristic of the diffusion processes and the necessity of a correction which it is usually difficult, if not impossible, to make.

III. BASIC EQUATION FOR THE ANALYSIS OF ADSORPTION KINETICS.

In heterogeneous catalysis, it is often found that the kinetics of adsorption obeys a law which can be expressed by the formula :

$$\frac{d\theta}{dt} = V_o \exp(- a\theta)$$

in which V_o is the initial adsorption velocity (for $\theta = 0$).

Most authors explain that this formula, called the Elovich equation [3], is obtained by a linear variation of the adsorption activation energy with the coverage. More than one hypothesis has been offered as to the origin of this variation of activation energy. Systems have been suggested implying heterogeneity of active sites without interaction between adsorbed molecules [4] or homogeneity of sites with interaction between the molecules of the adsorbate [5]. In this latter case, parameter a of equation (2) serves as a coefficient of interaction. More recently, a concept has been suggested [6] which implies the creation of energy chains on the surface of the solid.

Similar considerations have also been adopted to measure adsorption in an electrolytic medium and have led to various isothermal expressions [7-8]. However, in some cases, although the kinetics observed has the Elovich form, it is unlikely that a pronounced heterogeneity of the sites or interactions in the adsorbate should be expected. We therefore considered it wise to

see if other processes of reasoning, not presupposing a relationship between the adsorption activation energy and the coverage, would result in obtaining functions of the same form.

Let us consider first the case of non-dissociative adsorption of a compound on a surface so homogeneous that the reaction surface is the same as the apparent surface.

The general equation for the kinetics of adsorption is :

$$\frac{d\theta}{dt} = \frac{kT}{h} C\ (1-\theta)\ \exp(-\frac{W}{RT}) - \frac{kT}{h}\theta\ \exp(-\frac{W'}{RT}) \qquad (3)$$

in which:

k, T, h and R have their usual meanings,

C is the partial pressure of the active substance,

and W and W' are respectively the activation energies of adsorption and desorption.

For low coverages, it is possible to disregard the desorption term $\frac{kT}{h}\theta\ \exp(-\frac{W'}{RT})$.
We then have :

$$\frac{d\theta}{dt} = \frac{kT}{h} C\ (1-\theta)\ \exp(-\frac{W}{RT}) \qquad (4)$$

The term $(1-\theta)$ for $\theta \ll 1$, can be identified at the start of the development in series of $(\exp - \theta)$, which means that equation (4) is equivalent under these circumstances to :

$$\frac{d\theta}{dt} = \frac{kT}{h} C\ \exp(-\frac{W}{RT})\ \exp(-\theta) \qquad (5)$$

Consequently, we see in this case that the kinetics observed can be described by a law or formula analagous to equation (2), the term a then being equal to 1.

When, for a reaction of the same type, the reacting surface is composed of two fractions X_o and Y_o characterized by sites having different activation energies W_1 and W_2, we can write expressions analagous to equation (4) for X_o and Y_o.

Assuming :

$$\theta_x + \theta_y = \theta \qquad \text{et} \qquad \frac{d\theta_x}{dt} + \frac{d\theta_y}{dt} = \frac{d\theta}{dt}$$

we obtain by means of a development in limited series a fonction $\frac{d\theta}{dt} = f(t)$ of the form :

$$\frac{d\theta}{dt} = mX_o + nY_o - t(X_o m^2 + Y_o n^2) \qquad (6)$$

with: $m = \frac{kT}{h} C \exp(-\frac{W_1}{RT})$

and $n = \frac{kT}{h} C \exp(-\frac{W_2}{RT})$

Equation(2)expressed in the form $\frac{d\theta}{dt} = f(t)$ leads, with the same approximations, to :

$$\frac{d\theta}{dt} = V_o - V_o^2 \, a \, t \qquad (7)$$

Equation (6) can therefore be identified with equation (7), in which the term a has the following value :

$$a = \frac{X_o m^2 + Y_o n^2}{(X_o m + Y_o n)^2}$$

Similar treatment carried out for a surface which can be decomposed into n fractions also gives us, for $\frac{d\theta}{dt} = f(t)$, a formula which can be identified with equation (7).

It is easy to show that when $(W_2 - W_1) < 50$ cal., a tends toward 1, and the system acts substantially the same as in the case of a homogeneous surface. On the other hand, when $(W_2 - W_1) > 200$cal surface Y_o can be considered inactive and in that case a is equal to $\frac{1}{X}$ that is to say to the ratio of the apparent surface to the active surface.

Let us now consider the case of a dissociative adsorption produced on a surface the active fraction of which is X_o. The kinetics of the reaction :

$$AB + {}_S{}^M \rightarrow AM_{S'} + BM_{(S-S')}$$

in which S is the number of sites occupied after adsorption of an AB molecule, can be written neglecting desorption :

$$\frac{d\theta}{dt} = \frac{kT}{h} C X_o \exp(-\frac{W}{RT}) \left[1 - \frac{\theta}{X_o} \right]^S \qquad (8)$$

or else, when $\frac{\theta}{X_o} << 1$:

$$\frac{d\theta}{dt} = \frac{kT}{h} C X_o \exp(-\frac{W}{RT}) \exp(-\frac{S}{X_o} \theta). \qquad (9)$$

This expression can be identified with equation (2) with $a = \frac{S}{X_o}$.

It is readily seen that many adsorption reactions have kinetics similar to that of Elovich without any phenomena of variation of adsorption activation energy being involved.

It is therefore absolutely necessary to take dissociation parameters and surface factors into account in order to evaluate the terms of any intermolecular interaction which may exist.

Equation (9) expresses effects of surface activity and of dissociation. It can be filled out to allow for a possible variation of adsorption activation energy. In that way we have a very general equation of the form [1] :

$$\frac{d\theta}{dt} = \frac{kT}{h} C X_o \exp(-\frac{W_o}{RT}) \exp(\frac{S + \alpha}{X_o} \theta) \qquad (10)$$

in which α represents the interaction coefficient and W_o is the initial adsorption activation energy.

The relationship must now be established between the experimental value q and the electrode coverage θ. θ is defined here as the proportion of the number of sites occupied by the adsorbed substances to the total number S_o of sites existing on the surface of the electrode. If S is the number of sites occupied after the adsorption of one hydrocarbon molecule (an adsorption which may have created other adsorbed particles by dissociation) and Z the number of electrons exchanged in the oxidation of the adsorbed molecule and its products of dissociation the relation between q and θ is written :

$$\theta = q \frac{N S}{Z F S_o} \qquad (11)$$

in which N is the Avogadro number and F the Faraday.

The quantity q is determined in such a way that it is exclusively a function of the oxidation or of the reduction of the adsorbate. Corrections should be made to eliminate any effects of double layer or of electrochemical transformation of the surface.

Combining equations (9) and (10), we obtain :

$$\text{Ln} \frac{dq}{dt} = \text{Ln}\left[\frac{kT}{h} C X_o \frac{Z F S_o}{N S} \exp\left(- \frac{W_o}{RT}\right)\right] - q \frac{N S}{Z F S_o} \left(\frac{S+\alpha}{X_o} \right) \qquad (12)$$

Plotting the $\frac{dq}{dt} = f(q)$ function in a semi-logarithmic form gives us a straight line the ordinate of which at point of origin L_o and the slope P_o are expressed, respectively, as follows :

$$L_o = \text{Ln}\left[\frac{kT}{h} C X_o \frac{Z F S_o}{N S} \exp\left(- \frac{W_o}{RT}\right) \right] \qquad (13)$$

$$P_o = \frac{N S}{Z F S_o} \left(\frac{S+\alpha}{X_o}\right) \qquad (14)$$

Generally speaking, four parameters are unknown : X_o, S, W_o and α. When parameters X_o and S are constant within a given temperature range, an examination of the variation of L_o as a function of T enables us to know the value of W_o.

Knowledge of an additional factor is then necessary in order to determine the other parameters on the basis of equations (13) and (14). This additional factor may be relative to X_o or to the parameter S. Measurements of the double layer differential capacity generally enable us to obtain information on these parameters. As regards S, it is possible to relate the double layer capacity C_d to θ [9] in the following way :

$$C_d = C\theta + C'(1-\theta) \qquad (15)$$

in which C and C' are the specific capacities of the surface whether covered or not. Continuing equations (11) and (15) we obtain the additional factor of relationship which was sought between C_d, q and S.

We find therefore that it is possible in this way to determine the characteristic values of an adsorption kinetic by resorting to only a minimum of assumptions.

IV. RESULTS.

This research was carried out on five alkanes (CH_4, C_2H_6, C_3H_8, n-C_4H_{10} and iso-C_4H_{10}), three alkenes (C_2H_4, C_3H_6 and n-C_4H_8) and on acetylene. The temperatures for the tests were fixed at 80°C and 90°C. The electrolyte medium was constituted by a normal solution of sulphuric acid or phosphoric acid. The electrode was a polished platinum plate. Before each phase of adsorption, this electrode was subjected to an electrochemical treatment [10] the purpose of which was to ensure perfect reproductibility of the surface condition of the metal.

For each hydrocarbon under the conditions stated above, we obtained the q=f(t) curves representing, according to the adsorption time t the quantity of electricity corresponding to the oxidation of the adsorbed substances.

The functions Ln dq/dt = f(q) were plotted on the basis of the q=f(t) curves. Some interesting features of regularity appeared in this form of expression. By way of example, the curves obtained from the tests made in H_2SO_4 N at 80°C are shown in figure 1.

Exploitation of these curves and of the differential capacity measurements enable us to determine the constants characteristic of the adsorption kinetics involved. Moreover, the special behavior of methane enabled us to make a separate calculation of these parameters. In fact, the stability of the methane molecule entails identical dehydrogenation at 80°C and at 90°C, which is confirmed by the identical slopes of the Ln dq/dt = f(q) curves plotted at both of these temperatures. $W_{o(80°)}$ is therefore equal to $W_{o(90°)}$ in the case of CH_4 and it is possible to compute its value from the ratio of the initial adsorption velocities.

The values of the parameters thus determined are shown in tables I, II and III.

V. DISCUSSION.

An examination of the results enables us to formulate a number of remarks concerning the reaction mechanism involved in the course of the deposit of hydrocarbons on platinum.

It can be noted that in all the cases studied, with the exception of isobutane, the number of sites occupied by the products resulting from the adsorption of a molecule is equal to the number of carbon atoms contained in the molecule plus two. It can be assumed that the adsorption is dissociative and causes a break of C-H bonds in such a way that two hydrogen atoms are released, which occupy two sites. The carbon radical resulting from this dissociation is deposited on a number of sites equal to the number of carbon atoms which it contains.

This preferential dissociation involving the C-H bonds has already been suggested by various authors.

In the case of the alkanes and the ethylenes, as in the case of acetylene, the dehydrogenation probably occurs in the end groups of the chain. This assumption is also supported by the fact that the deposit of one molecule of isobutane results in the occupation of 7 sites. In fact, the presence in the molecule of this reactive agent of an extra methyl group appears to cause the break up of a third C-H bond.

This rate of site occupation does not necessarily indicate that each occupied site comprises a link with an adsorbed particle. Our examination of the very slight variation of W_o as a function of the number of carbon atoms contained in the molecules of hydrocarbons of the same series suggests rather that the number of bondings between the products of dissociation and the platinum remains constant. These bondings take place both between the platinum and the dehydrogenated end groups and between the platinum and the hydrogen atoms resulting from that dissociation. The other sites occupied are not linked but simply covered by the middle part of the chain.

It is worthy of note that the values found for S agree with the theoretical expectations and are different from those heretofore determined by chemical methods /11/.

In the final analysis, we are inclined to suggest a reaction system which includes as the final stage of the reaction occurring at zero current the formation of both adsorbed H and a C_xH_y radical comprising bondings with the platinum. However, it must be pointed out that if this radical reacts with its environment (O or OH compounds, for example), the number of sites occupied may then be the same as for the C_xH_y radical alone. The suggested system therefore constitutes only one of the possible solutions for a given number of sites.

It should also be stressed that, under the assumption of adsorption accompanied by chemical reactions leading to partial oxidation of the C_xH_y radical, the coulometric measurement will not depend at all on the state of oxidation. In fact, if the anodic pulse causes the formation of CO_2 and H_2O, the number of coulombs will always be the same regardless of the state of oxidation of the substance adsorbed to the extent that this oxidation can only involved the oxygen derived from the water or anions of the acid.

A number of observations can also be made in regard to the values found for the coefficient α. Actually, for a given medium and temperature, this coefficient increases as a function of the length of the molecule adsorbed. Moreover, α is subject to a decided increase when, in the case of molecules having the same number of carbon atoms, the number of radicals undergoing a breakage of bond increases. This would seem to indicate that the greater the separation of the end groups the smaller will be the intramolecular interactions and the larger the term α when measured.

Coefficient α is usually lower for an ethylene hydrocarbon than for a saturated hydrocarbon, with the same number of carbon atoms and an identical degree of dissociation. It is also observed that acetylene shows a very high interaction coefficient. This probably has to do with the fact that the dehydrogenation of this compound produces a highly reactive carbon containing residue which may react on the environmental medium.

Attention should be called to the fact, however, that even with the highest values of the interaction coefficient α, the variations of the adsorption activation energy W as a function of the coverage remain comparatively low. In fact, in the case of isobutane, a reactive agent which involves the strongest interaction, the variation of W is about 620 cal/mole while the coverage increases from 0 to 0.1 (which was the case in our experiments).

As regards the effect of the nature of the electrolyte on the value of coefficient α, the results obtained indicate a decided variation of this parameter according to whether the medium is sulphuric or phosphoric acid. This interaction coefficient is therefore not only linked with forces of attraction or repulsion between adsorbed molecules but also with the action of the ions of the electrolyte. It is probable that the effect of the anions is dominant, which would be in full agreement with the specific adsorption of H_3PO_4 ions brought out in other articles on the subject /12-13/.

REFERENCES

1 - D.DONIAT. Thesis, Paris 1969.

2 - M.BONNEMAY, G.BRONOËL, D.DONIAT and E.LEVART. International Conference on Electrochemical Power Sources systems for Space Applications, Paris, December 1967.

3 - S.Ju.ELOVICH and G.ZHABROVA. Zh. Fiz.Khim. 13(1939)1716 and 1775

4 - J.ZELDOWITZ. Acta Physicochem. 1 (1935) 961.

5 - M.BOUDART. J.Am.Chem.Soc.74 (1952) 3556.

6 - G.D.SAKHAROV. Dokl. Ak. Nauk. SSSR 180 (1968) 154.

7 - A.N.FRUMKIN. Z.Phys. Chem. 116 (1925) 466.

8 - B.B.DAMASKIN. Elektrokhim.1 (1965)63.

9 - A.N.FRUMKIN. Z.Physik 35 (1926) 792.

10- S.GILMAN. J.Phys.Chem. 66 (1962) 2657.

11- S.GILMAN. Trans.Farad.Soc.515 (1965) 2546.

12- J.BRAVACOS, M.BONNEMAY, E.LEVART and A.A.PILLA. C.R.Acad. Sc., Paris, 265 (1967) 337.

13- O.A.PETRII, R.V.MARVET and Zh. N.MALYSHEVA. Elektrokhimija 3 (1967) 1141.

TABLE I

Hydrocarbon	z	S	W_o cal/mole	α
CH_4	8	2,1	22 500	11
C_2H_6	14	3,9	23 300	0,94
C_3H_8	20	4,7	23 200	3,80
$n.C_4H_{10}$	26	5,6	22 900	5,59
$iso.C_4H_{10}$	26	6,6	23 200	8,85
C_2H_4	12	3,8	22 300	1,34
C_3H_6	18	4,7	21 700	3;38
$n.C_4H_8$	24	5,7		4,22
C_2H_2	10	3,9	22 400	5,81

in H_2SO_4 at 80°C

TABLE II

Hydrocarbon	z	S	W_o cal/mole	α
CH_4	8	2,1	22 500	11
C_2H_6	14	4,2	23 300	1,66
C_3H_8	20	5,1	23 100	3,91
$n.C_4H_{10}$	26	6,1	22 900	9,99
C_2H_4	12	4,1	21 900	4,29
C_3H_6	18	5,1	21 200	5,87
$n.C_4H_8$	24	6,15		9,08
C_2H_2	10	4,2	21 300	5,14

in H_2SO_4 at 90°C

TABLEAU III

Hydrocarbon	z	S	W_o cal/mole	α
CH_4	8	1,9	22 400	15
C_2H_6	14	3,7	22 100	7,6
C_3H_8	20	4,6	22 000	13,9
C_2H_4	12	3,6	21 500	5,6
C_3H_6	18	4,6	21 000	12,1
C_2H_2	10	3,8	19 200	11,9

in H_3PO_4 at 80°C

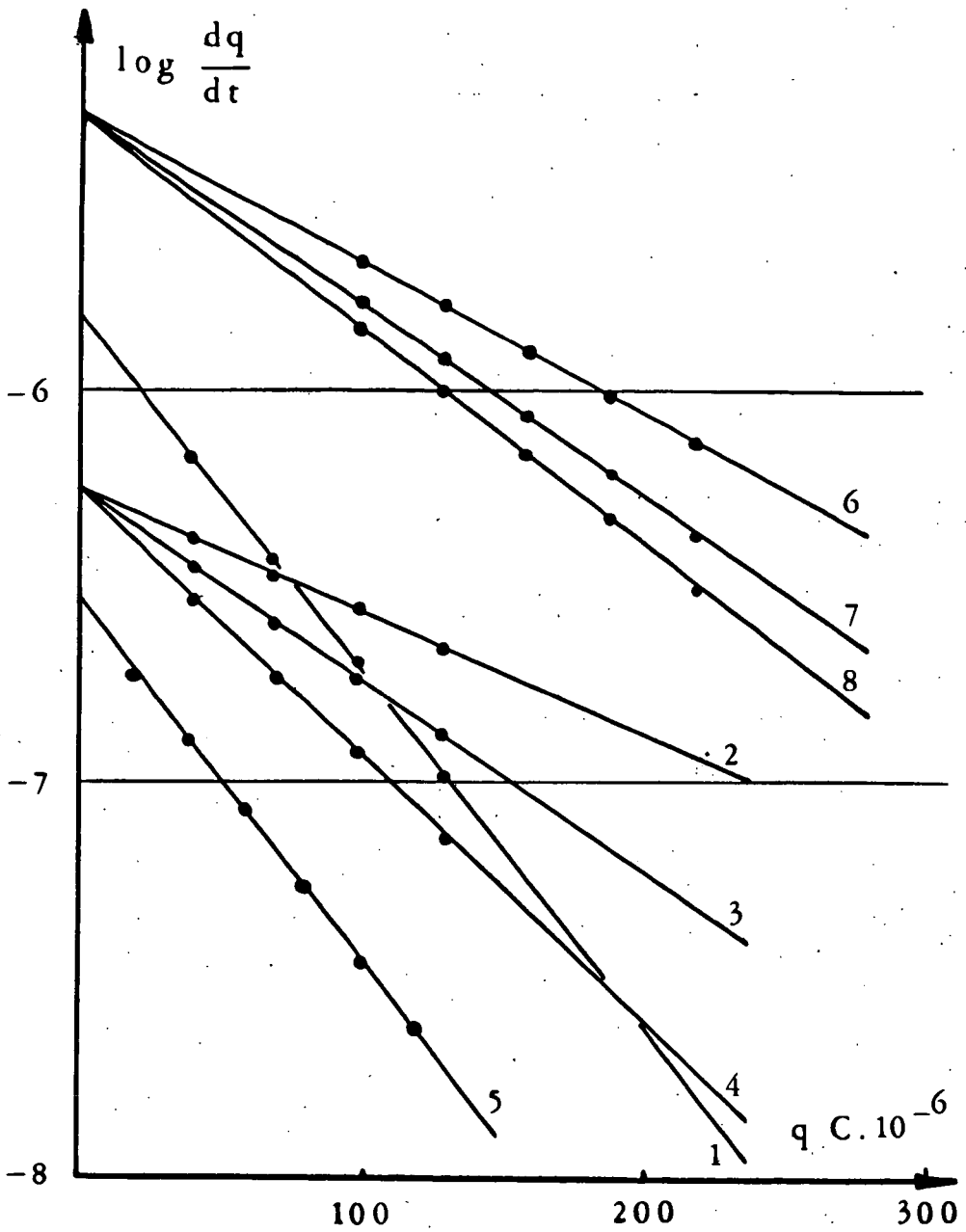

FIGURE 1 Plots of $\log_{10}$ dq/dt versus q in H_2SO_4 N medium at 80°C for :

1- CH_4; 2-C_2H_6; 3-C_3H_8; 4- n.C_4H_{10}; 5-iso-C_4H_{10};

6-C_2H_4; 7-C_3H_6; 8- n.C_4H_8.

STUDY OF ELECTROCHEMICAL PROCESSES BY THE ROTATING DOUBLE RING ELECTRODE

W. Vielstich

Bonn, Germany

ABSTRACT

During the last decade it has been proven that the rotating disc electrode is a very useful tool for stationary investigations of electrode processes and preceding or following chemical reactions. The occurance of intermediate products has been successfully studied by a disc electrode with an additional concentric ring.

For the investigation of particles with a very short lifetime the double ring electrode, suggested by Heusler and Schurig, should be of special advantage. We have solved the hydrodynamic problem for the double ring electrode by a numerical calculation.

The experimental device is suited for measurements up to 400 rps.

Experimentel results will be presented for the following systems:

a) iron (III) - iron (II) - sulfate/H_2SO_4 (to check the calculation),
b) carbonmonoxide/formate in alkaline solution,
c) methanol/formaldehyde in KOH-electrolyte.

SOLUBILITY OF GASEOUS HYDROCARBONS IN AQUEOUS SOLUTIONS: INITIAL MECHANISM FOR PROPANE ADSORPTION ON PLATINUM

Dorothy D. Williams, John A. Christopulos, and Gabriel J. DiMasi

Power Sources Division, Electronic Components Laboratory
USAECOM, Fort Monmouth, New Jersey

INTRODUCTION

Early methods for the determination of gaseous hydrocarbon solubility in aqueous solution were based on static techniques.[1,2] Basically, the static technique involves bringing together an excess volume of gas and a measured quantity of gas-free solvent in an equilibrium cell, which is rocked for several hours to attain gas-solution equilibrium. Subsequent removal of the dissolved gas by manometric techniques,[3] however, appears to lack precision and becomes unwieldy. Therefore methods for hydrocarbon solubility determinations[4,5] were developed which applied inert gas-stripping techniques to isolated samples of gaseous hydrocarbon-saturated solutions. Collection of the stripped gaseous hydrocarbons was made on various adsorbents at reduced temperature (-80°C). The hydrocarbons subsequent release was effected by raising the temperature allowing the sample to be swept into a gas-liquid chromatograph (GLC). This GLC technique as developed by Swinnerton and Linnebom was found satisfactory for measurement of trace quantities of gas dissolved in solution, however, a desirable gas-saturation chamber was lacking. Thus it was necessary to develop a new dynamic method for gas-saturating aqueous solutions (electrolytes) which simulates gas-saturation as it exists in fuel cells. The technique described herein is being used to determine solubilities of gaseous hydrocarbons (propane) in the following fuel cell electrolytes: perchloric, sulfuric, phosphoric, and trifluoroacetic acids at 1 molar concentrations. Solubilities of propane in these electrolytes were used in conjunction with propane adsorption rate data obtained through linear anodic sweeps[6] to elucidate the mechanism of initial propane adsorption on smooth platinum.

EXPERIMENTAL

A Hewlett-Packard Model 5750 gas chromatograph equipped with dual flame ionization and thermal conductivity detectors was used. A six foot column packed with Chromosorb W coated with diisodecyl phthalate was used for the analysis and helium was employed as carrier gas. Research grade propane (99.9 mole percent) was obtained from Phillips Petroleum Company. The apparatus for propane saturation of electrolyte and subsequent collection of dissolved propane is shown in Fig. 1.

Propane is first humidified by passing through a glass-jacketed scrubber (A) having the same electrolyte and temperature as the test solution. The humidified propane bubbles through a jacketed vessel (B) effecting saturation of the electrolyte (150 ml). The gas train continues through line D and 3-way valves 1 and 2 to a 104 ml jacketed saturation-stripping chamber (E) containing 84 mls of electrolyte. Thus, a volume corresponding to 20 ml is reserved for propane during transit. All gas flow rates are measured and adjusted using a bubble flow meter. Excess propane exits from this chamber via 3-way valve 3 and 2-way valve 4 into a waste trap. The propane saturation process requires 30 minutes at a flow rate of 2.5 cc per second. Then 3-way valve 1 is turned to allow propane saturated electrolyte from vessel B to flow into the saturation-stripping chamber (E) via line C until it becomes filled. As soon as this is accomplished, 3-way valves 2 and 3 are closed simultaneously, to seal the saturation-stripping chamber. To purge outer line F of propane humidified helium is passed through line G and valves 3 and 4 before sample collection begins. Thirty minutes of helium purge is required to clear

line F of propane. To collect the sample 2-way valves 4 and 5, 3-way valves 2 and 3 and 2-way valve 6 are turned to allow humidified helium to strip the dissolved propane from the 104 ml chamber (E), the gas flows through line F, valve 5, drying tubes of magnesium perchlorate, and valve 6 into a closed test tube containing 5 mls of purified toluene maintained at -80°C. Stripping and collection of propane requires 30 minutes. The test tube of toluene is then removed from the gas train, capped, and brought to room temperature. A 10 microliter aliquot sample is removed and injected via hypodermic syringe into the gas-liquid chromatograph. Before the next propane saturation run, 3-way valve 2, and 2-way valve 7 are turned to allow the electrolyte-filled chamber (E) to drain to starting level of 84 ml.

CALIBRATION

The Hewlett-Packard gas chromatograph Model 5750 used in this work is equipped with a Mosley Recorder and a Disc Integrator Model 229 to record and integrate peak area. Propane retention time is 0.4 minutes at a column temperature of 89°C and a helium carrier gas flow rate of 20 cc per min. The chart speed was one inch per minute. To calibrate the gas chromatograph 20 microliter of pure propane gas was injected using a Hamilton gas-tight syringe. The number of integrator counts was recorded and used as a standard. Since the ratio of area to volume for the standard is directly proportional to the area-volume ratio of the sample the quantity of propane in the sample was calculated.

The technique[6] employed to obtain data on the rate of propane adsorption at a smooth platinum electrode was a modified version of the multipulse potentio-dynamic (MPP) sequence with a linear anodic sweep (las) of 10 volts per second. This sequence allows measurement of charge required to completely strip the propane adsorbed at the study potential at various times. This is accomplished by subjecting the anode to the MPP sequence in presence, first of helium and then propane. The charge obtained with helium, Q_{He}, is subtracted from that in the presence of propane, Q_p, to obtain the desired charge difference ΔQ. The duration of the study potential step was identical for both Q_{He} and Q_p measurements.

RESULTS AND DISCUSSION

In these experiments the molarity of the acid was considered constant. Using this basis a series of results relating the mole fraction of dissolved propane to temperature are shown (Fig. 2). Both 0.5 and 1.0 molar sulfuric acid solutions have approximately the same solubility within the conditions of the experiment; thus, indicating that in this example ionic concentrations do not substantially interfere with the solubility of propane. Another interesting feature concerning this acid is that the quantity of dissolved gas does not vary with temperature between 20° and 65°C.

However, in examining the solubility data for the other acids one finds a similarity between the phenomena displayed in water as a function of temperature and that in perchloric, trifluoroacetic, and phosphoric acids. In these data one finds that at 65°C the solubility of propane in all the acids and in water is the same quantity within the precision of the experiments. At lower temperatures a difference in the quantity of dissolved gas was observed. For example, at 40°C an appreciable difference has been measured. At 20°C the propane gas is now adsorbed in the largest quantity in water while the amount in the acid solutions has some dependence on the character of the acid. Figure 2 also illustrates the anomalous behavior[7] of water in which a maximum propane solubility is observed. Similar behavior is displayed in all the acids examined with the exception of sulfuric. The degree of hydration associated with sulfuric acid may account for this invariant behavior for propane solubility at these temperatures.

The solubility data once obtained can be used in making certain statements concerning the initial process of propane adsorption on a smooth platinum surface measured by linear anodic sweeps. If semi-infinite linear diffusion is assumed, the rate of accumulation of charge is given by[8]

$$Q = 2nF \frac{D}{\pi}^{\frac{1}{2}} C_{C_3H_8} t^{\frac{1}{2}}$$

The symbols have their usual significance. Although it has been previously shown[9] that the overall oxidation of propane to carbon dioxide and water involves 20 electrons, it has been determined that using las techniques n should be equal to 17 electrons[10] since three hydrogen atoms are lost upon adsorption at potentials equal to or greater than 0.3 volts. Therefore, using the measured values of propane dissolved in solution we may calculate from the linear portions of Figs. 3 and 4 the diffusivity of propane in perchloric acid as $0.156(10^{-6})$ cm^2 sec^{-1} and in sulfuric acid as $0.067(10^{-8})$ cm^2 sec^{-1}. These calculations are in agreement with the approximate inverse relationship of diffusivity and viscosity. In Fig. 5 one can see that the viscosity of perchloric is less that that of sulfuric acid.

Another interesting phenomenon which seems evident is the change in slope (Fig. 4) as a function of potential in perchloric acid. These apparent deviations are observed at times of one second and are in contrast with the diffusion-limited process portrayed in sulfuric acid (Fig. 3) as a function of potential. In sulfuric acid the initial adsorption is diffusion-controlled for approximately 60 seconds at 0.2 and 0.3 volts while deviations from linearity occur after 8 seconds at 0.4 volts. These times are in general agreement with observations of Brummer[10] in concentrated phosphoric acid.

Further consideration of the data at anodic potentials of 0.3 and 0.4 volts is shown in Fig. 6. Here, in the perchloric acid anion environment propane adsorption can be described by

$$Q = A + B \log t$$

in which Q=charge per cm^2, t=time, and A and B are parameters which depend on the type of adsorption occurring. This relationship continues until a time invariant condition is achieved on the platinum surface. Since this difference in behavior in the two acids has already been found not to be a function of the propane concentration, other possible explanations are considered.

It has already been postulated[11] that at potentials less anodic than reversible oxygen the electrochemical formation of "O" type species from the electrolyte may proceed via the mechanism

$$(1) \qquad Pt + H_2O_{(ads)}Pt \rightleftharpoons "Pt(OH)" + H^+ + e^-$$

This type of reaction, of course, will proceed at an electrode surface at which the least specific anion adsorption occurs. Since, perchloric acid anions are less adsorbed than sulfate the rate of formation of the partially oxigenated species on platinum will proceed at a faster rate due to the concentration of H_2O at the interface. Evidence of decreased perchloric anion adsorption has already been presented by some of the authors.[6] Here it was shown that the total propane adsorbate

was greater in perchloric acid indicating it has a lesser degree of anion coverage. Since reaction (1) then occurs it is possible that at 0.3 volts in very short times some of the adsorbed species may undergo this mechanism

$$(2) \quad C_3H_8 + Pt \rightarrow C_3H_7\text{-}Pt + H^+ + e^- \text{ (fast)}$$

$$(3) \quad C_3H_7\text{-}Pt + \text{"Pt(OH)"} \rightarrow C_2H_7C\text{-}OH \text{ (slow)}$$

$$(4) \quad 2Pt + C_2H_7\,C\text{-}OH \rightarrow Pt\ C\text{-}OH + Pt\ C_2H_5 + 2H^+ + 2e^-$$

Similar type mechanisms[12,13] have been suggested, but the possibility of reaction (1) occurring is made more evident by the work of Hunger.[14] This postulated mechanism demonstrates a curious position. For in perchloric acid as compared to sulfuric the competition of anions for active sites decreases, hence the degree of partial oxygenation of platinum increases. With this condition, O-type hydrocarbon species are formed and the carbon-carbon bonds are more easily broken. Therefore, the amount of available sites decreases and the rate of further deposition becomes adsorption-controlled at these low anodic potentials. In contrast, the diffusion controlled mechanism in sulfuric acid may indicate the lack of surface reactions and subsequent increase in surface coverage due to the formation of free radicals and oxygenated species originating from propane at the potentials studied. Interestingly enough, the adsorption of methanol,[15] a partially oxygenated compound, also follows an adsorption isotherm.

CONCLUSIONS

The solubility of propane seems to be about the same in the electrolytes studied. Thus, the initial rate of propane adsorption is influenced by surface conditions at the platinum anode. The tendency of the anion to specifically adsorb and the rate of partial oxidation of the platinum surface seem to be interrelated factors which dictate the initial mechanism of propane adsorption.

REFERENCES

1. Ostwald: Manual of Physico-Chemical Measurements, pp 172-5. The Macmillan Co., London (1894).

2. Avarnoose and McKetta, J. J., Petroleum Refiner (37) 275, 1958.

3. VanSlyke and coworkers, Biol. Chem. (105) 571, 1934.

4. Swinnerton, J. W., and Linnenbom, V. J., Jour. of Gas Chromatography (5) 570, 1967.

5. Walker, R. D., Jr., Quarterly Progress Report No. 10, Contract No. DA-49-186-AMC-45 (X), 1963.

6. Christopulos, J. A., Pilla, A. A., DiMasi, G. J., Paper presented at the Boston Meeting, Electrochem. Soc., 7 May 1968.

7. Tammann, G., Z. Anorg, Allgem Chem. (235) 49-61, 1937.

8. Laitinen, H. A., Kolthoff, I. M., J. Am. Chem. Soc. 61, 3344 (1939).

9. Binder, H., Kohling, A., Krupp, H., Richter, K., and Sandstede, G., J. Electrochem. Soc. 112, 355 (1965).

10. Brummer, S. B., Ford, J. I., Turner, M. J., J. Phys Chem., 69, 3424 (1965).

11. Conway, B. E., Marincic, N., Gilroy, D., and Rudd, E., J. Electrochem Soc. 113, 1144 (1966).

12. Vasil'ev, Yu. B., and Bogotskii, V. S., Fuel Cells Consultants Bureau New York, p. 107 (1966).

13. Brummer, S. B., and Cahill, K., J. Electroanal Chem. 21, 463 (1969).

14. Hunger, H., (private communication).

15. Vasil'ev, Yu. B., and Bogotskii, V. S., ibid, p. 100.

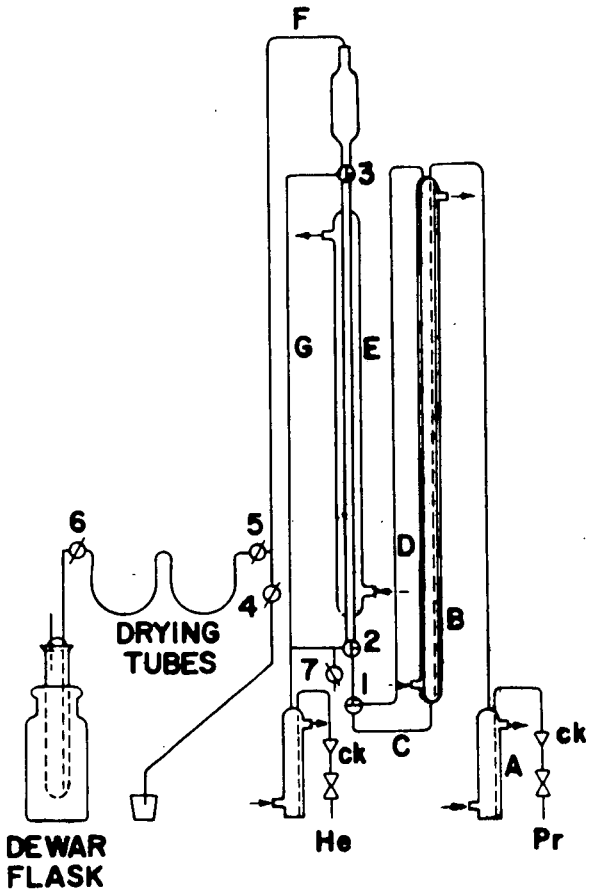

Fig. 1 GAS SOLUBILITY APPARATUS

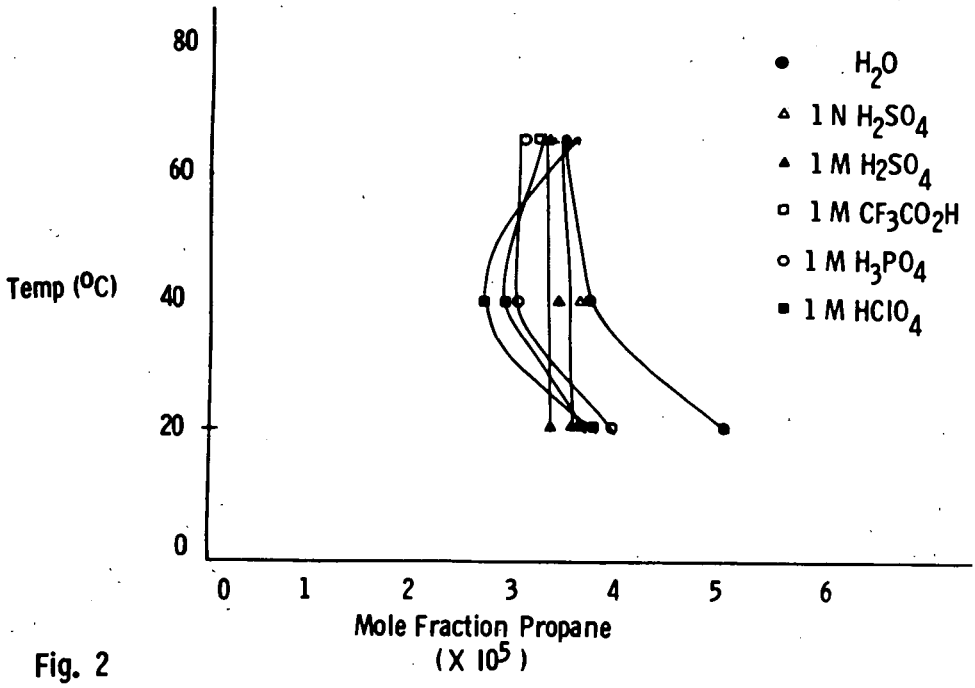
Temp (°C)
80
60
40
20
0
0
1
2
3
4
5
6
Mole Fraction Propane
(X 10⁵)
H₂O
1 N H₂SO₄
1 M H₂SO₄
1 M CF₃CO₂H
1 M H₃PO₄
1 M HClO₄

Fig. 2

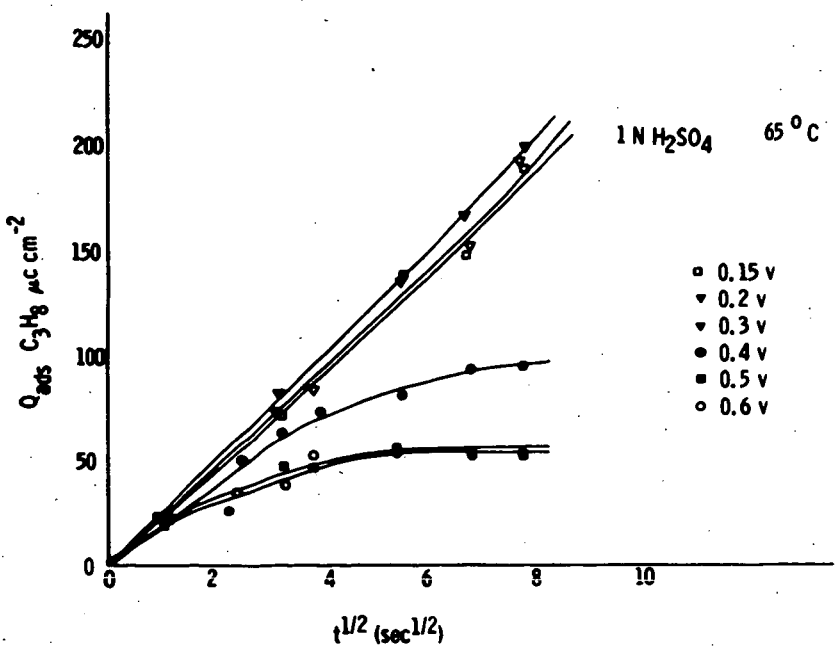
Q_ads C₃H₈ μc cm⁻²
250
200
150
100
50
0
0
2
4
6
8
10
t^1/2 (sec^1/2)
1 N H₂SO₄
65 °C
0.15 v
0.2 v
0.3 v
0.4 v
0.5 v
0.6 v

Fig. 3

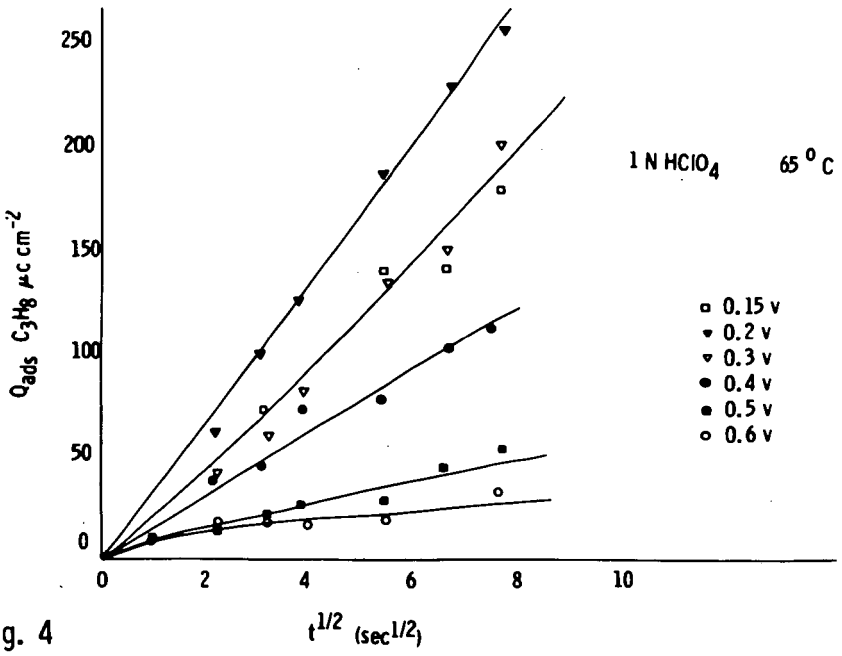
250
200
150
100
50
0
0
2
4
6
8
10
Q_{ads} C_3H_8 $\mu c\ cm^{-2}$
$t^{1/2}$ $(sec^{1/2})$
1 N $HClO_4$ 65 °C
0.15 v
0.2 v
0.3 v
0.4 v
0.5 v
0.6 v

Fig. 4

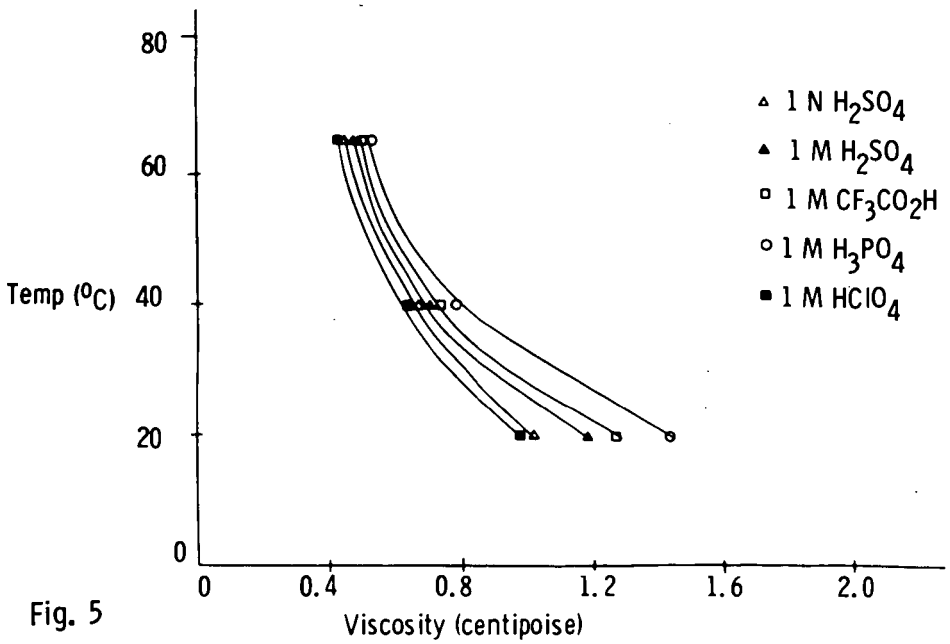
80
60
40
20
0
0
0.4
0.8
1.2
1.6
2.0
Temp (°C)
Viscosity (centipoise)
1 N H_2SO_4
1 M H_2SO_4
1 M CF_3CO_2H
1 M H_3PO_4
1 M $HClO_4$

Fig. 5

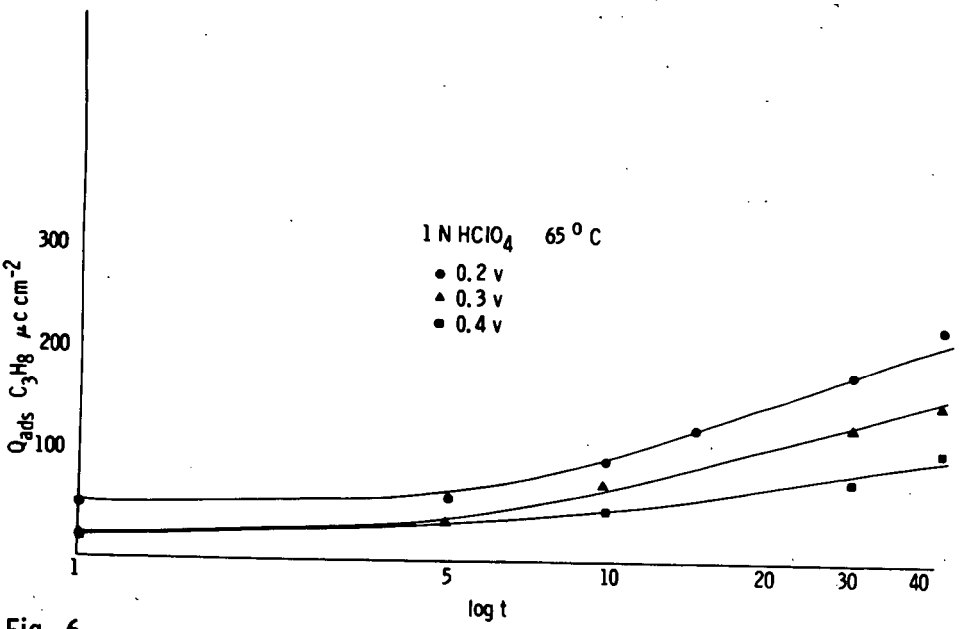
1 N HClO4 65 °C
0.2 v
0.3 v
0.4 v
Qads C3H8 μc cm-2
300
200
100
1
5
10
20
30
40
log t

Fig. 6

A THIN-FILM SOLID-ELECTROLYTE FUEL CELL

A. O. Isenberg
W. A. Pabst
E. F. Sverdrup
D. H. Archer

Westinghouse Electric Corporation
Research Laboratories

ABSTRACT

The chemical energy of coal can be directly converted into electrical energy by solid-electrolyte fuel cells. These fuel cells operate at about 1000°C and use a doped-zirconia solid electrolyte. A thin-film, solid-electrolyte cell has been fabricated by successively applying: 1) a porous fuel electrode; 2) a dense, continuous yttria doped zirconia electrolyte; and 3) a porous air electrode layer on a porous ceramic tube 1.3 cm in diameter and 5 cm long. Each of these three layers was less than 30 μ thick. The electrolyte was produced by chemical vapor deposition and the electrodes by sintering processes.

The cylindrical cell was tested with H_2 (~ 3% H_2O) fuel gas inside and air outside the tube. The open circuit voltage of the cell was 1.06 volt -- within 2% of the theoretical value. The operating voltage was 0.73 volt at 517 milliamperes/cm^2. The resistive losses checked closely those calculated from the resistivity and thickness of the electrolyte and the resistance of the electrodes. The polarization losses were less than 0.10 volt for the porous cobalt-zirconia fuel electrode and a 0.20 volt for the air electrode. While the performance of the cell thus exceeds that projected for an initial 100-kilowatt coal-burning fuel-cell power plant, further work is required to improve the air electrode and to interconnect such thin-film cells in a battery.

Work sponsored by the Office of Coal Research, U. S. Department of the Interior -- N. P. Cochran and P. H. Towson, Contract Monitors.

A THIN-FILM SOLID-ELECTROLYTE FUEL CELL

A. O. ISENBERG
W. A. PABST
E. F. SVERDRUP
D. H. ARCHER

WESTINGHOUSE ELECTRIC CORPORATION
RESEARCH LABORATORIES
PITTSBURGH, PENNSYLVANIA 15235

A THIN-FILM SOLID-ELECTROLYTE FUEL CELL

A. O. Isenberg
W. A. Pabst
E. F. Sverdrup
D. H. Archer

Westinghouse Electric Corporation
Research Laboratories
Pittsburgh, Pennsylvania 15235

ABSTRACT

The chemical energy of coal can be directly converted into electrical energy by solid-electrolyte fuel cells. These fuel cells operate at about 1000°C and use a doped zirconia solid electrolyte. A thin-film, solid-electrolyte cell has been fabricated by successively applying: 1) a porous fuel electrode; 2) a dense, continuous yttria doped zirconia electrolyte; and 3) a porous air electrode layer on a porous ceramic tube 1.3 cm in diameter and 5 cm long. Each of these three layers was less than 30μ thick. The electrolyte was produced by chemical vapor deposition and the electrodes by sintering processes.

The cylindrical cell was tested with H_2(~3% H_2O) fuel gas inside and air outside the tube. The open circuit voltage of the cell was 1.06 volt -- within 2% of the theoretical value. The operating voltage was 0.73 volt at 517 milliamperes/cm^2. The resistive losses checked closely those calculated from the resistivity and thickness of the electrolyte and the resistance of the electrodes. The polarization losses were less than 0.10 volt for the porous cobalt-zirconia fuel electrode and a 0.20 volt for the air electrode. While the performance of the cell exceeds that projected for an initial 100-kilowatt coal-burning fuel-cell power plant, further work is required to improve the air electrode and to interconnect such thin-film cells in a battery.

INTRODUCTION

Electrical energy can be generated using coal as a fuel by direct electrochemical conversion using solid electrolyte fuel cells.[1] A solid electrolyte fuel cell can be visualized as shown in Figure 1. The oxygen receives electrons at the air electrode (cathode), migrates through the electrolyte as an ion and transfers the electrons at the fuel electrode (anode) reacting with the fuel gas to form H_2O and CO_2. The electrolyte is a yttria doped zirconia which has an oxygen ion transfer number very close to one. The electrodes are either metallic or consist of electronically conducting oxides. This fuel cell operates at temperatures near 1000°C where the oxygen ions are mobile. A fluidized coal bed, receiving heat from the fuel cells, gasifies the coal and generates the fuel for the cells. Since the goal of this work is central station power, the fuel cell power plant has to compete with conventional power generating plants. This means that the solid electrolyte fuel cells have to be fabricated using low cost production techniques and that the costs of expensive materials (i.e. the yttria doping of the electrolyte) have to be minimized. The thin-film fuel cell

Work sponsored by the Office of Coal Research, U.S. Department of the Interior -- N. P. Cochran and P. H. Towson, Contract Monitors.

represents an important step toward this goal. To prepare such thin film fuel cells complex ceramic machining and assembling techniques[2] are replaced by a less expensive film deposition process. The reduction of electrolyte thickness from nearly 1000 microns to about 30 microns reduces the calculated cell resistance from 1Ω to about 3 x 10^{-3}Ω per square centimeter of active cell area at the operating temperature. This paper reports the construction and performance of a thin-film fuel cell.

CELL PREPARATION

The cell was built on a cylindrical porous ceramic support tube coated first with the fuel electrode, then the thin film electrolyte, and finally by the air electrode. The fuel flows through the inside of the tube and diffuses through the porous structure of the support tube to the fuel electrode. Combustion products diffuse in the opposite direction. A concentration gradient is built up with increasing combustion product content along the tube axis. Air flows over the outside air electrode.

As support tube for the cell we used a 1.3 cm O.D. stabilized zirconia tube with a wall thickness of 1.5 mm. The measured open porosity of the support tube was 15 percent.

The tube was covered over a length of nearly 15 cm with a fuel electrode consisting of a 20 to 30μ thick cobalt-zirconia cermet layer. This layer was applied by sintering.

The fuel electrode was covered with a thin film electrolyte by chemical vapor deposition.

The x-ray analysis of the electrolyte films confirmed a fully cubic structure of the electrolyte.

Film thicknesses obtained from a three hour chemical vapor deposition run are about 30μ to 50μ. Cross section analysis of various films grown in a number of experiments show that pores up to 10 microns in the cermet fuel electrode can be bridged with a gas-tight electrolyte film.

After the electrolyte film was applied to a 4 cm long cell it was assembled into the tester for testing at 950°C. As Figure 2 shows, alumina adapter tubes fit over the cell tube ends. Gold washers seal the cell tube to the alumina tubes. The assembly was compressed by means of an alumina rod running through the center of the tubes. Threaded brass tubing was glued to the alumina rod ends to allow the tubes to be placed under a controlled compression using a spring on one end of the assembly. Since the gold washers are pressed against the thin fuel electrode located between support tube and thin-film electrolyte, they provide electrical contact to the fuel electrode. A platinum wire was welded on to one washer representing a potential probe and a 1.5 mm thick palladium silver wire was welded to the other washer as current lead to the fuel electrode.

An air electrode consisting of a three layer coating of platinum was applied in three separate sintering steps. The platinum was sintered in air while the inside of the cell was purged with forming gas. The platinum air electrode was backed up with a platinum screen current collector. A 1.5 mm thick palladium silver wire acted as the current lead on the air side of the cell.

The cell was equipped with a thermocouple which acted also as a potential probe for the air electrode. An electrolyte reference electrode was placed beside the air electrode. Figure 3 shows the cell. The total active cell area, determined by the air electrode size, was 5.8 cm^2. A cross section through the thin film cell structure is shown in Figure 4.

EXPERIMENTAL RESULTS

The cell was tested using hydrogen containing nearly 3% water as the fuel. The flow rate indicated by flowmeters was 400 to 500 ccm per minute. Air was supplied by natural convection to the outside of the cell.

The cell was operated at 950°C. The electrical characteristics are shown in Figure 5. The polarization characteristics of the fuel and the air electrode include the ohmic and non-ohmic part of the polarization. The measured open cell voltage was 1060 mV over the entire test period of nearly 100 hours. A maximum current density of 720 mA/cm^2 was obtained at a cell voltage of 618 mV. The cell was operated for a 96 hour test at a continuous current load of 500 mA/cm^2. The cell voltage at this current level is plotted versus time in Figure 6.

Current interruption tests[3] showed an ohmic potential drop in the cell of 30 mV at a current density of 630 mA/cm^2. The resistance drop in the fuel electrode, calculated from the square resistance of the fuel electrode, does not exceed 5 mV at this current level. The resistance of the air electrode was neglected because of the heavy current collector. The difference of 25 mV is due to the potential drop in the electrolyte.

From these data, the calculated resistivity of the thin film electrolyte is:

$$\rho[\Omega\cdot cm] = \frac{0.025}{0.630 \times 30 \times 10^{-4}} \left[\frac{V\cdot Cm^2}{A\cdot cm}\right] = 13\ [\Omega\cdot cm]$$

This compares very favorably with the resistivity of sintered zirconia doped with 10 mole percent yttria which is between 11 and 12 ohm centimeters at this temperature.

SUMMARY

A high temperature fuel cell using a thin-film zirconia electrolyte, prepared by chemical vapor deposition, was tested successfully under current load in a single cell design. The test proved the gas tightness of the electrolyte. Resistive losses checked closely with those calculated from the resistivity and thickness of the electrolyte and resistance of the electrodes. The tested cell was thermally cycled four times without damaging the thin film structure. The performance of this single cell exceeds that required for the initial 100-kilowatt coal-burning fuel-cell power plant. Fuel electrode tests indicate that thin-film fuel cells will perform equally well on the fuel gas derived from the fluidized coal bed used in that plant.

The development of the thin-film fuel cell is an important step toward a commercial power generating system capable of producing electrical energy from coal at overall efficiencies approaching 60 percent. Further work is required to provide the thin-film cells with low-cost air electrodes and to interconnect them in batteries.

REFERENCES

(1) Zahradnik, R. L., Elikan, L., and Archer, D. H., "A Coal-Burning Solid-Electrolyte Fuel Cell Power Plant," ADVANCES IN CHEMISTRY SERIES, Number 47, page 343, 1965.

(2) Ibid.

(3) Sverdrup, E. F., Archer, D. H., Alles, J. J., Glasser, A. D., "Testing of Electrodes for High-Temperature, Solid-Electrolyte Fuel Cells," Hydrocarbon Fuel Cell Technology, Academic Press Inc., New York, 1965.

Dwg. 859A486

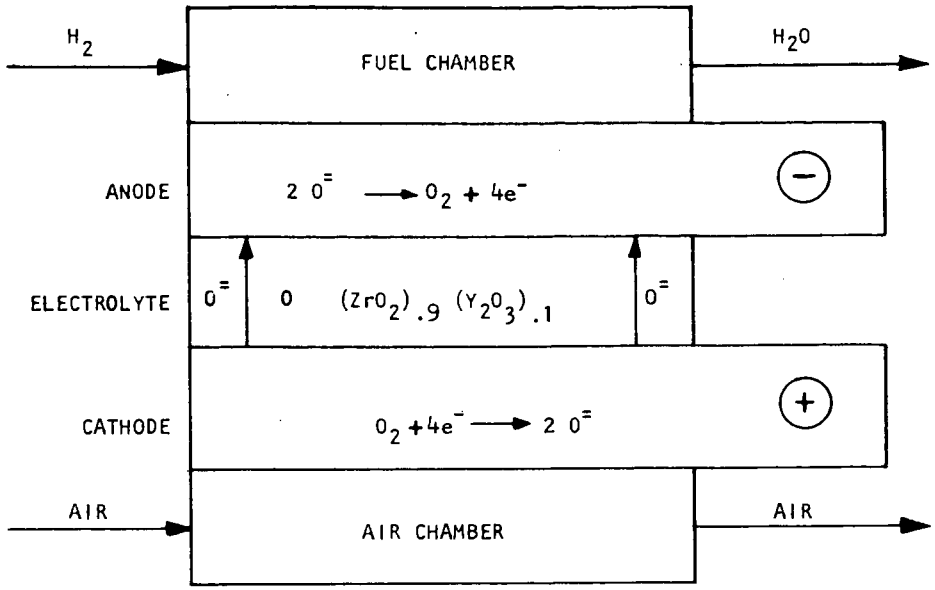

FIG. 1 OPERATING PRINCIPLE OF A SOLID ELECTROLYTE FUEL CELL

Dwg. 859A485

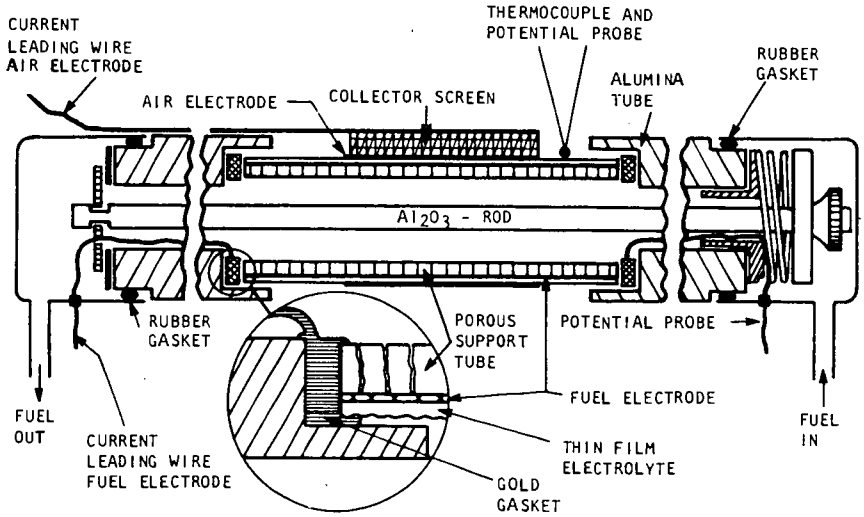

FIG. 2 TEST ARRANGEMENT FOR A THIN FILM ELECTROLYTE FUEL CELL

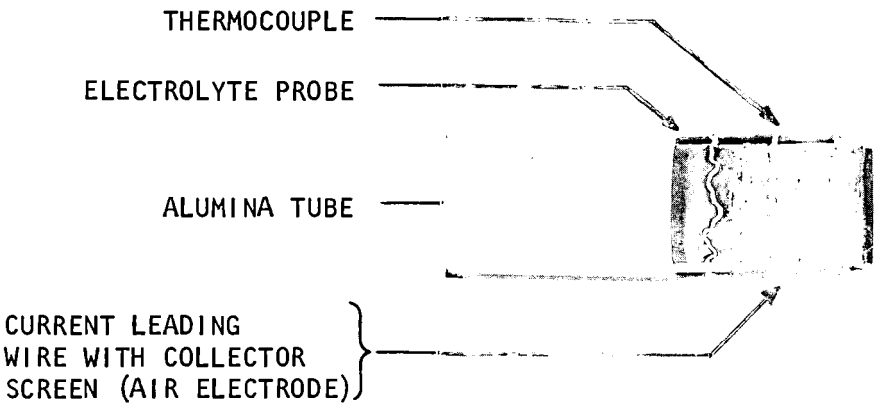

FIG. 3 ASSEMBLED THIN FILM ELECTROLYTE FUEL CELL

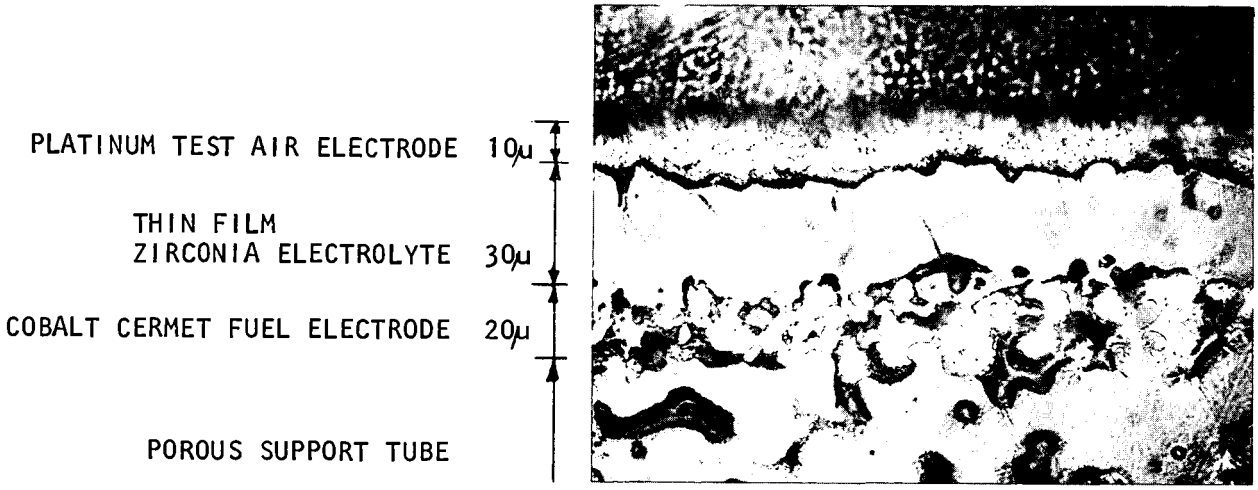

FIG. 4 CROSS SECTION THROUGH A THIN FILM
ELECTROLYTE FUEL CELL AFTER OPERATION

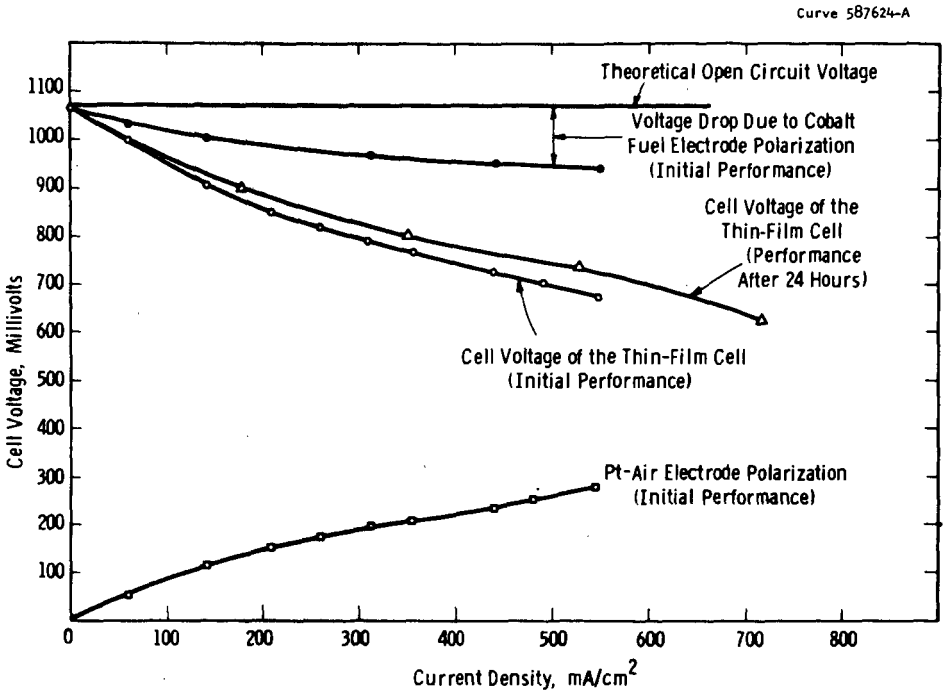

FIG. 5 PERFORMANCE OF A THIN FILM FUEL CELL AT 950°C WITH H_2+ 3% H_2O AS FUEL AND WITH AIR

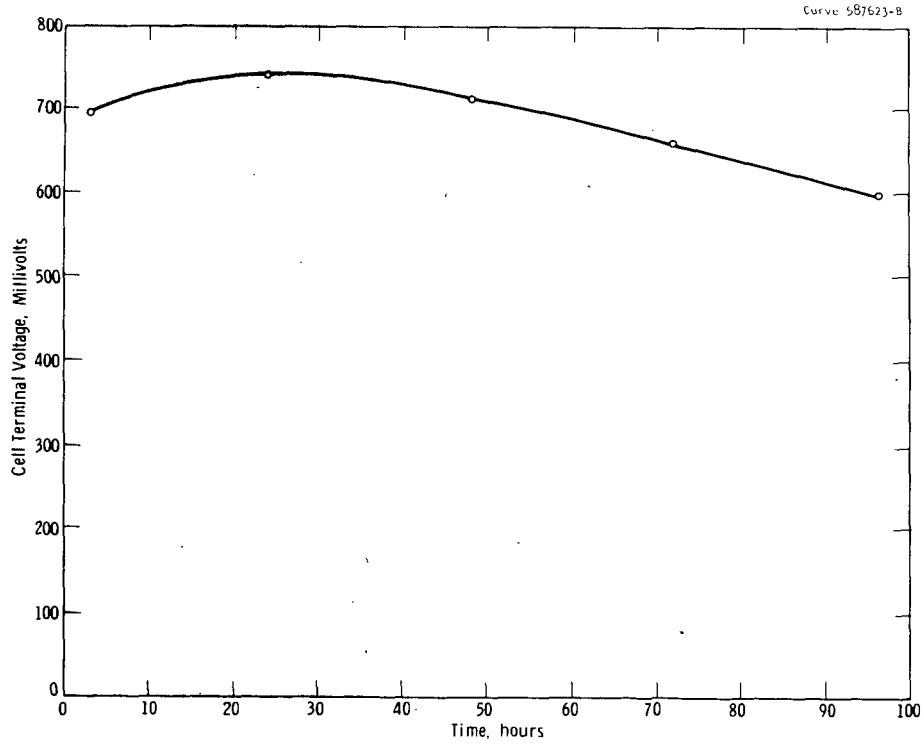

FIG. 6 TIME DEPENDENCE OF CELL PERFORMANCE (CELL VOLTAGE AT A LOAD OF 500 mA/cm^2)